Optimization of spin-orbit magnetic-state readout in metallic nanodevices

A thesis presented for the degree of Doctor of Philosophy

by

Inge Groen

Under the supervision of

Prof. F. Casanova & Prof. L. Hueso

eman ta zabal zazu

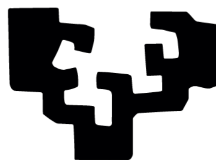

Universidad del País Vasco Euskal Herriko Unibertsitatea

The University of the Basque Country

February 2022

(cc) 2022 Inge Groen (cc by-nc 4.0)

Abstract

Nowadays, a life without mobile phones, laptops, cars, televisions and other similar devices is for many people unimaginable. On a larger scale, these product are made possible and affordable by automated manufacturing in big factories. The electronic devices as well as the automated manufacturing machinery all dependent on nanoelectronics. The developments in nanoelectronics in the last decades gave us smaller, faster and more energy efficient technologic solutions leading to modern day life. However, the environmental impact of this industrialization became apparent and more energy efficient technological solutions have to be found.

A more energy efficient change starts from the smallest building blocks of our technology, that is, integrated circuits such as a central processing unit. Such circuits use nanoelectronics to store and compute information. Traditionally, these integrated circuits are constructed out of complementary metal-oxide-semiconductors (CMOS). A promising field for improved technological solutions is spintronics. Several spin-based devices are already complementing CMOS technology permitting improved reading via spin valves exploiting tunneling magnetoresistance, and writing via spin-transfer torque or spin-orbit torque, of magnetic states in magnetic random access memory (MRAM). In spite of the development and implementation of spin-based devices for reading and writing memory states in MRAM, these devices are not able to generate a voltage or current that allows driving of subsequent elements, and enabling logic operations for beyond-CMOS applications. Logic operations are used for computing information in integrated circuits. Spin-based logic could provide advances in this area by integrating memory elements and logic operations within the same circuit.

The magneto-electric spin-orbit (MESO) logic device is a spin-based device recently proposed by Intel and the main motivation behind this thesis. The MESO device consists out of two nodes connected by a ferromagnetic material (FM). The FM is the memory and two possible in-plane ferromagnetic states along the easy

axis can be associated to the logic bits "1" and "0". The magneto-electric node is for writing of the magnetic state via collective switching of ferromagnetism and ferroelectricity or ferroelasticity. The spin-orbit node is designed to readout the magnetic state exploiting spin-charge interconversion (SCI) in strong spin-orbit coupling materials (SOM).

Various MESO devices can be connected to form cascaded gates doing an inverter operation. In these cascaded gates, a MESO device is connected to the next MESO device, such that the output of the spin-orbit node is the input for the next magneto-electric node. Hence, to achieve stable, energy efficient, and fast switching of the next FM element, the required spin-orbit node output voltage and current are 100 mV and 1 μA, respectively.

In this thesis, we use spin Hall devices, that are the spin-orbit node in the MESO device, for reading the magnetic states of the FM. Efficient detection of magnetic states at nanoscale dimensions is important for the development of MESO devices. In chapter 5, we show a favourable scaling law for the detection of an in-plane magnetic state of a FM electrode by using the inverse spin Hall effect in cobalt–iron/platinum ($Co_{50}Fe_{50}$/Pt) nanostructured devices. We obtain a large spin Hall signal of 0.3 Ω at room temperature by reducing the dimensions of the local spin Hall device. Even more, an effective spin-charge interconversion rate for the CoFe/Pt system is quantified and we predict that this spin–orbit detection of magnetic states could also be used to drive MESO logic.

The local configuration of the FM/SOM nanostructured device is prone to spurious signals. In chapter 6, we address spurious Hall effects that can contaminate the spin Hall signal in these local FM/SOM devices. The most pronounced Hall effects in the $Co_{50}Fe_{50}$/Pt nanostructures are the planar Hall effect and the anomalous Hall effect generated in the FM electrode. We find that the planar Hall effect, induced by misalignment between magnetization and current direction in the FM electrode, is manifested as a shift in the measured baseline resistance, but does not alter the spin Hall signal at saturated field. The anomalous Hall effect, arising from the charge-current distribution within the FM, adds to the spin Hall signal at saturated magnetic field. However, the effect can be removed by minimizing the shunting effect via proper design of the device. We conclude that local spin injection in FM/HM nanostructures is a suitable tool for measuring spin Hall signals and, therefore, a valid method for magnetic state readout in prospective spin-based logic.

We achieved enhanced output signals (0.03 mV with a bias current of 100 μA) by downscaling the local FM/SOM devices but larger spin Hall signals of around 1 kΩ (100 mV with a bias current of 100 μA) are required to read the magnetic state of a FM element in potential applications such as MESO logic. We shows in chapter 5 that introducing Ta as the SOM, results in an enhancement of the output signal by one order of magnitude 3.4 Ω.

In chapter 7, we explore spin properties of sputtered β-phase W to predict the expected SCI output signals in a local CoFe/W device. A lateral spin valve is employed to acquire the spin diffusion length and the SCI efficiency of this β-W as the local FM/SOM devices do not permit individual extraction of these two spin properties. A large SCI is measured, however, an unexpected oxide layer with a significant resistance is observed at the interface between Cu and W electrodes, denying the access to the spin properties of W. The interfacial spin absorption and SCI are quantified using an universal theoretical framework and present values larger than those of Cu/BiO_x and Cu/Au interfaces and corresponding bulk spin properties in Pt. This type of interfaces with large SCI efficiency might be beneficial for the readout in the MESO device. Additionally, although the aim of this study was not to obtain a highly resistive interface layer with large SCI but to investigate bulk properties of W, the take-home message of this chapter became that interface properties have to be carefully considered when studying spin transport in metallic devices.

To conclude, this thesis presents the first steps of the optimization of the magnetic-state readout component for the envisioned MESO-logic device. We established that (i) reducing the device dimension of FM/SOM nanostructured devices leads to an enhancement of the output signals; (ii) spurious effects in the device due to the local configuration can be avoided by proper design of the FM and SOM electrodes; (iii) interface properties and interfacial SCI have to be carefully considered when studying spin transport in metallic devices and such interface might be applicable for the MESO-logic devices.

Even tough we did not achieve the required values for the realization of cascaded gates with MESO devices, we did find a guideline for further improvement of the output signals. Besides the independent scaling laws for voltage and charge output signals, the use of other materials systems with large SCI efficiency and high resistivities seems to be promising for enhanced output signal. Further experiments are required to demonstrate the use of our device as a current source for driving spin logic circuits, but we anticipate that a MESO-logic device is feasible.

Resumen

La nanoelectrónica domina nuestro mundo. Los dispositivos móviles, los portátiles y las enormes fábricas automatizadas que los producen existen debido a los avances en nanotecnología de las últimas décadas. Aunque que se han logrado grandes éxitos, aún continúa la búsqueda de soluciones tecnológicas más pequeñas, rápidas y energéticamente eficientes que permitan una maquinaria más sofisticada y personalizada. Actualmente, los circuitos integrados, como las unidades centrales de procesamiento (CPU), se basan en la tecnología del semiconductor complementario de óxido metálico (CMOS). Los avances en el proceso de fabricación de los dispositivos CMOS permitieron una reducción importante del tamaño de los transistores, lo que resultó en transistores más rápidos, de menor consumo y más baratos.

Aunque la tecnología CMOS ha tenido éxito en las últimas 4 décadas, hoy está llegando a su límite. Los dieléctricos más delgados y los canales más cortos en dispositivos CMOS de pequeña escala los hacen más propensos a sufrir fugas y calentamiento, lo que limita la densidad y la velocidad del dispositivo. Por tanto, es necesario encontrar una tecnología más allá de CMOS que permita reducir estos efectos para poder continuar con las mejoras tecnológicas en la eficiencia informática. Este nuevo horizonte tecnológico, llamado beyond-CMOS, debe permitir una alta eficiencia energética y densidad lógica computacional, memoria no volátil en lógica (y viceversa) y debe ser compatible con arquitecturas tradicionales y emergentes. Hasta ahora, la investigación se ha centrado en la implementación de nuevos materiales en combinación con nuevos dispositivos/arquitecturas, así como en aprovechar la nueva física.

Una alternativa a CMOS en la que se está avanzando considerablemente es la espintrónica, donde además de la carga electrónica también se aprovecha el espín del electrón. En la espintrónica se estudian la inyección, el transporte, la manipulación y la detección del grado de libertad de espín de los electrones. Nuestros

ordenadores procesan y almacenan información en código binario, es decir, "1" y "0". Los metales ferromagnéticos pueden tener uno de dos estados magnéticos, dependiendo de la alineación de los espines electrónicos. Por tanto, estos materiales pueden utilizarse para almacenar información si asociamos cada uno de los dos estados magnéticos a "1" y "0". La espintrónica proporciona los medios para escribir y leer estos estados magnéticos.

El primer paso para la lectura de estados magnéticos, por el cual A. Fert y P. Grünberg recibieron el premio Nobel de física (2007), fue el descubrimiento de la magnetorresistencia gigante (GMR) a finales de la década de 1980. La GMR permite la detección de pequeños campos magnéticos y gracias a esto sirvió para desarrollar la llamada válvula de espín, la cual encontró rápidamente aplicación en cabezales de lectura magnéticos en discos duros. Una versión mejorada de la válvula de espín es la unión de túnel magnética (MTJ), basada en la magnetorresistencia túnel (TMR). Este tipo de válvula puede utilizarse como elemento de memoria en la memoria de acceso aleatorio magnetorresistiva (MRAM) y permite obtener una densidad superficial mucho mayor que las válvulas de espín clásicas.

La escritura de estados magnéticos en uniones MTJ integradas en MRAM se logró por primera vez mediante campos de Oersted inducidos por corrientes de carga. Un nuevo tipo de MRAM, el MRAM de par por transferencia de espín (spin-transfer torque, STT), permite optimizar el proceso de escritura. La producción en masa de la MRAM basada en STT por parte de las principales compañías de electrónica (Sony, Intel y TSMC) comenzó en 2020. Uno de los últimos avances en el proceso de escritura de estados magnéticos es el desarrollo del MRAM de par espín-órbita (spin-orbit torque, SOT), el cual se basa en conceptos de spin-orbitronics, que aprovecha el acoplamiento entre el momento magnético de espín y el momento orbital de electrones.

A pesar del desarrollo y la implementación de dispositivos basados en el espín para la lectura (a través de TMR) y la escritura (a través de STT o SOT) de estados magnéticos en MRAM, dichos dispositivos no son capaces de generar un voltaje o corriente que permita operar los siguientes elementos conectados del circuito para realizar operaciones lógicas con ellos. Las operaciones lógicas se utilizan para la computación de la información en circuitos integrados. La lógica basada en espín podría proporcionar avances en este campo, ya que haría posible integrar tanto elementos de memoria como operaciones lógicas en un mismo circuito. Un dispositivo lógico basado en espín propuesto recientemente por Intel es el dispositivo lógico magnetoeléctrico espín-orbita (MESO). Dicho dispositivo es básicamente un inversor. Su puerta en cascada (cascaded gate) permite realizar operaciones

lógicas mediante la conexión de un dispositivo MESO a otro. En una puerta en cascada de este tipo, la salida del primer dispositivo MESO es la entrada para el siguiente. La simulación de una unidad lógica aritmética de 32 bits basado en tecnología MESO ha dado resultados muy prometedores: comparado con tecnologías CMOS avanzadas y otras propuestas beyond-CMOS, la simulación MESO tiene un menor consumo de energía, un mayor rendimiento y una menor densidad lógica superficial. Para lograr una conmutación (switching) estable, energéticamente eficiente y rápida del elemento ferromagnético en el próximo dispositivo MESO, el voltaje de funcionamiento y la corriente de lectura requeridos son 100 mV y 1 µA, respectivamente. El objetivo principal de esta tesis es la realización y optimización del proceso de lectura en el dispositivo lógico MESO.

El dispositivo MESO tiene dos nodos: uno magnetoeléctrico (ME) para escribir, y otro espín-órbita (spin-orbit, SO) para leer el estado magnético de un material ferromagnético. El proceso de escritura en el nodo ME se basa en la conmutación colectiva ferromagnética y ferroeléctrica o ferroelástica debido a su potencial para conseguir una energía de conmutación ultrabaja. El nodo SO consiste en un material ferromagnético que actúa como memoria y como el material de acoplamiento espín-órbita fuerte (SOM) utilizado para la lectura. La lectura de los estados magnéticos se logra aplicando una corriente de polarización a través del dispositivo de tal manera que se inyecta una corriente polarizada en espín en el SOM. La interconversión espín-carga (SCI) en el SOM transforma la corriente de espín en una corriente de carga transversal y crea una diferencia de potencial entre los dos extremos de la capa SOM. La corriente de salida y el voltaje serán opuestos dependiendo de si el estado magnético es "1" o "0".

Tal y como se describe en el párrafo anterior, el SCI convierte la corriente de espín en corriente de carga o viceversa. El origen de este efecto es el fenómeno de acoplamiento espín-órbita (spin-orbit coupling, SOC), es decir, la interacción entre el momento angular de espín y el momento angular orbital. Dicho acoplamiento puede aparecer en sistemas bidimensionales y tridimensionales como metales pesados, interfaces de heteroestructuras, aislantes topológicos y dicalcogenuros de metales de transición. En los dispositivos estudiados para esta tesis se han utilizado metales pesados (HM) como SOM.

La SCI en HM ha sido ampliamente estudiada, en particular en el caso del Pt, que, además de tener una alta eficiencia SCI y también es un material estable, es decir, no se oxida, lo que lo convierte en un candidato perfecto para estudiar dispositivos de lectura. Los metales pesados muestran un efecto SCI en volumen, es decir, el efecto Hall de espín (spin-Hall effect, SHE, carga a espín) y el efecto Hall de espín

inverso (inverse spin-Hall effct, ISHE, espín a carga). La relación entre la densidad de corriente de carga y la densidad de corriente de espín es el ángulo Hall de espín para el SHE (y viceversa para el ISHE) y define la eficiencia de la SCI. Tanto el ISHE como el SHE se pueden usar para detectar el estado de magnetización de un elemento ferromagnético (FM) en una nanoestructura: el ISHE se puede usar para convertir una corriente de espín inyectada eléctricamente desde el elemento FM en un voltaje, y el SHE se puede usar para convertir una corriente de carga en una corriente de espín, que luego es detectada por el potencial electroquímico dependiente del espín del elemento FM.

Un ejemplo típico de nanoestructuras metálicas que utilizan el SHE (ISHE) para la inyección (detección) de espín son las válvulas de espín laterales (LSV) desarrolladas para cuantificar el SHE a través de técnicas no locales. Estos dispositivos consisten en un electrodo FM y un electrodo SOM, que están separados por un canal no magnético (NM) con SOC débil para transportar las corrientes de espín entre ellos. La LSV de configuración no local funciona con la inyección de corrientes de espín puro. El uso de corrientes de espín puro es conveniente para la cuantificación del SHE, ya que elimina las señales espurias asociadas a efectos locales. Por el contrario, para una aplicación potencial como la lógica MESO, las LSV presentan la desventaja de una fuerte reducción de la señal de espín causada por la caída exponencial de la corriente de espín y la derivación de la corriente de carga generada en el canal de transporte, así como el flujo de retorno (backflow) del espín en el electrodo FM. Debido a esto, las señales Hall de espín son relativamente pequeñas, alrededor de 0.1–1.0 mΩ. Una forma de superar estos problemas es eliminando el canal de transporte e inyectando y detectando la corriente de espín directamente en la interfaz FM/SOM, como en el nodo SO. La inyección/detección de espín local en nanoestructuras FM/SOM más simples puede mejorar la señal Hall de espín, llegando ésta a alrededor de 1-10 mΩ. Sin embargo, para leer el estado magnético de un elemento FM en aplicaciones potenciales como la lógica MESO, se requieren señales Hall de espín incluso más grandes, de alrededor de 1-10 kΩ.

Las nanoestructuras FM/SOM están formadas por un electrodo nanoestructurado SOM en forma de T y un electrodo FM cuya punta se encuentra sobre la intersección de la nanoestructura en forma de T. El dispositivo funciona como el nodo SO. La magnetización del electrodo FM se alinea y se conmuta a lo largo del eje fácil con un campo magnético externo. El ISHE se mide aplicando una corriente de polarización I_{bias} desde el electrodo FM al electrodo SOM. Se inyecta una corriente polarizada en espín en el SOM. El SOC fuerte del SOM produce una corriente de carga ISHE transversal, que se detecta como un voltaje V_{ISHE} en condiciones de

circuito abierto a lo largo del electrodo SOM transversal. La inversión de la magnetización induce un cambio de signo de V_{ISHE}. La resistencia Hall de espín R_{ISHE} se define como $V_{\mathrm{ISHE}}/I_{\mathrm{bias}}$ y la diferencia entre los dos estados de resistencia, asociados a los dos estados de magnetización, es la señal Hall de espín. Ésta se utiliza para cuantificar los dispositivos. En el capítulo 5, informamos sobre una ley de escala favorable para la lectura de un estado magnético por SHE en dispositivos nanoestructurados FM / SOM locales y mostramos que se pueden obtener grandes señales Hall de espín de 0.3 Ω a temperatura ambiente. En particular, utilizamos el ISHE para la conversión de espín a carga en nanoestructuras $Co_{50}Fe_{50}$/Pt y encontramos que el voltaje de salida (necesario para leer la magnetización en el plano) y la corriente de salida (necesaria para los elementos del circuito en cascada) se pueden mejorar de forma independiente al disminuir las dimensiones del dispositivo. Las grandes señales Hall de espín resultan de las pequeñas dimensiones y altas resistividades de Pt y CoFe, mientras que la tasa de conversión efectiva de espín a carga permanece constante para el sistema CoFe/Pt.

Además, extrapolando nuestros datos, sugerimos que la señal Hall de espín podría acercarse aún más a los valores requeridos para implementar la lógica MESO mediante el uso de materiales alternativos. Sin embargo, se requieren más experimentos para demostrar el uso del dispositivo FM/SOM local como fuente de corriente para operar circuitos lógicos de espín. Prevemos que el acoplamiento (locking) entre momento y espín en aislantes topológicos y el efecto Rashba en interfaces podrían usarse para lograr una mayor eficiencia del SCI con alta resistividad. Esto podría llevar a una mejora en la lectura de voltaje en dispositivos miniaturizados y en su salida de corriente, dos ingredientes que son esenciales para la realización de operaciones lógicas en aplicaciones computacionales.

El capítulo 6 trata los voltajes transversales espurios que pueden surgir en la configuración de medición electrónica local de los dispositivos nanoestructurados FM /SOM debido a la utilización de corrientes polarizadas por espín en lugar de corrientes de espín puro. Los efectos Hall que emulan fuertemente el (I)SHE son el efecto Hall anómalo (AHE) y el efecto Hall plano (PHE). Para poder hallar el SHE real y hacer una lectura fiable del estado magnético en el dispositivo lógico MESO, es necesario entender los diferentes efectos espurios de Hall en las nanoestructuras FM/HM en forma de T: el PHE en el FM se debe a la desalineación de la magnetización y la corriente de carga en la dirección plana, y el AHE aparece debido a las líneas verticales en la distribución de densidad de carga-corriente no homogénea en el lado FM de la región de inyección (el efecto Hall ordinario en el

HM causado por campos magnéticos generados por el electrodo FM es despreciable).

Debido a que el PHE aparece con una simetría diferente a la del ISHE, una desalineación del ángulo entre el campo magnético externo y el electrodo FM puede inducir un cambio en la resistencia transversal y distorsionar su forma. Este desplazamiento del PHE se puede obtener y corregir realizando una medición de la resistencia transversal en función del ángulo. Sin embargo, la contribución del PHE no afecta la lectura de la señal Hall de espín en campos magnéticos saturados. Por otro lado, el AHE aparece con la misma simetría que el ISHE, y por lo tanto, desenredar la señal de Spin Hall no es sencillo. Sin embargo, combinando mediciones eléctricas con simulaciones con el método elementos finitos en tres dimensiones, se puede estimar la contribución de AHE a la señal medida. Otras simulaciones muestran que la contribución del AHE se puede minimizar ajustando los espesores de los electrodos FM y HM. Hallamos que el AHE representa menos del 10% de la señal medida para la muestra $co_{50}Fe_{50}$(15 nm)/Pt(8 nm) utilizada en el estudio.

Nuestros resultados muestran que los efectos espurios de Hall en nanoestructuras FM/HM en forma de T se pueden distinguir y minimizar. Por lo tanto, confirman que estos dispositivos se pueden utilizar como una herramienta sencilla para medir la señal Hall de espín y extraer la eficiencia de conversión de espín a carga del sistema, así como como un método fiable para la lectura de estados magnéticos en el plano. La importancia de la evaluación comparativa de materiales se enfatiza en el capítulo 5, donde buscamos reemplazar el material SOM en el dispositivo FM/SOM local por otro material con una eficiencia SCI mayor, como Pt, para cumplir con los requisitos del dispositivo MESO. Dos candidatos metálicos obvios son el W y el Ta, que se han estudiado ampliamente y tienen una eficiencia SCI intrínseca mayor que la de Pt. W y Ta tienen un ángulo Hall de espín negativo, lo que significa que el SHE desvía electrones en dirección opuesta en comparación con el SHE en Pt. Sin embargo, esto no importa para la lectura con nuestro dispositivo Hall de espín local porque investigamos la diferencia entre los dos estados magnéticos saturados. La mejora de la eficiencia Hall de spin debería llevar a un aumento en la tasa efectiva del SCI del sistema FM/SOM. Además, las resistividades de W y Ta son en general mayores que la resistividad de Pt. Esto sería ventajoso para el factor geométrico que cubre la derivación eléctrica (shunting). Sin embargo, el aumento de la resistividad también generaría más backflow, reduciendo la cantidad de corriente de espín inyectada. Para evitar una reducción del backflow para SOM de alta resistencia, la implementación de una interfaz re-

sistiva sería beneficiosa. Presentamos una mejora significativa de la señal Hall de espín en un dispositivo SH local de CoFe/Ta con una interfaz resistiva de AlOx.

En el capítulo 7 queríamos explorar los materiales y las propiedades de espín de W pulverizado para predecir las señales Hall de espín esperadas de un dispositivo SH local CoFe/W. Se emplea una válvula de espín lateral no local para adquirir la longitud de difusión del espín y la eficiencia SCI del W, ya que los dispositivos FM/SOM locales no permiten la extracción individual de las propiedades del espín. Se mide un SCI grande, sin embargo, se observa una capa de interfaz de óxido inesperada con una resistencia de interfaz significativa entre los electrodos Cu y W, impidiendo el acceso a las propiedades de espín de W. La absorción de espín interfacial y el SCI se cuantifican utilizando el marco teórico universal y son más altas en comparación con los sistemas Cu/BiOx y Cu/Au, pero comparables con Pt. Aunque el objetivo de este estudio no era obtener una capa de interfaz resistiva alta con SCI alto, sino estudiar las propiedades de volumen de W, el mensaje de este capítulo es que las propiedades de la interfaz deben considerarse cuidadosamente al estudiar el transporte de espín en dispositivos metálicos. Sin embargo, este tipo de interfaces podría servir para el proceso de lectura en un dispositivo MESO.

En conclusión, esta tesis presenta los primeros pasos en la optimización del componente de lectura de estado magnético para un posible dispositivo lógico MESO. Podemos concluir que (i) la reducción de la dimensión de los dispositivos nanoestructurados FM/SOM conduce a una mejora de las señales de salida; (ii) los efectos espurios en el dispositivo debidos a la configuración local pueden evitarse mediante el diseño adecuado de los electrodos FM y SOM; (iii) las propiedades de interfaz y el SCI interfacial deben considerarse cuidadosamente a la hora de estudiar el transporte de espín en dispositivos metálicos. Aunque no logramos los valores requeridos para la realización de las puertas en cascada en los dispositivos MESO, sí encontramos una guía para una mayor mejora de las señales de salida. Además de presentar leyes de escalado independientes para las señales de salida de voltaje y carga que muestran que la reducción de las dimensiones del dispositivo aumenta las señales de salida, sugerimos que el uso de otros materiales con mayor SCI y altas resistividades podría llevar a un aumento adicional en la señal de salida. Se requieren más experimentos para demostrar el uso de nuestro dispositivo como fuente de corriente para operar circuitos lógicos de espín, pero prevemos que un dispositivo lógico MESO es posible.

Optimization of spin-orbit magnetic-state readout in metallic nanodevices

Abstract i

Resumen iv

1 The rise of spin-orbitronics 1

1.1 The silicon era 2
1.2 Spin-based writing and reading of magnetic states 3
1.3 Magneto-electric spin-orbit logic 5
1.4 This thesis 9

2 What about spins? 11

2.1 Spin transport 12
2.1.1 Spin 12
2.1.2 Charge and spin current 13
2.1.3 Spin accumulation and diffusion 16
2.1.4 Spin relaxation mechanisms 19
2.2 Bulk spin-charge interconversion 20
2.2.1 Spin-orbit coupling 21
2.2.2 Ordinary and anomalous Hall effect 22
2.2.3 Spin Hall effect 23
2.2.4 Mechanisms behind the spin Hall effect 25
2.3 Interfacial spin-charge interconversion 28
2.3.1 Rasbha Effect 28
2.3.2 Rasbha-Edelstein Effect 29
2.3.3 Other interfacial spin-orbit coupling effects 31
2.3.4 Universal spin-charge interconversion efficiency 33

3 Spin-orbitronic devices for the spin Hall effect 35

3.1 Materials benchmarking 36
3.2 Spin Hall effect devices: an overview 38

3.3 Lateral spin valves . . . 41
3.3.1 The basic working principle . . . 41
3.3.2 Conventional lateral spin valve . . . 41
3.3.3 Spin absorption technique . . . 45
3.3.4 Non-local spin Hall technique . . . 48
3.3.5 Limiting cases (bulk or interfacial) . . . 52
3.4 Local spin Hall device . . . 53
3.4.1 One-dimensional spin diffusion model . . . 53

4 Experimental techniques **59**
4.1 Nano-fabrication processes . . . 60
4.2 Characterization methods . . . 65
4.2.1 Electronic measurements . . . 65
4.2.2 Electron Microscopy . . . 66
4.2.3 X-ray characterization . . . 67
4.3 Finite element method simulations . . . 69
4.3.1 Interface resistance . . . 69
4.3.2 Electrical shunting . . . 70

5 Spin–orbit magnetic-state readout in scaled ferromagnetic/heavy metal nanostructures **73**
5.1 Experimental details . . . 75
5.2 Spin Hall signal for magnetic state detection . . . 76
5.3 Temperature dependence of the spin Hall signal . . . 78
5.4 Geometrical scaling of output current & voltage . . . 80
5.5 Equivalent circuit of the local spin Hall device . . . 81
5.6 Favourable miniaturization for spin Hall signals . . . 83
5.7 The spin Hall signal in a CoFe/Ta device . . . 86
5.8 Conclusions . . . 88
5.9 Appendices . . . 90
5.9.1 Reproducibility of the giant spin Hall signal and signal offset 90
5.9.2 3D numerical spin diffusion model . . . 91
5.9.3 Estimation of the anomalous Hall effect contribution . . . 93
5.9.4 Thermal effects . . . 95

6 Disentangling spin, anomalous, and planar Hall effects in ferromagnetic/ heavy metal nanostructures **97**
6.1 Device structure and fabrication . . . 98
6.2 Spin Hall effect . . . 99
6.3 Planar Hall effect . . . 100

6.4 Anomalous Hall effect 103
6.5 Conclusions 108
6.6 Appendices 109
6.6.1 PHE contamination in the SHE measurement 109
6.6.2 Ordinary Hall effect in the CoFe/Pt local spin Hall device . 111
6.6.3 The transverse resistance loop in the presence of the PHE . 114

7 Interfacial spin-charge interconversion in metallic Py/Cu/W lateral spin valve 117
7.1 Characterization of W 119
7.2 Py/Cu/W lateral spin valve 122
7.3 Characterization of the Cu/W interface 123
7.4 Spin absorption as the storyteller 126
7.5 Electrical shunting in the Cu/WO_x/W structure 128
7.6 Interfacial spin-charge interconversion at the Cu/WO_x interface . 130
7.7 Conclusions 133
7.8 Appendices 135
7.8.1 The sputter conditions defining the W resistivity 135
7.8.2 TEM characterization of the Cu/W interface 137
7.8.3 The spin properties of Py and Cu 138
7.8.4 Spin diffusion length for bulk spin absorption 139
7.8.5 3D FEM for shunting in the Cu/WO_x/W structure 140

8 The future of the MESO-logic device 143

References 161

Glossary 163

Chapter 1

The rise of spin-orbitronics

1.1 The silicon era

Nanoelectronics dominate our world. Mobile devices, laptops and huge automated factories all exists due to the developments in nanotechnology over the last decades. Whereas great successes have been achieved, the search for smaller, faster and more energy efficient technological solutions allowing more sophisticated and customized machinery is on going.

Currently, integrated circuits (such as a central processing unit (CPU)) are constructed out of complementary metal-oxide-semiconductors (CMOS) technology. The most famous building block of modern circuits is the CMOS field-effect transistor, fabricated by controlled oxidation of a semiconductor, typically silicon [1]. This transistor consists of a source and drain connected by a semiconducting channel in which the conductivity is controlled with a voltage gate. The control of the conductivity by the gate gives the transistor the ability to amplify or switch electronic signals.

The advancements in the fabrication process of CMOS devices allowed for a significant size reduction of the transistors resulting in faster, lower power, and cheaper transistors [2]. In 1965, Gordon E. Moore realized that, due to these improvements, the number of transistors on a micro-chip doubled every two years. This became to be known as Moore's law [3]. Some years later (1974) Dennard's law was introduced, which states that as the dimension of the devices go down, the power consumption stays constant [4]. These two laws have been the driving force of technological progress which led to improved integrated circuits and subsequently smaller and faster computers.

Though CMOS has been successful over the last 4 decades, the technology has reached a limit. Thinner dielectrics and shorter channels make scaled CMOS devices more prone to leakage and heating effects, constraining the downscaling of CMOS devices and, hence, device density and speed [5]. A beyond-CMOS technology, that permits reduction of leakage and heating effect, and continuation of the technological improvements in computer efficiency, has to be found. Even more, beyond-CMOS technology should allow high energy efficiency and computational logical density, non-volatile memory-in-logic (and vice versa) and has to be compatible with traditional and emerging architectures [6, 7]. Research has been focused on implementing new materials in combination with new devices/architectures as well as taking advantage of new physics such as spintronics and spin-orbitronics [8].

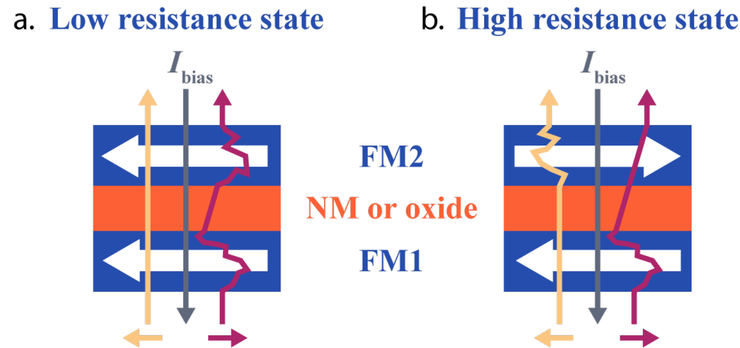

Figure 1.1: Reading of magnetic states in spin valves. A basic vertical spin valve constructed of FM1 with a fixed magnetization and FM2 with a switchable magnetization separated by a NM or oxide. The spin current with opposite spin orientations are indicated by yellow and red arrows. The spin-dependent scattering in the FMs when applying a bias current (grey arrow) gives rise to two different resistance states, the **a)** low resistance state (parallel configuration) and **b)** high resistance state (anti-parallel configuration), allowing for readout of the magnetic states.

1.2 Spin-based writing and reading of magnetic states

One of the thriving alternatives for CMOS is spintronics [9], where in addition to electron charge also electron spin is exploited. Spintronics involves the study on injection, transport, manipulation and detection of the spin degree of freedom of electrons and emerged from the observation of giant magnetoresistance (GMR) in the late 1980s. GMR was rapidly transferred to applications as magnetic field sensors and led to the Nobel prize in physics for A. Fert and P. Grünberg in 2007. The field of spintronics started with GMR but also pushed the search for other spin-based device solutions.

GMR occurs in metallic heterostuctures and describes the considerable change in electrical resistance of the structure when subjected to a magnetic field [10, 11]. The most basic GMR structures are vertical spin valves constructed of a non-magnetic metal (NM) layer sandwiched between two ferromagnetic metal (FM) layers as shown in figure 1.1a. FM1 of the spin valve has a fixed magnetization, while FM2 has a magnetization that can easily be switched, also known as the free layer. The electrical resistance of the structure depends on the relative magnetization in the FM layers, i.e., the spin-dependent scattering, when electric current is driven through the heterostructure (figure 1.1). Typically, the parallel and anti-parallel orientation of the FM layers in the spin valve lead to a low resistance

state and a high resistance state, respectively. The normalized difference between the low and high resistance, the magnetoresistance (MR) ratio, can reach about 15 %. This allows detecting small magnetic fields, therefore GMR spin valves were quickly used as magnetic read-heads in a hard drive.

An improved version of the spin valve is a magnetic tunnel junction (MTJ) [12, 13]. In these junctions, the NM is replaced by an oxide resulting in a FM/oxide/FM heterostructure. This device shows tunneling magnetoresistance (TMR), in which the current applied to FM1 has to obtain a certain energy in order to tunnel through the oxide and reach FM2. The MTJ relies on the relative orientation of the magnetization, like the spin valves based on GMR, but usually have a much higher MR ratio, easily reaching 500% [14–16].

Our computers process and store information in binary code meaning "1" and "0". FM can be used to store information by associating two opposite magnetized states to "1" and "0". The two distinct resistance states in MTJs are linked to the magnetization of the free FM layer, accordingly, MTJs can be used as a memory element in magnetoresistive random access memory (MRAM). This generation of spintronic devices with MTJs granted for a significant enhancement of the areal density [17, 18].

The writing of magnetic states in MTJs integrated in MRAM was first accomplished by Oested fields induced with charge currents, as displayed in figure 1.2a. This approach was used in the first commercial MRAMs in 2004 [19]. A second generation of spintronic devices was envisioned for further improvement of the writing process, relying on spin-transfer torque (STT) to switch the FM free layer, STT-MRAM [20, 21]. STT is an effect that can modify the orientation of the magnetization in FM2 due to a spin torque between two FM layers generated by a spin-polarized high-density current (figure 1.2b). The direction of the high-density current defines the magnetic state. Mass production of STT-based MRAM by the major electronics companies (Sony, Intel and TSMC) started in 2020 [22]. The drawback of this technology is the high-density current that has to be applied through the MTJ, making the device susceptible to break down and consequently limits its durability.

One of the latest advancement for writing magnetic states include spin-orbitronics where the coupling between spin magnetic momentum and electron orbital momentum is utilized for spin-orbit torque (SOT)-MRAM [23, 24]. In this approach, the MTJ is in direct contact with a material possessing spin-orbit coupling (SOC), a spin-orbit coupling material (SOM). A high-density current through the SOM pro-

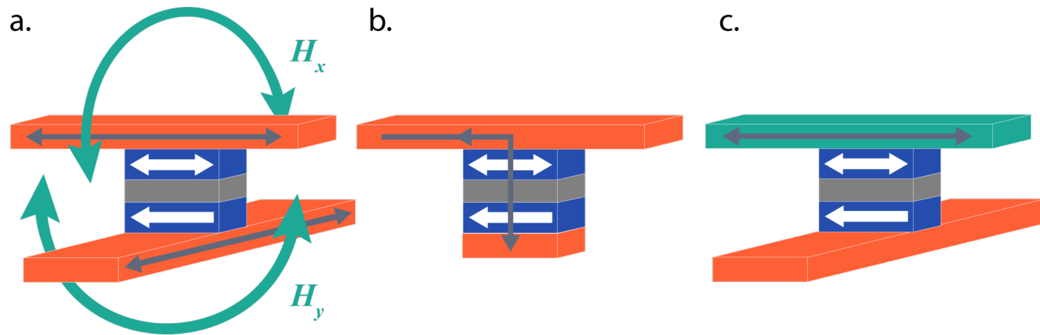

Figure 1.2: Writing of magnetic states for different MRAM generations. The writing of the magnetic states in MTJs can be achieved by the following three methods; **a)** Field-driven writing of magnetic states is done by inducing Oested fields (H_y and H_x) with two bias currents (grey arrows). Note that NM electrodes are presented in orange; **b)** STT relies on a torque between FM2 and the spin-polarized high-density current created by a bias current and FM1; **c)** In the SOT device, a SOM electrode (turquoise) is connected to FM2 in the MTJ. A bias current through the SOM causes charge-to-spin conversion producing a transverse pure spin current that exerts a torque on FM2 switching its magnetization. In all methods, the magnetic state in FM2 can be switched by reversing the current direction.

duces a pure spin current perpendicular to the interface with the FM. A SOT induced by the spin current can transfer angular momentum from the spin current to the FM, switch the magnetization in the FM (figure 1.2c) and write the magnetic state in this way [25, 26]. The first commercially available MRAM incorporating SOT is about to hit the market. The advantage of the SOT-MRAM is that high-density current through the MTJ is evaded. However, the writing of the magnetic state with SOT also relies on a high-density current. This density current is still one order magnitude larger than in STT and, therefore, further optimization of this technology is needed, which is actually one of the main objectives in spintronics today.

1.3 Magneto-electric spin-orbit logic

In spite of the development and implementation of spin-based devices for reading via TMR and writing via STT or SOT of magnetic states in MRAM, these devices are not able to generate a voltage or current that allows driving the subsequent elements and enable logic operations. Logic operations are used for com-

puting information in integrated circuits. Spin-based logic could provide advances in this field by integrating memory elements and the logic operations within the same circuit. Intel recently proposed the magneto-electric spin-orbit (MESO) device for spin-orbit logic [27]. This MESO device is the main motivation of this thesis and, during the time of this PhD project, we worked in close collaboration with Intel on the optimization of magnetic-state readout in the MESO device for spin-orbit logic.

The MESO device is constructed of two nodes. A magneto-electric (ME) node for writing of the magnetic state in the FM (figure 1.3a, right) and a spin-orbit (SO) node for reading of the magnetic state (figure 1.3a, left). The two possible in-plane ferromagnetic states along the easy axis of the FM can be associated to logic bits "1" and "0". Various MESO devices can be connected by a NM electrode to create cascaded gates. In the MESO proposal, the operation is spin-based but the transport of information is charge-based.

The writing process in the ME node (figure 1.3a, right) is established by collective switching, a switch that changes the order parameter defined by Landau's theory [27]. The collective switching is one of the leading solutions for computational advances owing the potential for ultralow switching energy and switching voltage. The MESO device includes ferroic order parameters with the collective switching of ferromagnetism and ferroelectricity or ferroelasticity.

Magnetization in FMs is an order parameter controlled by spin current or voltage. The ME material, actuator for magnetization of the FM, can be ferroelectric with polarization as a voltage-defined order parameter [28] or ferroelastic with strain as the order parameter controlled by strain or voltage [29]. A promising candidate for writing is the multiferroic BiFeO combined with ferromagnetic CoFe [27, 30]. In the MESO device, opposite input voltages generate a change of polarization or strain in the ME layer, that will induce exchange bias and coupling, and subsequently, a reversal of the magnetization in the FM. The polarization/magnetization reversal in ME/FM heterostructures is very energy efficient and should therefore enable aJ switching [7]. The energy barrier that provides switching stability relates to the switching speeds, retention times, and thermal fluctuations where the switching speed is characterized by the input current of the ME node.

Figure 1.3a (left) is the SO node for reading of the magnetic state. The readout of these magnetic states is done by applying a bias current through the stack such that a spin-polarized current is injected in the SOM. SCI in the SOC layer will transform the spin current into a transverse charge current and create a potential difference

between the two ends of the SOM layer. The output current and voltage will be opposite depending if the magnetic state is "1" or "0".

The MESO device, as shown in figure 1.3a, can be connected to another MESO device to form a cascaded gate doing an inverter operation. In such a cascaded gate, the SO node is connected to the next ME node, such that the output of the SO node is the input for the ME node. Hence, to achieve stable, energy efficient, and fast switching of the next FM element, the required SO node output signals for operating spin-orbit logic with the MESO device are 100 mV and 1 μA, respectively [7, 27].

Integration of the MESO device in a 32-bit arithmetic logic unit (ALU) has been simulated to compare the performance of this proposal to advanced CMOS and other proposals for beyond-CMOS technology. Figure 1.3b shows that the optimized MESO technology is predicted to have the lowest energy consumption. Figure 1.3c presents that MESO has a higher throughput in comparison to existing CMOS technology as well as the other beyond-CMOS proposals. Figure 1.3d displays that the areal logic density is lower than high performance CMOS and low voltage CMOS [27]. All this is due to the combination of the fields of magnetoelectrics and spin-orbitronics.

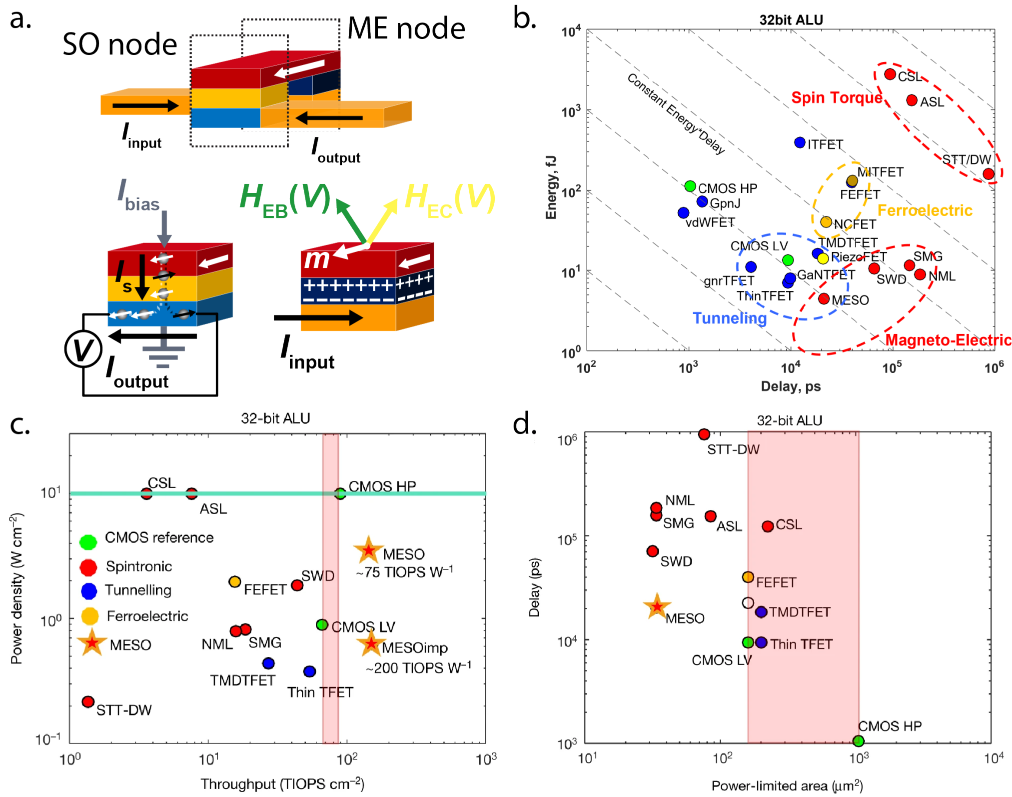

Figure 1.3: The MESO device and its performance in an ALU. a) A low-voltage-charge-based MESO device acting as an inverter. The ME node (right) includes a NM (orange), ME layer (dark blue) and FM layer (red). A current and voltage applied to the node will activate a switch of the FM magnetization (white arrow) exploiting coupling between the ME and the FM layers. The SO node (left) consists of FM layer (red), spin injection layer (yellow) and SOM (light blue). The magnetization can be read out by applying a bias current (I_{bias}), that will inject a spin-polarized current (I_{s}, where the opposite spin polarizations are presented by black and white arrows) into the SOM layer. A charge current I_{output} and a voltage potential difference V is generated via the SCI. The black arrows show the directions of the input and output currents of the device. **b)** The energy consumption versus the delay time [*courtesy of Ian A. Young*]; **c)** the power density versus operation per second and; **d)** the delay time versus power-limited area (that is, the areal density) of a 32-bit ALU with MESO in comparison to advanced CMOS and other beyond-CMOS proposals. Adapted from [6, 27]

1.4 This thesis

Chapter 1 (*The rise of spin-orbitronics*) gives a brief overview of the evolution of nanoelectronics in integrated circuits. While the modern circuits are still mainly constructed of CMOS technology, new technology based on spintronics and spin-orbitronics has been making their entry into the market. From the progress in the field of spin-orbitronics sprouted a proposal for spin-orbit logic with the MESO device. In the remainder of this thesis, we will focus on the optimization of the output current and voltage of the readout component in the MESO device.

Chapter 2 (*What about spins?*) provides the theoretical background that is needed to understand the spin physics that is used for designing and optimizing our nanodevices. The main topics are spin, spin transport, spin-orbit coupling, and spin-charge interconversion.

Chapter 3 (*Spin-orbitronic devices for the spin Hall effect*) presents the nanodevices that are used in this work: the lateral spin valve and the local spin Hall device. It discusses the considerations for designing the nanodevices based on the spin properties of different materials. Additionally, the spin transport and spin-charge interconversion are derived in both devices using the 1D spin-diffusion model.

Chapter 4 (*Experimental techniques*) gives details about the techniques used for fabrication and analyzing the lateral spin valve and the local spin Hall device. This includes nanofabrication, electrical measurements, electron microscopy, x-ray characterization, and 3D finite element method simulations.

The following two chapter are both studies on the local spin Hall device which is the readout element of the MESO device. **Chapter 5** (*Spin–orbit magnetic-state readout in scaled ferromagnetic/heavy metal nanostructures*) shows that enhanced output signals are achieved by downscaling the dimensions of the device. Even more, a separate scalability of the voltage and current output signals is found and a guideline for further improvement of these output signals is established. **Chapter 6** (*Disentangling spin, anomalous, and planar Hall effects in ferromagnetic/heavy metal nanostructures*) is about identification of spurious Hall effects that possibly lead to output signal reduction. Also, we specify adjustments that can be made to minimize such effects.

Chapter 7 (*Interfacial spin-charge interconversion in metallic Py/Cu/W lateral spin valve*) is a story on the importance of interfaces in metallic lateral spin valves. We discovered a highly resistive oxide layer between the Cu and W electrode and analysed the interfacial spin absorption and spin-charge interconversion at the Cu/oxide interface. The acquired spin-charge interconversion efficiency is quite large, making this interfacial system promising for magnetic-state readout in MESO devices.

Chapter 8 (*The future of the MESO logic device*) will be used to summarize the main results of this thesis and present future research steps that should lead to the realization of spin-orbit logic with the MESO device.

Chapter 2

What about spins?

2.1 Spin transport

Spintronic and spin-orbitronic devices aim at utilizing the spin degree of freedom of electrons for writing and reading of magnetic memory and logical information processing. The understanding of spin and spin transport is key for the development of these devices. Additionally, the relation between spin current and more conventional charge current is essential for comprehending the generation, injection, manipulation and detection of spin currents.

2.1.1 Spin

An electron is an elementary particle that carries negative electrical charge. The physics of an electron in an atom can be fully described by its four quantum numbers; the principal quantum number (n), the orbital quantum number (l), the magnetic quantum number (m_l) and the spin quantum number (m_s). The theory of Niels Bohr considers the hydrogen atom as a planetary model, hence a charged electron orbiting around a nucleus. n is defined as the quantized radius in which an electron is allowed to orbit and determines the energy level of the orbit. l relates to the orbital angular momentum **L** that describes the shape of motion of the electron around the nucleus. m_l describes the orientation in space of an orbital with a given energy n and shape l. m_s specifies the intrinsic angular momentum **S** that was postulated by G. Uhlenbeck and S. Goudsmit (1925) as the rotation of an electron about its own axis [31]. Therefore, the intrinsic angular moment is also known as spin. The Stern-Gerlach experiment (1922), in which silver atoms are deflected in opposite directions when moving though an inhomogenous magnetic field, provided experimental proof that atomic particles have an **S** with quantized spatial orientation [32].

The physics of spin was impossible to explain with the spinning electron model and spin was not well understood until the relativistic quantum mechanical derivation of Paul Dirac. Spin, a purely quantum mechanical parameter, posses discrete quantized values presented as the projection along an axis, usually the z-axis, that is $S_z = \hbar m_s$. The distribution of electrons is described by the Fermi-Dirac statistics, therefore m_s can take two discrete values $+\frac{1}{2}$ and $-\frac{1}{2}$, generally named spin up and spin down. Furthermore, electrons, being fermions, have to obey the Pauli exclusion principle which states: "*no two electrons can occupy the same quantum state*", resulting in the following definition [33]:

$$\mathbf{S} = \frac{\hbar}{2}\boldsymbol{\sigma}, \tag{2.1}$$

where $\boldsymbol{\sigma}$ are the Pauli spin matrices [34]. Even though spin cannot be explained by classical physics, it ultimately corresponds to a spin magnetic moment, that can be written as:

$$\boldsymbol{\mu}_\mathrm{S} = -g\frac{e}{2m_e}\mathbf{S}, \tag{2.2}$$

where e and m_e are the electron charge and mass, respectively. The Landé factor $g = -2.0023$ for electrons. For the understanding of the spin-related physics in this thesis, it is important to remember that spin $\mathbf{S}$ can take two values, spin up and spin down, with an associated spin magnetic moment $\boldsymbol{\mu}_\mathrm{S}$.

2.1.2 Charge and spin current

Solid materials consist of a periodic array of atoms held together by electromagnetic force. Within the solid, the atomic orbital can overlap creating electronic energy bands that describe the range of energy levels that electrons are allowed to occupy within the solid. The energy levels in conductors are continuous and the electrons are considered to behave as a so-called free electron gas. Here, the conduction of electron charge and spin in metals will be discussed.

An electron carries both charge and spin. The existence of a charge current, the flow of electron's charge in the presence of an electric field $\boldsymbol{E}$, is well established and is integrated in our modern day technology. The spin current, flow of spin angular momentum, is lesser known and the control of it is developed more recently.

The relation between the charge current density $\boldsymbol{j}_\mathrm{c}$ and $\boldsymbol{E}$ is:

$$\boldsymbol{j}_\mathrm{c} = \sigma\boldsymbol{E}, \tag{2.3}$$

where the conductivity σ is described by the Drude model and derived more than a century ago as:

$$\sigma = \frac{N(E_\mathrm{F})e^2\tau_e}{3m_e}, \tag{2.4}$$

where $N(E_\mathrm{F})$ is the electron density of states at the Fermi level. The electron momentum scattering time τ_e is proportional to the electron mean free path, the average distance an electron travels between two scattering events, $l_e = \tau_e v_\mathrm{F}$ with v_F being the Fermi velocity. The inverse of conductivity $(1/\sigma)$ is resistivity ρ.

The spin current and its relation to the charge current will be elucidated by reviewing the electron transport in NMs and FMs. Equation 2.4 shows that conductivity is defined by electrons at the Fermi level. Charge current in a NM is usually carried by s-band electrons. Figure 2.2c shows the density of states of spin-up $[N_\uparrow(E)]$ and spin-down $[N_\downarrow(E)]$ electrons in the s-band of a NM. NMs do not posses intrinsic magnetization and the properties of the two spin types at the Fermi level are equal $[N_\uparrow(E_\mathrm{F}) = N_\downarrow(E_\mathrm{F})$ and $\tau_\uparrow(E_\mathrm{F}) = \tau_\downarrow(E_\mathrm{F})$, where $\tau_\uparrow$ and $\tau_\downarrow$ are the spin-dependent momentum scattering time for spin up (↑) and spin down (↓)]. Thus, there is no difference in conductivity for electrons with spin up or spin down $(\sigma_\uparrow = \sigma_\downarrow)$.

In FMs, the charge current is conveyed by the s-band electrons and additional 3d-band electrons at the Fermi level. As 3d-band electrons are more localized than s-band electrons, 3d-band electrons define the degree of scattering of the more mobile s-band electrons and, consequently, the conductivity. Figure 2.2a shows the density of states for s-band and 3d-band electrons in a FM. FMs have a net magnetization due to an intrinsic exchange interaction E_ex that energetically favours parallel alignment of one type of spin carrier and induces a shift in the 3d-sub-band energy. The 3d-sub band in FMs are not completely filled therefore the shift E_ex generates an unbalance in the density of states of the spin-up and spin-down 3d-electrons at the Fermi level $[N_\uparrow(E_\mathrm{F}) \neq N_\downarrow(E_\mathrm{F})]$ creating majority and minority spin carriers. This unbalance means that the spin-down s-electrons have a different scattering rate (with the associated 3d-electrons) and mobility than the spin-up s-electrons, resulting in a conductivity that is different for the two types of spin carriers.

Electrical conduction in a FM was explained by Mott in the two-channel model, where the spin-up and spin-down electrons are considered to be flowing in two independent transport channels without interaction between the different spin carriers [35]. Fert and Campbell experimentally verified the validity of this model when studying the change of conductivity in ferromagnetic materials such as Fe, Ni, Co and their alloys [36]. The electrical conductivities for spin up and spin down as given by the two-channel model are

$$\sigma_\uparrow = \frac{N_\uparrow(E_\mathrm{F})e^2\tau_\uparrow}{3m_e} \quad \text{and} \quad \sigma_\downarrow = \frac{N_\downarrow(E_\mathrm{F})e^2\tau_\downarrow}{3m_e}. \tag{2.5}$$

The two independent spin channels can be considered as two parallel resistors with a total electrical conductivity $\sigma = \sigma_\uparrow\sigma_\downarrow/(\sigma_\uparrow + \sigma_\downarrow)$. The difference in spin transport of spin-up and spin-down electrons in FMs is characterized by the spin polarization:

$$P = \frac{\sigma_\uparrow - \sigma_\downarrow}{\sigma_\uparrow + \sigma_\downarrow}, \tag{2.6}$$

such that, $\sigma_\uparrow = \sigma(1 + P)/2$ and $\sigma_\downarrow = \sigma(1 - P)/2$. In the particular case of a NM, $P = 0$ and $\sigma_\uparrow/2 = \sigma_\downarrow/2 = \sigma$.

The spin carrier flow per unit time and unit area through the two associated spin transport channels, in the presence of a constant $\boldsymbol{E}$, is given by the current density:

$$\boldsymbol{j}_\uparrow = \sigma_\uparrow\boldsymbol{E} \quad \text{and} \quad \boldsymbol{j}_\downarrow = \sigma_\downarrow\boldsymbol{E}. \tag{2.7}$$

The total charge current density ($\boldsymbol{j_c}$) and spin current density ($\boldsymbol{j_s}$) are, respectively, given by

$$\boldsymbol{j}_\mathbf{c} = \boldsymbol{j}_\uparrow + \boldsymbol{j}_\downarrow, \tag{2.8}$$

$$\boldsymbol{j}_\mathbf{s} = \boldsymbol{j}_\uparrow - \boldsymbol{j}_\downarrow. \tag{2.9}$$

Figure 2.1a shows that the electron transport of an equal spin-up and spin-down population ($\boldsymbol{j}_\uparrow = \boldsymbol{j}_\downarrow$), results in a charge current ($\boldsymbol{j_c} \neq 0$) and no spin current ($\boldsymbol{j_s} = 0$). This is typically the case in a NM. Note that, even though a NM does not have an intrinsic spin polarization, a spin current can be injected as explained in the upcoming section 2.1.3. Figure 2.1b displays a difference between spin-up and spin-down currents ($\boldsymbol{j}_\uparrow \neq \boldsymbol{j}_\downarrow$), that consequently leads to both a net charge current ($\boldsymbol{j_c} \neq 0$) and spin current ($\boldsymbol{j_s} \neq 0$). Such spin-polarized current is commonly observed in FMs. Finally, it is possible to have a pure spin current, that is, opposite flow of spin-up and spin-down currents with no overall charge current ($\boldsymbol{j}_\uparrow = -\boldsymbol{j}_\downarrow$), as shown in figure 2.1c. The pure spin current is one of the most appreciated ingredients of spintronics, as it permits reduced the heat dissipation.

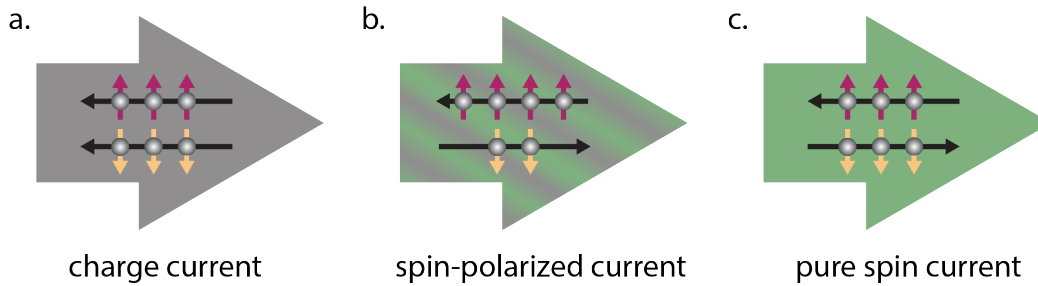

Figure 2.1: Types of electron current. The electron charge is displayed by grey circles and spin-up and spin-down electrons are represented by red and yellow arrows, respectively. Black arrows indicate the direction of flow of the spin carriers. **a)** Charge current, flow of electron charge (big grey arrow) with no net flow of spin. **b)** Spin-polarized current, a flow of both electron charge and spin (big grey/green arrow) due to an unbalance of the spin-up and spin-down carriers. **c)** Pure spin current, flow of only spin (big green arrow). The charge current is canceled by the electron charges moving in opposite direction.

2.1.3 Spin accumulation and diffusion

A electron flow through a simple transparent FM/NM interface is used as an example to explain the concepts of spin accumulation and spin diffusion. When applying an electric field to the FM/NM system, an out-of-equilibrium spin population at the FM/NM interface is created due to the mismatch in the spin density of states of the FM and NM. This results in a shift in the spin population of the s-sub band in the NM close to the interface as illustrated in figure 2.2b.

The shift can be explained in terms of electrochemical potential. The electrochemical potential is given by $\mu = \mu_{ch} - eV$ with μ_{ch} being the chemical potential, the energy associated to the addition of one particle to a system, and eV being the potential energy. The driving force of electron transport comes from either a spatial variation in the electron density $\boldsymbol{\nabla} n$ or an electric field $\boldsymbol{E} = -\boldsymbol{\nabla} V$. Here, the diffusive model ($\boldsymbol{\nabla} n \neq 0$, $\boldsymbol{E} = 0$) is used to describe electron transport at the FM/NM interface region. Diffusive transport can be fully defined by the difference in the electrochemical potential $\delta\mu_0$ between FM and NM.

Figure 2.2d shows the landscape of the total electrochemical potential μ_0 $[= (\mu_\uparrow + \mu_\downarrow)/2]$ close to the FM/NM interface. The electrochemical potential of the spin-up ($\mu_\uparrow$) and spin-down ($\mu_\downarrow$) population are related to the spin population in the spin-sub bands (figure 2.2a, 2.2b and 2.2c). Away from the interface, $\mu_\uparrow$ and $\mu_\downarrow$ are in equilibrium and equal to μ_0. However, $\mu_\uparrow$ and $\mu_\downarrow$ split close to the FM/NM interface

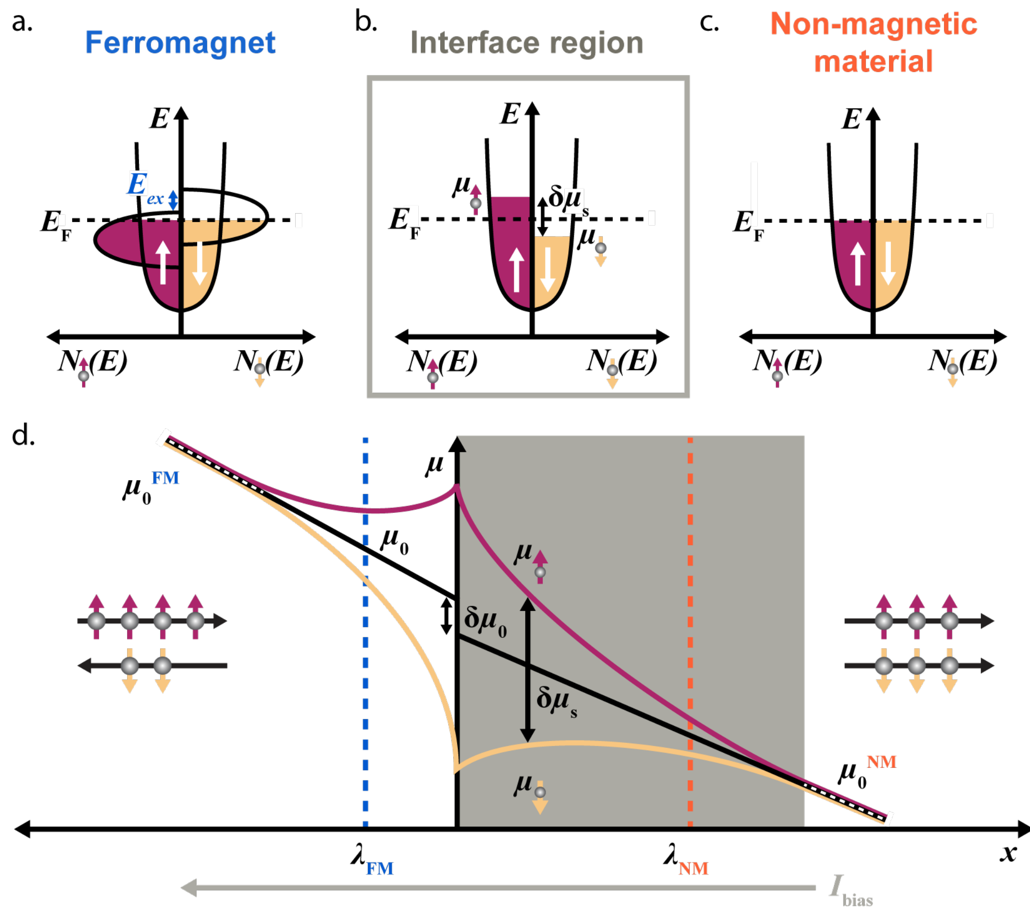

Figure 2.2: Electrochemical landscape of the FM/NM interface. The band structure of the s-band electrons have a parabolic shape and one of the 3d-band electrons have a closed ellipsoidal shape. The spin-up and spin-down electrons are displayed in purple and yellow, respectively. **a)** The FM band structure with s-band and 3d-band electrons. The intrinsic exchange energy (E_{ex}) between spin-up and spin-down electrons in FMs induces a shift in the 3d-sub bands altering the density of states ($N_\uparrow$ and $N_\downarrow$) at the Fermi level (E_{F}). **b)** The spin accumulation ($\delta\mu_{\text{s}}$) in the s-band of the NM close to the FM/NM interface due to a change in chemical potential of the spin-up and spin-down electrons, i.e., $\mu_\uparrow$ and $\mu_\downarrow$, induced by spin injection from the FM with I_{bias}. **c)** The s-band in a NM where the density of states are equal for spin-up and spin-down electrons. **d)** Schematic representation of the electrochemical potential landscape close to the FM/NM interface, for I_{bias} flowing along the $-x$-direction. The lines represent the electrochemical potential μ_0 (black) and the chemical potential for the majority $\mu_\uparrow$ (purple) and minority $\mu_\downarrow$ (yellow) spin population. The transition from FM to the NM produces a potential drop ($\delta\mu_0$) in μ_0 at the interface due to the spin accumulation ($\delta\mu_{\text{s}}$). $\delta\mu_{\text{s}}$ diffuses away from the interface into the FM and NM with the spin diffusion lengths λ_{FM} and λ_{NM} which defines the spin diffusion via $e^{x/\lambda}$.

causing spin accumulation:

$$\delta\mu_{\rm s} = \mu_{\uparrow} - \mu_{\downarrow}, \tag{2.10}$$

see figure 2.2d and 2.2b. Note that μ_0 is discontinuous as the spin accumulation introduces a potential drop $\delta\mu_0$. This discontinuity is related to the spin accumulation as:

$$\delta\mu_0 = \frac{2\delta\mu_{\rm s}}{P}. \tag{2.11}$$

In the case of a transparent interface, $P = P_{\rm FM}$ (equation 2.6). In the case of a resistive interface in the tunneling regime, $P = P_{\rm I}$, the interface polarization, defined as:

$$P_{\rm I} = \frac{N_{\uparrow}(E_{\rm F}) - N_{\downarrow}(E_{\rm F})}{N_{\uparrow}(E_{\rm F}) + N_{\downarrow}(E_{\rm F})}. \tag{2.12}$$

$\delta\mu_{\rm s}$ is maximum at the interface. The polarization of the diffusive spin current decays away from the interface over a characteristic time, the spin relaxation time $\tau_{\rm s}$ that is described by the spin-flip times ($\tau_{\uparrow\downarrow}$ and $\tau_{\downarrow\uparrow}$) as $1/\tau_{\rm s} = 1/\tau_{\uparrow\downarrow} + 1/\tau_{\downarrow\uparrow}$. In the diffusive regime, the spin diffusion length λ is given by $\sqrt{D\ \tau_{\rm s}}$ where D is the diffusion constant. Figure 2.2d displays the decay of the spin accumulation in both the FM ($-x$ direction) and the NM ($+x$ direction).

The statistical behaviour of such an out-of-equilibrium system at the FM/NM interface can be described by the Boltzmann equation model. Valet and Fert [37] showed that the Boltzmann equation model reduces to a macroscopic model when the mean free path is much smaller than the spin diffusion length ($l_e \ll \lambda$) such that the diffusion equations will become [37]:

$$j_{\uparrow} = \frac{\sigma_{\uparrow}}{e}\frac{\partial\mu_{\uparrow}}{\partial x} \quad \text{and} \quad j_{\downarrow} = \frac{\sigma_{\downarrow}}{e}\frac{\partial\mu_{\downarrow}}{\partial x}, \tag{2.13}$$

and

$$\frac{e}{\sigma_{\uparrow}}\frac{\partial j_{\uparrow}}{\partial x} = +\frac{\delta\mu_{\rm s}}{\lambda_{\uparrow}^2} \quad \text{and} \quad \frac{e}{\sigma_{\downarrow}}\frac{\partial j_{\downarrow}}{\partial x} = -\frac{\delta\mu_{\rm s}}{\lambda_{\downarrow}^2}, \tag{2.14}$$

given that the current density flow is in the x direction, perpendicular to the FM/NM interface and j_i, μ_i, σ_i and λ_i are the current densities, chemical potentials,

conductivities and spin diffusion lengths for the spin-up (i $=\uparrow$) and spin-down (i $=\downarrow$) population. Equation 2.13 simply reduces to Ohm's law in the limit $l_e \ll \lambda$. Equation 2.14 expresses particle conservation in steady-state conditions.

By considering charge conservation (equation 2.8), the spin accumulation $\delta\mu_{\rm s}$ (equation 2.10), and combining equation 2.14 with equation 2.13, the spin diffusion equations can be rewritten as:

$$\frac{\partial^2 \delta\mu_{\rm s}}{\partial x^2} = \frac{\delta\mu_{\rm s}}{\lambda^2}, \tag{2.15}$$

and

$$\frac{\partial^2}{\partial x^2}(\sigma_\uparrow \mu_\uparrow + \sigma_\downarrow \mu_\downarrow) = 0, \tag{2.16}$$

where λ is given by: $1/\lambda^2 = 1/\lambda_\uparrow^2 + 1/\lambda_\downarrow^2$. The general solution of these spin diffusion equations for the spin accumulation is:

$$\delta\mu_{\rm s} = Ae^{-x/\lambda} + Be^{x/\lambda}, \tag{2.17}$$

where the integration constants A and B have to be determined in each material by taking into account the proper boundary condition (BC) at the FM/NM interface ($x = 0$). The spin diffusion equations and its associated solution will be further developed in chapter 3 to determine the spin transport in the lateral spin valve (LSV) and the local spin Hall device.

2.1.4 Spin relaxation mechanisms

The spin transport is governed by λ, and many efforts to find suitable materials with long λ are underway in this field. In order to work with spin currents and design spintronic and spin-orbitronic devices, it is important to understand the relaxation mechanisms of spin. λ is material dependent and can be as short as sub-nanometers up to hundreds of micrometers depending on the spin relaxation mechanisms within the material. Different relaxation mechanisms are characterized by the relation between the spin relaxation time (τ_s) and the momentum relaxation time (τ_e). τ_s is the period of time within the electron preserves the spin. τ_e is the time in which the electron conserves the electron momentum ($\boldsymbol{k}$).

The **Elliot-Yafet relaxation mechanism** [38, 39] is observed in conductors with spatial inversion symmetry and no magnetic impurities indicating degenerate spin states ($E_{\boldsymbol{k}\uparrow} = E_{\boldsymbol{k}\downarrow}$). The spin relaxation in these type of materials is dominated by scatter centers like phonons, non-periodic impurities and grain boundaries. The mechanism is explained as spin-flip scattering due to the interaction of the spin with the local electric field (SOC) generated by the scatter centers. The spin-flip has a probability to occur during the scattering event, hence $\tau_s \propto \tau_e$. This relaxation mechanism dominates in semiconductors such as Si [40] and Ge [41], light metals with weak SOC, namely Cu [42, 43], Ag [44–46], and Al [43] and heavy metals with strong SOC including Pt [47] and Ta [48].

The **D'yakonov-Perel relaxation mechanism** [49] occurs in conductors with broken spatial inversion symmetry such that the spin states are non-degenerate ($E_{\boldsymbol{k}\uparrow} \neq E_{\boldsymbol{k}\downarrow}$) but the Kramer degeneracy (the conservation of time-reversal symmetry) is maintained ($E_{\boldsymbol{k}\uparrow} = E_{-\boldsymbol{k}\downarrow}$). The non-degeneracy of the spin states generates a momentum-dependent effective magnetic field, which leads to spin precession and subsequently spin relaxation. The electron momentum is modified during a scattering event, changing the effective magnetic field working on the electron and modifying the axis along which the spin presses in between scatter centers. The relation between the spin momentum relaxation and the momentum relaxation is $\tau_s \propto 1/\tau_e$. This is understood by considering that the more frequently the electron scatters (short τ_e), the less time it spends between one scatter center and another and therefore, there is less time for spin precession (long τ_s). The spin relaxation in III-V semiconductors (GaAs [50, 51]) as well as two-dimensional electron gas (2DEG) [52] and very thin metal films [47, 48] in which the inversion symmetry breaking is originates from an interface or surface, are covered by the D'yakonov-Perel relaxation mechanism.

2.2 Bulk spin-charge interconversion

The discovery of the spin Hall effect (SHE), that exploits SOC to convert spin current to charge current or vice versa, has lead to the birth of the field of spin-orbitronics. Devices based on spin-orbitronics are being realized and implemented in MRAM and are seen as a promising approach for more energy efficient logic circuits such as MESO logic. The exploration of SOC, SCI and the mechanisms behind SCI in this section are essential for understanding the advancements made in this thesis.

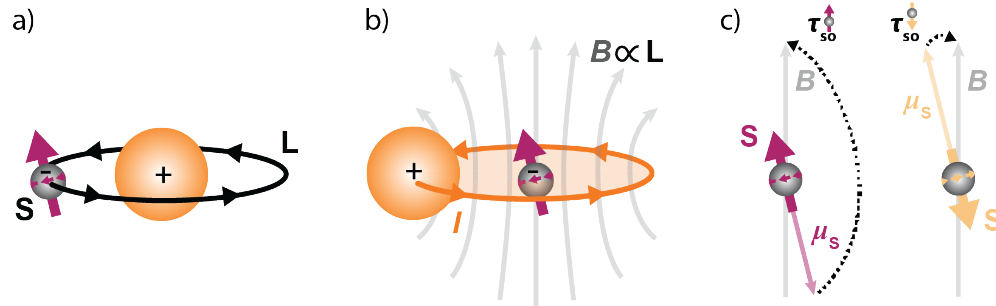

Figure 2.3: Spin-orbit coupling. The electron charge is displayed by the grey circle while the positive nucleus of the atom is presented by the orange circle. The spin-up and spin-down are indicated by red and yellow arrows, respectively. **a)** Representation of the electron with spin **S** orbiting around the nucleus of an atom where the motion of the electron is defined by **L**. **b)** In the reference frame of the electron, the positively charged nucleus orbits around the electron, creating a closed current loop ($\boldsymbol{I}$) which subsequently generates a magnetic field $\boldsymbol{B}$ proportional to **L**.

2.2.1 Spin-orbit coupling

Spin-orbit coupling (SOC) is the interaction between spin angular momentum **S** and orbital angular momentum **L** (see section 2.1.1). Figure 2.3a shows a simplified model of an atom with a negatively charged electron and an associated **S** orbiting around a positively charged nucleus where the orbital shape is given by **L**. From the rest frame of the atom, the electron seems to not feel any magnetic moment besides $\boldsymbol{\mu}_\mathrm{S}$ (section 2.1.1).

The relativistic effect of SOC is **S** interacting with the effective magnetic field that electrons feels in absence of an external magnetic field. The coupling between $\boldsymbol{\mu}_\mathrm{S}$ and this effective magnetic field $\boldsymbol{B}$ results in a splitting of atomic energy levels, similar to the Zeeman splitting, with a spin-orbit Hamiltonian:

$$H_\mathrm{SO} = -\boldsymbol{\mu}_\mathrm{S} \cdot \boldsymbol{B}, \tag{2.18}$$

The atom will now be considered from the rest frame of the electron in order to understand the effective magnetic field induced by **L**. In classical electrodynamics, a magnetic moment is defined in terms of an electric current and the area enclosed by the current loop. Figure 2.3b shows the atom configuration as seen from the rest frame of the electron. The positively charged nucleus, that orbits around the electron is the current loop $\boldsymbol{I}$, generating $\boldsymbol{B}$. **L** defines the shape of the current loop. The magnetic field will exert a torque $\boldsymbol{\tau}_\mathrm{SO}$ on $\boldsymbol{\mu}_\mathrm{S}$ of the electron. Figure 2.3c shows

a simplified picture of the coupling between $\boldsymbol{B}$ and $\boldsymbol{\mu}_{\mathrm{S}}$. While $\boldsymbol{B}$ is constant, $\boldsymbol{\mu}_{\mathrm{S}}$ reverses for spin-up and spin-down ($\boldsymbol{\tau}^{\uparrow}_{\mathrm{SO}} \neq \boldsymbol{\tau}^{\downarrow}_{\mathrm{SO}}$), making SOC spin-dependent.

In a crystallographic phase, a quasi free electron in the conduction band does not experience the strong nuclear attraction as when considering a single atom but it feels the overall potential gradient created by internal effects. The SOC arising from these different effects correspond to the potential within the solid. The potential acting on the electron is composed of a periodic component connected to the band structure and a non-periodic component associated to impurities, boundaries and external applied field. Even more, SOC can also appear in systems with broken inversion symmetry, such as metallic surfaces and interfaces. All these components can give rise to a variety of spin-dependent transport phenomena among which SCI.

2.2.2 Ordinary and anomalous Hall effect

Edwin Herbert Hall (1879) discovered what is nowadays known as the ordinary Hall effect (OHE), which explains the deflection (in the y direction) of charge carriers (electrons and holes) in NM conductors under the influence of an in-plane electric field (E_x) and an out-of plane magnetic field (H_z) considering the Lorentz force [53]. The deflected electrons and holes create a charge accumulation at the edges, as shown in figure 2.4a, which can be measured as a transverse resistance R_{xy}. The transverse resistance displays a linear dependence with the magnetic field and the slope gives the Hall coefficient (R_{OHE}) that can be used to determine the carrier density of a NM [$n = 1/(eR_{\mathrm{OHE}})$ where the electrical charge of an electron is $-e$].

Just two years later (1881), Hall observed that the same effect in FM was much larger in comparison to NMs. Even more, FMs possess a R_{xy} when applying an electric field in the absence of an external magnetic field ($H_z = 0$) [54]. This anomalous Hall effect (AHE), adding to the OHE, could not be understood for more than 70 years, until Karplus and Luttinger (1954) recognized that the AHE was due to intrinsic out-of-plane magnetization (m_z) that introduces spin-dependent scattering, i.e., SOC [55]. Therefore, when the electric field is applied to a FM, a spin-polarized current is generated (see section 2.1.3) which interacts with this SOC, deflecting the spin-up and spin-down carriers in opposite directions. Subsequently, due to the difference in the spin-up and spin-down population, the charge accumulation at the two edges is not the same and a measurable voltage is induced at $H_z = 0$. Figure 2.4b displays the electron flow due to the AHE. The AHE was the first observation of a charge current to spin-polarized current conversion.

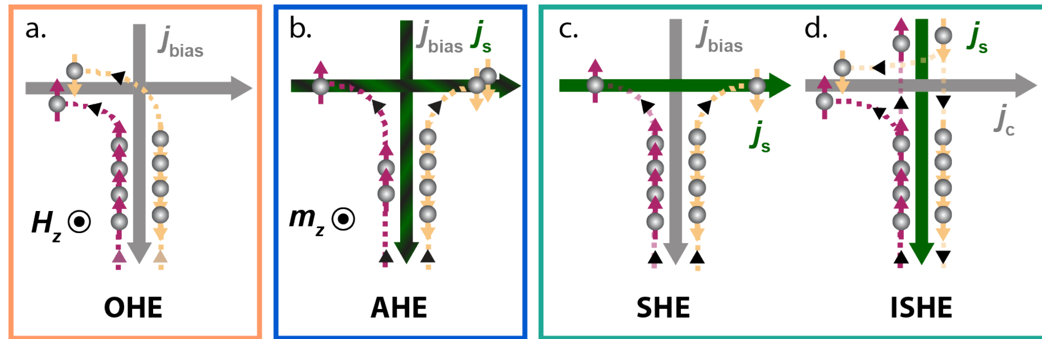

Figure 2.4: The Hall effects. Illustration of the charge (grey circle) and spin (red and yellow arrow) flow of different Hall effects with the charge, spin and spin-polarized current presented by arrows in grey, green and grey/green, respectively. The flow of opposite spin carriers (red and yellow dashed line) are defined by the type of effect being; **a)** the ordinary Hall effect in NM induced by an external magnetic field H_z, **b)** the anomalous Hall effect in FM produced by the internal magnetization m_z and SOC, **c)** the spin Hall effect and **d)** the inverse spin Hall effect in NM generated by SOC.

2.2.3 Spin Hall effect

The existence of spin-dependent scattering in FMs, that provided the explanation for AHE, implies that this type of scattering should also occur in NMs, hinting at a spin Hall effect (SHE) [56]. The SHE was predicted by D'yakanov and Perel in 1971 based on asymmetric Mott scattering, which is a type of spin-dependent scattering [57, 58]. However, contrary to FMs, NMs have a balanced spin population, therefore the deflection of spin-up and spin-down carriers results in a pure spin current (meaning no net charge current, section 2.1.2) which, at that time, was challenging to observe. Around 1999, the interest in the SHE revived by predictions of the extrinsic SHE [59, 60] as well as the intrinsic SHE [61, 62]. Soon after, the SHE was confirmed by optical experiments [63, 64]. The SHE can thus be defined as the conversion of charge current into a transverse pure spin current induced by SOC. The reciprocal effect of the SHE, named the inverse spin Hall effect (ISHE), accounts for the conversion of a spin current into a transverse charge current due to SOC and was measured by electrical means one year after the SHE [65, 66]. Nowadays, there are many different optical and electrical approaches to measure the SHE and ISHE [56]. Section 3.2 displays an overview of SHE measurement devices.

The SHE arises when an electric field, leading to a charge current, is applied to a NM with SOC. The SOC deflects the opposite spin carriers to opposite edges of the NM creating a spin accumulation. NMs do not have a intrinsic spin polarization, that is why the spin accumulation at the edges does not involve a charge accumu-

lation as in the case of the AHE in FMs, meaning that SHE produces a pure spin current. An illustration of the SHE is presented in figure 2.4c. In the case of the ISHE, a spin current (can be both a spin polarized or pure spin current) is injected into an NM and the opposite spin carriers are deflected in the same direction creating a transverse charge current as shown in figure 2.4d. The relationship between the charge current density ($\boldsymbol{j}_\mathbf{c}$) and the spin current density ($\boldsymbol{j}_\mathbf{s}$) for the SHE and ISHE, respectively, are:

$$\boldsymbol{j}_\mathbf{s} = \left[\frac{\hbar}{e}\right] \theta_\mathrm{SH}(\boldsymbol{j}_\mathbf{c} \times \hat{\mathrm{s}}), \tag{2.19}$$

and

$$\boldsymbol{j}_\mathbf{c} = \left[\frac{e}{\hbar}\right] \theta_\mathrm{SH}(\boldsymbol{j}_\mathbf{s} \times \hat{\mathrm{s}}), \tag{2.20}$$

where $\hat{\mathrm{s}}$ is the spin orientation and the charge-to-spin conversion efficiency as well as the spin-to-charge conversion efficiency is given by the spin Hall angle θ_SH, as the SHE and the ISHE obey the Onsager reciprocity [67].

The spin Hall angle is defined as the ratio of the transverse resistivity ρ_xy (conductivity σ_xy) and the longitudinal resistivity ρ_xx (conductivity σ_xx),

$$\theta_\mathrm{SH} = \frac{\sigma_\mathrm{xy}}{\sigma_\mathrm{xx}} = -\frac{\rho_\mathrm{xy}}{\rho_\mathrm{xx}}, \tag{2.21}$$

since $\rho_\mathrm{xy} = -\sigma_\mathrm{xy}/(\sigma_\mathrm{xy}^2 + \sigma_\mathrm{xx}^2)$ and $\rho_\mathrm{xx} = 1/\sigma_\mathrm{xx}$. θ_SH can be obtained via several different methods like ferromagnetic resonance (FMR) spin pumping, spin-torque FMR and non-local spin valves (section 3.2). Since each technique has a slightly different way of measuring and analysing, a large variation in θ_SH is reported for the same materials [56, 68, 69]. There are three obvious reasons for this discrepancy; i) In this work, θ_SH is defined as $\sigma_\mathrm{xy}/\sigma_\mathrm{xx}$ with σ_xy in units of $\hbar/e$ in order to have consistency with other AHE and SHE measurements and theoretical expressions [70, 71]. Some other works define $\theta_\mathrm{SH} = 2\sigma_\mathrm{SH}/\sigma_\mathrm{xx}$ or σ_SH in units of $\hbar/(2e)$ giving a θ_SH that is a factor of 2 larger compared to our formalism.; ii) the estimation of θ_SH involves an FM/NM heterostructure in most techniques. The interface has to be taken into account properly, meaning the interface resistance and spin memory loss has to be determined experimentally for each device, as the interface can affect the spin transport significantly [72–75]. A wrong evaluation of the interface leads to a wrong estimation of θ_SH; iii) θ_SH is dependent on the resistivity of the material, i.e., θ_SH is not a intrinsic materials property [76, 77]. The variation of θ_SH with the resistivity can be understood when looking at the origin of SOC as will be elucidated in section 2.2.4.

2.2.4 Mechanisms behind the spin Hall effect

The origin of the SOC leading to the bulk SCI was first studied and resolved for the AHE [78] and is commonly accepted to apply as well to the SHE [56, 79]. The resistivity can be defined by an intrinsic component related to the band structure and an extrinsic component that includes structural defects. The total transverse resistivity of a material is given by;

$$-\rho_{\mathrm{xy}} = \rho_{\mathrm{xy}}^{\mathrm{int}} + \rho_{\mathrm{xy}}^{\mathrm{ext}}, \tag{2.22}$$

where $\rho_{\mathrm{xy}}^{\mathrm{int}}$ and $\rho_{\mathrm{xy}}^{\mathrm{ext}}$ are the transverse resistivities induced by intrinsic and extrinsic effect, respectively.

The **intrinsic contribution** is defined by the electronic band structure of the perfect crystal (without any non-periodic structural defects) as a consequence of spin-dependent band splitting in the presence of SOC. Karplus and Luttinger were the first to recognize that the AHE is the transverse deflection of electrons as a result of SOC in between scattering events [55]. Later, it became clear that this SOC is a consequence of an effective magnetic field that originates from a non-zero Berry phase curvature [80–83]. Figure 2.5a illustrates the intrinsic scattering mechanism in the presence of an electric field ($\boldsymbol{E}$). The intrinsic transverse resistivity is given by: $\rho_{\mathrm{xy}}^{\mathrm{int}} = \sigma_{\mathrm{xy}}^{\mathrm{int}} \rho_{\mathrm{xx}}^{2}$ with $\sigma_{\mathrm{xy}}^{\mathrm{int}}$ being the intrinsic transverse conductivity also know are the intrinsic anomalous Hall conductivity $\sigma_{\mathrm{AH}}^{\mathrm{int}}$ in FMs or the intrinsic spin Hall conductivity $\sigma_{\mathrm{SH}}^{\mathrm{int}}$ in NMs. The $\sigma_{\mathrm{SH}}^{\mathrm{int}}$ is dependent on the Berry curvature at the Fermi level and is a constant value linked to the band structure of each material. Figure 2.6a presents σ_{SH} for 4d and 5d transition metals which shows the close relation with the band structure as the transition metals with the d-bands more than half filled have a positive $\theta_{\mathrm{SH}}^{\mathrm{int}}$ and a negative $\theta_{\mathrm{SH}}^{\mathrm{int}}$ is observed for transition metals with the d-bands less than half filled [83].

The **extrinsic contributions** are produced by spin-dependent structural defect scattering. The asymmetry of the defects can form a variation in the potential landscape creating an effective SOC that leads to the deflection of the electrons during scattering events. The trajectory of the deflected electrons is given by the type of scattering. Two distinct mechanisms induced by SOC in impurities can be distinguished, namely skew scattering and side-jump mechanism.

- **Skew scattering** is related to spin-dependent chiral features which appear for scattering events that produce a disordered potential in the presence of SOC, larger then the intrinsic band splitting. This scattering mechanism finds

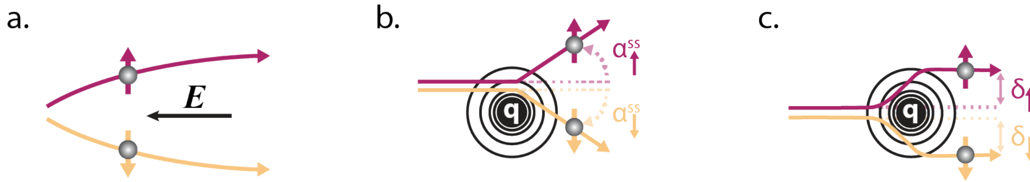

Figure 2.5: Mechanisms of the spin Hall effect Sketches of the intrinsic and extrinsic mechanisms that drive the spin Hall effect. The spin-up and spin-down electrons and their trajectory are presented by red and yellow, respectively. **a)** The intrinsic mechanism determined by an external electric field E in combination with the band structure affecting the spin-up and spin-down electrons differently. The extrinsic effects depend on scatter centers with a charge q that are presented as black concentric circles. **b)** Skew-scattering mechanism with deflection angle α^{ss}. **c)** The side-jump mechanism induces a lateral deflection δ. Adapted from [84].

its origin in Mott scattering [58, 85], was first identified in FMs by Smit [86, 87] and later shown to be present in NMs [59, 60]. Figure 2.5b displays skew scattering where the asymmetrical electron deflection of the different spin carriers yield a transverse angle α^{ss}. The contribution of the skew scattering mechanism to the extrinsic transverse resistivity is $\rho_{\mathrm{xy}}^{\mathrm{ss}} = \alpha^{\mathrm{ss}}\rho_{\mathrm{xx,0}}$ where $\rho_{\mathrm{xx,0}}$ is the residual resistivity.

- **Side-jump mechanism** describes the remaining contributions to the total transverse resistivity $(-\rho_{\mathrm{xy}})$ not covered by the intrinsic mechanism or the skew-scattering mechanism. This contribution was first noticed but discarded by Smit [86] and reintroduced by Berger [88]. This mechanism is explained by the fact that the two electron spin carriers experience opposite electrics field when approaching or passing a scatter center, causing a lateral displacement of the electron that is opposite for spin-up and spin-down as presented in figure 2.5c. The contribution of the side-jump mechanism to the extrinsic transverse resistivity is $\rho_{\mathrm{xy}}^{\mathrm{sj}} = \sigma_{\mathrm{xy}}^{\mathrm{sj}}\rho_{\mathrm{xx,0}}^2$, with $\sigma_{\mathrm{xy}}^{\mathrm{sj}}$ being the transverse conductivity term associated to side-jump.

The extrinsic mechanisms can give rise to the observed variation in θ_{SH} for the same materials grown by various deposition techniques and in different groups creating different impurities. The extrinsic contribution can be utilized to engineer a material to augment θ_{SH}. Figure 2.6b shows the theoretically calculated enhancement of α^{ss}, i.e., the skew-scattering spin Hall angle, by doping five different materials with a variety of impurities. The materials identified to posses large α^{ss} are dilute alloys such as Ag(Bi), Cu(Bi), and Cu(Pb) [89]. This indicated that that

alloying light materials (Cu, Ag and Au) with heavy impurities (Bi, Ir and Pb) gives the higher α^{ss}. It is also experimentally confirmed that alloying can positively enhance θ_{SH} [90–92]. Even more, studies have shown that θ_{SH} can be tuned by the controlling the amount of doping, that is the percentage on impurities in the host material. [93–96].

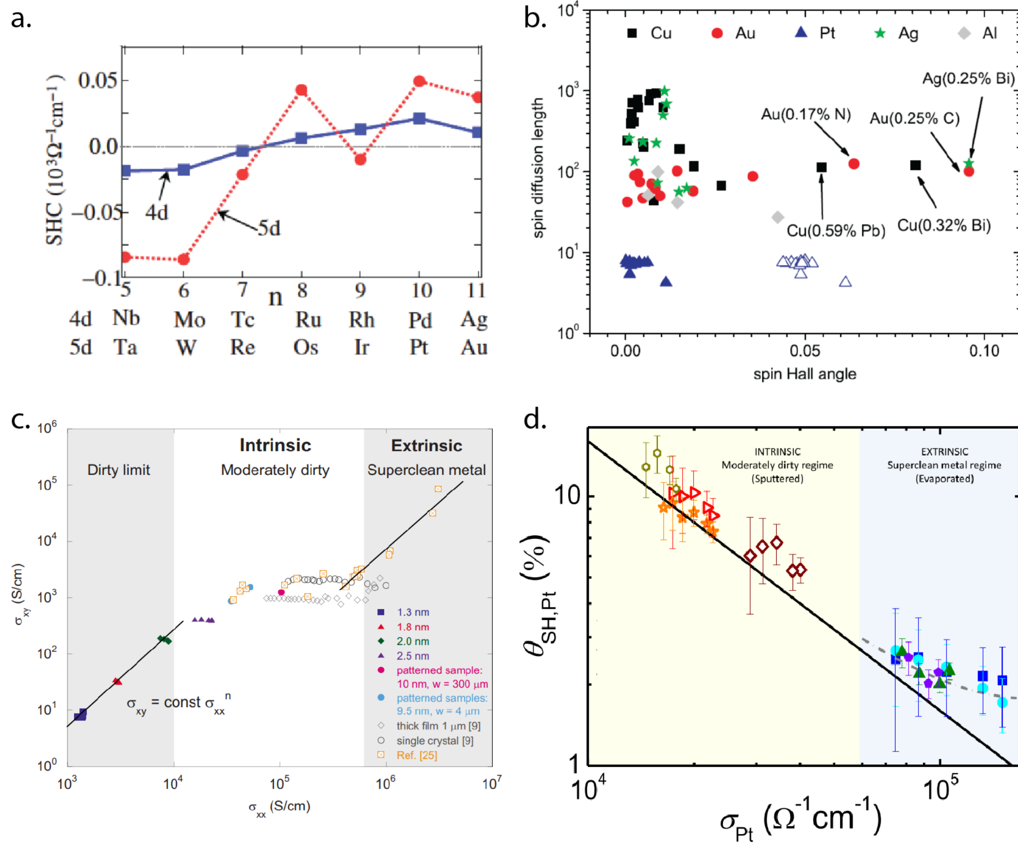

Figure 2.6: Observation of intrinsic and extrinsic scattering mechanisms. a) The intrinsic spin Hall conductivity (SHC) dependence on the the number of electrons n in the outer shell of 4d and 5d transition metals based on microscopic tight binding calculations [83]. **b)** A theoretical study on the skew-scattering mechanism shows the skew-scattering angle (θ_{SH} considering only the skew-scattering contribution) versus the spin diffusion length of different alloys with different host materials [89]. The intrinsic and the extrinsic regime are experimentally unveiled to be associated to the moderately dirty and superclean limit, respectively, for **c)** the AHE in Fe(100) [97] and **d)** the SHE in Pt [76].

All the contributions together makes the total spin Hall resistivity (equation 2.22) become [78]:

$$-\rho_{\mathrm{xy}} = \sigma^{\mathrm{int}}_{\mathrm{xy}}\rho^2_{\mathrm{xx}} + \alpha^{\mathrm{ss}}\rho_{\mathrm{xx},0} + \sigma^{\mathrm{sj}}_{\mathrm{xy}}\rho^2_{\mathrm{xx},0}, \tag{2.23}$$

Resistivity dependent studies can be used to reveal the contribution of each mechanism. Note that the residual resistivity can be tuned by impurities as mentioned above but also by other material structural defects, e.g. the size of grain boundaries. Figure 2.6c shows three distinct regimes for the AHE in Fe(100) where the dominating mechanism for the moderately dirty regime is identified as the intrinsic mechanism and the superclean limit agrees with extrinsic mechanism [97]. The dirty regime has not been connected to a scattering mechanism. Figure 2.6d shows the same trend for the SHE in the prototypical SHE material Pt [76].

2.3 Interfacial spin-charge interconversion

Spin-charge interconversion is also observed in two-dimensional (2D) systems with SOC, the most famous one being the Edelstein effect. The Edelstein effect can be utilized for SCI in devices in a similar way as the SHE. Moreover, the Edelstein effect can also appear unexpectedly at interfaces established at device connections of different electrodes. For the development and optimization of spin-orbitronic devices, it is key to know the origin of the SCI, that is, the effect from which the SCI arises.

2.3.1 Rasbha Effect

Materials that posses SOC and asymmetry in the crystal potential (broken space inversion symmetry) obtain a k-dependent spin-band splitting, i.e., the degeneracy of the energy bands of opposite spin carriers is lifted. This type of spin-band splitting was first discovered by Dresselhaus [98] in uniaxial non-centrosymmetric crystals, such as GaAs or InSb. The band splitting in these materials derives from bulk inversion symmetry breaking. Later, Vas'ko [99] and Bychkov and Rashba [100, 101] noted that this spin-band splitting also occurs in quantum wells and 2DEGs owing to a confined potential that breaks structural inversion symmetry. Furthermore, such spin-band splitting is seen in Au(111) interfaces as well [102]. The spin-momentum locking at interfaces in Rasbha systems brings about 2D spin-polarized states under the influence of an electric field which will be explained for Rashba systems in section 2.3.2.

The splitting of the energy bands with opposite spin carriers in k-space induced by the Rasbha effect is shown in figure 2.7a. The structural inversion asymmetry at the surface or interface make the Rashba SOC hold an electric potential normal to the surface or interface. The Rashba Hamiltonian describing the interaction between the momentum ($\hbar\boldsymbol{k}$) and spin is given by:

$$H_R = \alpha_{\mathrm{R}}(\hat{\boldsymbol{z}} \times \boldsymbol{k})\boldsymbol{\sigma}, \tag{2.24}$$

where $\hat{\boldsymbol{z}}$ is the direction normal to the 2D plane and α_R is the Rashba coefficient, proportional to the strength of the SOC and electric potential. $\boldsymbol{k}$ is the wavevector and for each $\boldsymbol{k}$ the energy of the band splitting for the two spin carriers is given by:

$$E_{\uparrow(\downarrow)}(k) = \frac{\hbar^2 k^2}{2m_e} \pm \alpha_{\mathrm{R}} k. \tag{2.25}$$

Figure 2.7a displays the spin texture at the Fermi level produced by the Rashba effect. The two contours have different size and opposite helicity. In the next section, the role of the Fermi contours in the SCI will be unfolded.

2.3.2 Rasbha-Edelstein Effect

Edelstein realized that an electric current in asymmetric 2DEGs results in spin accumulation, at present known as the Edelstein effect [103]. About 20 years later, the Edelstein effect in Rasbha systems, that is the Rashba-Edelstein effect (REE), was experimentally demonstrated at the interface between two NMs [104]. Now, the REE is known to be present in other all-metallic interface [105–112], metal/oxide interfaces [113–116] and 2DEGs in all-oxide structures [117–121].

The REE relies on the spin-band split surface or interface states with, consequently, a spin polarization that is locked to its momentum. In equilibrium, the spin-band splitting along the k-axis with the two concentric Fermi contours (figure 2.7a) has a balanced spin population and momentum. The system can be brought out-of-equilibrium by an electric field $\boldsymbol{E} = E_x\hat{x}$ that displaces the Fermi contours resulting in a spin accumulation μ_{s}. Figure 2.7b depicts the displacement of the Fermi contours when subjected to an electric field in the form of a charge current density $j_{\mathrm{c},x}$. The accelerated electrons induce a change in all energy states opposite to the electric field direction. In k-space this translates to a shift in the Fermi contours Δk_x such that the spin population of different spin carriers are not compensated ($\mu_\uparrow \neq \mu_\downarrow$). Hence, the system obtains an average spin accumulation $\langle\mu_{\mathrm{s}}\rangle$ proportional to Δk_x. The spin accumulation can diffuse in a third dimension resulting in

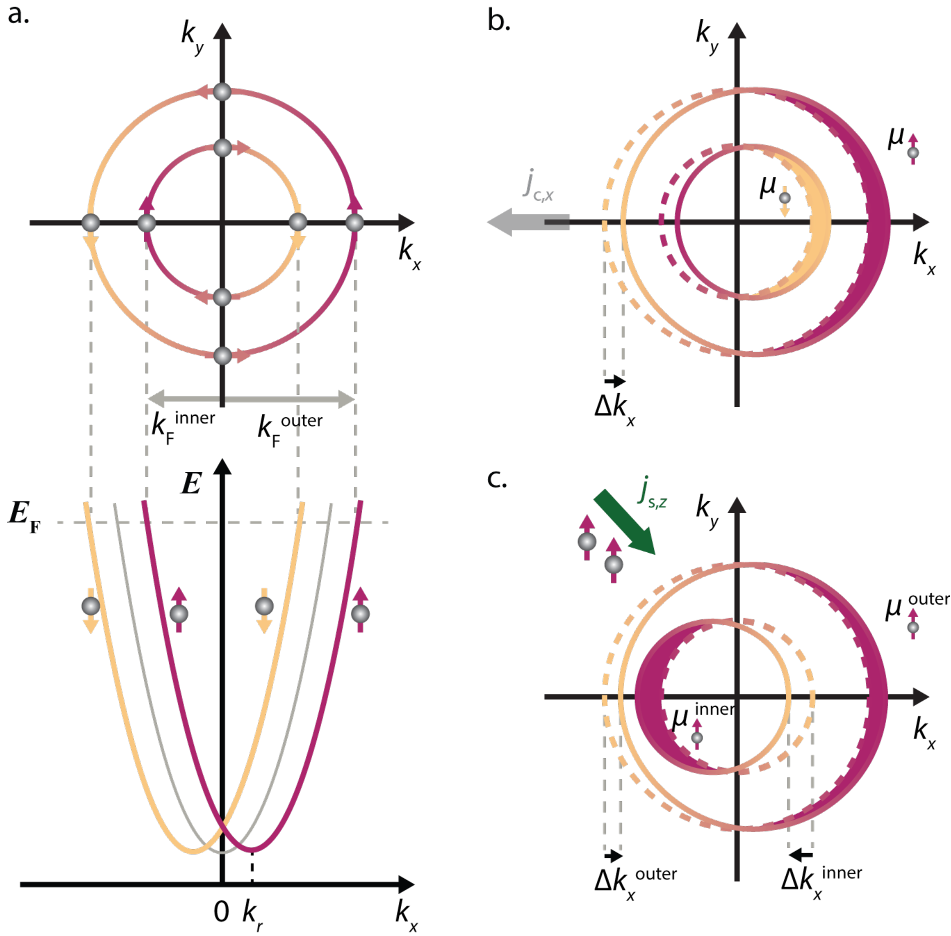

Figure 2.7: Rashba systems and the Edelstein effect. a) The spin-dependent band splitting in Rashba systems in k_x (lower panel) with the grey curve presenting the reference band and the shifted curves for spin-up and spin-down are the red and and yellow curve, respectively. The cut at the Fermi level (upper panel) shows two circular contours with the inner contour having a spin texture rotating clockwise and the outer contour rotating anti-clockwise with radii $k_{\mathrm{F}}^{\mathrm{inner}}$ and $k_{\mathrm{F}}^{\mathrm{outer}}$. **b)** REE: the charge current density $j_{\mathrm{c},x}$ creates a shift of the Fermi contours Δk_x which produces spin accumulation in the inner contours with spin-down $\mu_{\downarrow}$ and the outer contour with spin-up $\mu_{\uparrow}$. There will be a net spin accumulation $\langle \mu_{\mathrm{s}} \rangle$, as $\mu_{\downarrow} \neq \mu_{\uparrow}$, that can flow out of the Rashba system as a spin current. **c)** inverse Rashba-Edelstein effect (IREE): injection of spin current $j_{\mathrm{s},z}$ makes the Fermi contours move in opposite directions $\Delta k_x^{\mathrm{inner}}$ and $\Delta k_x^{\mathrm{outer}}$. Both contours are assumed to host the same amount of spins $\mu_{\uparrow}^{\mathrm{inner}} = \mu_{\uparrow}^{\mathrm{outer}} = \langle \mu_{\mathrm{s}} \rangle / 2$ such that $\Delta k_x^{\mathrm{inner}} \neq \Delta k_x^{\mathrm{outer}}$ and an electric field, i.e., a 2D charge current, is formed.

a three-dimensional (3D) spin current density. The charge-to-spin conversion via the REE is given by [122]:

$$q_{\mathrm{REE}} = \frac{\boldsymbol{j}_{\mathbf{s}}^{\mathbf{3D}}}{\boldsymbol{j}_{\mathbf{c}}^{\mathbf{2D}}} \quad [\mathrm{m}^{-1}]. \tag{2.26}$$

Reciprocally, the conversion of a spin accumulation to a charge current is called the inverse Rashba-Edelstein effect (IREE) and is illustrated in figure 2.7c. When subjecting a Rashba system to a spin accumulation, containing a spin polarization in y, the two Fermi contours will shift in opposite directions yielding a displacement in momentum in opposite directions. Even more, the radii of the contours $k_{\mathrm{F}}^{\mathrm{outer}}$ and $k_{\mathrm{F}}^{\mathrm{inner}}$ for the respective outer and inner contour at the Fermi level are different. Therefore, the momentum displacement of the two contours $\Delta k_{\mathrm{F}}^{\mathrm{outer}}$ and $\Delta k_{\mathrm{F}}^{\mathrm{inner}}$ gives $\Delta k_{\mathrm{F}}^{\mathrm{outer}} \neq \Delta k_{\mathrm{F}}^{\mathrm{inner}}$, supposing that the spin accumulation is divided evenly in the two contours. The total momentum displacements of the Fermi contours, defined by α_{R} (see equation 2.24), produces a 2D charge current density $\boldsymbol{j}_{\mathbf{c}}^{\mathbf{2D}}$. The efficiency of IREE, given by the ratio of the injected spin current density and the resulting charge current density, is the IREE length:

$$\lambda_{\mathrm{IREE}} = \frac{\boldsymbol{j}_{\mathbf{c}}^{\mathbf{2D}}}{\boldsymbol{j}_{\mathbf{s}}^{\mathbf{3D}}} \quad [\mathrm{m}]. \tag{2.27}$$

As a consequence of the 2D character of the charge current and the 3D character of the spin current, the dimension of λ_{IREE} is in unit of length and q_{REE} in units of the inverse length. The difference in dimension of λ_{IREE} and q_{REE} thwarts the Onsager reciprocity in the form as was established for the SHE. However, experimental observations of Onsager reciprocity in Rasbha systems have been made [112]. A discussion on the comparison between the 3D and 2D SCI efficiencies is given in section 2.3.4.

2.3.3 Other interfacial spin-orbit coupling effects

As mentioned before, a thorough understanding of charge and spin transport in systems with SOC is crucial for the electric control of spin currents and the importance of interfacial SOC in FM/NM systems becomes increasingly more clear [72–75, 123]. The Rashba SOC, that appears at the interface of a Rashba system, depends on the intrinsic mechanism of the 2DEG. But, while the 2DEG in oxide/oxide interfaces is well defined, the interpretation of a 2DEG in all-metallic or metal/oxide interfaces is more complex which leaves room for other effects, that for convenience will be called extrinsic interfacial SOC here.

In an ideal world, the growth of heterostructures will produce sharp interfaces. However, in reality, sharp interfaces are hard to grow and structural defects, strain, roughness and atomic interdiffusion is difficult to prevent. The extrinsic interfacial SOC easiest to imagine is interdiffusion. Section 2.2.4 shows that alloying of materials can enhance θ_{SH} due to the implementation of spin scatter centers with SOC. Interdiffusion is basically local alloying of the interface meaning that the ad-atoms can create SOC via skew-scattering and/or side-jump mechanisms spawning the extrinsic interfacial SOC permitting local SCI.

This local SCI produced by extrinsic mechanisms is similar to the extrinsic SHE so it could be thought of as an "interfacial" SHE. Interfacial SHE will have the same symmetry as the bulk SHE and be different from the REE. It can contribute positively or negatively to the total SCI depending on the sign of θ_{SH} of the local SCI in comparison to the one of bulk SHE. For example, a work on the Py/Bi interface shows a θ_{SH} akin to the interface opposite to θ_{SH} of bulk Bi [124].

The interfacial SHE can be distinguished from the REE as the symmetries of the spin current density, charge current density and polarization are different, but only in specific measurement configurations. Such configurations should for example permit the injection of spin current from opposite directions of the interface region, that in the REE would lead to a sign change while the interfacial SHE remains unchanged. However, in theoretical works, the enhancement of the SCI by an interfacial contribution is mostly ascribed to Rashba SOC but named interfacial SHE [125–127]. For example, the study based on first-principles calculations on Fe/Au bilayers shows the existence of a strong interfacial SHE, in addition to the bulk SHE, due to strong Rashba SOC [126]. Interestingly, they comment that the interfacial spin Hall currents are found not to be confined at the interface but extend tens of nanometers. This would mean that the energy bands can be affected up to tens of nanometers into the materials by the structural inversion asymmetry at the interface.

Interfacial SOC can also be observed at the surface of topological insulators. In topological insulators the spin-band of the Dirac cones can split due to surface topology [128]. Similar to the Rashba system, the spin-momentum locking at the surface of the topological insulators can generate 2D spin-polarized states when subjected to an electric field. However, this work deals predominantly with metallic devices, therefore topological insulators will not be further discussed.

Another possibility is spin-dependent scattering of Bloch bulk states from the interface, sometimes called spin-orbit filtering [129–133]. Spin-orbit filtering occurs

because carriers with spins parallel and anti-parallel to the interfacial spin-orbit field experience different spin-dependent scattering amplitudes. This type of scattering can convert unpolarized electrons via reflection and transmission into spin-polarized electrons. Furthermore, it is known to happen at NM interfaces with SOC even if the bulk currents are unpolarized.

In order to overcome the discussion on the origin of the interfacial SOC an universal theoretical framework was developed [134]. This framework describes SCI in NM/oxide interfaces with interfacial SOC independent of microscopic details. The model was first applied to Cu/BiO_x interface [116]. Later, it was expanded to explain the SCI in NM/NM interface [111]. The formulation is based on drift-diffusion equations supplemented with two interfacial BC covering i) interfacial SCI and ii) spin losses at the interface. No assumptions are made about the origin of the interfacial SOC. In the end, the model is able to describe the SCI with two parameters, the spin-charge conductivity σ_{sc} and the interfacial spin-loss conductance $G_{\|}$. Even more, it is found that $\sigma_{\mathrm{sc}}/G_{\|}$ is equivalent to λ_{IREE}. However, there is not a straightforward way to describe q_{REE} in terms of $G_{\|}$ and σ_{sc}, because q_{REE} is not a intrinsic parameter and depends on geometrical parameters beyond the interface. This indicates that $G_{\|}$ and σ_{sc} are more suitable parameters to describe interfacial SCI. Finally, this model gives that $\sigma_{\mathrm{sc}} = \sigma_{\mathrm{cs}}$ (where σ_{cs} is the interfacial charge-spin conductivity) which resolves the problem of reciprocity for interfacial SCI.

2.3.4 Universal spin-charge interconversion efficiency

The focus in the development of devices lies often in the efficiency, so also in spin-orbitronic devices. While the existence of both bulk and interfacial SCI has been well established, there is no general definition for the SCI efficiency. Lately, topological insulators and 2D systems made of graphene and transition metal dichalcogenides attract a lot of attention [135–137]. In order to compare these new upcoming systems with the 3D systems and to make proper choices for design and materials systems in spin-orbitronic devices, an universal SCI efficiency would be convenient.

The SCI efficiency is generally defined by the ratio of the charge and spin current densities. For the SHE and ISHE this is θ_{SH}, which is dimensionless, whereas the efficiency of the IREE is λ_{IREE} and REE is q_{REE} with the respective dimensionalities $[\mathrm{m}]$ and $[\mathrm{m}]^{-1}$. The difference arrives from the fact that the SHE and ISHE involve 3D charge current and 3D spin current. In contrast, the REE and IREE pertain 2D

charge current and 3D spin current. For this reason, a comparison between the efficiencies is far from obvious.

Several suggestions have been made to resolve this conundrum. One of them being an effective θ^*_{SH} for the 2D system given by $\sqrt{\lambda_{\mathrm{IREE}}\, q_{\mathrm{REE}}}$. [112] Others mention the multiplication of λ_{IREE} and the division of q_{REE} by the thickness of the 2DEG or the spin diffusion length [138]. Even though theoretically a 2D system does not have a thickness and the spin diffusion length in such system depends on the material connected to the 2D system to probe the SCI.

A more interesting proposal for a direct comparison of efficiencies of the 3D and 2D systems, provided by Rojas-Sánchez and Fert, is to redefine θ_{SH} [138]. This seems logical as it is known that θ_{SH} is not an intrinsic parameter but contains both the intrinsic and extrinsic contribution (equation 2.21 and 2.23). They introduce $\lambda^*_{\mathrm{ISHE}} = \theta_{\mathrm{SH}}\lambda$ and $q^*_{\mathrm{SHE}} = 0.38\theta_{\mathrm{SH}}/\lambda$ as the efficiencies for the direct and inverse effects, respectively. In the 3D system, it is valid to included λ as the SCI happens in the materials and λ can be observed independently of the measurement probes. Finally, in this paper, the comparison between 3D systems and one specific 2D system is taken from the gain, that is, the ratios $\lambda_{\mathrm{IREE}}/\lambda^*_{\mathrm{ISHE}}$ and $q_{\mathrm{REE}}/q^*_{\mathrm{SHE}}$.

A different approach for the description of SCI would be to consider the universal theoretical framework that has been described at the end of section 2.3.3 [111, 116, 134]. This model describes the SCI with the interfacial spin loss conductance $G_{\|}$ and the interfacial spin-charge conductivity σ_{sc}. In interfaces, σ_{sc} plays the role of σ_{SH} in 3D systems and $G_{\|}$ can be considered as the 2D equivalent of $\rho\lambda$ in 3D systems (see section 3.1). As mentioned, the universal SCI efficiency at interfaces is given by $\sigma_{\mathrm{sc}}/G_{\|}$, the equivalent of λ_{IREE}.

Chapter 3

Spin-orbitronic devices for the spin Hall effect

3.1 Materials benchmarking

An important element for designing spin-orbitronic devices is benchmarking of materials. The decision on which materials to use for the different components of the devices defines the spin injection and detection, SCI efficiency and the voltage and current output. The choice of materials depends on the spin properties of the materials themselves as well as on the combination of the materials and their interfaces.

Spin-related devices deal with injection, transport and detection of spin currents by connecting materials with different spin properties. First of all, the connection will have an interface which can promote or demote the spin transport between the two materials. The interface transparency is defined by the growth and fabrication techniques, but also by the growth affinity of the two materials and the growth order [139]. Secondly, the opposition of a material to spin flow, the spin resistance, has to be considered. The spin resistance is given by $R_\mathrm{s} = \rho\lambda/[(1-P^2)A]$ where A is the cross-sectional area through which the spin current is flowing, ρ is the electrical resistance, λ is the spin diffusion length and P is the polarization. The polarization will be finite for FMs and zero for NMs. A is determined by λ being relatively long or short compared to the dimensions of the electrodes, as will be shown below for the different types of materials. The important dimensions are the width w_X and thickness t_X for an electrode of material X.

Groups of materials with similar spin properties can be identified with the knowledge from chapter 2. Here, the spin transport materials, ferromagnetic materials (FMs) and non-magnetic materials with strong SOC will be highlighted as these are the type of materials used in the devices described in this thesis. Each of these types has a different but specific function within the device design. Also, the spin resistance of the interface will be considered.

Spin transport materials are NMs that grant spin current flow over "long" distances meaning that there is little spin-flip scattering and λ (section 2.1.3) is relatively long (about hundreds of nanometers at room temperature). These materials are characterized by weak SOC. Examples of good metallic spin transporters are Cu, Ag and Al [140] and, more recently, it is shown that graphene (a single layer of carbon atoms) is also a good spin transporter [141]. NMs electrodes in spin-orbitronic nanodevices posses a relatively long λ, that is, $\lambda_\mathrm{NM} \gg w_\mathrm{NM}, t_\mathrm{NM}$, such that the spin resistance is defined as:

$$R_s^{\mathrm{NM}} = \frac{\rho_{\mathrm{NM}}\lambda_{\mathrm{NM}}}{w_{\mathrm{NM}}t_{\mathrm{NM}}}. \tag{3.1}$$

Ferromagnetic materials are used for electrical spin injection via spin accumulation (section 2.1.3) in spintronic and spin-orbitronic devices. The FMs exhibit spontaneous magnetization in the absence of an external magnetic field because of an exchange interaction that promotes parallel alignment of the electron spins. Ferromagnetism is found in transition metals with partially filled electron shells, in line with Hund's rule indicating that the first electrons in a electrons shell tend to align. Co, Ni and Fe and most of their alloys such as NiFe and CoFe are examples of FM. These FMs have a relatively high spin polarization P_{FM} (equation 2.6) which is preferred for spin injection. FMs have generally a short λ, i.e., $\lambda_{\mathrm{FM}} \ll w_{\mathrm{FM}}, t_{\mathrm{FM}}$, therefore the spin resistance of a FM electrode connected to a second electrode of specified material M becomes:

$$R_s^{\mathrm{FM}} = \frac{\rho_{\mathrm{FM}}\lambda_{\mathrm{FM}}}{w_{\mathrm{FM}}w_{\mathrm{M}}(1-P_{\mathrm{FM}}^2)}. \tag{3.2}$$

Strong spin-orbit coupling materials (SOMs) own the ability for SCI due to SOC and can be used to generate spin currents or to read out spin signals (section 2.2.1). The spin-dependent scattering in such a SOM deflects electrons causing SCI via the SHE (section 2.2.3), REE (section 2.3.2) or other interfacial SCI (section 2.3.3). The heavy metals (HMs) Pt, Ta and W are the most studied and the most frequently used SOMs in spin-orbitronic devices. Other materials or materials systems that can host SOC are Rashba systems (section 2.3.1), topological insulators and transition metal dichalcogenides [142]. The spin resistance of SOMs connected to a second electrode of specific material M, is:

$$R_s^{\mathrm{SOM}} = \frac{\rho_{\mathrm{SOM}}\lambda_{\mathrm{SOM}}}{w_{\mathrm{SOM}}w_{\mathrm{M}}\tanh\left(t_{\mathrm{SOM}}/\lambda_{\mathrm{SOM}}\right)}. \tag{3.3}$$

Usually λ_{SOM} is very short, meaning that $\lambda_{\mathrm{SOM}} \ll w_{\mathrm{SOM}}, t_{\mathrm{SOM}}$, and leading to

$$R_s^{\mathrm{SOM}} = \frac{\rho_{\mathrm{SOM}}\lambda_{\mathrm{SOM}}}{w_{\mathrm{SOM}}w_{\mathrm{M}}}. \tag{3.4}$$

Interfaces at the connection of different electrodes can play a important role in the working principle of spintronic devices as it can influence the spin flow in the device significantly. There are two types of interfaces. The first type are transparent

interfaces that result in ohmic contacts and avoid Schottky barriers. In this case, the spin transport only dependents on the spin resistance of the two materials. The second type of interfaces are resistive interfaces, typically tunnel barriers. A tunnel barrier is sometimes preferred as it can overcome the spin resistance mismatch of the two electrode and assist to inject more spin current and reduce the spin backflow [143]. However, unwanted interfaces with resistance can appear due to oxidation of the materials or residuals from the fabrication process. This kind of interfaces often demote the spin injection and/or detection because of a high spin resistance, that is given by:

$$R_s^{\mathrm{I}} = \frac{R_{\mathrm{I}}}{1 - P_{\mathrm{I}}^2}. \tag{3.5}$$

where R_{I} is the interface resistance and P_{I} is the interface polarization as given by equation 2.12 in a system with no interfacial spin-memory loss.

3.2 Spin Hall effect devices: an overview

Although it is not simple to measure the spin accumulation originating from the SHE, various methods have been developed over the years and each method with its own complexity [56]. The most commonly used measurement techniques will be briefly introduced to understand the ravel of extracting the spin Hall properties (section 2.2.3).

Magneto-optical Kerr effect (MOKE) describes the changes to light reflected from a magnetized surface or, in the case of the SHE, the spin accumulation. MOKE senses the spin accumulation at opposite edges of a film induced by the SHE when applying a charge current (figure 3.1a). The first experimental observation of the SHE was in semiconducting GaAs by MOKE [63]. The advantage of MOKE is that the measurement can be done directly on a thin film of the SOM. However, the spin accumulation is confined close to edges and the magnetization associated to the spin accumulation is tiny, therefore, MOKE is especially hard for metals [144]. Even so, recently, the θ_{SH} and λ of a Pt thin film was established with MOKE [71].

Ferromagnetic resonance spin pumping is the precession of magnetization in a FM layer induced by microwave radiation that injects (pumps) a direct current (DC) spin current into an adjacent SOM layer. The injected spin current will create a transverse charge current due to the ISHE in the SOM (figure 3.1b). The first

measurement of the voltage drop caused by ISHE in Pt using spin pumping was realized in 2006 [65].

Spin-torque ferromagnetic resonance (ST-FMR) is a technique that relies on the damping-like torque between the FM and the SOM. The SHE in the SOM is used to create a transverse spin current by applying an alternating current (AC) charge current. The spin current is injected into the FM thereby exerting an oscillating spin torque on a FM that leads to an oscillatory anisotropic magnetoresistance resulting in a detectable DC voltage (figure 3.1c). The demonstration of the SHE with ST-FMR was first accomplished in NiFe/Pt [145].

Lateral spin valve (LSV) with the non-local spin Hall technique is a nanostructured device in which the spin injection and detection are spatially separated by a spin channel. The separation permits injection of a pure spin current and avoids detection of spurious effect arising from the bias currents. One type of LSV is a device consisting of a FM electrode and a SOM cross-shaped electrode. The FM

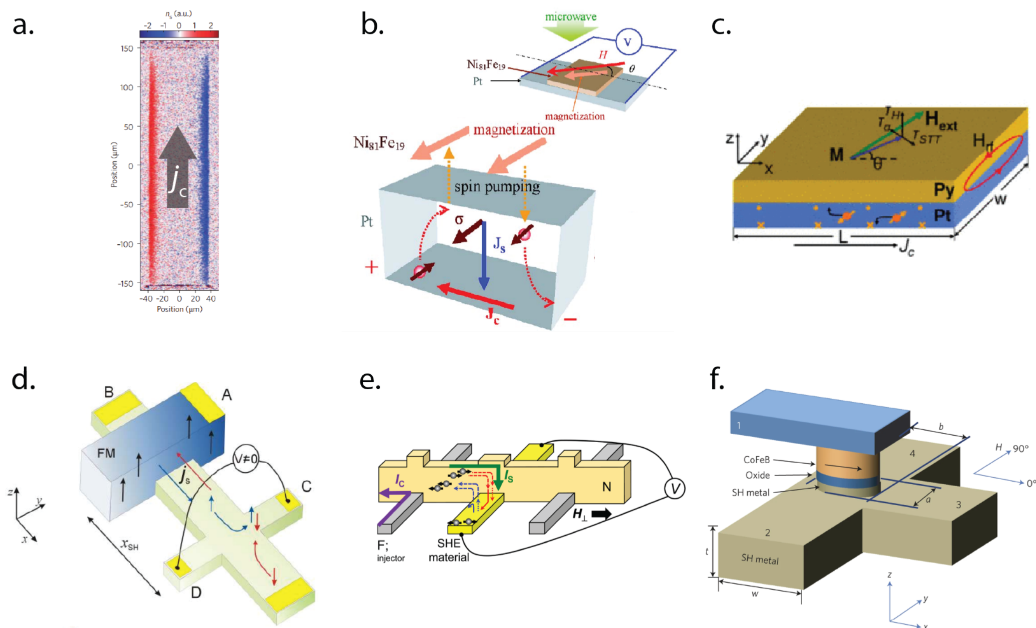

Figure 3.1: Popular techniques for SHE detection a) Optical detection using MOKE [146]; **b)** Spin pumping [65]; **c)** ST-FMR [145] and; **d)** Lateral spin valve with the non-local spin Hall technique with a FM and a cross-shaped SOM electrode [147]; **e)** Lateral spin valve with the non-local spin Hall technique with a FM electrode parallel to SOM electrode transversely connected by a NM spin channel [148]; **f)** Local spin Hall device [149].

is employed to electrically inject the spin current into the SOM and the ISHE can be measured in the transverse arms of the SOM electrode (figure 3.1d) [66]. This measurement, however, requires the SOM to have a long λ and large θ_{SH} which usually does not appear together. In a variation of this LSV, a NM spin channel is introduced to connect two parallel electrodes of FM and SOM (figure 3.1e). The NM has a long λ_{NM}, such that the NM spin channel permits the spin current to flow over a longer distance in comparison to the SOM spin channel. The SOM detection electrode will absorb part of the spin current from the NM (when placed at a distance $< \lambda_{\mathrm{NM}}$) inducing a spin current in the SOM and the charge current generated via the ISHE can be probed transversely. The reciprocity of the SHE and ISHE was confirmed using such a non-local spin Hall technique [67]. This method is used in this thesis in an attempt to extract the spin properties of W, therefore this technique is elaborated on in section 3.3 and utilized in the study presented in chapter 7.

Local spin Hall devices are the local variation of the non-local spin Hall technique in LSVs where the FM electrode is in direct contact with a T-shaped SOM electrode with an optional tunnel barrier at the intersection of the FM and SOM electrodes (figure 3.1f). The local spin Hall device has been proven to adequately detect the SHE in SOMs such as Pt, Ta, W [149]. This local configuration permits spin injection with higher spin current density compared to the non-local configuration but is more prone to spurious effects coming from the charge current. Section 3.4 will further discuss the local spin Hall device as this technique is employed in the chapters 5 and 6.

The SHE properties of a variety of materials that have been measured with these different techniques are listed in a recent article about the prospect of spin-orbitronic devices [150]. There is no general consensus on the spin Hall angle for a specific material extracted by the different measurement techniques. Each technique has its own complexity and simplification in the used models. Consequently and unavoidably, systematic estimations and/or spurious effects arise, resulting in different θ_{SH}. This is evident for the heavily studied Pt. A further discussion on the origin of the spread in the experimentally observed θ_{SH} for a particular material can be found in section 2.2.3.

3.3 Lateral spin valves

The LSV is a nanostructured device that permits electrical injection and detection of pure spin current in a way that spurious effects arising from charge current are eliminated from the detected signal. Three different measurement configurations will be explained that permit extraction of the following spin properties: i) the (long) spin diffusion length of NM and the polarization of FM, ii) the spin diffusion length of SOMs, and iii) the SCI of SOMs

3.3.1 The basic working principle

In the LSV, a non-local technique can be used where injection and detection of pure spin current are separated by a spin transport channel as shown in figure 3.2a. A charge current is applied from the NM into a FM, creating a spin accumulation at the FM/NM interface (section 2.1.3). The spin accumulation will diffuse away from the FM within the NM ($+x$-direction) as a pure spin current with a characteristic decay length λ_{NM}. The detector, a second electrode, is placed at a distance L (with $L \sim \lambda_{\mathrm{NM}}$) from the injector. The materials choice for the detector depends on the desired spin properties to be measured. Additionally, an electrode in between the injector and detector can be included to absorb a part of the spin current, allowing the spin properties of the middle electrode to be obtained. Figure 3.2b displays a LSV pointing out the dimensions and the coordinates of the system which are used in the derivation for the different measurement configurations discussed in the following sections.

3.3.2 Conventional lateral spin valve

Figure 3.3a illustrates a FM/NM/FM LSV consisting of two FM electrodes (FM1 and FM2) that are connected via a NM channel with a long spin diffusion length. The spin flow in the device can be described by the one-dimensional (1D) spin diffusion model. A charge current is applied from the NM into the FM in order to inject a spin accumulation thus implicitly a spin current into the NM. Within this model, the spin currents in the FM and NM are assumed to only have a z and x component, respectively. Therefore, the spin diffusion equation (equation 2.15) in the NM and FMs electrodes are:

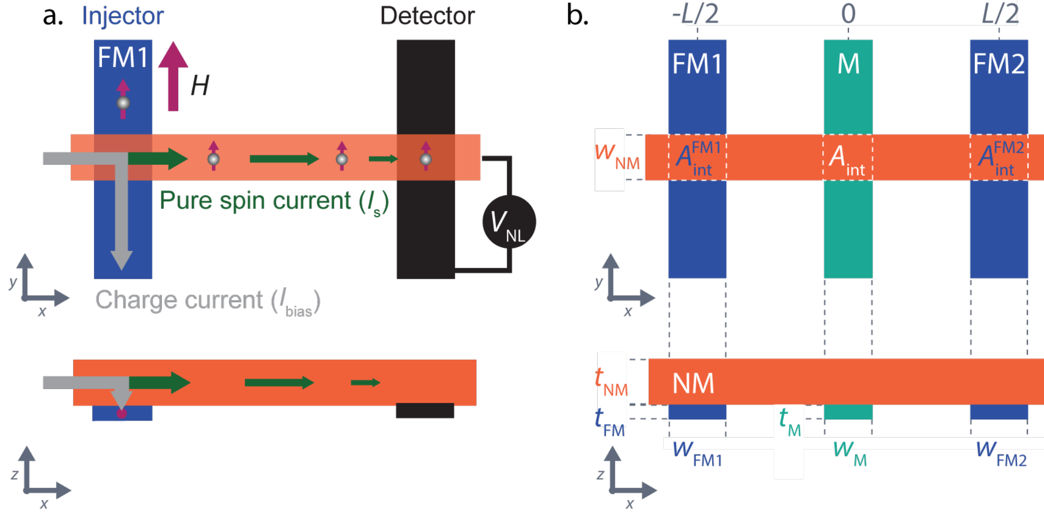

Figure 3.2: The non-local lateral spin valve. a) A pure spin current (I_s, green arrows) is injected into a spin transport channel (orange electrode) towards the detector (black electrode) by applying a charge current (I_{bias}, grey arrow) into the FM injector (blue electrode). The spin current that reaches the detector, which can be another FM, creates a potential (V_{NL}) that can be measured in open-circuit conditions. The spin current can also be manipulated in the channel by for example placing an extra electrode (M) as depicted in **b**. **b)** The important device dimensions for the derivations in the section 3.3.2, 3.3.3 and 3.3.4. The width and thickness are given by w_i and t_i for i = NM, FM1, FM2, M and the interface area A^j_{int} with j = FM1, FM2 and M. The inter electrode distance is L where FM1, M and FM2 are positioned at $x = -L/2$, $x = 0$, $x = L/2$, respectively. The NM/M interface is at $z = 0$.

$$\frac{\partial^2 \mu_s^{\text{NM}}}{\partial x^2} = \frac{\mu_s^{\text{NM}}}{\lambda^2_{\text{NM}}}, \tag{3.6}$$

$$\frac{\partial^2 \mu_s^{\text{FM}}}{\partial z^2} = \frac{\mu_s^{\text{FM}}}{\lambda^2_{\text{FM}}}. \tag{3.7}$$

The spin accumulation within the electrodes decays exponentially (equation 2.17) as:

$$\mu_s^{\text{NM}}(x) = Ae^{-|x+\frac{L}{2}|/\lambda_{\text{NM}}} + Be^{-|x-\frac{L}{2}|/\lambda_{\text{NM}}}, \tag{3.8}$$

$$\mu_s^{\text{FM}}(z) = Ce^{-z/\lambda_{\text{FM}}}, \tag{3.9}$$

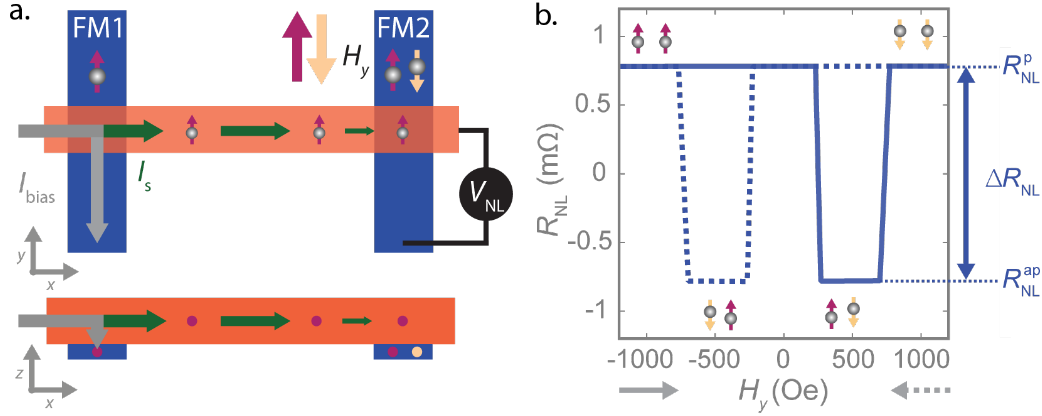

Figure 3.3: The standard spin signal with a conventional LSV a) A conventional LSV has a FM injector and detector bridged by a NM channel. A charge current I_{bias} is applied between the injector and the NM to inject a spin current. The detector will measure a different potential V_{NL} depending on the magnetization of the FM with respect to the spin current. The FM electrodes are designed such that the magnetization switches at different magnetic field. This permits observation of the parallel and anti-parallel configuration when sweeping an external magnetic field (H_y). **b)** The magnetic field dependence of the non-local spin resistance $R_{\text{NL}} = V_{\text{NL}}/I_{\text{bias}}$. At large negative magnetic fields, FM1 and FM2 are parallel aligned with R^{p}_{NL}. As H_y becomes positive (solid blue line), one FM electrode will switch such that R_{NL} changes to $R^{\text{ap}}_{\text{NL}}$ until the other FM electrode switches and the FMs are again parallel aligned with R^{p}_{NL}. Similar behaviour is observed when sweeping the magnetic field from positive to negative (dashed blue line). The non-local spin signal ΔR_{NL} is the difference in resistance between the parallel and anti-parallel state $R^{\text{p}}_{\text{NL}} - R^{\text{ap}}_{\text{NL}}$.

where A, B and C are integration constants. FM1 is located at $x = -L/2$ and FM2 is located at $x = +L/2$ (figure 3.2b).

This results in a pure spin current in the NM towards the side where no charge current is flowing ($-L/2 + x$). The amount of spin injected and detected depends on the boundary conditions at the NM/FM interfaces given by the continuity of $\boldsymbol{j}_{\text{s}}$:

$$A_{\text{NM}}\,(j^{\text{NM}}_{\text{s},x}\big|_{-\frac{L}{2}^-} - j^{\text{NM}}_{\text{s},x}\big|_{-\frac{L}{2}^+}) = A^{\text{FM1}}_{\text{int}}(j^{\text{FM1}}_{\text{s},z} - eP_{\text{FM1}}J_{\text{bias}})_{z=0}, \tag{3.10}$$

$$A_{\text{NM}}\,(j^{\text{NM}}_{\text{s},x}\big|_{\frac{L}{2}^-} - j^{\text{NM}}_{\text{s},x}\big|_{\frac{L}{2}^+}) = A^{\text{FM2}}_{\text{int}}\,j^{\text{FM2}}_{\text{s},z}\big|_{z=0} \tag{3.11}$$

where $A^{\text{FM}}_{\text{int}}$ is area of the NM/FM interfaces and A_{NM} is the cross-sectional area of the NM electrode ($w_{\text{NM}}t_{\text{NM}}$). The P_{FM1} is the polarization of FM1 and J_{bias} is the

charge current density injected at $x = -L/2$ (figure 3.2b). The NM/FM interfaces are considered to be transparent, such that continuity of the chemical potentials at the interface give:

$$(\mu_s^{NM} - \mu_s^{FM1})_{x=-\frac{L}{2}, z=0} = 0, \tag{3.12}$$

$$(\mu_s^{NM} - \mu_s^{FM2})_{x=\frac{L}{2}, z=0} = 0. \tag{3.13}$$

The detected non-local voltage at FM2 ($x = L/2$) is given by the expression:

$$eV_{NL} = P_{FM2}\mu_s^{FM2} \tag{3.14}$$

and the corresponding non-local resistance is

$$R_{NL} = \frac{V_{NL}}{J_{bias}A_{int}^{FM1}}. \tag{3.15}$$

Figure 3.3b shows R_{NL} while sweeping an external magnetic field H_y. FM1 and FM2 are designed in such a way that the switching field (the magnetic field at which the magnetization m reverses) are different for each FM electrode. Saturating m such that the FMs are parallel (↑↑) gives a positive R_{NL}. While sweeping H_y through zero, m of one of the FM reverses, due to the difference in switching fields, resulting in an anti-parallel magnetic configuration (↑↓). When H_y continues to increase, the second FM will switch and the magnetic configuration is parallel again (↓↓). Even though this parallel configuration is opposite to the starting configuration, R_{NL} is the same because the chemical potential difference between the two electrodes is probed. The difference in R_{NL} between the parallel and anti-parallel magnetic configuration is the non-local spin signal ($\Delta R_{NL} = R_{NL}^{p} - R_{NL}^{ap}$) is given by

$$\Delta R_{NL} = 4R_s^{NM}P_{FM1}P_{FM2}\frac{e^{L/\lambda_{NM}}}{r_1 r_2 e^{2L/\lambda_{NM}} - 1}. \tag{3.16}$$

where $r_i = 1 + 2Q_{FMi}$ introducing $Q_{FMi} = R_s^{FMi}/R_s^{NM}$ for $i = 1, 2$. ΔR_{NL}, being defined as the difference between two resistance state allows removing of any baseline in the signal. In the case that both FM are equivalent ($P_{FM1} = P_{FM2} = P_{FM}$, $w_{FM1} = w_{FM2}$ and $r_1 = r_2$), equation 3.16 reduces to:

$$\Delta R_{NL} = 4R_s^{NM}P_{FM}^2\frac{e^{L/\lambda_{NM}}}{r_1^2 e^{2L/\lambda_{NM}} - 1}. \tag{3.17}$$

This relationship can be used to determine λ_{NM} and P_{FM} by measuring the LSV for various lengths L of the spin channel and fitting the decay of the measured spin signal to equation 3.17. This method works when L is in the order of λ. Realistically, due to the limiting dimensions of device fabrication, it means that λ can only be extracted for materials with a λ on the order of a few hundred nanometers, e.g., light NM metals as Al, Cu or Ag. For materials with shorter λ, the spin current is lost within L and will not reach the detector as a consequence this method is not adequate for SOM and FM.

3.3.3 Spin absorption technique

The λ of metallic materials such as SOM and FM, that typically are a few nm, can be obtained by the spin absorption technique. For this technique, an additional electrode in the middle of the FMs is added to the LSV as presented in figure 3.4a. The measurement of the non-local spin signal is the same as in the conventional LSV, meaning that the spin current is injected via FM1 and detected by FM2. However, the electrode in the middle of the transport channel will absorb part of the spin current, reducing the measured spin signal. The absorbed spin current depends on the spin resistance of the middle electrode and the interface between the NM and the middle electrode. In this thesis, the spin absorption technique is used to study the properties of a SOM, therefore, the middle electrode is considered to be a SOM electrode in the remainder of this derivation.

Recently, it has been emphasized that the interface of the NM/SOM has to be considered for proper quantification of the bulk SCI [72–74, 151–154]. Interfacial spin absorption and SCI in NM/oxide (O) as well as in NM/NM interfaces have been observed with LSVs (section 2.3). Therefore, the measurement configuration for extracting the bulk λ_{SOM} is also susceptible to observations of spin absorption by the NM/SOM interface. In following analyses, it is considered that the interface between the NM and SOM might play a significant role.

The spin diffusion problem, equation 3.6 and 3.7, needs to be expanded by including the middle absorbing electrode. The spin diffusion length in SOM is pretty short, such that only the variation of $\mu_{\mathrm{s}}^{\mathrm{SOM}}$ in the z-direction is considered. The spin diffusion equation in the SOM is

$$\frac{\partial^2 \mu_{\mathrm{s}}^{\mathrm{SOM}}}{\partial z^2} = \frac{\mu_{\mathrm{s}}^{\mathrm{SOM}}}{\lambda_{\mathrm{SOM}}^2}. \tag{3.18}$$

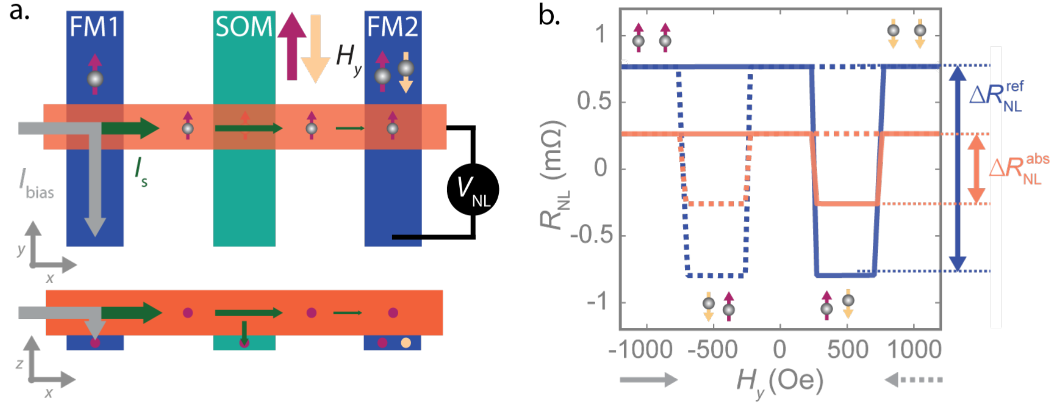

Figure 3.4: Spin absorption is deployed to extract the spin diffusion length of a SOM middle electrode. **a)** The LSV for the absorption technique has a FM injector and detector and a SOM middle electrode. The SOM will absorb part of the spin current that is flowing in the NM channel (see green arrows) reducing the spin current that arrives to the detector. **b)** The non-local spin resistance R_{NL} versus the external magnetic field H_x in the LSV for spin absorption. The orange line gives the non-local spin signal $\Delta R_{\text{NL}}^{\text{abs}}$ of this LSV. The blue line gives the non-local spin signal of a reference LSV without a middle electrode ($\Delta R_{\text{NL}}^{\text{ref}}$, figure 3.3a, b). The fact that $\Delta R_{\text{NL}}^{\text{abs}} < \Delta R_{\text{NL}}^{\text{ref}}$ indicates that the SOM electrode absorbs some of the spin current. The amount of spin current absorbed can be related to the SOM spin resistance.

This additional electrode, creating an additional spin sink, changes the solution in the NM electrode (equation 3.8) into

$$\mu_{\text{s}}^{\text{NM}}(x) = Ae^{-\frac{|x|}{\lambda_{\text{NM}}}} + Be^{-\frac{|x+\frac{L}{2}|}{\lambda_{\text{NM}}}} + Ce^{-\frac{|x-\frac{L}{2}|}{\lambda_{\text{NM}}}} \tag{3.19}$$

and the spin current density is

$$j_{s,x}^{\text{NM}} = \frac{\sigma_{\text{NM}}}{\lambda_{\text{NM}}}\left[A\ \text{sign}(x)\ e^{-\frac{|x|}{\lambda_{\text{NM}}}} + B\ \text{sign}(x+\frac{L}{2})\ e^{-\frac{|x+\frac{L}{2}|}{\lambda_{\text{NM}}}} + C\ \text{sign}(x-\frac{L}{2})\ e^{-\frac{|x-\frac{L}{2}|}{\lambda_{\text{NM}}}}\right]. \tag{3.20}$$

The solution of the spin diffusion equations within the FM electrodes become:

$$\mu_{\text{s}}^{\text{FM}}(z) = De^{-z/\lambda_{\text{FM}}}, \tag{3.21}$$

$$j_{\text{s},z}^{\text{FM}} = -\frac{\sigma_{\text{FM}}}{\lambda_{\text{FM}}}(1-P_{\text{FM}}^2)De^{-z/\lambda_{\text{FM}}}, \tag{3.22}$$

and in the SOM electrode they are:

$$\mu_{\mathrm{s}}^{\mathrm{SOM}}(z) = Ee^{-z/\lambda_{\mathrm{SOM}}}, \tag{3.23}$$

$$j_{\mathrm{s},z}^{\mathrm{SOM}} = \frac{\sigma_{\mathrm{SOM}}}{\lambda_{\mathrm{SOM}}} Ee^{-z/\lambda_{\mathrm{SOM}}}. \tag{3.24}$$

In the 1D approximation, the spin properties of the NM electrode in the volume below the intersection with the SOM electrode correspond to a single point $x = 0$, that being the case, the boundary conditions at $x = 0$ are

$$\mu_{\mathrm{s}}^{\mathrm{NM}}\big|_{0+} = \mu_{\mathrm{s}}^{\mathrm{NM}}\big|_{0-} \tag{3.25}$$

$$A_{\mathrm{NM}}(j_{\mathrm{s},x}^{\mathrm{NM}}\big|_{0-} - j_{\mathrm{s},x}^{\mathrm{NM}}\big|_{0+}) = A_{\mathrm{int}} j_{\mathrm{s},z}^{\mathrm{NM}}\big|_{0}, \tag{3.26}$$

where $A_{\mathrm{NM}} = t_{\mathrm{NM}} w_{\mathrm{NM}}$ is the cross-sectional area of the NM electrode and $A_{\mathrm{int}} = w_{\mathrm{SOM}} w_{\mathrm{NM}}$ is the NM/SOM interface area. At the NM/SOM interface $(z = 0)$, the boundary conditions read

$$j_{\mathrm{s},z}^{\mathrm{SOM}} - j_{\mathrm{s},z}^{\mathrm{NM}}\big|_{z=0} = -G_{\mathrm{s}}^{\parallel} \left. \frac{\mu_{\mathrm{s}}^{\mathrm{NM}} + \mu_{\mathrm{s}}^{\mathrm{SOM}}}{2} \right|_{x=0,z=0}, \tag{3.27}$$

$$\frac{1}{2}(j_{\mathrm{s},z}^{\mathrm{SOM}} + j_{\mathrm{s},z}^{\mathrm{NM}})_{z=0} = \frac{1}{R_{\mathrm{s}}^{\mathrm{I}}}(\mu_{\mathrm{s}}^{\mathrm{NM}} - \mu_{\mathrm{s}}^{\mathrm{SOM}})_{x=0,z=0}, \tag{3.28}$$

where $G_{\mathrm{s}}^{\parallel}/A_{\mathrm{int}}$ gives the interfacial spin-loss conductance $G_{\parallel}$ and $R_{\mathrm{s}}^{\mathrm{I}}$ is the spin resistance of the NM/SOM interface. We assume that $w_{\mathrm{SOM}} \ll \lambda_{\mathrm{NM}}$ such that $\mu_{\mathrm{s}}^{\mathrm{NM}}$ just below the interface can be considered constant.

Finally, considering identical FM electrodes separated by a distance L and a SOM electrode in the middle, the non-local spin absorption signal is:

$$\Delta R_{\mathrm{NL}}^{\mathrm{abs}} = \frac{8P_{\mathrm{FM}}^2 Q_{\mathrm{FM}} R_{\mathrm{s}}^{\mathrm{FM}} e^{\frac{L}{\lambda_{\mathrm{NM}}}}[2Q_{\parallel}(r_3 - 1) + Q_{\mathrm{RI}} Q_{\mathrm{SOM}}]}{r_1^2 e^{\frac{2L}{\lambda_{\mathrm{NM}}}}[4Q_{\parallel} r_3 + 2(Q_{\mathrm{RI}} + 2)Q_{\mathrm{SOM}} + Q_{\mathrm{RI}}] - 2r_1 e^{\frac{L}{\lambda_{\mathrm{NM}}}}(4Q_{\parallel} + Q_{\mathrm{RI}} + 4Q_{\mathrm{SOM}}) + 4Q_{\parallel}(2 - r_3) + 2(2 - Q_{\mathrm{RI}})Q_{\mathrm{SOM}} + Q_{\mathrm{RI}}}, \tag{3.29}$$

where $r_3 = r_{\mathrm{SOM}} = 1 + 2Q_{\mathrm{SOM}}$ and $Q_{\mathrm{SOM}} = R_{\mathrm{s}}^{\mathrm{SOM}}/R_{\mathrm{s}}^{\mathrm{NM}}$ of the middle electrode. The NM/SOM interface is represented by $Q_{\mathrm{RI}} = R_{\mathrm{s}}^{\mathrm{I}}/R_{\mathrm{s}}^{\mathrm{NM}}$ and $Q_{\parallel} = 1/(R_{\mathrm{s}}^{\mathrm{NM}} G_{\mathrm{s}}^{\parallel})$.

Figure 3.4b shows the magnetic field dependence of R_{NL} and the reduction of the non-local spin absorption signal $\Delta R_{\mathrm{NL}}^{\mathrm{abs}}$ in comparison to the non-local spin reference signal $\Delta R_{\mathrm{NL}}^{\mathrm{ref}}$ (figure 3.3b). The ratio of $\Delta R_{\mathrm{NL}}^{\mathrm{abs}}$ (the spin signal with the middle electrode, equation 3.29) and $\Delta R_{\mathrm{NL}}^{\mathrm{ref}}$ (the spin signal without the middle electrode, equation 3.16) is given by:

$$\frac{\Delta R_{\mathrm{NL}}^{\mathrm{abs}}}{\Delta R_{\mathrm{NL}}^{\mathrm{ref}}} = \frac{2(r_1 e^{\frac{L}{\lambda_{\mathrm{NM}}}} + 1)[2Q_{\parallel}(r_1 - 1) + Q_{\mathrm{RI}}Q_{\mathrm{SOM}}]}{r_1 e^{\frac{L}{\lambda_{\mathrm{NM}}}}[4Q_{\parallel} r_3 + 2(Q_{\mathrm{RI}} + 2)Q_{\mathrm{SOM}} + Q_{\mathrm{RI}}) + 4Q_{\parallel}(r_3 - 2] - 2(2 - 2Q_{\mathrm{RI}})Q_{\mathrm{SOM}} - Q_{\mathrm{RI}}} \tag{3.30}$$

The non-local spin absorption signal permits to acquire λ_{SOM} when knowing the spin properties of the NM and FM. This derivation is valid as long as the spin profile in the NM over w_{SOM} is subservient, hence $w_{\mathrm{SOM}} < \lambda_{\mathrm{NM}}$.

3.3.4 Non-local spin Hall technique

Non-local spin Hall technique is a frequently used tool to acquire the SCI efficiency of bulk SOM (section 2.2.3). This technique uses the same LSV structure as described in the spin absorption technique but with a different measurement configuration. The injection of the spin current is identical to the spin injection in the LSV's explained in section 3.3.2 and 3.3.3. In order to measure the ISHE, the detector is the SOM middle electrode (figure 3.6a). The SHE can be measured by inverting the injector and detector (figure 3.6b). Figure 3.5 illustrates the spin flow in ISHE and SHE at the NM/SOM interface area.

Figure 3.6a displays the ISHE measurement in SOM. The spins are aligned by an external magnetic field (H_x) along the hard axis of the FM1 electrode (x-direction), a requirement for observing the SCI with this technique. The pure spin current is injected from the FM1 electrode into the NM channel by I_{bias}. Subsequently, the spin current decays towards the SOM electrode, where it is partially absorbed. The spin current $I_{s,z}$ originating from this spin absorption is converted into a charge current I_{ISHE} via the ISHE (figure 3.5a). I_{ISHE} is measured by detecting the transverse voltage V_{ISHE} along the SOM electrode. The produced I_{ISHE}, and therefore V_{ISHE}, will revert when changing the FM1 magnetization with the external magnetic field as shown in figure 3.7. The difference in the ISHE resistance $R_{\mathrm{ISHE}} = V_{\mathrm{ISHE}}/I_{\mathrm{bias}}$ for the two saturated magnetizations is twice the ISHE signal $2\Delta R_{\mathrm{ISHE}}$.

The SHE is discerned by interchanging the injector and detector with respect to the ISHE measurement, as presented in figure 3.6b. A charge current is applied

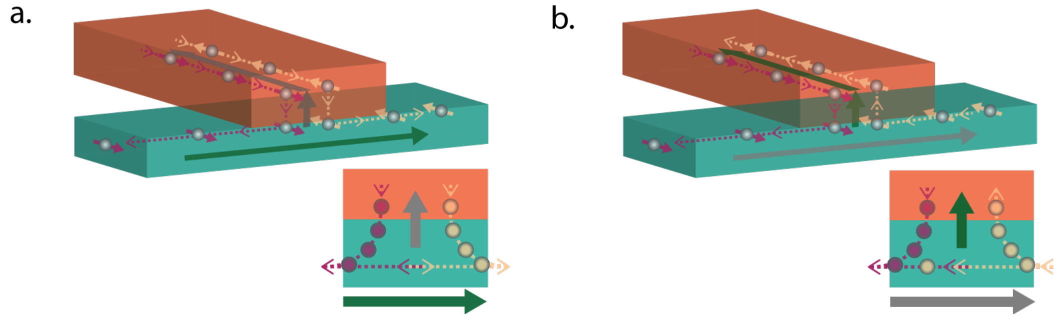

Figure 3.5: Bulk spin-charge interconversion in a NM/SOM heterostructure. a) SHE: a spin current (green arrow) injected into a SOM deflects the spin carriers in the same direction creating a charge current. **b)** ISHE: a charge current (grey arrow) injected into a SOM deflects the spin carriers in opposite direction generating a spin current.

to SOM, in which the SHE takes place and a spin current $I_{\mathrm{s},-z}$ is brought about (figure 3.5b). This spin current will diffuse into the NM channel and travel towards the FM, that acts as the detector. The spin accumulation is probed by an open-circuit voltage V_{SHE} across the FM/NM interface. The SHE resistance is defined as $R_{\mathrm{SHE}} = V_{\mathrm{SHE}}/I_{\mathrm{bias}}$. Figure 3.7 shows that the R_{SHE} as a function of H_x changes sign compared to $R_{\mathrm{ISHE}}(H_x)$ due to the swapping of the injector and the detector. Onsager reciprocity [67, 155] dictates that the spin Hall signal is the same as the inverse spin Hall signal, $|\Delta R_{\mathrm{SHE}}| = |\Delta R_{\mathrm{ISHE}}|$ as illustrated in 3.7.

In this analyses, bulk and interfacial SCI will be considered for the same reason as explained in section 3.3.3. This means that the measured signal tagged as $R_{\mathrm{(I)SHE}}$ in figure 3.7 will be R_{SC} containing the contribution of both the bulk and interfacial SCI. Here, we derive the expression for R_{SC}. The charge current density induced by the SHE, hence SCI in the bulk SOM, is given by

$$j_{\mathrm{c},y} = -\sigma_{\mathrm{SOM}} \frac{\partial \mu_{\mathrm{c}}^{\mathrm{SOM}}}{\partial y} - \sigma_{\mathrm{SH}} \frac{\partial \mu_{\mathrm{s}}^{\mathrm{SOM}}}{\partial z}, \tag{3.31}$$

and the charge current density produced at the NM/SOM interface through interfacial SCI is

$$j_{\mathrm{c,int}} = \sigma_{\mathrm{SC}} \frac{\mu_{\mathrm{c}}^{\mathrm{SOM}} + \mu_{\mathrm{c}}^{\mathrm{NM}}}{2} \delta(z). \tag{3.32}$$

σ_{SH} is the spin Hall conductivity and σ_{SC} is the interfacial spin-charge conductivity (the equivalent of the σ_{SH} for the interface).

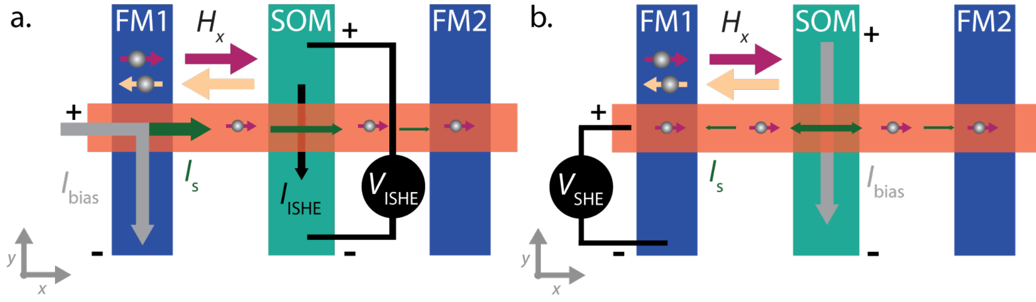

Figure 3.6: Spin-charge interconversion measurement using the non-local spin Hall technique a) The measurement of the ISHE in the SOM electrode. A pure spin current is injected from the FM into the NM, that decays towards SOM, where it is partially absorbed. The spin current $I_{s,z}$ along z with a polarization along x is converted to a charge current I_{ISHE} along y and detected via a potential difference V_{ISHE}. An external magnetic field can switch the magnetization of FM, consequently inverting the polarization of the spin current and reversing the direction of I_{ISHE}. **b)** The SHE measurement has the injector and detector interchanged in comparison to the ISHE case explained in **a**. A spin accumulation is created at the NM/SOM interface by applying a charge current I_{bias} through SOM. Spin accumulation, produced by the SHE due to SOC in SOM, will diffuse into the NM $I_{s,-x}$. The spin current is probed by the FM electrode giving V_{SHE}. A switching of the magnetization of FM reverses $\pm V_{\mathrm{SHE}}$.

The average current flowing in the SOM electrode is obtained by averaging over the cross section $A_{\mathrm{SOM}} = t_{\mathrm{SOM}} w_{\mathrm{SOM}}$. This current should vanish because the experiment probes a voltage in open-circuit conditions and, therefore,

$$0 = -\sigma_{\mathrm{SOM}} \frac{\partial \mu_c^{\mathrm{SOM}}}{\partial y} + \sigma_{\mathrm{SH}} \frac{1}{t_{\mathrm{SOM}}} \mu_s^{\mathrm{SOM}}(0) + \sigma_{\mathrm{SC}} \frac{1}{t_{\mathrm{SOM}}} \left. \frac{\mu_s^{\mathrm{SOM}} + \mu_s^{\mathrm{NM}}}{2} \right|_{z=0}, \tag{3.33}$$

and integrating over y gives

$$eV_{\mathrm{SC}} = -\mu_c^{\mathrm{SOM}} \Big|_{-\frac{L_y}{2}}^{+\frac{L_y}{2}} = -\frac{\sigma_{\mathrm{SH}}}{\sigma_{\mathrm{SOM}}} \frac{w_{\mathrm{NM}}}{t_{\mathrm{SOM}}} \mu_s^{\mathrm{SOM}}(0) - \frac{\sigma_{\mathrm{SC}}}{\sigma_{\mathrm{SOM}}} \frac{w_{\mathrm{NM}}}{t_{\mathrm{SOM}}} \left. \frac{\mu_s^{\mathrm{SOM}} + \mu_s^{\mathrm{NM}}}{2} \right|_{z=0, x=0}. \tag{3.34}$$

The spin-charge resistance is defined as

$$R_{\mathrm{SC}} = \frac{V_{\mathrm{SC}}}{J_{\mathrm{bias}} A_{\mathrm{int}}^{\mathrm{FM}}}, \tag{3.35}$$

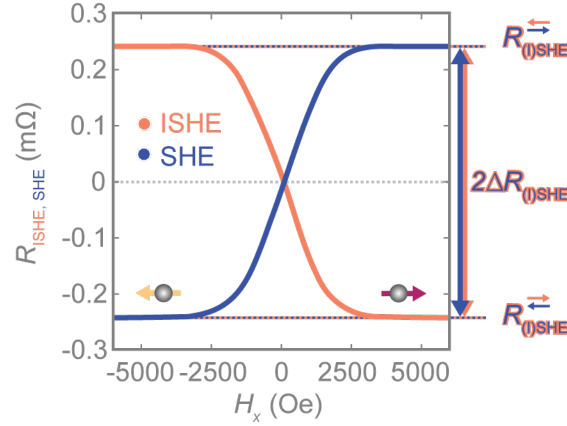

Figure 3.7: Spin Hall signal by the non-local spin Hall technique. The ISHE resistance ($R_{\rm ISHE}$) and SHE resistance ($R_{\rm SHE}$) as a function of the external magnetic field (H_x). The $R_{\rm ISHE}$ transitions smoothly from a saturated negative H_x, to at saturated positive H_x. The gradual change is coming from the FM magnetization which undergoes a coherent rotation. The SHE shows the same behaviour but reversed due to the swapping of the current and voltage probes. The difference in $R_{\rm ISHE}$ (or $R_{\rm SHE}$) between the saturated values is the spin-charge signal $2\Delta R_{\rm (I)SHE}$.

so combining equation 3.34 and equation 3.35 results in

$$R_{\rm SC} = \frac{w_{\rm NM} R_{\rm s}^{\rm FM}}{t_{\rm SOM}\sigma_{\rm SOM}} \frac{4P_{\rm FM} e^{\frac{L}{2\lambda_{\rm NM}}} [2Q_{\parallel}\sigma_{\rm SC}(Q_{\rm RI}+2Q_{\rm SOM}) + Q_{\rm SOM}\sigma_{\rm SH}(4Q_{\parallel}-Q_{\rm RI}))]}{r_1 e^{\frac{L}{\lambda_{\rm NM}}} [4Q_{\parallel} r_3 + 2(Q_{\rm RI}+2)Q_{\rm SOM} + Q_{\rm RI}] + 4Q_{\parallel}(r_3-2) - 2(2-2Q_{\rm RI})Q_{\rm SOM} + Q_{\rm RI}}. \tag{3.36}$$

Note that equation 3.36 is derived considering the presence of the second FM electrode, as presented in the spin absorption technique (figure 3.4a).

The change of polarization of the spin current, when reversing the magnetization of the FM injector, induces a detectable change in $R_{\rm SC}$. The difference in $R_{\rm SC}$ between the saturated positive and negative magnetization of the FM is twice the spin-charge conversion signal, $2\Delta R_{\rm SC} = R_{\rm SC}^{\rightarrow} - R_{\rm SC}^{\leftarrow}$.

The 1D spin diffusion model arrives to equation 3.36 that explains the theoretical value of the SCI signal in this non-local spin Hall devices. However, what is not included in the model is the electrical shunting $x_{\rm SOM}$ of the $I_{\rm ISHE}$ produced in the SOM electrode by the NM channel. When this electrical shunting is not considered, the spin-charge conductivity will be underestimated. Therefore, $x_{\rm SOM}$ is obtained by 3D finite element method (FEM) simulations (see section 4.3.2) such that, fi-

nally,

$$\Delta R_{\mathrm{SC}} = x_{\mathrm{SOM}} \frac{w_{\mathrm{NM}} R_{\mathrm{s}}^{\mathrm{FM}}}{t_{\mathrm{SOM}} \sigma_{\mathrm{SOM}}} \frac{4 P_{\mathrm{FM}} e^{\frac{L}{2\lambda_{\mathrm{NM}}}} (2 Q_{\parallel} \sigma_{\mathrm{SC}} (Q_{\mathrm{RI}} + 2 Q_{\mathrm{SOM}}) + Q_{\mathrm{SOM}} \sigma_{\mathrm{SH}} (4 Q_{\parallel} - Q_{\mathrm{RI}}))}{r_1 e^{\frac{L}{\lambda_{\mathrm{NM}}}} (4 Q_{\parallel} r_3 + 2 (Q_{\mathrm{RI}} + 2) Q_{\mathrm{SOM}} + Q_{\mathrm{RI}}) + 4 Q_{\parallel} (r_3 - 2) - 2 (2 - 2 Q_{\mathrm{RI}}) Q_{\mathrm{SOM}} + Q_{\mathrm{RI}}} \tag{3.37}$$

3.3.5 Limiting cases (bulk or interfacial)

The equations derived in the sections 3.3.3 and 3.3.4 describe a system with both bulk and interfacial contributions to spin absorption and to SCI. However, when the bulk properties ($1/R_{\mathrm{SOM}}$ and σ_{SH}) are on the same order of magnitude as the interface properties ($G_{\mathrm{s}}^{\parallel}$ and σ_{SC}), there are two unknown parameters for the same contribution ($1/R_{\mathrm{SOM}}$ and $G_{\mathrm{s}}^{\parallel}$, σ_{SH} and σ_{SC}) and no weight can be given to the bulk and interface properties such that bulk and interface contributions can not be distinguished. But, if one of the two dominate over the other, the spin properties can be extracted considering the following two limiting cases:

Bulk contribution only: no interfacial spin absorption nor interfacial spin-charge interconversion ($G_{\mathrm{s}}^{\parallel} = 0, Q_{\parallel} = \infty, \sigma_{\mathrm{SC}} = 0$).

$$\Delta R_{\mathrm{NL}}^{\mathrm{abs}} = \frac{4 P_{\mathrm{FM}}^2 Q_{\mathrm{FM}} R_{\mathrm{s}}^{\mathrm{FM}} (r_3 - 1) e^{\frac{L}{\lambda_{\mathrm{NM}}}}}{r_1^2 r_3 e^{\frac{2L}{\lambda_{\mathrm{NM}}}} - 2 r_3 e^{\frac{L}{\lambda_{\mathrm{NM}}}} - r_3 + 2}, \tag{3.38}$$

$$\frac{\Delta R_{\mathrm{NL}}^{\mathrm{abs}}}{\Delta R_{\mathrm{NL}}^{\mathrm{ref}}} = \left[1 + \frac{2}{r_3 - 1} \left(\frac{1}{2} - \frac{1}{1 + r_1 e^{\frac{L}{\lambda_{\mathrm{NM}}}}} \right) \right]^{-1}, \tag{3.39}$$

$$\Delta R_{\mathrm{SC}} = \Delta R_{\mathrm{(I)SHE}} = x_{\mathrm{SOM}} \frac{w_{\mathrm{NM}} R_{\mathrm{s}}^{\mathrm{FM}}}{t_{\mathrm{SOM}} \sigma_{\mathrm{SOM}}} \frac{4 P_{\mathrm{FM}}^2 Q_{\mathrm{SOM}} \sigma_{\mathrm{SH}} e^{\frac{L}{2\lambda_{\mathrm{NM}}}}}{r_1 r_{\mathrm{SOM}} e^{\frac{L}{\lambda_{\mathrm{NM}}}} + r_{\mathrm{SOM}} - 2}. \tag{3.40}$$

Interfacial contribution only: merely interfacial spin absorption and interfacial spin-charge interconversion ($G_{\mathrm{SOM}} = 0, Q_{\mathrm{SOM}} = \infty, \sigma_{\mathrm{SH}} = 0$).

$$\Delta R_{\mathrm{NL}}^{\mathrm{abs}} = \frac{4 P_{\mathrm{FM}}^2 Q_{\mathrm{FM}} R_{\mathrm{s}}^{\mathrm{FM}} (r_{\mathrm{RI}} - 1) e^{\frac{L}{\lambda_{\mathrm{NM}}}}}{r_1^2 r_{\mathrm{RI}} e^{\frac{2L}{\lambda_{\mathrm{NM}}}} - 2 r_3 e^{\frac{L}{\lambda_{\mathrm{NM}}}} - r_{\mathrm{RI}} + 2}, \tag{3.41}$$

$$\frac{\Delta R_{\mathrm{NL}}^{\mathrm{abs}}}{\Delta R_{\mathrm{NL}}^{\mathrm{ref}}} = \left[1 + \frac{2}{r_{\mathrm{RI}} - 1}\left(\frac{1}{2} - \frac{1}{1 + r_1 e^{\frac{L}{\lambda_{\mathrm{NM}}}}}\right)\right]^{-1}, \tag{3.42}$$

$$\Delta R_{\mathrm{SC}} = x_{\mathrm{SOM}} \frac{w_{\mathrm{NM}} R_{\mathrm{s}}^{\mathrm{FM}}}{t_{\mathrm{SOM}} \sigma_{\mathrm{SOM}}} \frac{4 P_{\mathrm{FM}}^2 Q_{\parallel} \sigma_{\mathrm{SC}} e^{\frac{L}{2\lambda_{\mathrm{NM}}}}}{r_1 r_{\mathrm{RI}} e^{\frac{L}{\lambda_{\mathrm{NM}}}} + r_{\mathrm{RI}} - 2}, \tag{3.43}$$

given that $r_{\mathrm{RI}} = 1 + 2Q_{\parallel}$.

3.4 Local spin Hall device

The local spin Hall device can be used to measure the SCI in a SOM by locally injecting a spin-polarized current at the FM/SOM interface. The direct contact between SOM and FM makes these devices the local variation of the previously described non-local spin Hall device with potentially larger output signals. Even more, the FM/SOM nanostructures can be used for validation of the proposed MESO logic device (section 1.3) as the device is the equivalent of the magnetic state readout (SO node).

3.4.1 One-dimensional spin diffusion model

The FM/SOM nanostructures consist of a T-shaped SOM electrode and a FM electrode where the tip of the FM is overlapping with the intersection of the T-shaped nanostructure. Figure 3.8a and b show the device configuration of the ISHE and SHE measurement setup, respectively, where the magnetization m of the FM electrode is aligned along the easy axis and can be switched with an external magnetic field H_x. The ISHE is measured by applying a bias current I_{bias} from the FM electrode into the SOM electrode. A spin-polarized current is injected into SOM ($-z$), polarized in the x-direction. The ISHE in SOM produces a transverse charge current (I_{ISHE}), that is detected as a voltage (V_{ISHE}) in open circuit conditions along the transverse arms of the SOM T-shaped electrode. The reversal of m induces a sign change of V_{ISHE}. It is convenient to define the ISHE resistance as $R_{\mathrm{ISHE}} = V_{\mathrm{ISHE}}/I_{\mathrm{bias}}$.

Figure 3.9a present R_{ISHE} as a function of H_x for the ISHE measurement configurations in the local spin Hall device. It shows that, as long as the magnetization is aligned along the +x-direction, the ISHE induces a constant R_{ISHE}. The reversal of

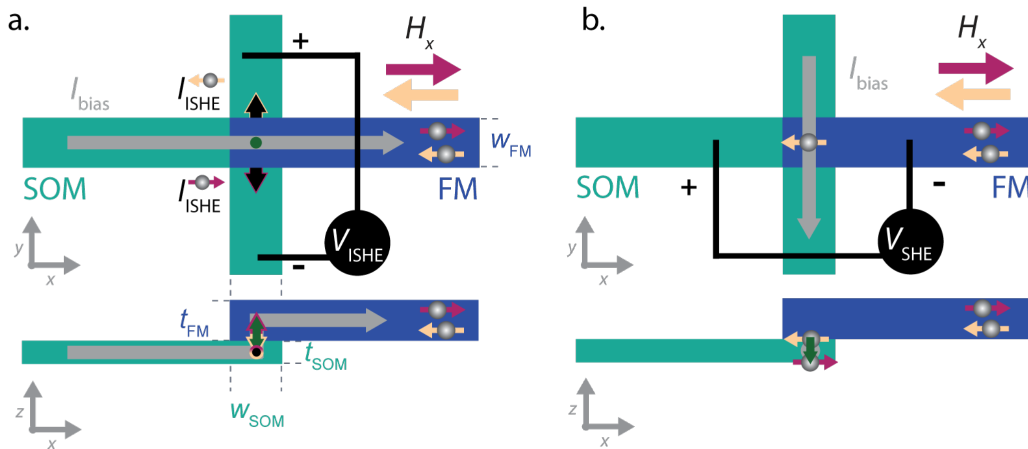

Figure 3.8: Spin-charge interconversion in a FM/SOM local spin Hall device. The local spin Hall device consists of a FM electrode and a T-shaped SOM electrode. The applied bias current I_{bias} and the spin current are presented by grey and green arrows, respectively. The opposite spin polarization is given by red and yellow arrows and the associated magnetic field H_x has the same color. **a)** The ISHE is measured by applying I_{bias} from the SOM to FM and probing the voltage on the transverse SOM electrode. I_{bias} generates a spin-polarized current with a polarization defined by the magnetization of FM. The spin current will be converted into a charge current (I_{ISHE}) observable as open-circuit ISHE voltage (V_{ISHE}). V_{ISHE} changes sign when reversing the magnetization of the FM with the external magnetic field. **b)** For the SHE configuration, the I_{bias} is applied to the vertical SOM electrode generating a spin current in $-z$ that results in a spin accumulation at the FM/SOM interface. The spin accumulation is probed by the magnetization of the FM while the electrochemical potentials changes when the FM is aligned parallel or anti-parallel with respect to the polarized spin accumulation. Therefore, the SHE voltage (V_{SHE}) is obtained by probing the interface.

the magnetization to $-x$-direction by sweeping H_x switches R_{ISHE} to $-R_{\text{ISHE}}$. The transition between the positive and negative resistance state is sharp. The same behavior is observed when sweeping H_x in opposite direction, with a hysteresis associated to the magnetization of the FM electrode. The two resistance states can be associated with the magnetic state of the FM (i.e., we are reading out the magnetic state) and the difference between these two resistance states is the ISHE signal $2\Delta R_{\text{ISHE}}$.

Reciprocally, in the SHE configuration, I_{bias} is applied through the transverse SOM electrode such that a spin current polarized in the x-direction is generated via SHE, resulting in spin accumulation at the surfaces of the SOM. The top surface can be

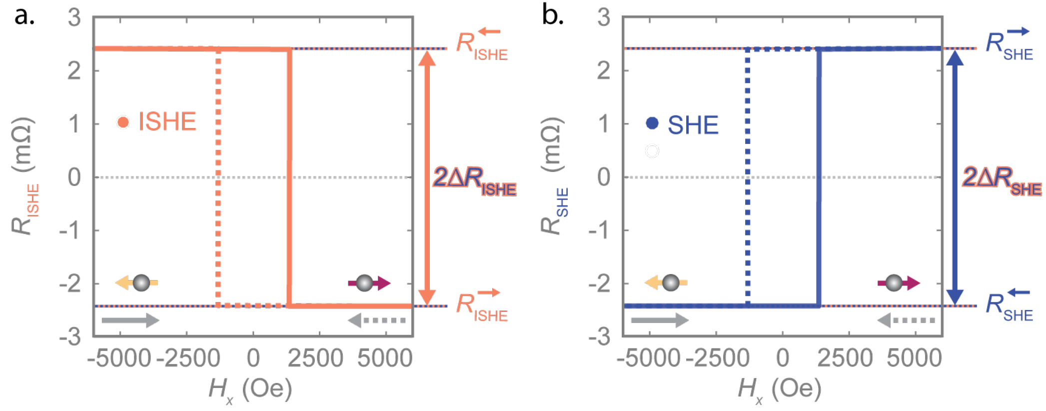

Figure 3.9: Spin Hall signal in a local spin Hall device. a) A sketch of the ISHE resistance R_{ISHE} as a function of the external magnetic field H_x. A sharp transitions from R_{ISHE} at saturated magnetization with negative H_{-x}, to $-R_{\text{ISHE}}$ at reversed saturated magnetization with positive H_x. **b)** The R_{SHE} versus H_x shows opposite behaviour compared to R_{ISHE} due to the swapping of the current and voltage probes. The trace is a solid line and retrace is a dashed line. In both cases, the difference in R_{ISHE} and R_{SHE} at saturated magnetic fields is $2\Delta R_{\text{(I)SHE}}$.

probed with the FM electrode as the Fermi level of the FM electrode aligns with the electrochemical potential of the majority (minority) spins of the spin accumulation and a positive (negative) interface voltage V_{SHE} is created when m is oriented along $+x$ $(-x)$. Figure 3.9b displays the spin Hall resistance R_{SHE} that is defined as $V_{\text{SHE}}/I_{\text{bias}}$. The ISHE and SHE signals will have the same magnitude and opposite sign, as expected from the Onsager reciprocity [67].

The output of the ISHE (R_{ISHE}) in the local spin Hall device is developed by an analytic 1D spin diffusion model based on the two-channel model (section 2.1.2) [156, 157]. The injected vertical current density flowing through the NM/SOM interface gives rise to a local spin accumulation. The spin accumulation profile in the FM and SOM, is given by solution of the spin diffusion equations, that is

$$\mu_{\text{SOM}}(z) = \frac{\cosh\left(\frac{t_{\text{SOM}}+z}{\lambda_{\text{SOM}}}\right)}{\cosh\left(\frac{t_{\text{SOM}}}{\lambda_{\text{SOM}}}\right)}\mu(0), \tag{3.44}$$

$$\mu_{\text{FM}}(z) = \frac{\cosh\left(\frac{t_{\text{FM}}+z}{\lambda_{\text{FM}}}\right)}{\cosh\left(\frac{t_{\text{FM}}}{\lambda_{\text{FM}}}\right)}\mu(0), \tag{3.45}$$

taking $z = 0$ at the interface. μ, t and λ are the spin accumulation, the thickness and the spin diffusion length, respectively. Subscripts SOM and FM denote the materials.

The interface is considered transparent, subsequently the electrochemical potential for spin-up and spin-down electrons are assumed to be continuous through the FM/SOM interface and the spin current is conserved. At the FM/SOM interface, in open-circuit conditions, the BC reads:

$$-\frac{1}{\rho^*_{\mathrm{FM}}}\frac{\partial \mu_{\mathrm{FM}}}{\partial z} + P_{\mathrm{FM}} j_{\mathrm{c},z} = -\frac{1}{\rho_{\mathrm{SOM}}}\frac{\partial \mu_{\mathrm{SOM}}}{\partial z} \tag{3.46}$$

$j_{\mathrm{c},z}$ is the charge current density in the z-direction and ρ_{SOM} is the resistivity of SOM and $\rho^*_{\mathrm{FM}} = \rho_{\mathrm{FM}}/(1 - P^2_{\mathrm{FM}})$ is the effective resistivity of FM.

The local spin accumulation at the interface is

$$\mu(0) = \frac{P_{\mathrm{FM}} j_{\mathrm{c},z}}{\frac{1}{\rho_{\mathrm{SOM}}\lambda_{\mathrm{SOM}}}\tanh\left(\frac{t_{\mathrm{SOM}}}{\lambda_{\mathrm{SOM}}}\right) + \frac{1}{\rho_{\mathrm{FM}}\lambda_{\mathrm{FM}}}\tanh\left(\frac{t_{\mathrm{FM}}}{\lambda_{\mathrm{FM}}}\right)}, \tag{3.47}$$

and the transverse current density generated by the ISHE is given by:

$$j_{\mathrm{c},y} = \theta_{\mathrm{SH}} j_{\mathrm{s},z} = -\theta_{\mathrm{SH}}\frac{1}{\rho_{\mathrm{SOM}}}\frac{\partial \mu}{\partial z}. \tag{3.48}$$

I_{ISHE} is obtained by integrating the charge current density over the area where the spin-charge conversion takes place:

$$I_{\mathrm{ISHE}} = \iint_{-t_{\mathrm{SOM}}}^{0} j_{\mathrm{c},y}\, dz\, dx = \theta_{\mathrm{SH}}\frac{1}{\rho_{\mathrm{SOM}}}\int [\mu(0) - \mu(-t_{\mathrm{SOM}})]\, dx, \tag{3.49}$$

and by implementing equation 3.44 and 3.47, equation 3.49 can be rewritten as

$$I_{\mathrm{ISHE}} = \theta_{\mathrm{SH}}\lambda_{\mathrm{SOM}} P_{\mathrm{FM}} \frac{1 - \frac{1}{\cosh\left(\frac{t_{\mathrm{SOM}}}{\lambda_{\mathrm{SOM}}}\right)}}{\tanh\left(\frac{t_{\mathrm{SOM}}}{\lambda_{\mathrm{SOM}}}\right) + \frac{\rho_{\mathrm{SOM}}\lambda_{\mathrm{SOM}}}{\rho^*_{\mathrm{FM}}\lambda_{\mathrm{FM}}}\tanh\left(\frac{t_{\mathrm{FM}}}{\lambda_{\mathrm{FM}}}\right)} \int j_{\mathrm{c},z}\, dx, \tag{3.50}$$

The current distribution in y is considered to be homogeneous meaning that $I_{\mathrm{bias}} = \iint j_{\mathrm{c},z}\, dx\, dy = w_{\mathrm{FM}} \int j_{\mathrm{c},z}\, dx$. Accordingly, $\int j_{\mathrm{c},z}\, dx$ is replaced by $I_{\mathrm{bias}}/w_{\mathrm{FM}}$, leading to the final expression for the charge current induced by the ISHE

$$I_{\mathrm{ISHE}} = \theta_{\mathrm{SH}}\lambda_{\mathrm{SOM}}P_{\mathrm{FM}}\frac{1-\frac{1}{\cosh\left(\frac{t_{\mathrm{SOM}}}{\lambda_{\mathrm{SOM}}}\right)}}{\tanh\left(\frac{t_{\mathrm{SOM}}}{\lambda_{\mathrm{SOM}}}\right)+\frac{\rho_{\mathrm{SOM}}\lambda_{\mathrm{SOM}}}{\rho^{*}_{\mathrm{FM}}\lambda_{\mathrm{FM}}}\tanh\left(\frac{t_{\mathrm{FM}}}{\lambda_{\mathrm{FM}}}\right)}\frac{I_{\mathrm{bias}}}{w_{\mathrm{FM}}}. \tag{3.51}$$

The value of I_{ISHE} is small and challenging to measure [158], therefore the signal is detected via the transverse voltage in open-circuit conditions, V_{ISHE} (figure 3.8a). The voltage output is defined by $R_{\mathrm{T}}I_{\mathrm{ISHE}}$ with

$$R_{\mathrm{T}} = \frac{w_{\mathrm{FM}}}{\left(\frac{t_{\mathrm{FM}}}{\rho_{\mathrm{FM}}}+\frac{t_{\mathrm{SOM}}}{\rho_{\mathrm{SOM}}}\right)w_{\mathrm{SOM}}}, \tag{3.52}$$

the resistance of the transverse SOM electrode including electrical shunting with the FM. Hence, the voltage output normalized to the applied current, the ISHE resistance is

$$R_{\mathrm{ISHE}} = \frac{V_{\mathrm{ISHE}}}{I_{\mathrm{bias}}} = \frac{\theta_{\mathrm{SH}}\lambda_{\mathrm{SOM}}P_{\mathrm{FM}}}{\left(\frac{t_{\mathrm{FM}}}{\rho_{\mathrm{FM}}}+\frac{t_{\mathrm{SOM}}}{\rho_{\mathrm{SOM}}}\right)w_{\mathrm{SOM}}}\frac{1-\frac{1}{\cosh\left(\frac{t_{\mathrm{SOM}}}{\lambda_{\mathrm{SOM}}}\right)}}{\tanh\left(\frac{t_{\mathrm{SOM}}}{\lambda_{\mathrm{SOM}}}\right)+\frac{\rho_{\mathrm{SOM}}\lambda_{\mathrm{SOM}}}{\rho^{*}_{\mathrm{FM}}\lambda_{\mathrm{FM}}}\tanh\left(\frac{t_{\mathrm{FM}}}{\lambda_{\mathrm{FM}}}\right)}, \tag{3.53}$$

and $\Delta R_{\mathrm{ISHE}} = (R^{\rightarrow}_{\mathrm{ISHE}} - R^{\leftarrow}_{\mathrm{ISHE}})/2$.

For systems constructed out of materials with spin diffusion length much shorter than the thickness, as is generally the case for both the SOM and FM ($t_{\mathrm{SOM}}/\lambda_{\mathrm{SOM}} \gg 1, t_{\mathrm{FM}}/\lambda_{\mathrm{FM}} \gg 1$), the normalized current and voltage output simplify to

$$\frac{I_{\mathrm{ISHE}}}{I_{\mathrm{bias}}} = \frac{1}{w_{\mathrm{FM}}}\frac{\theta_{\mathrm{SH}}\lambda_{\mathrm{SOM}}P_{\mathrm{FM}}}{1+\left(\frac{\rho_{\mathrm{SOM}}\lambda_{\mathrm{SOM}}}{\rho^{*}_{\mathrm{FM}}\lambda_{\mathrm{FM}}}\right)} \tag{3.54}$$

$$\Delta R_{\mathrm{ISHE}} = \frac{V_{\mathrm{ISHE}}}{I_{\mathrm{bias}}} = \frac{1}{\left(\frac{t_{\mathrm{FM}}}{\rho_{\mathrm{FM}}}+\frac{t_{\mathrm{SOM}}}{\rho_{\mathrm{SOM}}}\right)w_{\mathrm{SOM}}}\frac{\theta_{\mathrm{SH}}\lambda_{\mathrm{SOM}}P_{\mathrm{FM}}}{1+\left(\frac{\rho_{\mathrm{SOM}}\lambda_{\mathrm{SOM}}}{\rho^{*}_{\mathrm{FM}}\lambda_{\mathrm{FM}}}\right)}. \tag{3.55}$$

The ISHE measurement in the local spin Hall device (figure 3.8) can be compared to the one in the non-local spin Hall device (figure 3.6). Both techniques, extract $2\Delta R_{\mathrm{(I)SHE}}$ (figure 3.7 and figure 3.9) and thus the SCI properties. However, $2\Delta R_{\mathrm{(I)SHE}}$ in the local spin Hall device is in general easier to observe because the local spin injection results in higher injected spin current densities in comparison to the non-local device and, hence, produces larger $2\Delta R_{\mathrm{(I)SHE}}$.

3

Chapter 4

Experimental techniques

4.1 Nano-fabrication processes

Devices in this thesis, as presented in section 3.3 and section 3.4, are basically several electrodes of different materials that overlap in certain areas to make a connection. Each electrode structure of a specified material is fabricated by temporary mask that defines the electrodes areas before the deposition of the desired material. The process is repeated for each structure.

All the devices in this work are fabricated on Si substrate with 150 nm of thermally oxidized SiO_2. Figure 4.1 displays the nano-fabrication process of the SOM electrode for the local spin Hall devices consisting of the following consecutive steps:

1. **Spin-coating resist**
2. **Electron beam lithography**
3. **Developing of the resist**
4. **Ar-ion milling for surface cleaning**
5. **Deposition of the material**
6. **Lift-off**

Spin-coating is the application of a thin layer of electron-sensitive polymer resist by spinning the substrate very fast in a controlled fashion, step 1 in figure 4.1. All the devices presented in this thesis are fabricated by using a positive tone electron-sensitive resist. When using positive tone resist, the chemical bonds are broken in electron-beam (e-beam) exposed areas. The solubility of this exposed areas is changed with respect to the unexposed area such that the exposed areas can be more easily dissolved in a specific solvent. In this way, we can make a mold, i.e., our temporary mask. The type of resist depends on the thickness of the to-be deposited materials as well as the deposition method.

A commonly used resist combination is a double layer of positive tone resist called PolyMethylMethAcrylaat (PMMA). In our recipe, both layers, PMMA A4 495 and PMMA A2 950, are spin-coated at 4000 rpm and baked for 90 seconds at 180°C.The samples are baked in order to evaporate residual solvents. The qualification of A4 and A2 give the percentage of molecules dissolved in anisol defining the layer thickness to be $\sim$ 50 nm for PMMA A4 495 and $\sim$150 nm for PMMA A2 950. The

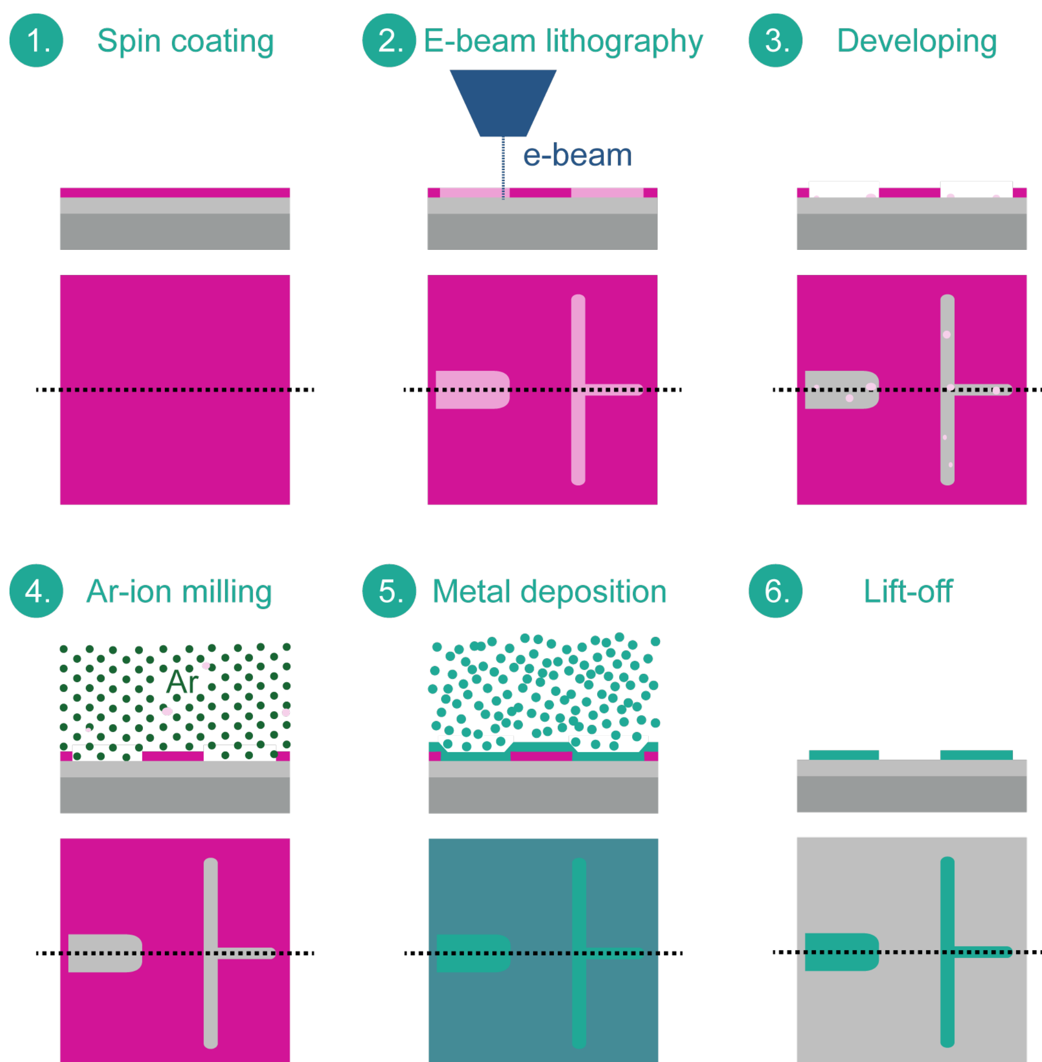

Figure 4.1: Fabrication process for nanostructures The illustration shows a top view and side view (indicated by the black dashed line in the top view) of the sample in the different steps of the fabrication process. The shades of grey represent the Si/SiO_2 substrate. The electron sensitive resist is pink and the e-beam is blue. The Ar atoms are shown as green circles. The metal structures are displayed in turquoise and the metal atoms are turquoise circles.

numbers 495 and 950 stand for the molecular weight in kDa for the respective PPMA's. The lower molecular weight (495 kDa) of the first (lower) layer, makes it that more bonds are broken during e-beam exposure in comparison to the second (upper) layer with the higher molecular weight (950 kDa). The ordering of the layers creates an undercut such that lift-off, removal of residual resist of the mask, can be performed successfully.

The configuration of the sputter system available for this study makes the sputtering not completely unidirectional, such that for very narrow electrodes the resist creates a shadow effect resulting in a thinner electrode thickness compared to the thickness calibrated for a thin film, as shown in figure 4.2. The shadow effect can be suppressed by minimizing the resist thickness but keeping in mind that the resist thickness should be higher than the electrode thickness and still allow proper lift-off. In this work, also single layer PMMA A4 495 is used for materials that are deposited via sputtering (see deposition techniques below), taking advantage of the reduced layer thickness of the resist. Another way to deal with the shadow effect is by calibrating the electrode thickness itself instead of the thin film thickness meaning one can use double layer PMMA and effectively sputtering more material than the calibrated thin film thickness in order to reach the desired electrode thickness.

An other positive tone resist is ZEP, a $(1:1)$ copolymer of α-chloromethacrylate and α-methylstyrene. The spin-coating is preformed at 4000 rpm and the samples are

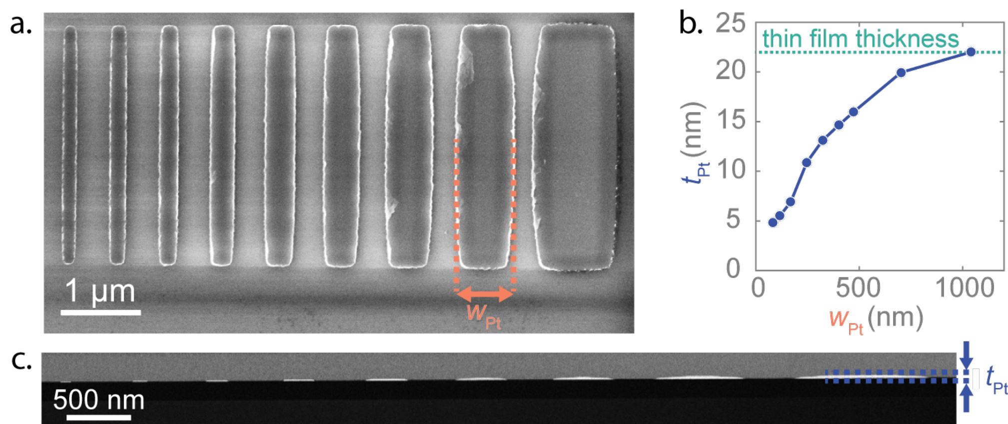

Figure 4.2: The reduced electrode thickness with the electrode width due to a shadowing effect while sputtering. a) A top-view SEM image of nine sputtered Pt electrodes with varying width w_{Pt} between 100 and 1000 nm fabricated with double layer PMMA. **b)** The electrode thickness t_{Pt} is significantly reduced by decreasing the width of the Pt electrodes. This data has been obtained from **c)** a TEM images displaying a side view of all the electrodes. The bottom layer in black is the SiO_x of the substrate. The Pt electrodes show up white. The wider electrodes on the right have a similar thickness as the thin film. The narrow electrodes on the left are much thinner as the wider electrodes on the right demonstrating the reduction in electrode thickness with decreasing electrode width.

baked for 5 minutes at 180°C. The thickness comes out to be about 2 micrometers. This resist is utilized for materials that heat up the sample significantly and harden the resist during deposition. The hardening makes it difficult to remove the resist after deposition. This problem can be avoided by using a thicker resist layer, such as ZEP, as the chances of hardening the full layer of resist is less likely and the lift-off process can be carried out properly.

Electron-beam lithography is the technique of scanning a highly focused e-beam to draw a pattern in e-beam sensitive resist, step 2 in figure 4.1. The resist exposed to the e-beam weaken or harden the polymeric bonds for positive and negative tone resist, respectively. The e-beam is generated by a W-based field emission source and focused by a series of electrostatic and magnetic lenses. The electron-beam lithography (EBL) pattern generators available in *CIC nanoGUNE BRTA* are the *Raith 150*$^{\text{two}}$ and the *e-line*$^{+}$.

Developing of the resist is the immersion of the sample in a solvent to dissolve the areas that are exposed to the e-beam. This will uncover the electrode structures and finalize the temporary mask formed by the remaining resist, step 3 in figure 4.1. The developer for PMMA is a mixture of Methylisobutylketon and Isopropyl alcohol [MIBK:IPA (1:3)] and, for ZEP, the developer is ZED-N50 (n-Amyl acetate). Developing times between 30 and 60 seconds are used.

Ar-ion milling for surface cleaning is a technique whereby the ions of an inert gas, typically Ar, are accelerated from an ion beam source towards a sample in vacuum, step 4 in figure 4.1. The highly energetic ions will etch material from the sample surface. In our devices, ion milling is performed to remove any remaining residuals at the surface and provide homogeneous growth of the to-be deposited material. Additionally, for the subsequent processes in which electrodes are connected to underlying electrodes, the milling ensure a clean interface. Even more, this technique can be used to remove oxide layers from materials that oxidize. We use a *4wave* ion-beam miller. The Ar-ion milling for surface cleaning is performed with a 10 ° angle of incidence and the sample is rotating at 15 rpm. The Ar-ion flow is 15 s.c.c.m., the acceleration voltage is 50 V, the beam current is 50 mA and the beam voltage is 300 V.

Deposition of the material is done by physical vapour deposition (PVD). PVD covers a variety of vacuum deposition methods to grow thin films characterized by a condensed phase material that is sublimated into a gaseous phase and then deposited to a thin film returning to a condensed phase. The three PVD methods utilized for the devices used in this thesis are:

- E-beam evaporation: is used for metals like Ti and also for FM like permalloy (NiFe) and CoFe. A target anode, that is, a crucible with the pellets of the preferred material, is bombarded with an e-beam originating from a charged W-filament and steered inside the crucible by electric and magnetic fields under high vacuum. The e-beam triggers the metal atoms to transform into the gaseous phase once they gained enough energy. These atoms precipitate into solid phase, coating the sample with a thin layer of the metal.The e-beam evaporation have been executed in a high vacuum evaporation system (base pressure of $\sim 10^{-7}$ mbar) by *Kurt J. Lesker Company* and a ultra-high vacuum evaporation system (base pressure of $\sim 10^{-10}$ mbar) by *CreaTec*.

- Thermal evaporation: is used for metals like Au and Cu. In the case of Au, the metal is heated by a high density current that is applied to a thermal boat containing the to-be deposited metal in the form of wire or pellets. Through heat transmission, the metal will be heated until the surface atoms will gain sufficient energy to leave the surface. Subsequently, the atoms will travel the vacuum chamber and deposit on the sample surface. The thermal evaporation of Au has also been performed in the high-vacuum evaporation system of *Kurt J. Lesker Company* mentioned above. Alternatively, for Cu, the metal is accommodated by a crucible with a electric filament wound around that evaporates the metal by radiative heating. The Cu is deposited in an UHV evaporation system by *CreaTec*.

- Magnetron Sputtering: is used for deposition of heavy metals, FM and oxides for capping layers. For sputtering of materials, an Ar plasma is created in a vacuum chamber. The ionized Ar^+ atoms are accelerated towards the target material by a configuration of magnets below the target. The target material is eroded by the accelerated ions as neutral particles either as individual atoms or clusters of atoms. The neutral particles are ejected and will travel towards the sample coating the surface. An UHV Magnetron Sputtering system by *AJA INTERNATIONAL* that contains seven different targets has been used for this thesis.

Lift-off is the removal of the temporary mask, that is the resist and the metal deposited on top of the resist, step 6 in figure 4.1. A harmless method is by dipping the sample in a remover, which for PMMA is acetone and for ZEP is ZD MAC (dimethylacetamide).

Ar-ion milling for removal of sharp edges is a process in which Ar-milling (explained in "Ar-ion milling for surface cleaning") is utilized to remove sharp vertical

edges from electrodes. Such edges can form when during the fabrication process of hard materials, some material, deposited on the walls of the pattern in the resists, does not detach from the electrode during the lift-off process. Ar-ion milling for removal of these edges is done to avoid interpenetration of one material into another, when in subsequent fabrication processes electrodes are connected. Interpenetration of materials could block the function for which the interface was designed. The Ar-ion milling is performed in a *4wave* ion-beam miller with an incidence angle of 80° to irradiate the sample from the side. The sample is rotating at 15 rpm. The beam conditions are the same as for the interface milling, that is, the Ar-ion flow is 15 s.c.c.m., the acceleration voltage 50 V, the beam current 50 mA and the beam voltage of 300 V.

4.2 Characterization methods

The first characterization method presented are electronic measurements. The electronic configuration is of utmost importance for doing precise measurements and extracting meaningful spin properties. Additionally, electron microscopy and x-ray characterization are used for determining deposition rates and quantification of crystallographic phases.

4.2.1 Electronic measurements

All electrical measurements are carried out in the physical property measurement system (PPMS) developed by *Quantum Design*. A PPMS is a low-temperature system with a superconducting magnet for measuring material properties such as electrical and thermal transport properties and magnetic properties. The system consist of a controller and a cryostat. The cryostat is an all-metal construction with vacuum insulation and intermediate temperature radiation shielding in the form of cryogenic liquids as nitrogen and helium (He). The system in our lab is equipped with a He reliquefier such that the He gas originating form the boiling He liquid can be reliquefied and reused. The PPMS allows low temperature measurements down to 1.8 K. A superconducting magnetic coil, immersed in liquid He is located at the bottom of the system providing the possibility to perform magneto-transport measurements within a magnetic field range of ± 9 T.

The sample is placed inside of the cryostat in a vacuum space (i.e., sample space) in between the magnetic system with the use of a stick. In this work, a rotating stick has been used such that also angle dependencies with respect to the magnetic field

can be explored. The sample is attached to a chip carrier or puck that fits into the stick. The puck has eight electrical contacts available for the measurement. The electrical connection between a device on the sample and the puck is established by Al wires using a *West bond* wirebonder. The wirebonder can make bond on pads as small as 100 μm $\times$ 100 μm such that multiple devices can be fabricated on the same substrate.

In addition to the standard electrical setup, a *Keithley 2182A* nanovoltmeter and a *Keithley 6221* current source as well as a switchboard are implemented. The switchboard lets us select the current and voltage probes that will be connected to the electrical measurement setup. For the measurement, the current is applied by the *Keithley 6221* current source and voltage is probed by the *Keithley 2182A* nanovoltmeter, using the four terminal method. A "DC reversal" technique, also known as "delta mode", is employed for the measurements in this thesis. In delta mode, an alternating positive and negative current is injected and the voltage is measured every time the polarity of the current changes.

$$V = \frac{V(+I) - V(-I)}{2}, \tag{4.1}$$

where $V(+I)$ and $V(-I)$ are the voltages for the positive and negative charge current, respectively. This technique keeps the voltage that has a linear response with the applied current, while removing thermoelectric effect and baseline drifts, which reduces the noise [159]. Therefore, it is adequate for low-resistance measurements. The delta mode is equivalent to the 1st harmonic signal of an AC lock-in measurement.

4.2.2 Electron Microscopy

Electron microscopy is a technique to make high-resolution images and visualize details of organic and inorganic samples such as microorganisms, cells, molecules, metals, and crystal structures. This high-resolution imaging is realized by illuminating the samples with a focused beam of accelerated electrons. The highly energetic electrons will interact with the sample. Reflected, deflected and transmitted electrons containing information of the sample can be detected. Two types of electron microscopy techniques used for this thesis will be briefly introduced.

Scanning electron microscopy (SEM) can sense the emission of low-energy secondary electrons and high-energy backscattered electrons probing the topography

and composition of the sample surface. SEM is employed to image our devices with few nanometer resolution in order to inspect the alignment of the nanostructured devices and measure the dimensions (width and length) of the electrodes in the devices. The SEM images presented in this thesis have been made with the EBL systems *Raith 150^{two}* and *Raith e-line^{+}*.

Transmission electron microscopy (TEM) detects electrons that are transmitted through a sample. TEM images show a 2D projection of a sample providing information about the crystal structure and the presence of structural defects and/or impurities. In combination with energy dispersive X-ray analysis (EDAX) the material composition can also be extracted. The disadvantage of this technique is that the samples need to be very thin ($\sim$ 100 nm), flat, and the preparation technique should not introduce any artifacts. In this thesis, we use TEM to inspect the interface between two electrodes (Chapter 7) and it is also used to confirm the reduction of electrode thickness when employing sputtering (figure 4.2). The TEM images were obtained by Prof. A. Chuvilin on a *Titan 60-300* electron microscope (*FEI Co.*) equipped with EDAX detector (*Ametek Inc.*).

4.2.3 X-ray characterization

X-rays, also known as Röntgen radiation after its discoverer Wilhelm Conrad Röntgen, is a form of high energy electromagnetic radiation that is used to investigate the atomic and molecular structure of a crystal. X-ray characterization techniques radiates x-rays on a sample to extract crystallographic information. The X-rays that penetrate into the crystal interact with its periodic atomic structure, reflecting part of the radiation. Figure 4.3 shows the diffraction process on a crystal lattice. Constructive and destructive interference generate a diffraction pattern, containing information about the crystal structure. The angles for coherent scattering, hence constructive interference, of the incoming waves from a crystal lattice is given by Bragg's law:

$$n\lambda_{\mathrm{x-ray}} = 2d\sin{(\Theta)}, \tag{4.2}$$

where n is the diffraction order, $\lambda_{\mathrm{x-ray}}$ is the wavelength of the incident wave, d is the distance between the atomic planes and Θ is the scattering angle respect to the surface plane.

We have used the *X'Pert PRO* by *PANalytical* equipped with a X-ray tube for X-ray generation, a precise goniometer and a detector with *Medipix2* solid state pixel

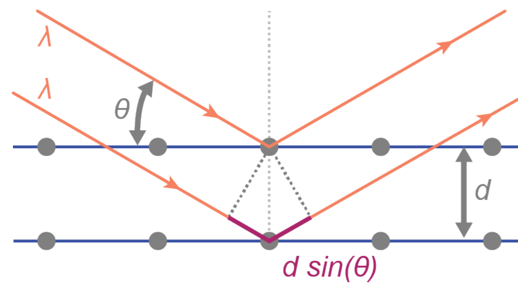

Figure 4.3: Bragg diffraction. Diffraction of two rays with identical wavelength and phase approach a crystalline solid and are scattered by two different atoms in different atomic planes.

detector technology. The anode material used for X-ray generation is made of Cu corresponding to Cu K_α radiation with $\lambda_{K_\alpha} = 0.154$ nm. The sample is placed on the sample stage on top of a silicon piece for reducing background signals. The detection can be done by scanning the angle of the generator and detector in several ways depending on the properties to be probed.

X-ray reflectivity measurements are performed by rotating both the generator and detector by the same grazing angle of incidence Θ such that the specular diffraction is observed. The X-rays reflected from the top and bottom surface of a thin film produce an interference pattern that are observed as Kiessig fringes. The periodicity of these fringes give the thickness of the thin film. This technique is utilized to calibrate the deposition rate of materials.

X-ray crystallography is measuring the angles and intensities of diffracted rays. The diffraction pattern will give peaks at specific angles Θ that can be associated to the distance between atomic planes (equation 4.2) and even more the crystallographic phases in the material. In general, for the X-ray diffraction (XRD) both the injector and detector are rotating for a Θ-2Θ scan. More sensitive method is grazing incidence x-ray diffraction (GIXRD) where the generator is fixed at a grazing incidence angle and the detector is rotating, that allows longer scattering paths inside the film, thus, more information. This technique is used for investigating the crystallographic phases in W (Chapter 7).

4.3 Finite element method simulations

Finite element method (FEM) is a numerical calculation method for solving partial differential equations in 2D or 3D structures. FEM subdivides a large element in smaller, simpler finite elements connected by nodes. The simulation solves the physical problem for each small element and the solution of the large element can be obtained by introducing BCs between the small element. We have used 3D FEM simulation to obtain interface resistances and electrical shunting in our devices.

4.3.1 Interface resistance

Interface resistance refers to electrical contact resistance at the junction of two electrodes in an electric circuit. Besides the charge current flow, the interface resistance also affects the spin current flow through an interface, inducing spin memory loss and changing the spin backflow. The nanostructured devices in chapter 3 consist of several connected electrodes. Consequently, the interface resistance at the junctions in the nanostructured devices have to be considered in order to correctly determine spin properties such as spin diffusion length and SCI efficiency as emphasized as well by refs. [72, 73].

The voltage drop caused by the interface resistance R_i can be measured by a 4-probe measurement configuration shown in figure 4.4 via $R_\mathrm{4p} = V/I_\mathrm{bias}$. When a junction between electrode 1 and electrode 2, with associated resistances R_1 and R_2, possesses a high impedance interface ($R_\mathrm{i} > R_1, R_2$), the measured resistance $R_\mathrm{4p} \sim R_\mathrm{i}$. However, at low impedance interfaces ($R_\mathrm{i} < R_1, R_2$), because of an inhomogeneous current flow and voltage drop, we find $R_\mathrm{4p} < R_\mathrm{i}$. This can even result in the observation of a negative interface resistance [160, 161].

Metal/metal systems, such as the devices in this thesis, are susceptible to low impedance interfaces and we have observed negative R_i in our devices. However, a negative interface resistance is not a real physical quantity, thus, in order to recover the real value of the R_i from the measured R_4p, 3D FEM simulations can be used. In the simulation, the 4-probe measurement is replicated considering the dimensions and the resistivities of the electrodes in the real experiment. Figure 4.4a displays the model, the mesh and the electronic setup in the simulation. Figure 4.4b shows an example of a low impedance interface with an inhomogeneous current density flow across the interface.

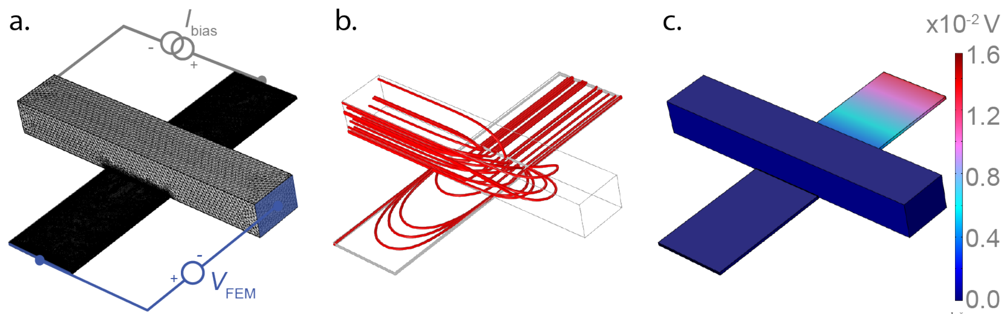

Figure 4.4: FEM simulation for 4-probe interface resistance measurements. a) The geometry, mesh and measurement configuration of the 4-probe measurement. **b)** A low impedance interface resistance results in inhomogeneous current density (red lines). **c)** The electrical potential driven by the applied current.

When simulating a sharp interface, meaning no net interface thickness, R_i can be found by varying the contact impedance ($R_\mathrm{i}A_\mathrm{i}$) while probing the voltage V_FEM. Figure 4.4c display the change in chemical potential in the structure when bias current is applied. The contact impedance for which $V_\mathrm{FEM}/I_\mathrm{bias}$ is equal to the experimentally obtained R_4p relates to the actual R_i. In the case the junction hosts an interface layer with a certain thickness t_i, an additional layer is added to the model, simulating this interface layer. R_i is acquired by varying the resistivity ρ_i $(= R_\mathrm{i}/t_\mathrm{i})$ of this layer and finding ρ_i for which $V_\mathrm{FEM}/I_\mathrm{bias}$ matches R_4p.

The 3D FEM simulations have been used to determine the interface resistances in our nanostructured devices. In chapter 5 and chapter 6, the devices have a small interface resistance resulting in transparent interfaces in which the charge and spin current flow are little to nothing affected by the interface. However, in chapter 7, the interface resistance is found to be significant having a dramatic impact on the measurements of the spin properties.

4.3.2 Electrical shunting

The non-local spin Hall device can be used to measure the SCI in SOM (section 3.3.4), however, the shunting factor x needs to be determined in order to extract the spin Hall angle, see equation 3.37. The verb "to shunt" means to turn away or follow a different path. Electrical shunting is when the electrical current flows through the lowest-resistance path by passing around different components in the circuit. More specifically, in non-local spin Hall devices this means that the horizontal ISHE current (I_ISHE) generating the ISHE voltage V_ISHE is partially shunted

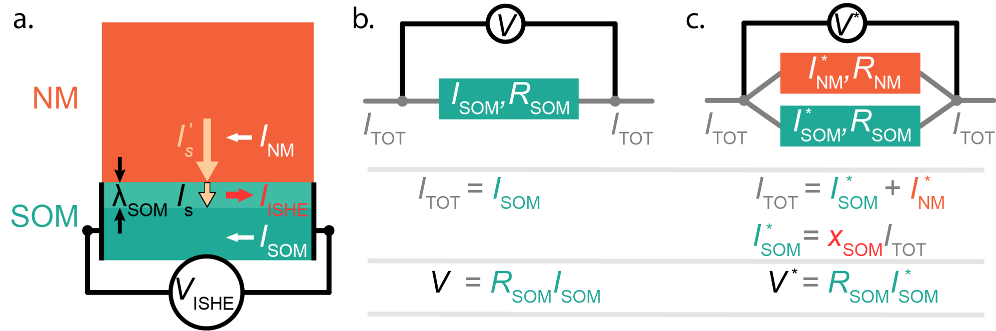

Figure 4.5: The shunting factor for the inverse spin Hall effect measurement. a) An illustration of the ISHE at the NM/SOM interface region of a non-local spin Hall device where the spin injection and spin-to-charge conversion takes place. The current I_{ISHE} is generated in the SOM over a distance defined by the spin diffusion length λ_{SOM}. The V_{ISHE} created by I_{ISHE} is probed in open-circuit conditions resulting in the flow of I_{Cu} and I_{SOM} in the opposite direction as I_{ISHE}. This figure is adapted from ref. [158]. Electric circuit and Kirchhoff's laws for **b)** a single resistor, the SOM electrode and **c)** two parallel resistors, the NM and SOM electrode. The latter is the simple model for the measurement configuration in panel **a**. The voltage drop over the single resistor circuit V and the double resistor circuit V^* are different due to the electric shunting.

by the NM electrode connected to the SOM electrode. Figure 4.5a shows a sketch of spin-to-charge conversion in a non-local spin Hall device (section 3.3.4) where the ISHE voltage is probed at the two ends of the SOM electrode in open-circuit conditions. In this condition the I_{ISHE} flows back into the NM as I_{NM} and the SOM as I_{SOM} [158].

The shunting can be better understood by looking at the current flow in a simple electric circuit. Figure 4.5b displays the electric circuit that can be compared to the situation in which there is no NM electrode but only the SOM electrode. This electric circuit without electrical shunting is described by equation 3.36. Figure 4.5c shows the electric circuit with two parallel resistors in which shunting through the both resistors takes place. This electric circuit can be considered as a simple model to describe the ISHE measurement in figure 4.5a. The current flow and voltage drop in the SOM electrode are not the same for the situation with and without shunting. Ohm's law and Kirchhoff's laws show that $I_{\text{SOM}} = I^*_{\text{SOM}}/x_{\text{SOM}}$ and $V = V^*/x_{\text{SOM}}$, where x_{SOM} is the percentage of the total current flowing through the SOM electrode with R_{SOM}. Finally, the V_{ISHE} that has to be included in equation 3.36 is $V_{\text{ISHE}} = V = V^*/x_{\text{SOM}}$ leading the appearance of x_{SOM} in equation 3.37.

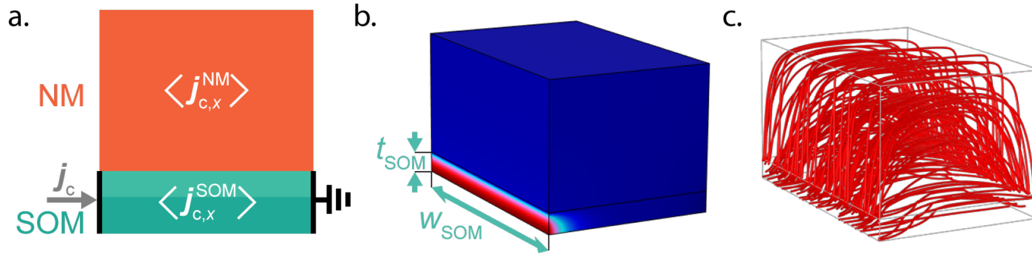

Figure 4.6: The 3D FEM simulation for electric shunting. a) A charge-current density $\mathbf{j}_c$ is applied though the cross-section of the SOM electrode $A_{\text{SOM}} = w_{\text{SOM}} t\text{SOM}$ to simulate the charge current generated by the ISHE. The x-component of the volume average charge current density $\langle j_x^{\text{SOM}} \rangle$ in the NM and SOM is obtained from the simulation and is the used to get the electric shunting factor x_{SOM}. **b)** The electrical potential simulated in the 3D FEM and created by the $\mathbf{j}_c$ through A_{SOM} (more of less the red region). **c)** The charge current density distribution in the non-local spin Hall device from which $\langle j_x^{\text{SOM}} \rangle$ is derived.

The 1D model with the two electrodes as two parallel resistors helps to comprehend the shunting factor but fails to exactly reproduce the electrical shunting in the non-local spin Hall device. In the real device, the two electrode are connected at every point of the interface thus not two independent parallel resistors. 3D FEM simulations can overcome this problem as an electric connection at the overall interface of the SOM and NM electrodes can be included by setting proper BCs. The 3D FEM simulation improve the estimation of x_{SOM} of I_{ISHE} in the non-local spin Hall devices and, therefore, allows determining more precise SCI parameters.

The 3D FEM simulations will contain a geometry as depicted in figure 4.6a. The charge current density $\boldsymbol{j}_c$ is applied to the cross-section of the SOM electrode $A_{\text{SOM}} = w_{\text{SOM}} t_{\text{SOM}}$. Kirchhoff's law for current (figure 4.5) gives that the electric shunting factor in the SOM electrode is

$$x_{\text{SOM}} = I^*_{\text{SOM}} / I_{\text{TOT}}. \tag{4.3}$$

Subsequently, the volume average x-component of the charge current density $\langle j_{c,x}^{\text{SOM}} \rangle$ is calculated within the simulation. The average charge current in the SOM electrode $\langle I_{c,x}^{\text{SOM}} \rangle$ is obtained by $\langle I_{c,x}^{\text{SOM}} \rangle = \langle j_{c,x}^{\text{SOM}} \rangle \times A_{\text{SOM}} = I^*_{\text{SOM}}$. The shunting factor is then determined by equation 4.3 with $I_{\text{TOT}} = |\boldsymbol{j}_c| A_{\text{SOM}}$. In this thesis, 3D FEM simulations performed in *COMSOL Multiphysics* are used to obtain the electric shunting for the non-local spin Hall device in chapter 7.

Chapter 5

Spin–orbit magnetic-state readout in scaled ferromagnetic/heavy metal nanostructures

Chapter 1 discusses how Moore's law has been driving the modern transistors to be scaled down to tens of nanometers, and that such favourable scaling will be essential for the development of alternative computing approaches based on spin logic. It also present that most common approach for sensing magnetic states relying on magnetoresistance are unfavourable in terms of energy with a decreasing device area. Even more, operations depending on magnetoresistance cannot generate a voltage or a current that can directly drive the next stage of the circuit, a requirement for energy-efficient logic devices.

The discovery of SCI phenomena (see chapter 2) is promising for the development of a second generation of spintronic devices that can integrate high-density memory with high-speed operations. Both the ISHE and SHE can be used to detect the magnetization state of a ferromagnetic (FM) element in a nanostructure. The first step towards realization of the MESO-logic (section 1.3), is to show that the SHE and the ISHE can be used to read the magnetic state of a magnetic element employing the local spin Hall device (section 3.4).

Typical examples of metallic nanostructures that use the SHE (ISHE) for spin injection (detection) are lateral spin valves developed to quantify the SCI via non-local techniques (see section 3.3.4). However, this non-local spin Hall device reaches small spin Hall signals of around 0.1–1.0 mΩ due to the diffusive decay of the spin current along the NM channel, spin losses at the two interfaces, and the shunting effect of the NM channel on the SOM electrode. Local spin injection/detection in simpler local spin Hall devices show improved spin Hall signals of around 1–10 mΩ [149, 157]. However, to read the magnetic state of an FM element in potential applications such as MESO logic, larger spin Hall signals of around 1–10 kΩ are required [7, 27].

In this chapter, we report a favourable scaling law for the spin Hall readout of a magnetic state in local FM/HM spin Hall devices and show that large spin Hall signals of 0.3 Ω at room temperature can be obtained. In particular, we use the ISHE for spin-to-charge conversion in CoFe/Pt nanostructures and find that the output voltage (needed to read the in-plane magnetization) and the output current (needed for cascading circuit elements) can be enhanced independently by decreasing the device dimensions. Large spin Hall signals result from the small dimensions and high resistivities of Pt and CoFe, whereas the effective spin-to-charge conversion rate remains constant for the CoFe/Pt system. Furthermore, by extrapolating our data, we suggest that the spin Hall signal could potentially be further increased to the values required to implement MESO logic by using alternative materials.

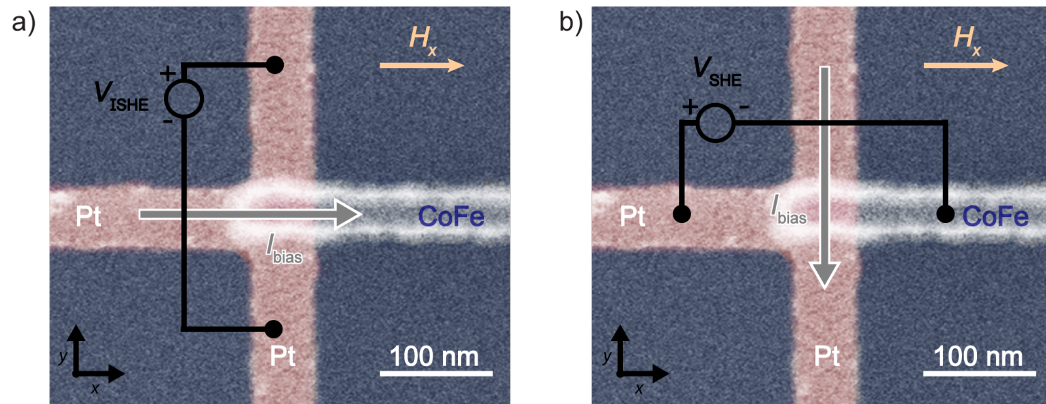

Figure 5.1: Inverse spin Hall effect and spin Hall effect measurement configurations for in-plane magnetic state detection. a) False-colored top-view SEM image of an FM/HM nanostructure with the ISHE measurement configuration. Blue indicates the CoFe electrode and yellow marks the T-shaped Pt nanostructure. The orientation of the external magnetic field H_x. **b)** The SHE measurement configuration in the same CoFe/Pt nanostructure.

5.1 Experimental details

The local spin Hall devices and the working principle of the measurement for the SCI and the magnetic state read-out is described in section 3.4. Figure 5.1 shows SEM images of a CoFe/Pt device, named LD1, used for this study. The measurement configuration for the ISHE and the SHE are also illustrated.

The devices are fabricated on SiO_2/Si substrates by repeating the fabrication process explained in section 4.1 twice. For the majority of the devices, the first step is to pattern the Pt electrode and, in the second step, the CoFe electrode is patterned. But, as we will see, the order of fabrication actually does not matter since devices LD6 and LD7, with the inverse structure (Pt/CoFe), display the same behaviour as the CoFe/Pt devices. The Pt layer is deposited by magnetron sputtering using conditions (1.3 A s^{-1}, 80 W of power, 1.0×10^{-8} mtorr of base pressure, 3 mtorr of Ar pressure) that favour high resistivity [76], whereas CoFe is e-beam evaporated (at 0.4 A s^{-1} and 5.0×10^{-7} mtorr of base pressure). The CoFe electrode is patterned to have a single magnetic domain, with the easy axis of the magnetization along the wire (x-direction). Between the two depositions, an Ar-ion milling process is performed for ~ 30 s to ensure a transparent CoFe/Pt interface.

Electronic transport measurements are performed using a PPMS in combination with a DC current source and a nanovoltmeter as elaborated in section 4.2.1 at temperatures ranging from 10 to 300 K. The applied current I_{bias} for the measurements is 10, 20 or 50 μA, limited by the maximum current density defined by the device dimensions. Note that the variation in I_{bias} does not alter the spin Hall signal. We will use an in-plane magnetic fields to control the magnetization **m** in the FM.

5.2 Spin Hall signal for magnetic state detection

Figure 5.2 shows the main results for device LD1 ($t_{\text{Pt}} = 6$ nm, $t_{\text{CoFe}} = 10$ nm and $w_{\text{Pt}} = 65$ nm). The (I)SHE resistances, $R_{\text{(I)SHE}} = V_{\text{(I)SHE}}/I_{\text{bias}}$ (see 3.4.1), is plotted as a function of the magnetic field at 10 K for the ISHE (figure 5.2a) and the SHE (figure 5.2b) configuration. The magnetic hysteresis loops of R_{ISHE} and R_{SHE} are reciprocal, following the Onsager relations. The two magnetization configurations of the FM electrode are clearly distinguished by the sharp resistance jump at the switching fields, as expected from the mechanism presented in section 3.4. The switching fields are similar to previous reports on 50-nm-wide CoFe wires [157]. The difference in the resistance between the two magnetization orientations is the spin Hall signal $2\Delta R_{\text{(I)SHE}} = 0.41\ \Omega$. This giant signal is reproducible, as shown in another device with similar geometry in section 5.9.1.

Figure 5.3a shows that the hysteresis loops stay well defined up to room temperature. Most importantly, the obtained spin Hall signals (300 mΩ [410 mΩ] at 300 K [10 K]) are three orders of magnitude higher than those measured in non-local measurements using Py/Cu/Pt lateral spin valves (0.15 mΩ [0.3 mΩ] at 300 K [10 K]). [76] The enhancement of the spin Hall signal is expected for the local spin detection technique, because it avoids the spin diffusion as well as the shunting effect in the Cu channel. Although these issues can be solved by replacing Cu with graphene [162], the simpler design of the local spin detection allows the downscaling of the metallic nanostructure to very low dimensions (device LD1 has a 6-nm-thick and 65-nm-wide Pt wire) and reproducibility for large-scale fabrication.

Remarkably, the spin Hall signals are ~ 20 times larger than those measured locally in related CoFe/Pt nanostructures (12 mΩ at 300 K) [157] and two orders of magnitude larger than those observed in a larger CoFeB/MgO/Pt structure (~ 1 mΩ at 300 K)[149]. We confirm that large spin Hall signal in our nanostructure comes from the reduced dimensions and enhanced resistivities (inset figure 5.3c) by measuring the hysteresis loop of R_{ISHE} in a device with larger dimensions (LD2, with

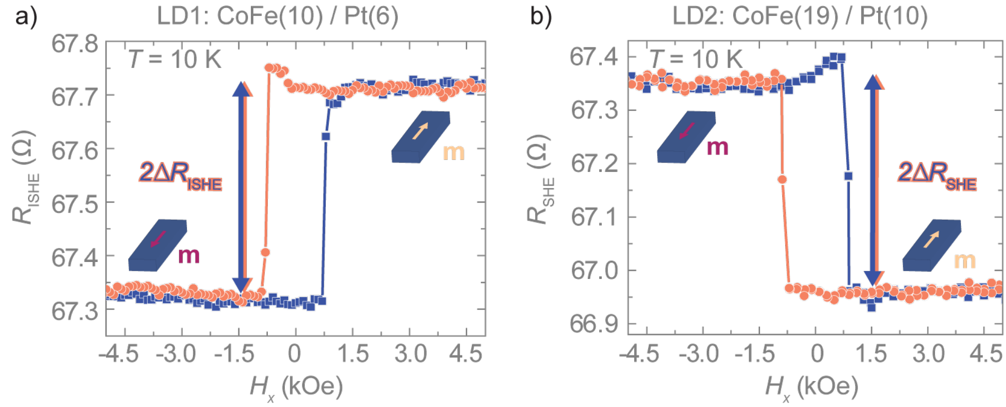

Figure 5.2: Spin Hall effect and inverse spin Hall effect resistance measurement. **a)** The ISHE resistance R_{ISHE} as a function of the magnetic field measured for device LD1 at 10 K. **b)** The SHE resistance R_{SHE} measure at the same conditions. Blue squares correspond to trace of the magnetic field and red circles to retrace. The two magnetization orientations **m** are indicated a black and red arrow.

$t_{\mathrm{Pt}} = 10$ nm, $t_{\mathrm{CoFe}} = 19$ nm and $w_{\mathrm{Pt}} = 160$ nm) and lower resistivities (inset figure 5.3d). Figure 5.3b shows the spin Hall signal to be 14 mΩ at 300 K, as expected, much smaller than that of device LD1.

The 1D spin diffusion model can be used to quantitatively explain the obtained spin Hall signals. The derivation of the spin Hall signal based on the 1D spin diffusion model arising from the local spin Hall device geometry (figure 5.1) is presented in section 3.4. Equation 3.55 describes the behaviour of the spin Hall signal such that for the CoFe/Pt local spin Hall device,

$$\Delta R_{\mathrm{ISHE}} = \frac{1}{\left(\frac{t_{\mathrm{CoFe}}}{\rho_{\mathrm{CoFe}}} + \frac{t_{\mathrm{Pt}}}{\rho_{\mathrm{Pt}}}\right) w_{\mathrm{Pt}}} \frac{\theta_{\mathrm{SH}} \lambda_{\mathrm{Pt}} P_{\mathrm{CoFe}}}{1 + \left(\frac{\rho_{\mathrm{Pt}} \lambda_{\mathrm{Pt}}}{\rho^{*}_{\mathrm{CoFe}} \lambda_{\mathrm{CoFe}}}\right)}, \tag{5.1}$$

which will now be used to explain the temperature dependence and the scalability of the CoFe/Pt devices.

5.3 Temperature dependence of the spin Hall signal

The temperature dependence of the experimental spin Hall signal compared to the calculated one provided by the 1D spin diffusion model validates the use of such a model for our local spin Hall devices. Figure 5.3c displays the spin Hall signal of LD1 for a temperature range from 10 K to 300 K and figure 5.3d show the same for LD2. The calculated spin Hall signal as a function of temperature using the 1D model (equation 5.1) is plotted as a black solid line. The material parameters considered for the calculation are based on the measured resistivities in the specific devices shown in insets of figures 5.3c and 5.3d. In particular, the value of the spin Hall angle of Pt given by $\theta_{\mathrm{SH}} = \sigma_{\mathrm{SH}}^{\mathrm{int}}\rho_{\mathrm{xx}} + \alpha_{\mathrm{SH}}^{\mathrm{skew}}$ (see section 2.2.3) with the intrinsic spin Hall conductivity $\sigma_{\mathrm{SH}}^{\mathrm{int}} = 1600\ [\hbar/e]\ \Omega^{-1}\ \mathrm{cm}^{-1}$ and the skew scattering angle α_{SS} =0.02 [76]. The spin diffusion length of Pt is also determined by its resistivity using $\rho_{\mathrm{Pt}}\lambda_{\mathrm{Pt}}$ =0.77 fΩ m^2 [163], because the spin relaxation in Pt is dominated by the Elliott–Yafet mechanism. [76, 163] Similarly, the spin diffusion length of CoFe is calculated via $\rho_{\mathrm{CoFe}}\lambda_{\mathrm{CoFe}} = 1.29$ fΩ m^2 [164]. Finally, we take P_{CoFe} =0.48 at all temperatures [164]. It is worth noting that the calculated spin Hall signal is not a fit to the experimental data, but a calculation from independent parameters.

The agreement between the calculation and the experimental data, especially good above 150 K, confirms the SHE of Pt as the origin of the signal. The deviation at lower temperatures could be caused by slight mismatches between the used parameters of the literature and the actual parameters. Alternatively, the presence of a strong interfacial spin-to-charge conversion at the FM/Pt interface [165] could be a substantial contribution in the thinnest Pt, an effect that might be more relevant at low temperatures [126].

For a more accurate calculation, we use a 3D finite-element method (FEM) to calculate the spin Hall signal (section 5.9.2), presented as a green dashed line in figure 5.3c and 5.3d. Although the 3D FEM accounts for the current distribution in the nanostructures, whereas the 1D model does not, it is worth noting that the calculated spin Hall signals for device LD1 (figure 5.3c) are almost identical, because the two models are equivalent in this thin and narrow nanostructure. However, the difference between the two models becomes more apparent in the larger nanostructure of device LD2, where the signals from the 3D model are lower than the ones from the 1D model (figure 5.3d).

To rule out possible artefacts that could mimic the spin Hall signals, a careful analysis is performed. The most probable spurious effect is the anomalous Hall effect

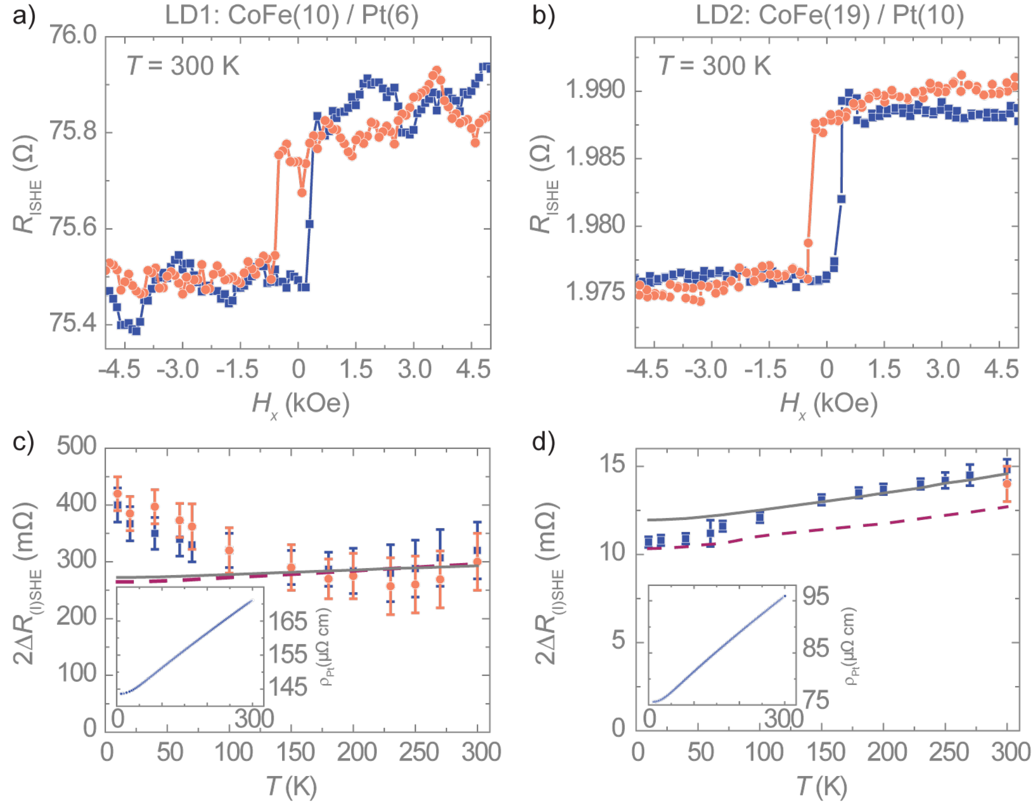

Figure 5.3: Temperature dependence of the spin Hall signals. a) The transverse resistances R_{ISHE} for the ISHE configuration (figure 5.1a) as a function of the magnetic field (trace and retrace) measured for device LD1 at 300 K. **b)** The transverse resistances R_{ISHE} for the ISHE configuration (figure 5.1a) as a function of the magnetic field measured for device LD2 at 300 K. **c)** The direct ($2\Delta R_{\mathrm{SHE}}$, red circles) and inverse ($2\Delta R_{\mathrm{ISHE}}$, blue circles) spin Hall signals as a function of temperature for device LD1. **d)** The same data for LD2. Error bars are calculated using the standard deviation associated with the statistical average of R_{ISHE} in both the positive and negative **m** states. The black solid line is a calculation of $2\Delta R_{\mathrm{(I)SHE}}$ versus temperature based on the 1D spin diffusion model (equation 5.1). The green dashed line is a 3D FEM simulation of $2\Delta R_{\mathrm{(I)SHE}}$ versus temperature based on the spin diffusion model, which also includes the contribution of the AHE in the CoFe. Insets show the measured Pt resistivities for each device.

[84], which could originate in the CoFe and would appear simultaneously with the spin Hall signal and with the same shape. The origin of the appearance of the AHE in the local spin Hall device is discussed in chapter 6. Section 5.9.3 shows the results on the AHE in the samples in LD1 and LD2. We find that the anomalous Hall contribution, which is already included in the calculated signal (green dashed line in figures 5.3c and 5.3d),is less than 5% of the total signal in both devices. Other spurious

signals arising from spin caloritronic effects [166] (section 5.9.4) is carefully considered and shown to be negligible compared to the spin Hall signal. Anisotropic magnetoresistance and ordinary Hall effect due to the stray field of the FM electrode can be neglected as well, as shown in section 6.6.2 and ref. [157]. In chapter 6, we will see that the planar Hall effect (PHE) does not influence the spin Hall signal.

5.4 Geometrical scaling of output current & voltage

In order to understand the geometrical scaling of the current and voltage output signal, a physical explanation of the different terms in equation 3.55 is elucidated and figure 5.4 provides visualisation of this explanation. P_{FM} defines the spin current I_{s} produced in the FM when applying the bias current I_{bias}. The spin resistance mismatch between the FM and the SOM is accounted for by $1/[1+(\rho_{\mathrm{SOM}}\lambda_{\mathrm{SOM}})\,/\,(\rho^{*}_{\mathrm{FM}}\lambda_{\mathrm{FM}})]$ that reduces the final spin current injected into the SOM ($I^{\prime}_{\mathrm{s}}$) by this factor. Therefore, $P_{\mathrm{FM}}/[1+(\rho_{\mathrm{SOM}}\lambda_{\mathrm{SOM}})\,/\,(\rho^{*}_{\mathrm{FM}}\lambda_{\mathrm{FM}})]$ is basically the spin injection efficiency term. Then, $\theta_{\mathrm{SH}}\lambda_{\mathrm{SOM}}$ establishes the amount of spin current converted into charge current I_{ISHE}, hence the SCI efficiency. Both these terms are only dependent on materials parameters and are not influenced by the shape of the nanostructure. As a result, they are gathered in what we will call an materials system "efficiency" factor:

$$\lambda_{\mathrm{eff}}=\theta_{\mathrm{SH}}\lambda_{\mathrm{SOM}}\frac{P_{\mathrm{FM}}}{1+\left(\frac{\rho_{\mathrm{SOM}}\lambda_{\mathrm{SOM}}}{\rho^{*}_{\mathrm{FM}}\lambda_{\mathrm{FM}}}\right)}\quad[\mathrm{m}]. \tag{5.2}$$

The unit of length is adequate for quantifying the SCI as seen before in section 2.3.4.

The remaining factor does dependent on dimensions, more specifically on the thickness of the two electrodes and the width of the SOM, although it does contain the resistivity of the materials involved, we will call it "geometrical" factor:

$$G=\frac{1}{\left(\frac{t_{\mathrm{FM}}}{\rho_{\mathrm{FM}}}+\frac{t_{\mathrm{SOM}}}{\rho_{\mathrm{SOM}}}\right)w_{\mathrm{SOM}}}\quad[\Omega\ \mathrm{m}^{-1}]. \tag{5.3}$$

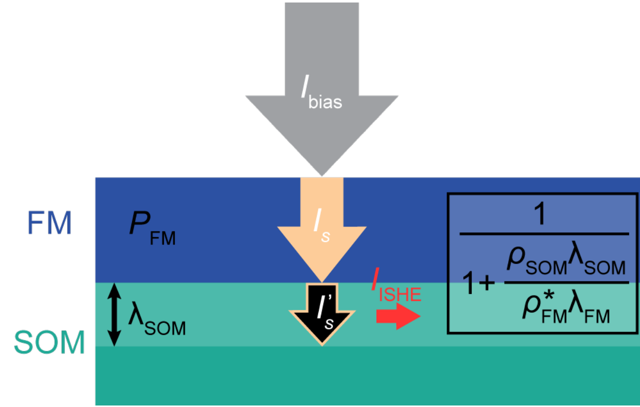

Figure 5.4: Illustration of the "efficiency" factor. The bias current I_{bias} and the polarization P_{FM} create a spin current I_{s} in the FM. The injected spin current $I_{\mathrm{s}}^{'}$ in the SOM will be a fraction of I_{s} defined by the spin resistance mismatch between the FM and SOM, that is, $1/[1+(\rho_{\mathrm{SOM}}\lambda_{\mathrm{SOM}})\,/\,(\rho_{\mathrm{FM}}^{*}\lambda_{\mathrm{FM}})]$. Finally, the ISHE current I_{ISHE} arising from the spin-to-charge conversion is given by $\theta_{\mathrm{SH}}\lambda_{\mathrm{SOM}}$.

This leads to :

$$\frac{I_{\mathrm{ISHE}}}{I_{\mathrm{bias}}} = \frac{1}{w_{\mathrm{FM}}}\lambda_{\mathrm{eff}} \tag{5.4}$$

and

$$R_{\mathrm{ISHE}} = G\lambda_{\mathrm{eff}}, \tag{5.5}$$

that present an easy differentiation of the scalability of the output current and output voltage in the local spin Hall device for its use in the MESO logic. The current and voltage output can be independently optimized by tuning the different lateral dimensions of the electrodes.

5.5 Equivalent circuit of the local spin Hall device

The scaling law presented in equation 5.5 can be understood by considering an equivalent circuit which is adapted from the transmission model for the ISHE introduced by Sayed et al.[167]. Based on this transmission model for materials with spin-momentum locking (including bulk SHE), the equivalent circuit of the ISHE configuration under open circuit condition can be described as a current source (I_{ISHE}) with an internal resistance (R_{T}) see figure 5.5a.

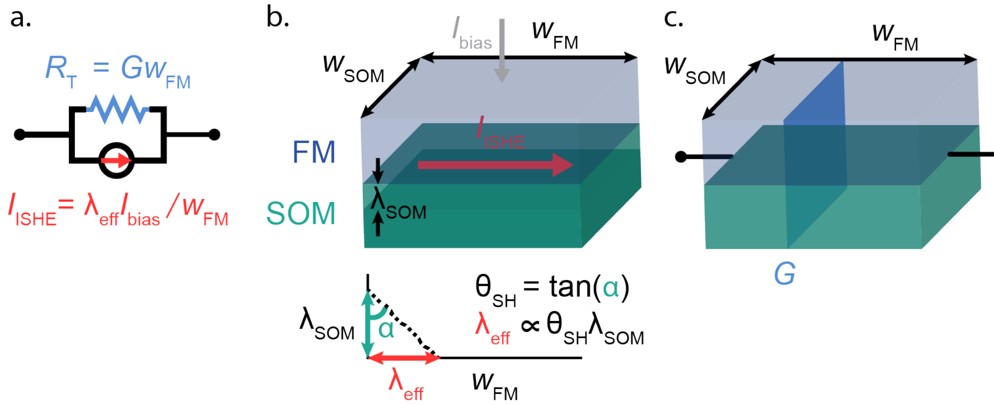

Figure 5.5: Physical explanation of the equivalent circuit a) Equivalent circuit of the ISHE measurement under open circuit condition: the ISHE can be described as a current source with an internal resistance. The measured voltage V_{ISHE} is the product of the two elements ($R_{\mathrm{T}} I_{\mathrm{ISHE}}$). **b)** Upper panel: Sketch of the active part of the device acting as the current source, where the relevant dimensions are tagged. Lower panel: Geometrical interpretation of the effective length, λ_{eff} . **c)** Sketch of the internal resistance, effectively a homogeneous slab with length w_{FM} and a transverse resistance per unit length, G.

The **current source** I_{ISHE} (equation 3.54 and 5.4) is proportional to the "efficiency" factor λ_{eff} and inversely proportional to the FM wire width (w_{FM}). This can be understood from the nature of the ISHE, where the θ_{SH} is a constant value given by the rate of current densities, i.e., $\theta_{\mathrm{SH}} = [\hbar/e]\boldsymbol{j_c}/\boldsymbol{j_s}$. Because of the transverse geometry of the SHE effect, the areas defining the two current densities are different. Whereas $w_{\mathrm{FM}} \times w_{\mathrm{SOM}}$ defines the area of the injected $\boldsymbol{j_s}$, $\lambda_{\mathrm{SOM}} \times w_{\mathrm{SOM}}$ defines the area of the output $\boldsymbol{j_c}$ (see upper sketch in figure 5.5b). The spin-polarized electrons injected into the SOM will deflect a constant angle α [$\tan(\alpha) = \theta_{\mathrm{SH}}$] at each scattering event. As far as the spins are conserved (i.e., over a depth λ_{SOM}), the spins will deflect towards the same side, acquiring a transverse velocity that leads to $\boldsymbol{j_c}$. Therefore, λ_{eff} can be seen as the effective length in the y-direction along which the $\boldsymbol{j_c}$ is generated (see lower sketch in figure 5.5b). Ideally, for a system with a λ_{eff} large enough to match the w_{FM}, the rate of the transverse charge current output I_{ISHE} to the applied charge current I_{bias} could reach one (equation 5.4).

The **internal resistance** is given by the transverse resistance R_{T} of the FM/SOM intersection region (equation 3.52). Here, w_{FM} plays the role of the length of the internal resistance and the "geometrical" factor is R_{T} per unit length (figure 5.5c).

Considering these two elements, the output voltage is simply given by $R_{\mathrm{T}} I_{\mathrm{ISHE}}$ (equation 3.55), which is inversely proportional to w_{SOM} and independent of w_{FM} while the output current is inversely proportional to w_{FM}. The factor G in equation 5.5 would correspond to the transverse resistance per unit length of the internal resistance and λ_{eff} would be the effective length along which the ISHE current is generated.

5.6 Favourable miniaturization for spin Hall signals

The scaling laws extracted from the 1D model are used to investigate the influence of miniaturization of the CoFe/Pt devices on the spin Hall signals. Table 5.1 lists the experimental spin Hall signals measured at room temperature in devices with different geometries. The devices are fabricated on eight different SiO_2/Si substrates (LD1–LD8). The resistivities and all geometrical parameters are obtained from the very same device where the spin Hall signal is measured.

The set of devices with varying w_{Pt} (LD3) and w_{CoFe} (LD4) allows us to confirm the dependence of the spin Hall signal with these two relevant dimensions of the device given by equation 5.1. Figures 5.6a and 5.6b plot the spin Hall signal for the set of devices with varying w_{Pt} and w_{CoFe}, respectively. We observed that the spin Hall signal is independent of w_{CoFe}, whereas it is inversely proportional to w_{Pt}, as predicted by equation 5.1. In this regard, the fitting parameter $a = 3.2 \pm 0.5\ \Omega\mathrm{nm}$ obtained from the plot in figure 5.6b should correspond to $a = \lambda_{\mathrm{eff}}/(t_{\mathrm{CoFe}}/\rho_{\mathrm{CoFe}} + t_{\mathrm{Pt}}/\rho_{\mathrm{Pt}})$ for this set of devices (LD4). Indeed, if we calculate a by taking into account the known parameters of the set of devices (LD4 in table 5.1) and the material parameters (from refs.[157, 163, 164]), a ranges from 3.21 to 3.85 Ωnm (arising from the dispersion of the resistivities in the set of devices).

Next, we will use the 1D model to perform a comprehensive analysis on the data of all the devices. Experimentally, a linear relation between the spin Hall signals and G is shown in figure 5.7a, confirming the prediction of a constant λ_{eff} for the overall set of CoFe/Pt devices. A linear fit of the data to equation 5.5 yields $\lambda_{\mathrm{eff}} = 0.05 \pm 0.01$ nm. This scaling plot confirms that the obtained giant spin Hall signal in device LD1 is given by the large value of G ($2.34\ \Omega\mathrm{nm}^{-1}$), achieved due to its small dimensions and high resistivities. This is thus a guideline that can be followed to obtain even higher spin Hall signals.

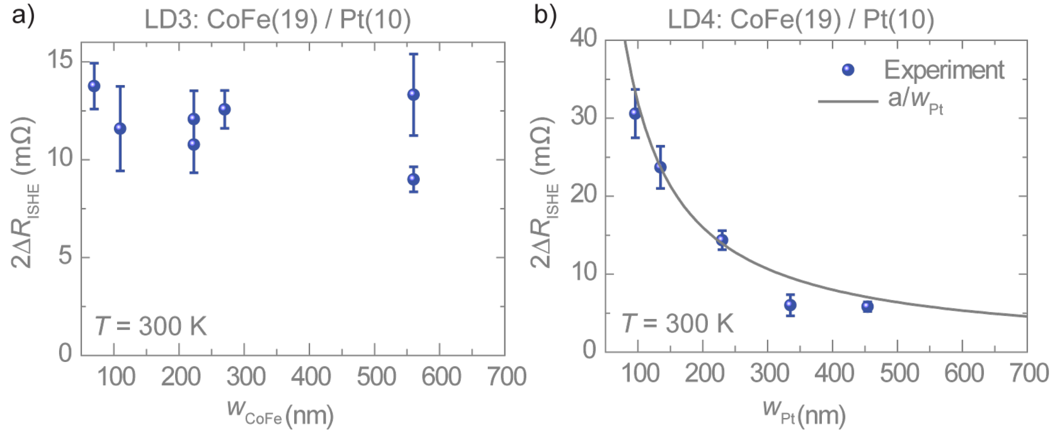

Figure 5.6: Width dependence of the spin Hall signal. a) Spin Hall signal as a function of the width of the CoFe electrode measured at room temperature in the set of devices LD3, where the width of the Pt wire is kept as $w_{\mathrm{Pt}} = 270$ nm. **b)** Spin Hall signal as a function of the width of the Pt wire measured at room temperature in the set of devices LD4, where the width of CoFe wire is kept as $w_{\mathrm{CoFe}} = 240$ nm. The black solid line is a fit of a/w_{Pt} to the experimental data. All devices have thicknesses of $t_{\mathrm{Pt}} = 10$ nm and $t_{\mathrm{CoFe}} = 19$ nm.

It is worth mentioning that the excellent match between the experimental values and the model given by equation 5.5 makes this local spin detection technique a promising alternative to quantify SCI efficiency, with a data analysis much simpler than other widely used local techniques such as harmonic Hall voltage measurements [168], spin-torque ferromagnetic resonance [163, 169] or spin pumping [128].

The spin Hall signal $\Delta R_{\mathrm{(I)SHE}}$ quantifies the rate of the transverse voltage output to the charge current input (I_{bias}). The giant values obtained in our optimized local devices allow us to read the in-plane magnetization state of an FM electrode, an essential ingredient for the MESO logic. However, the performance of the MESO logic also relies on the output current, as it is used to charge/discharge a magnetoelectric capacitor node to enable switching of the next logic gate [7, 27]. In particular, whereas the produced voltage directly determines the capability of switching the next FM element in the circuit with the magnetoelectric effect in the MESO concept [27], the produced current defines the switching energy and delay time. In this regard, the rate of the transverse charge current output I_{ISHE} to I_{bias} should also be maximized to minimize the switching energy. This rate is expressed by equation 5.4. The only difference with $\Delta R_{\mathrm{(I)SHE}}$ is the "geometrical" factor, which is simply given by $1/w_{\mathrm{CoFe}}$ instead of $1/[(t_{\mathrm{CoFe}}/\rho_{\mathrm{CoFe}} + t_{\mathrm{Pt}}/\rho_{\mathrm{Pt}})w_{\mathrm{Pt}}]$.

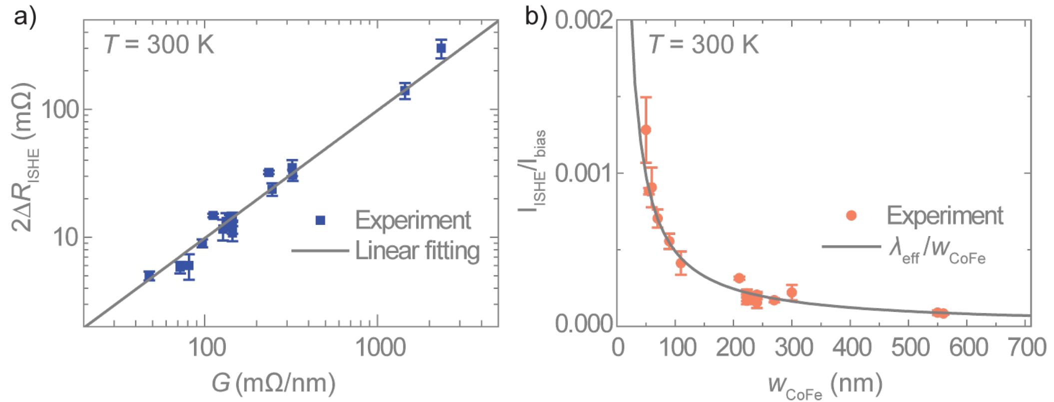

Figure 5.7: Favourable scaling law for the spin-to-charge conversion rates. a) Measured spin Hall signals at room temperature for the different devices shown in table 5.1 plotted as a function of the 'geometrical' factor G (blue solid squares). The black solid line is a linear fit to equation 5.1, with a slope that corresponds to two times of the 'efficiency' factor λ_{eff} (in nm). **b)** The net charge current conversion rate, extracted from the data in panel **a**, as a function of the width of the CoFe electrode (red solid circles). The black solid line is an independent plot of equation 5.4 (not a fit) obtained by fixing λ_{eff} to the value previously extracted from the linear fit in panel **a**. Error bars are calculated using the standard deviation associated with the statistical average of R_{ISHE} in both the positive and negative states of **m**.

Importantly, this shows that, in a specific materials system, the ISHE outputs in current and in voltage can be independently optimized by tuning different dimensions, that is, the ISHE current source and its internal resistance are controlled by different scaling laws (section 5.5). The spin Hall signals for the different devices are converted into $I_{\text{ISHE}}/I_{\text{bias}}$ and plotted as a function of w_{CoFe} in figure 5.7b. A clear enhancement of the charge current conversion rate by downscalling the width of CoFe wire is shown. The largest value $I_{\text{ISHE}}/I_{\text{bias}} = 1.3 \times 10^{-3}$ is achieved in the smallest $w_{\text{CoFe}} = 50$ nm. In the same figure, we can directly plot equation 5.4 with no fitting parameters, by simply using the previously obtained λ_{eff} for our system, which shows a perfect match with the experimental data. It is worth emphasizing that the downscalling of the FM width, in addition to the enhancement of the output current, also favours the reduction of the switching energy in the MESO device [27].

The results in figure 5.7b indicate that the requirements for improving the output charge current for MESO-based logic devices are (1) downscalling the FM nanostructure (w_{CoFe}) and (2) using a FM/NM system with a large λ_{eff}. Considering that the spin polarization of any magnetic material P_{FM} cannot be larger than 1, λ_{eff} can

mainly be enhanced by the SCI efficiency in the NM, that is, the $\theta_{SH}\lambda_{NM}$ product in bulk materials with strong SOC or the inverse Edelstein length λ_{IEE} at Rashba interfaces or in topological insulators. Interestingly, the SCI efficiency can reach several nanometers in systems such as Bi_2Se_3 ($\theta_{SH}\lambda_{NM} \approx 10$ nm)[170], graphene/MoS_2 ($\theta_{SH}\lambda_{NM} \approx 10$ nm) [135], α-Sn ($\lambda_{IEE} \approx 2.1$ nm)[128] or $LaAlO_3$/$SrTiO_3$ (λ_{IEE} up to 6.4 nm, tunable with gate voltage) [118]. Therefore, based on equation 5.4, by reducing the CoFe electrode width to few tens of nanometers and replacing Pt with one of these novel systems with large SCI efficiency, the I_{ISHE}/I_{bias} ratio could potentially approach one.

5.7 The spin Hall signal in a CoFe/Ta device

A CoFe/Ta local spin Hall device can help to validate the guideline we have drafted. Ta is chosen as the SOM because it has a higher spin Hall angle and resistivity than Pt [77]. Even more, a Ta/CoFe device can be used as a control experiment to confirm that the results presented in this work are primarily due to the SHE due to the fact that Ta has a negative spin Hall angle while Pt has a positive one resulting in reversed spin Hall signals.

Figure 5.8a shows a SEM image of the CoFe/Ta device with the measurement configuration for the ISHE. A T-shaped nanostructure made of Ta replaces the one made of Pt in figure 5.2a. The dimensions of the Ta and CoFe are $w_{Ta} = 90$ nm, $t_{Ta} = 10$ nm, $w_{CoFe} = 160$ nm and $t_{CoFe} = 15$ nm. The resistivity of the Ta is $\rho_{Ta} = 1600\ \mu\Omega$cm. In order to minimize the conductivity mismatch and inject the spin current from the CoFe to this high resistive Ta, a thin layer of AlO_x is deposited at the interface. A high value of the product between the interface area (A_i) and the interface resistance (R_i), $R_iA_i = 11.5\ \Omega\mu m^2$, is measured in a cross fabricated in the same device. Note that the implementation of the interface resistance changes the 1D spin diffusion model. For a local spin Hall device with a high R_iA_i, the parameters G^* and λ^*_{eff} are adapted from ref. [149] and defined as:

$$G^* = \rho_{Ta}t_{Ta}/w_{Ta} \tag{5.6}$$

and

$$\lambda^*_{eff} = P_{CoFe}\lambda_{Ta}\theta_{Ta}. \tag{5.7}$$

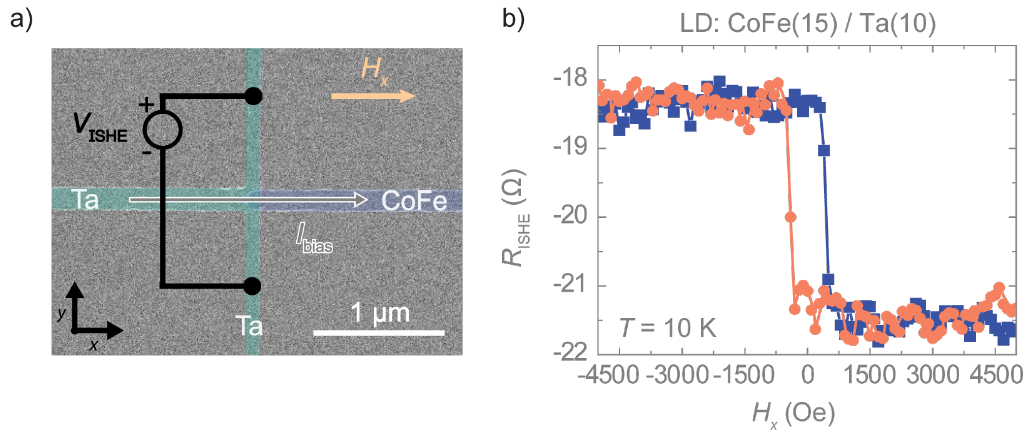

Figure 5.8: The spin Hall signal in a CoFe/Ta device. a) SEM image of a CoFe/Ta device with the measurement configurations for the ISHE. **b)** The transverse resistance R_{ISHE} as a function of the magnetic field (trace in blue and retrace in red) measured in the CoFe/Ta device at 10 K. The reverse sign of the spin Hall signal as compared to the signal of CoFe/Pt devices is observed.

Although they are slightly different from G and λ_{eff} for the transparent case, they have the equivalent role (section 5.4 and 5.5).

The transverse resistance R_{ISHE} as a function of the magnetic field, measured at 10 K, is displayed in figure 5.8b. It shows a spin Hall signal with reversed sign compared to the ones in Pt presented in section 5.2, as expected from the negative spin Hall angle of Ta. The signal, $2\Delta R_{\text{ISHE}} = -3.4 \pm 0.3\ \Omega$, is much higher than the ones reported in the Pt-based devices, mainly because of the high resistivity of the Ta leading to a high geometrical factor, which we calculate to be $G^* = 17.8\ \Omega/\text{nm}$. We can then extract $\lambda_{\text{eff}}^* = 0.10$ nm for the Ta/CoFe system, which is two tines larger than for the Pt/CoFe devices.

This control experiment confirms that all the results presented in this work are primarily due to the spin Hall effect. Furthermore, it shows that higher spin Hall signals can be obtained by adapting the local spin Hall device introduced here to other spin-orbit materials that increase the internal resistance of the ISHE current source (G) and/or the efficiency factor (λ_{eff}), as discussed in section 5.6.

5.8 Conclusions

We have reported favourable scaling of the spin Hall signal with decreasing dimensions of CoFe/Pt nanostructures using ISHE measurements. Our observation of large spin Hall signals of 0.3 Ω at 300 K with a local spin detection scheme could be useful in the implementation of spin–orbit-based reading in MESO logic devices [7, 27]. However, further experiments are required to demonstrate the use of our device as a current source for driving spin logic circuits. We anticipate that spin-momentum locking in topological insulators [128, 170], the Rashba effect at interfaces[118] and graphene/transition metal dichalcogenides van der Waals heterostructures [135, 171–173] could be used to achieve larger spin-to-charge conversion efficiencies with high resistivity. This would further improve the voltage readout of the miniaturized device and its current output (allowing cascading from one device to the next), two ingredients that are essential for logic operations in computational applications (section 1.3 and refs. [7, 27]).

5

Table 5.1: | Summary of devices and device parameters. Resistivities, dimensions and spin Hall signals at 300 K for different devices. The column of the spin Hall signal shows the mean value and the standard deviation associated with the statistical average of $R_{\mathrm{(I)SHE}}$ in both the positive and negative **m** states. The devices are fabricated on different SiO_2/Si substrates (LD1–LD8). *These samples are fabricated with opposite stacking order, that is, with Pt on top of CoFe.

Sample	ρ_{Pt} [$\mu\Omega$ cm]	ρ_{CoFe} [$\mu\Omega$ cm]	t_{Pt} [nm]	t_{CoFe} [nm]	w_{Pt} [nm]	w_{CoFe} [nm]	$2\Delta R_{\mathrm{(I)SHE}}$ [mΩ]
LD1	174.0	320.0	6	10	65	50	300 ± 50
LD2	96.0	42.0	10	19	160	210	14.8 ± 0.5
LD3a	95.7	116.8	10	19	270	70	13.8 ± 1.2
LD3b	47.7	108.9	10	19	270	560	9.0 ± 0.6
LD3c	93.7	110.0	10	19	270	550	13.3 ± 2.0
LD3d	95.9	112.9	10	19	270	270	12.6 ± 1.0
LD3e	97.6	100.2	10	19	270	110	11.6 ± 2.2
LD3f	106.1	116.9	10	19	270	220	12.1 ± 1.4
LD3g	106.1	116.9	10	19	270	220	10.8 ± 1.4
LD4a	71.2	104.9	10	19	95	240	30.6 ± 3.1
LD4b	73.0	116.0	10	19	135	240	23.7 ± 2.7
LD4c	74.9	114.0	10	19	230	240	14.4 ± 1.2
LD4d	70.1	84.6	10	19	335	240	6.0 ± 1.3
LD4e	72.7	113.8	10	19	450	240	5.8 ± 0.6
LD5	56.6	91.3	10	19	110	300	32.0 ± 0.6
LD6*	90.0	830.0	20	14	130	60	35 ± 5
LD7*	30.3	142.6	20	16	250	90	5.0 ± 0.2
LD8	225.0	92.5	8	15	35	55	140 ± 20

5.9 Appendices

5.9.1 Reproducibility of the giant spin Hall signal and signal offset

A giant spin Hall signal with a hysteresis loop following the magnetization state was obtained in another device fabricated on the same substrate as device LD1 presented in section 5.2. Figure 5.9a shows a SEM image of the nanostructure and the measurement configuration for ISHE. The dimensions of the Pt T-shaped nanostructure are identical to the ones in device LD1 ($t_{\mathrm{Pt}} = 6$ nm, $t_{\mathrm{CoFe}} = 10$ nm and $w_{\mathrm{Pt}} = 60$ nm), whereas the CoFe electrode is wider, $w_{\mathrm{CoFe}} = 300$ nm (cf. $w_{\mathrm{CoFe}} = 50$ nm in LD1). Figure 5.9b presents the transverse resistance R_{ISHE} as a function of the magnetic field at 10 K. As expected from equation 5.1, the spin Hall signal in this device is the same as for device LD1 shown in figures 5.2a and 5.2b.

Contrary to magnetoresistance-based effects, the signal offset of the transverse resistance must be zero in a symmetric nanostructure. Indeed, it is very low in this device ($\sim -0.1\ \Omega$). The non-zero offset in device LD1 ($\sim 67\ \Omega$, see figures 5.2a and 5.2b can be explained by the misalignment (~ 20 nm in y-direction) between the two steps of the nanofabrication during the e-beam lithography (see SEM images in figures 5.1a and 5.1b).

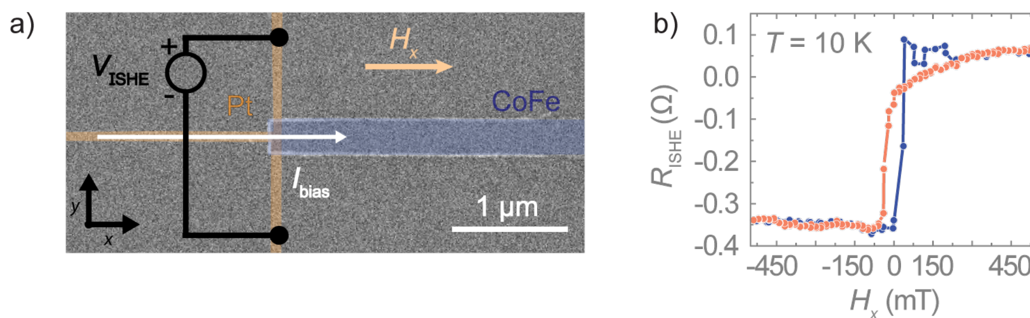

Figure 5.9: Reproducibility of giant spin Hall signal. a) SEM image of the second local spin Hall device on substrate LD1 and the ISHE measurement configuration. **b)** Transverse resistance R_{ISHE} as a function of the magnetic field (trace and retrace) measured at 10 K.

5.9.2 3D numerical spin diffusion model

FEM simulations are also performed within the framework of the two-current drift-diffusion model (section 2.1.2), with the collinear magnetization of the FM electrode along the easy axis. The geometry construction and 3D-mesh were elaborated using the free software GMSH with the associated solver GETDP [174, 175] for calculations, post-processing, and data flow control. The geometry and the mesh of the simulation are shown in figure 5.10. Since the top surface of Pt is cleaned by out-of-plane Ar-ion flow (see section 4.1 for the nanofabrication), only the top FM/NM interface is assumed to be transparent, without spin memory loss, and thus the electrochemical potentials for spin-up and spin-down electrons are continuous through the entire device. The lateral FM/NM interface is assumed to be insulating because the side surface of Pt is not etched. The Neumann boundary conditions are applied. The model is properly designed by taking into account that: i) the nanowires are long enough (i.e., longer than 3 times the spin diffusion lengths in the materials, and much longer than the nanowire widths) such that the spin current vanishes (in the ISHE configuration) at their ends; ii) the mesh size in the vicinity of the interface (where the spin-to-charge current conversion takes place) is set smaller in order to ensure that the SOC-based effects are calculated properly. Further details concerning the FEM model can be found in ref. [157].

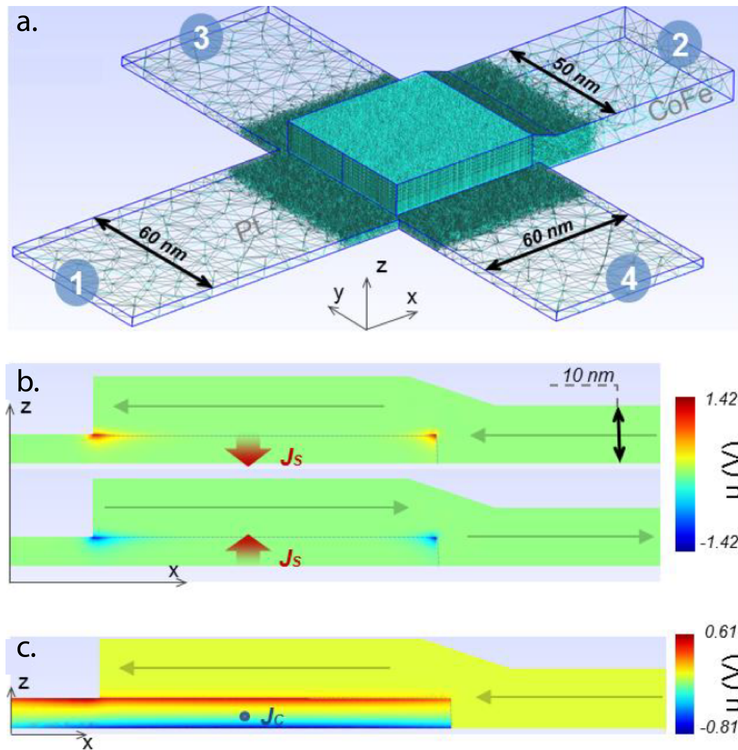

Figure 5.10: **3D FEM simulations for the spin Hall signal. a)** Geometry and mesh of the model used for retrieving the spin Hall signals. The numbers indicate the terminals for the current injection and voltage detection. Panels **b** and **c** present the $x - z$ cross-section contour of the spin accumulation profile (i.e., half the difference between the electrochemical potentials of the majority and minority spins) for the ISHE and SHE configurations, respectively. The spin current is proportional to the gradient of the spin accumulation. **b)** In the ISHE measurement configuration, the charge current flows from terminal 1 to 2 so that a spin-polarized current is injected along the z-direction though the CoFe/Pt interface. The polarization of the injected spin current depends on the magnetization state of the ferromagnetic electrode (along $+x$ or $-x$. In the case of the magnetization oriented along $+x$ (top panel), the spin accumulation is positive so that the z-component of the spin current is along $-z$ which leads to the appearance of a positive ISHE signal. In the case of the magnetization oriented along $-x$ (bottom panel), the spin accumulation is negative so that the z-component of the spin current is along $+z$ which leads to the appearance of a negative ISHE signal. **c)** In the SHE measurement configuration, the charge current flows from terminal 4 to 3, inducing a pure spin current along the z-direction. The resulting spin accumulation at the top surface of the Pt is then probed by the ferromagnetic electrode, leading to a voltage difference between terminal 1 and 2. Since all equations used for the simulations are linear, the injected current has been set to the unit current, i.e., 1 A.

5.9.3 Estimation of the anomalous Hall effect contribution

In the ISHE measurement configuration (figure 5.1a), the applied charge current flows along the z-direction at the intersection region. With the in-plane magnetization of the CoFe electrode being along the x-direction, a voltage signal originating from the AHE of CoFe could appear along the y-direction. Likewise, in the reciprocal SHE measurement (figure 5.1b), a part of the applied current in Pt along the y-direction would flow through the CoFe (with magnetization along x), giving rise to a vertical AHE electric field. This voltage gradient along the z-direction would be probed differently by the Pt terminal and the CoFe terminal, leading to the AHE signal. In both cases, the AHE signal will appear simultaneously with the spin Hall signal and with the same shape of the hysteresis loop. In general, this contribution is very small and can be neglected in most cases due to the geometrical configuration. In this section, we quantify the contribution of the AHE to the measured spin Hall signal for devices LD1 and LD2.

The AHE of CoFe is measured using a Hall configuration at a cross fabricated in the same devices as where the spin Hall signals are measured, as shown in the left panel of figure 5.11a. The transverse resistivity $\rho_{xy} = (V_{xy}/I_{\mathrm{bias}})\, t_{\mathrm{CoFe}}$ as a function of the out-of-plane magnetic field is shown in the right panel of figure 5.11a. The anomalous Hall resistivity ρ_{AH} is calculated from the high field extrapolations to zero field, as indicated in the plot. The anomalous Hall angle, $\theta_{\mathrm{AH}} = \rho_{\mathrm{AH}}/\rho_{\mathrm{CoFe}}$, as a function of temperature for devices LD1 and LD2 is plotted in figure 5.11c, where the resistivity of CoFe has been independently measured for each device (see figure 5.11b). The obtained θ_{AH} is used as an input for the 3D-FEM simulations presented in section 5.9.2. From the 3D simulations, we can extract the contribution of the AHE. The ratio between the AHE signal calculated by the 3D-FEM simulation and the experimental spin Hall signal is plotted in figure 5.11d showing that the contamination is between 2 and 5%. In chapter 6, we extensively study the AHE is the local spin Hall device.

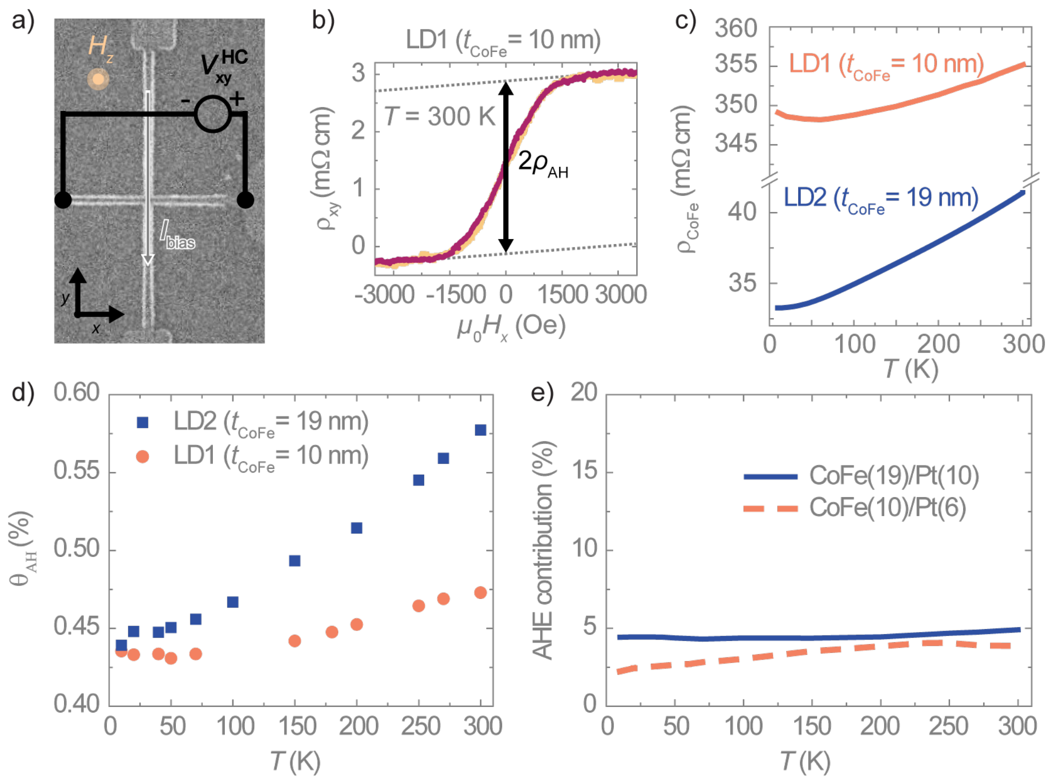

Figure 5.11: The anomalous Hall contribution to the spin Hall signal. a) Setup of the AHE measurement pictured on a CoFe cross of device LD1 and **b)** the corresponding transverse resistivity as a function of the out-of-plane magnetic field measured at room temperature. The black arrow indicates the anomalous Hall resistivity ρ_{AH}. **b)** Resistivity of CoFe in devices LD1 ($t_{\mathrm{CoFe}} = 10$ nm) and LD2 ($t_{\mathrm{CoFe}} = 19$ nm as a function of temperature. **c)** Anomalous Hall angle of devices LD1 and LD2 as a function of temperature obtained from the measurements shown in panels a and b. **d)** AHE contribution to the spin Hall signal as function of temperature for devices LD1 and LD2, which is calculated by the 3D-FEM model (section 5.9.2).

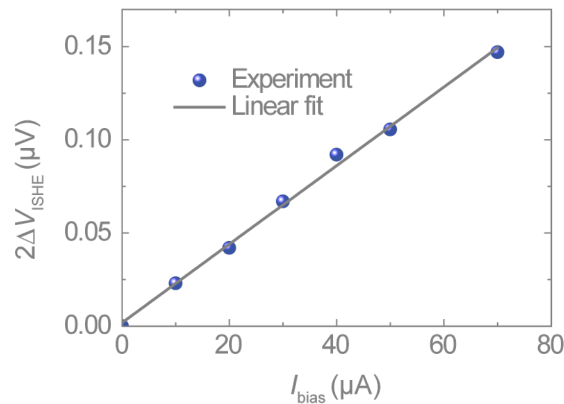

Figure 5.12: Ruling out thermal effects in the spin Hall signal. Spin Hall voltage as a function of the applied current measured at 10 K in device LD7b ($t_{\mathrm{Pt}} = 20$ nm, $t_{\mathrm{CoFe}} = 16$ nm and $w_{\mathrm{CoFe}} = 260$ nm). Red line is a linear fit to the experimental data. The applied current in the experiments shown in this chapter vary from 10 to 50 μA.

5.9.4 Thermal effects

Spin caloritronic effects (longitudinal spin Seebeck effect, planar Nernst effect) refer to the generation of spin voltage as a result of a temperature gradient. In our devices, a temperature gradient is possible due to the applied current through the CoFe/Pt interface and the generated spin voltage could be picked up when we measure with the ISHE configuration. To rule out the possibility of thermal contributions in our spin signals, we checked the dependence of the spin Hall signal with the applied current in device LD7b. The experiments show clearly a linear relationship between the ISHE voltage and the applied current (figure 5.12), whereas the thermal effects caused by a temperature gradient are proportional to the square of the applied current. Therefore, we confirm that no thermal effects contaminate the obtained spin Hall signals.

5

Chapter 6

Disentangling spin, anomalous, and planar Hall effects in ferromagnetic/heavy metal nanostructures

The spin Hall signals in FM/HM local spin Hall devices are easily measurable at room temperature and, furthermore, this device configuration permits independent scalable readout, in terms of voltage and current as shown in chapter 5, which makes it ideal for magnetic state readout in the MESO logic device. However, the local electronic measurement configuration in these devices, exploiting spin-polarized currents instead of pure spin currents, might give rise to spurious transverse voltages. The Hall effects that strongly emulate the (I)SHE are the anomalous Hall effect (AHE) [84] and the planar Hall effect (PHE) [176]. An understanding of different spurious effects in the FM/HM local spin Hall devices, which allows disentanglement of the proper SHE, is relevant for the reliability of magnetic state readout and the realization of the MESO logic device.

In this chapter, we disentangle the Hall effects that could contaminate the spin Hall signal when measuring the ISHE in FM/HM local spin Hall devices due to (1) misalignment of the magnetization and charge current in the planar direction, and (2) vertical lines in the inhomogeneous charge-current-density distribution at the FM side of the injection region. The former induces the PHE in the FM, whereas the latter can lead to the AHE in the FM. We identify that the PHE induces a shift of the baseline of the transverse resistance and distorts its shape, but does not affect the magnitude of the spin Hall signal. In contrast, the AHE appears with the same symmetry as the ISHE and, therefore, disentanglement from the spin Hall signal is not straightforward. However, by combining electrical measurements and a 3D FEM simulation, the AHE contribution to the measured signal can be estimated. Further modeling shows that the AHE contribution can be minimized by tuning the thicknesses of the FM and HM electrode in the device. We find that the AHE accounts for less than 10% of the measured signal for the CoFe(15 nm)/Pt(8 nm) device used in this chapter. Our results show that spurious Hall effects in FM/HM local spin Hall devices can be distinguished and minimized. Therefore, these devices can be used as a simple tool to measure the spin Hall signal and extract the spin-to-charge conversion efficiency of the system, as well as a reliable method for the readout of in-plane magnetic states as elaborated in chapter 5.

6.1 Device structure and fabrication

The local spin Hall device in this study consist of a T-shaped Pt nanostructure and an CoFe electrode, see figure 6.1 for a scanning electron microscopy (SEM) image of the device. The devices are fabricated on SiO_2(150 nm)/Si substrates in two steps, each step involving the fabrication process in section 4.1.

In the first step, Pt is deposited via magnetron sputtering (1.3 A/s, $p_{\mathrm{Ar}} = 3$ mTorr, $P = 80$ W, $p_{\mathrm{Base}} \sim 5 \times 10^{-8}$ mTorr at room temperature). After lift-off, Ar-ion beam milling is performed at grazing incidence to remove side walls on the Pt electrode. Before CoFe deposition, an Ar-ion beam milling is performed at normal incidence to clean the Pt surface and guarantee a highly transparent interface between the Pt and CoFe electrodes. Lastly, CoFe is deposited by magnetron sputtering (0.24 A/s, $p_{\mathrm{Ar}} = 2$ mTorr, $P = 30$ W, $p_{\mathrm{Base}} \sim 5 \times 10^{-8}$ mTorr at room temperature).

The width and thickness of the Pt and CoFe electrodes for the device presented in this work are $w_{\mathrm{CoFe}} = 185$ nm, $t_{\mathrm{CoFe}} = 15$ nm, $w_{\mathrm{Pt}} = 215$ nm, and $t_{\mathrm{Pt}} = 8$ nm. The resistivities are measured to be $\rho_{\mathrm{CoFe}} = 91$ $\mu\Omega$cm and $\rho_{\mathrm{Pt}} = 154$ $\mu\Omega$cm. The electrical transport measurements are performed in a PPMS (see section 4.2.1 for more details), where we apply an in-plane magnetic field at 300 K.

6.2 Spin Hall effect

Figure 6.1 shows a top-view SEM image of the device with the configuration of the ISHE measurement setup.The SHE measurement configuration is presented in figure 6.5a The measurement protocol is explained in section 3.4. Figures 6.2a and 6.2b present the transverse resistance, R_T, as a function of H_x for the ISHE and SHE measurement configurations, respectively. The behaviour of R_T is as expected from the theory (figure 3.9) and similar to the results presented for devices LD1 and LD2 in chapter 5. Figure 6.2a shows the transverse resistance for the ISHE configuration $R_{\mathrm{T}}^{\mathrm{ISHE}}$. If we assume that the overall observed signal purely comes from the ISHE, we extract a spin Hall signal $2\Delta R_{\mathrm{ISHE}}^{\mathrm{exp}} = (24 \pm 2)$ mΩ. Figure 6.2b presents the transverse resistance, R_T^{SHE}, for the SHE measurement configuration, which gives $2\Delta R_{\mathrm{SHE}}^{\mathrm{exp}} = (24 \pm 3)$ mΩ. The spin Hall signals of the ISHE and the SHE are the same, as expected from the Onsager reciprocity [67]. The focus of this study will be mainly on the ISHE, but the results are also valid for the SHE, as shown in section 6.6.1.

The 1D spin diffusion model, i.e., equation 5.5 describes the ISHE in FM/HM local spin Hall devices. We find that, for the CoFe/Pt local spin Hall device under study, $G = (220 \pm 20)$ mΩ nm. By combining G with the experimentally obtained spin Hall signal $2\Delta R_{\mathrm{ISHE}}^{\mathrm{exp}} = (24 \pm 2)$ mΩ, the efficiency of this CoFe/Pt local spin Hall device is estimated to be $\lambda_{\mathrm{eff}} = (0.055 \pm 0.007)$ nm, in good agreement with the efficiency for this system determined by the extensive study on the scalability of local spin Hall devices presented in chapter 5, which gives $\lambda_{\mathrm{eff}} = (0.05 \pm 0.01)$ nm.

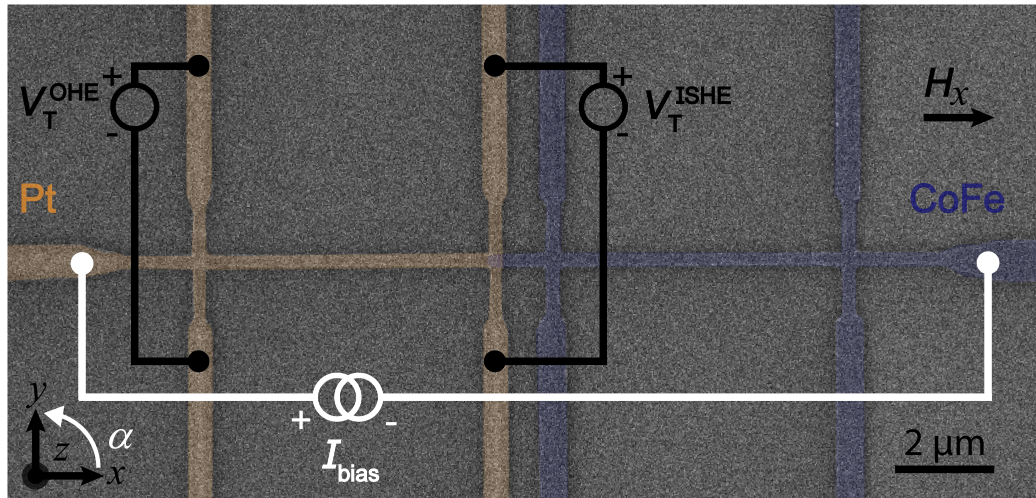

Figure 6.1: Inverse spin Hall, planar and ordinary Hall effect measurement. False-colored top-view SEM image of the FM/HM nanostructure with the ISHE and OHE measurement configurations, and the orientation of the external magnetic field H_x. Blue indicates the CoFe electrode and yellow marks the T-shaped Pt nanostructure.

Even though the efficiency of the CoFe/Pt system in this nanostructure is the same as the expected efficiency presented in chapter 5, it is of paramount importance to rule out possible spurious effects in the spin Hall signal. Since the ISHE resistance is a transverse signal, showing the hysteresis of the FM element, any contamination in the measurement must arise from other Hall effects present in the FM. The Hall effects with the most significant magnitudes are the PHE and the AHE. These originate in the CoFe wire and may appear in the transverse signal due to electrical shunting through Pt. The contribution of these Hall effects will depend mainly on the resistivities and thicknesses of the Pt and CoFe electrodes and the interface resistance. Although the ordinary Hall effect in Pt, in conjunction with out-of-plane fringe fields from the FM electrode tip, is also a potential source for a spurious signal, it is too weak to account for any measured signal as shown in section 6.6.2).

6.3 Planar Hall effect

It is known that ferromagnetic 3d metals and alloys possess a strong anisotropic magnetoresistance effect (AMR) due to s-d scattering processes from itinerant s-state to localized d-states. The AMR is manifested as the difference in the longitudinal resistance as a response to a parallel or perpendicular orientation of **m** with respect to the applied charge current density j_c, giving rise to two distinct

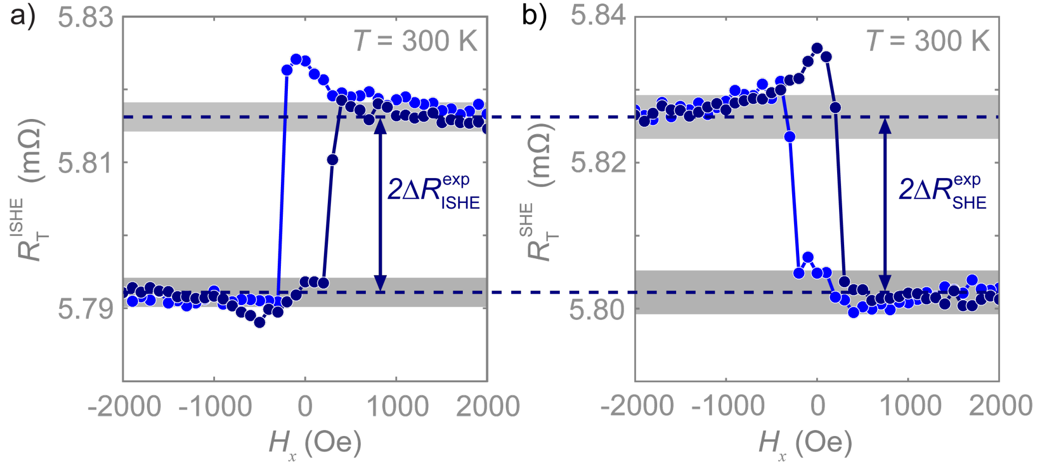

Figure 6.2: The transverse resistance of the inverse spin Hall effect and spin Hall effect. a) and **b)** Evolution of the transverse resistance ($R_\mathrm{T}^\mathrm{ISHE}$ in the ISHE configuration and $R_\mathrm{T}^\mathrm{SHE}$ in the SHE configuration, respectively) as a function of H_x (trace and retrace) measured at $I_\mathrm{bias} = 50\ \mu$A and 300 K. The difference between the low- and high-resistance states (dashed blue lines; the grey shaded area represents the associated error) is the experimentally obtained spin Hall signal $2\Delta R_\mathrm{(I)SHE}^\mathrm{exp}$.

6

resistivities, $\rho_\parallel$ and $\rho_\perp$ [177, 178]. The same phenomenon induces a transverse resistance, known as the PHE. The behavior of the planar Hall resistivity as a function of the angle φ between an in-plane magnetization $\mathbf{m} = (m\cos(\varphi), m\sin(\varphi), 0)$ and $\boldsymbol{j}_c$ is [179, 180]:

$$\rho_{xy}^\mathrm{PHE}(\varphi) = (\rho_\parallel - \rho_\perp)\cos(\varphi)\sin(\varphi) = \frac{(\rho_\parallel - \rho_\perp)}{2}\sin(2\varphi). \tag{6.1}$$

This means that the PHE does not influence the spin Hall signal in our device, except in the presence of a finite in-plane angle between I_bias and $\mathbf{m}$ of the CoFe electrode, as show in figure 6.3a. This could occur due to an angular misalignment in the experimental setup and/or in the nanofabrication.

To disentangle the PHE from the obtained spin Hall signal, the measurement configuration of the ISHE measurement setup (figure 6.2a) is used with an external magnetic field fixed at 5 kOe, while an in-plane rotation α of the device is performed. Since this field is large enough to overcome the shape anisotropy of the CoFe electrode, $\mathbf{m}$ will align with the field direction. In the measurement setup, an ISHE contribution will arise from the spin current polarized along the x-direction, which is proportional to $m\cos(\varphi)$. The contribution of the PHE will be proportional to $\sin(2\varphi)$ (equation 6.1).

Hence, the dependence of the total transverse resistance on the rotation angle α is described by

$$R_{\mathrm{T}}^{\mathrm{ISHE}} = R_{\mathrm{ISHE}} + R_{\mathrm{PHE}} + b = a_{\mathrm{ISHE}} \cos{(\alpha + \alpha_0)} + a_{\mathrm{PHE}} \sin 2(\alpha + \alpha_0) + b \quad (6.2)$$

where a_{ISHE} and a_{PHE} are the amplitudes of the ISHE and the PHE, respectively; α_0 is a misalignment angle; and b is the baseline resistance of the measurement. The ISHE and the PHE can thus be identified from the difference in the angular-dependent behaviour of the transverse resistances R_{ISHE} and R_{PHE}.

Figure 6.3b shows the experimental transverse resistance as a function of α (black solid dots) together with fitting of the data to equation 6.2 (dashed red curve). The obtained fitting parameters are $\mathrm{a}_{\mathrm{ISHE}} = (11.8 \pm 0.7)\ \mathrm{m}\Omega$, $\mathrm{a}_{\mathrm{PHE}} = -(99.3 \pm 0.7)\ \mathrm{m}\Omega$, $\alpha_0 = -(1.0 \pm 0.2)^\circ$ and $b = (5.8001 \pm 0.0005)\ \Omega$. The angle α_0 has a small and realistic value for misalignment between the applied magnetic field and the CoFe nanowire that depends on the placement of the sample in the measurement setup. The contributions of the ISHE and PHE to the fitting are also presented in figure 6.3b as the blue and cyan curves, respectively, showing that the PHE resistance has a much higher amplitude than that of the ISHE resistance. Figure 6.3c displays a magnification of the ISHE contribution from which we identify the PHE resistance, $R_{\mathrm{PHE}}^{0^\circ} = R_{\mathrm{PHE}}^{180^\circ} = (3.5 \pm 0.7)\ \mathrm{m}\Omega$, due to the presence of misalignment, whereas the ISHE resistance is $R_{\mathrm{ISHE}}^{0^\circ} = (11.8 \pm 0.7)\ \mathrm{m}\Omega$ and $R_{\mathrm{ISHE}}^{180^\circ} = -(11.8 \pm 0.7)\ \mathrm{m}\Omega$. The cyan dashed line represents the contribution of the PHE when α is 0° and 180° ($R_{\mathrm{PHE}}^{0^\circ/180^\circ}$). The blue dashed lines depict the difference between $R_{\mathrm{ISHE}}^{0^\circ}$ and $R_{\mathrm{ISHE}}^{180^\circ}$, i.e., the expected spin Hall signal from fitting $2\Delta R_{\mathrm{ISHE}}^{\mathrm{fit}}$, which correspond to $2\Delta R_{\mathrm{ISHE}}^{\mathrm{exp}}$ measured in the magnetic field dependence. Section 6.6.1 presents an analysis of the SHE configuration showing the same behaviour for the PHE resistance.

Figure 6.3d shows the magnetic field dependence of $R_{\mathrm{T}}^{\mathrm{ISHE}}$, the raw data which are plotted in figure 6.2a, after the baseline b, obtained from fitting, is subtracted. The positive and negative externally applied magnetic fields correspond to the angles 0° and 180°, respectively, in the angle dependence (figure 6.3c). The value of $2\Delta R_{\mathrm{ISHE}}^{\mathrm{exp}} = (24 \pm 2)\ \mathrm{m}\Omega$, as determined by the magnetic field dependence, is observed to be the same as that obtained from the angle dependence [$2\Delta R_{\mathrm{ISHE}}^{\mathrm{fit}} = (24 \pm 1)\ \mathrm{m}\Omega$], but shifted because of the PHE by an amount of $R_{\mathrm{PHE}}^{0^\circ/180^\circ}$. Hence, for a negative misalignment angle, at negative and positive saturation fields, the low and high resistive states are given by $(-R_{\mathrm{ISHE}} + R_{\mathrm{PHE}})$ and $(R_{\mathrm{ISHE}} + R_{\mathrm{PHE}})$, respectively. In the case of positive α_0 in this configuration, the PHE resistance would be negative and would shift the transverse resistance down (for more details, see section

6.6.3). We note that, as the PHE has the same contribution ($+R_{\mathrm{PHE}}$) to the negative and positive magnetic fields, $R_{\mathrm{T}}^{\mathrm{ISHE}}$ is shifted, but the extraction of $2\Delta R_{\mathrm{ISHE}}$ is not contaminated by the PHE.

It should be noted that a recent study also discusses the influence of the PHE in the local spin Hall device[181]. They observe that the PHE features can appear in transverse resistance at the zero-field magnetic state similar to what we discuss in section 6.6.3. For materials with large PHE, the shape of the transverse signal can be distorted notably, such that at zero field the two transverse resistance for opposite magnetic states are not easily identifiable. This is disadvantageous for the MESO device while its operation mode is at zero field. The PHE features can be suppressed by proper alignment of the FM electrode and the magnetic domains of the multiferroic material in the magneto-electric node. Another measure that can be taken to reduce these features is the implementation of a FM with small PHE, as discussed in Ref [181].

6.4 Anomalous Hall effect

The AHE is the transverse deflection of charge carriers, leading to a transverse voltage observed in materials with a net magnetization when a charge current is applied [84]. This effect is generally measured in a Hall cross with an out-of-plane magnetic field (H_z). Although, in our measurement configuration, the applied magnetic field in the FM/HM nanostructures is in plane (H_x), the AHE can be present due to an inhomogeneous distribution of the charge current density near the CoFe/Pt interface. Unlike the case of the PHE, the symmetry of the AHE and the SHE is the same, and thus, the two contributions cannot be disentangled through an angular-dependent measurement. Therefore, 3D FEM simulations, within the framework of the two-current drift-diffusion model [36, 182], are performed to retrieve the ISHE and AHE contributions to the total transverse resistance measured in the ISHE configuration ($2\Delta_{\mathrm{ISHE}}^{\mathrm{exp}}$ in figures 6.2a and 6.2c). The geometrical construction and 3D mesh (figure 6.4a) are elaborated using the free software GMSH [175] with the associated solver GETDP [174] for calculations, post-processing, and data-flow control. The top CoFe/Pt interface is assumed to be transparent with no spin-memory loss and the lateral CoFe/Pt interface is considered to be insulating, as the lateral side of Pt is not etched [10,18]. Furthermore, the spin polarization of CoFe and the spin Hall angle of Pt are set to $P_{\mathrm{CoFe}} = 0.48$ [164] and $\theta_{\mathrm{SH}} = 0.27$ [76], respectively. We assume that $\rho_{\mathrm{Pt}}\lambda_{\mathrm{Pt}} = 0.77\ \mathrm{f\Omega m^2}$ [163] and $\rho_{\mathrm{CoFe}}\lambda_{\mathrm{CoFe}} = 1.29\ \mathrm{f\Omega m^2}$ [164], such that, considering the resistivities of our Pt

and CoFe electrodes, the spin diffusion lengths are $\lambda_{\mathrm{Pt}} = 0.5$ nm and $\lambda_{\mathrm{CoFe}} = 1.4$ nm.

Figure 6.4a shows the electric potential in the FM/HM local spin Hall device when applying I_{bias} from port 1 to port 2 of the model. The inset of figure 6.4a shows a side view of our nanostructure with the distribution and orientation of the charge current density in the CoFe/Pt interface region. The charge current density possesses a component in the z-direction inside the CoFe electrode, perpendicular to the in-plane magnetization (x-direction). This can induce a transverse voltage in the y-direction due to the AHE with the same symmetry in the magnetic hysteresis loop as that of the ISHE. The transverse signal is the difference in electric potential between port 3 and port 4, which is normalized by the applied current.

The anomalous Hall angle $\theta_{\mathrm{AH}} = \rho_{\mathrm{AH}}/\rho_{\mathrm{CoFe}}$, which quantifies the strength of the AHE in materials, serves as an input parameter for the 3D FEM and is experimentally obtained using a standard Hall cross (HC) measurement. The inset of figure 6.4b presents a SEM image of a CoFe Hall cross, next to our CoFe/Pt local spin Hall device (see also figure 6.1), with the measurement configuration. A transverse voltage V_{xy}^{HC} appears when applying a bias current I_{bias} along the horizontal electrode and an external out-of-plane magnetic field (H_z). Figure 6.4b plots the transverse resistivity, $\rho_{xy}^{\mathrm{HC}} = (V_{xy}^{\mathrm{HC}}/I_{\mathrm{bias}})t_{\mathrm{CoFe}}$, as a function of H_z. The dashed lines are linear fits to the transverse resistivity under a large magnetic field, corresponding to the ordinary Hall contribution. The difference between the zero-field extrapolations of the two fits is twice the anomalous Hall resistivity, $2\rho_{\mathrm{AH}}$. We find that the anomalous Hall resistivity of CoFe in this nanostructure is $\rho_{\mathrm{AH}} = (0.562 \pm 0.001)\ \mu\Omega$ cm, such that the anomalous Hall angle yields $\theta_{\mathrm{AH}} \approx (0.618 \pm 0.001)\%$.

This experimental θ_{AH} is implemented in the 3D FEM to extract the AHE contribution to the transverse signal. We define $2\Delta R_{\mathrm{AHE}}$ as the difference between the transverse resistance induced by the AHE in the ISHE configuration at positive and negative saturated magnetization. As the magnetic hysteresis loops of the ISHE and the AHE are equal, the transverse resistance is the addition of the two contributions, i.e., $2\Delta R_{\mathrm{ISHE}}^{\mathrm{exp}} = 2\Delta R_{\mathrm{ISHE}} + 2\Delta R_{\mathrm{AHE}}$. Finally, from the 3D FEM, we extract the spin Hall signal and the AHE contribution to be $2\Delta R_{\mathrm{ISHE}} = (18 \pm 2)\ \mathrm{m}\Omega$ and $2\Delta R_{\mathrm{AHE}} = 2.1\ \mathrm{m}\Omega$. According to the 3D FEM, we should thus measure $2\Delta R_{\mathrm{ISHE}}^{\mathrm{exp}} = (20 \pm 2)\ \mathrm{m}\Omega$. The FM/HM interface in our nanostructures might not be as perfectly transparent as assumed in the 3D FEM simulation; this may lead to a small increase of the experimental spin Hall signal, but, indeed, the spin Hall signal obtained from the 3D FEM is, within error, in agreement with the spin Hall signal that is experimentally measured [$2\Delta R_{\mathrm{ISHE}}^{\mathrm{exp}} = (24 \pm 2)\ \mathrm{m}\Omega$].

From the simulations, we find that the AHE contribution to the total spin Hall signal is about 10% for the CoFe/Pt local spin Hall device under study. However, this contamination can be reduced by adjusting the thickness of the CoFe electrode. The magnitude of the z-component of the charge current density in CoFe depends on the thicknesses of the CoFe electrode and the Pt electrode. 3D FEM simulations, as discussed above, are performed for various CoFe thicknesses to extract the dependence of the AHE signal, considering the other parameters in the model system to be unchanged. Figure 6.4c shows that the AHE contribution to the measured signal can be positive or negative, depending on the thickness of the CoFe electrode. This can be understood by considering the modeled charge-current-density distribution, $\boldsymbol{j}_\mathbf{c}$, presented in the inset of figure 6.4a. At the tip of the CoFe electrode [left side of figure 6.4a], $\boldsymbol{j}_\mathbf{c}$ is observed to have components oriented in the $-z$ direction, while, in the area where the CoFe electrode starts to overlap with the Pt electrode (right side), $\boldsymbol{j}_\mathbf{c}$ is oriented in the $+z$ direction. The two orientations of the charge current density induce opposite AHE resistances that compete with one another. The charge-current-density distribution at the interface between the Pt and CoFe electrode depends on the thicknesses of both electrodes, and thus, the two AHE contributions can be compensated for by a suitable device geometry. The contribution of the AHE, according to our simulations, is eliminated when the CoFe thickness is about 13 nm for an 8-nm-thick Pt nanowire (red dashed line). Choosing the thickness of the FM electrode to be about 1.5 times the thickness of the HM electrode ($t_\mathrm{FM} \sim 1.5 t_\mathrm{HM}$) can be taken as a rule of thumb to minimize the AHE when the FM and HM resistivities are of the same order.

The different Hall effects discussed here for CoFe and Pt are present in any metallic FM (PHE and AHE) and HM(OHE); therefore, the method to disentangle these Hall effects shown in this work can be applied to any other metallic FM/HM system with a transparent interface.

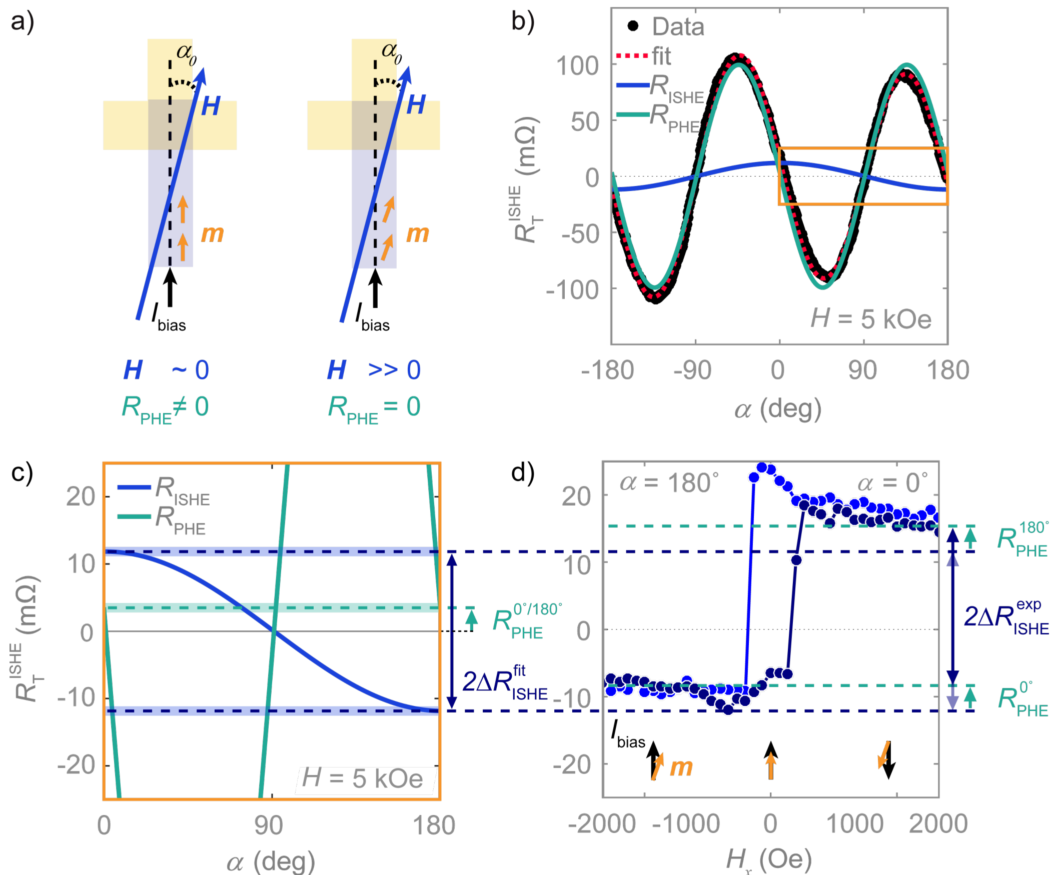

Figure 6.3: Disentanglement of the planar Hall effect from the inverse spin Hall effect. a) A representation of a FM electrode with a magnetization **m** and the influence of a misalignment angle α_0 between the applied current bias $I_{\text{bias}} = 50\ \mu$A and an external in-plane magnetic field **H**. Left panel: At small **H**, **m** aligns with the easy axis, which is parallel to I_{bias}, such that $\varphi = 0$ and the PHE contribution is zero. Right panel: At large **H**, **m** aligns with **H**, such that $\varphi = \alpha_0$ and the PHE contribution is nonzero. **b)** The transverse resistance $R_{\text{T}}^{\text{ISHE}}(\alpha)$ as a function of the in-plane angle α (defined in figure 6.1) at $I_{\text{bias}} = 50\ \mu$A and 300 K with a fixed magnetic field of 5 kOe. The black solid dots are the measured data whereas the red dashed line is a fit to equation 6.2. The fit is separated into an ISHE component and a PHE component shown by the blue and cyan curve, respectively. **c)** A zoom of the ISHE component presented in panel **b** indicated by the orange square. The cyan dashed line presents the magnitude of the PHE signal at $\alpha = 0°$ and $\alpha = 180°$ ($R_{\text{PHE}}^{0°/180°}$). **d)** The transverse resistance $R_{\text{T}}^{\text{ISHE}}$ versus the applied magnetic field H_x as given in figure 6.2a after subtraction of the baseline obtained from the fit ($b = 5.8001\ \Omega$). The high resistance state corresponds to $\alpha = 0°$ whereas the low resistance state corresponds to $\alpha = 180°$. A shift of the transverse resistance by an amount of $R_{\text{PHE}}^{0°/180°}$ (cyan dashed line) is observed at large magnetic fields where **m** and I_{bias} are misaligned. The experimental spin Hall signal $2\Delta R_{\text{ISHE}}^{\text{exp}}$ is the same as the spin Hall signal obtained from the fit on the angle dependence of the transverse resistance $2\Delta R_{\text{ISHE}}^{\text{fit}}$.

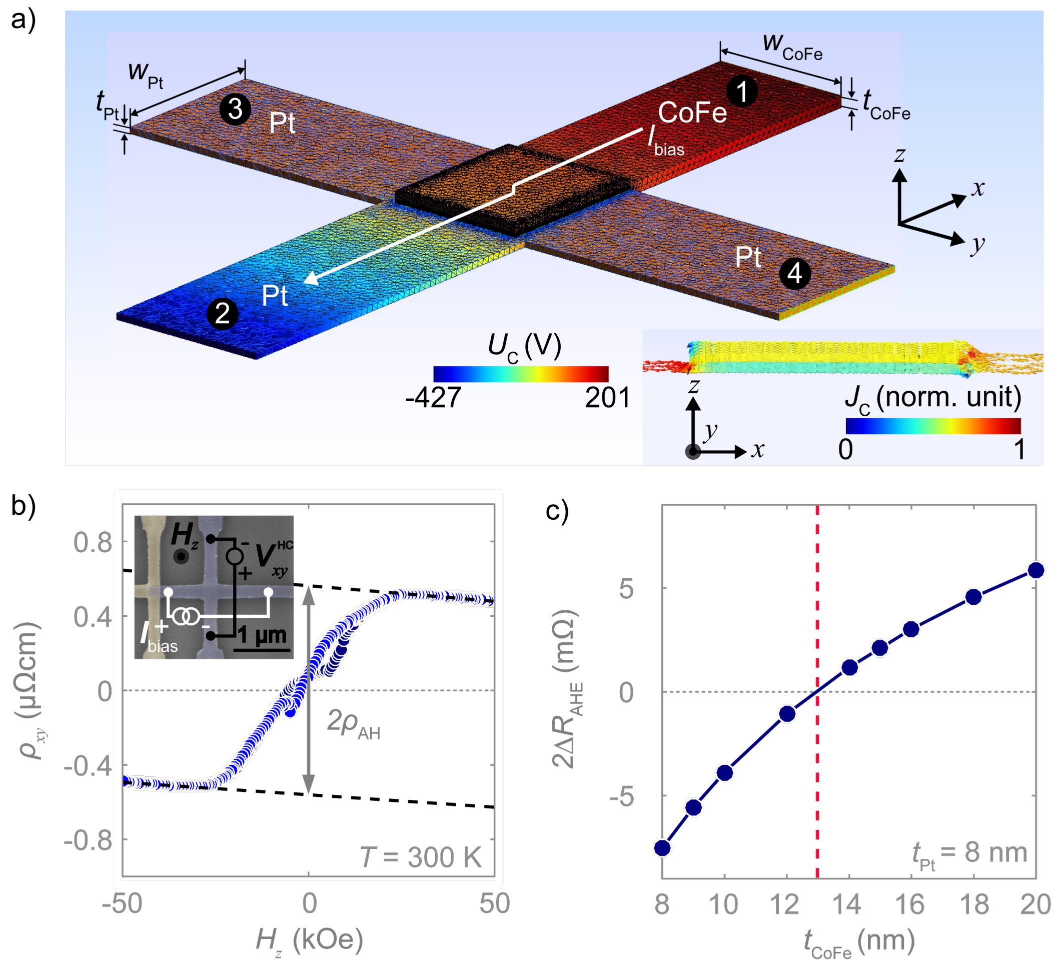

Figure 6.4: The anomalous Hall effect in a local spin Hall device. a) Geometry, mesh and the electric potential map of the 3D FEM model used for the FM/HM local spin Hall device to estimate the AHE in the ISHE configuration. The 3D color map of electrical potential induced by a bias current I_{bias} (white arrow) forced from the CoFe electrode (port 1) to the Pt electrode (port 2). As all the equations used for the simulations are linear, the voltage values correspond to an injected current arbitrarily set at 1 A. Inset: side view of the device (xz plane) picturing the charge current density lines. It shows the existence of a z-component in the charge current density which gives rise to the AHE in the CoFe electrode. **b)** The out-of-plane magnetic field dependence of the transverse resistivity in a CoFe cross-shaped nanostructure. The anomalous Hall resistivity ρ_{AH} extracted from this measurement is used to determine the strength of the AHE. Inset: AHE measurement setup with the CoFe Hall cross depicted in blue. **c)** The CoFe nanowire-thickness dependence of the AHE signal obtained using 3D FEM simulations. The line is a guide to the eye. The AHE can be eliminated by optimizing the thickness of the CoFe nanowire. The optimum CoFe thickness at which the AHE contribution vanished is $\sim$13 nm (red dashed line) in this device with a Pt nanowire thickness of 8 nm and the resistivities as presented in the text.

6.5 Conclusions

We have studied the appearance of spurious Hall effects in the CoFe/Pt local spin Hall devices that are promising for magnetic state readout via (I)SHE measurements. The strongest Hall effects are induced in the FM electrode (PHE and AHE) and transferred into the HM electrode, whereas the OHE in the HM caused by the stray fields of the FM electrode is negligible. The PHE appears with a different symmetry than the ISHE such that an angle misalignment between the magnetic field and the FM electrode can induce a shift in the transverse resistance. This PHE shift can be obtained and corrected for by performing a full angular-dependent measurement of the transverse resistance. The PHE contribution, however, does not affect the reading of the spin Hall signal at saturated magnetic fields. The AHE, though, appears with the same symmetry as the (I)SHE in the measurement. These two contributions can be disentangled by 3D FEM simulations. We observe an AHE contamination of 10% of the transverse resistance in our sample. Further investigation shows that optimizing the thickness of the CoFe electrode with respect to the Pt electrode minimizes of the AHE contribution. As the one-dimensional spin diffusion model accounts for any FM/HM system and the PHE and AHE are valid for all metallic FM, the results can be generalized to any metallic FM/HM T-shaped device. Finally, we emphasize that the FM/HM local spin Hall devices are an appropriate tool to measure the (I)SHE in which parasitic effect can be eliminated by proper alignment and optimized design of the nanostructures and are thus a viable option for future energy-efficient spin-based logic technology.

6.6 Appendices

6.6.1 PHE contamination in the SHE measurement

This chapter discusses how the PHE can be separated from the ISHE measurement in our CoFe/Pt nanostructures by analyzing the in-plane angle dependence of the transverse resistance. The same analysis holds true for the SHE measurement because of the Onsager reciprocity between the ISHE and the SHE [67]. Figure 6.5a presents a false-colored SEM image, showing the Pt and CoFe electrodes as the yellow and blue areas, respectively, and the SHE measurement configuration. Figure 6.5b graphs the in-plane angle dependence of the transverse resistance measured in this configuration $R_{\mathrm{T}}^{\mathrm{SHE}}(\alpha)$. The black solid dots are experimental data, and the dashed red line is the fitting to equation 6.2. The fitting parameters are a$a_{\mathrm{ISHE}} = -(10.3 \pm 0.8)$ mΩ, a$_{\mathrm{PHE}} = -(99.4 \pm 0.8)$ mΩ, $\alpha_0 = -(0.9 \pm 0.2)^{\circ}$ and $b = (5.8121 \pm 0.0005)$ Ω. These are comparable to the fitting parameters obtained from the ISHE measurements in section 6.3. The fit can be decomposed into a SHE and a PHE component due to the difference in the angle dependence, which is $\cos(\varphi)$ (blue line) and $\sin(2\varphi)$ (cyan line), respectively. Figure 6.5c displays a magnification of the area of interest, which is the orange box in figure 6.5b, to compare the angular dependence with the magnetic field dependence (figure 6.5d) of the transverse resistance. We extract the spin Hall signals as $2\Delta R_{\mathrm{SHE}}^{\mathrm{fit}} = (21 \pm 1)$ mΩ and $2\Delta R_{\mathrm{SHE}}^{\mathrm{exp}} = (24 \pm 3)$ mΩ, meaning that they are the same within the error bar. The PHE signal is $R_{\mathrm{PHE}}^{0^{\circ}/180^{\circ}} = (3.1 \pm 0.8)$ mΩ for the SHE measurement setup. Finally, we can conclude that the fitting correctly predicts the spin Hall signal and the PHE induces a shift in the baseline, equivalent to the results shown in section 6.3 for the ISHE.

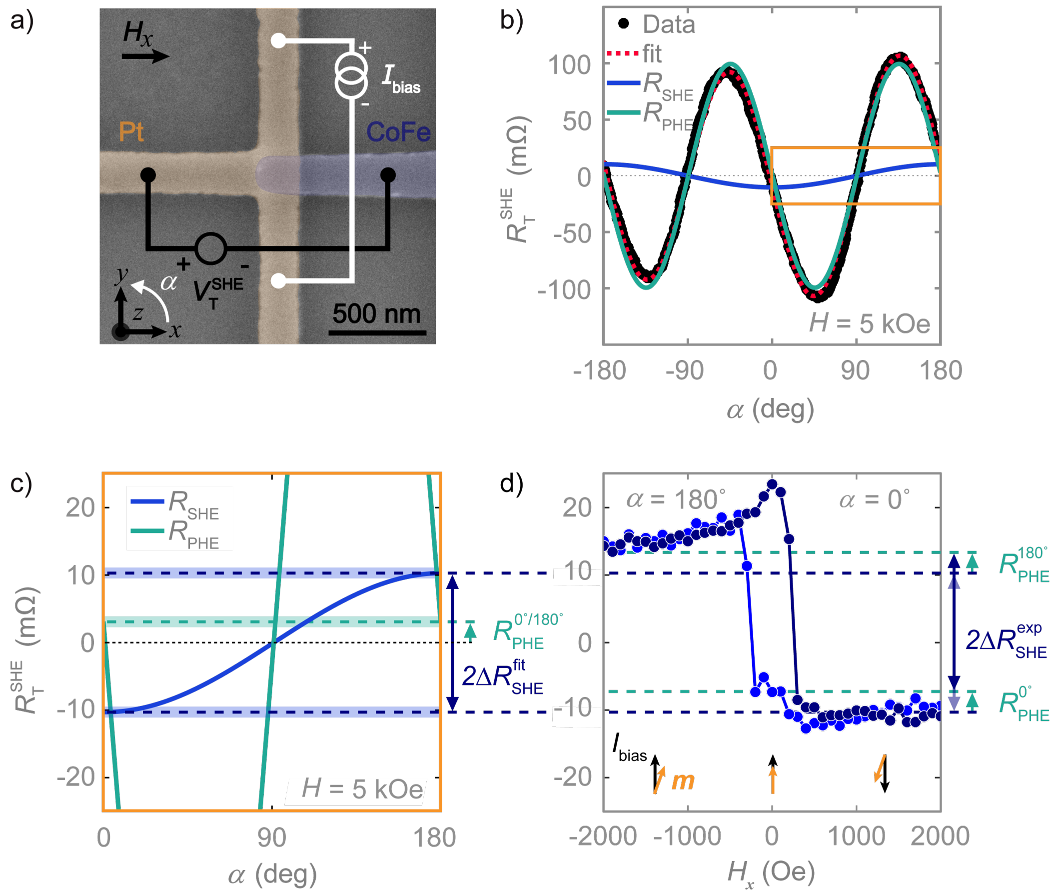

Figure 6.5: Disentanglement of the planar Hall effect from the spin Hall effect. a) False-colored top-view SEM image of the FM/HM local spin Hall device where the FM (CoFe) and HM (Pt) electrodes are indicated by blue and yellow, respectively. The SHE measurement configuration is displayed. The in-plane rotation of the magnetic field is described by the angle α. **b)** The transverse resistance $R_\mathrm{T}^\mathrm{SHE}$ as a function of α at 300 K with $I_\mathrm{bias} = 50\ \mu$A and a fixed magnetic field of 5 kOe. The black solid dots are the measured data, and the red dashed line is a fit to equation 6.2. The fit is separated into an SHE component and a PHE component shown by the blue and cyan curve, respectively. **c)** A zoom of ISHE component presented in panel **b** indicated by the orange square. The cyan dashed line presents the magnitude of the PHE signal at $\alpha = 0°$ and $\alpha = 180°$ ($R_\mathrm{PHE}^{0°/180°}$). **d)** The transverse resistance $R_\mathrm{T}^\mathrm{SHE}$ versus the applied magnetic field in the x-direction as given in figure 6.2b after subtraction of the baseline obtained from the fit ($b = 5.8121\ \Omega$). The low resistance state corresponds to $\alpha = 0°$ whereas the high resistance state corresponds to $\alpha = 180°$. A shift of the transverse resistance by an amount $R_\mathrm{PHE}^{0°/180°}$ (cyan dashed line) is observed at large magnetic fields where **m** and I_bias are misaligned. The experimental spin Hall signal $2\Delta R_\mathrm{ISHE}^\mathrm{exp}$ is the same as the spin Hall signal obtained from the fit on the angle dependence to the transverse resistance $2\Delta R_\mathrm{ISHE}^\mathrm{fit}$.

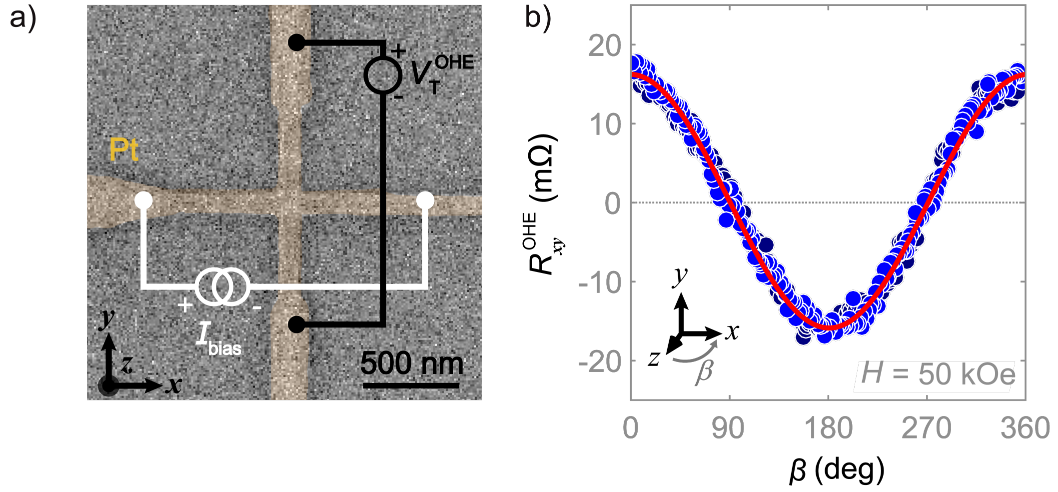

Figure 6.6: The ordinary Hall effect in a Hall cross of Pt. a) The ordinary Hall measurement configuration at the Pt Hall cross fabricated next to the local spin injection device. **b)** The angular dependence of the Hall resistance R_{xy}^{OHE} as a function of the angle β with a fixed magnetic field of 50 kOe. A fit to a $\cos(\beta)$ function is show as a red line.

6.6.2 Ordinary Hall effect in the CoFe/Pt local spin Hall device

The OHE in Pt is yet another Hall effect that could compete with the ISHE in the CoFe/Pt local spin Hall device. Magnetization at the tip of the CoFe electrode can induce a magnetic stray field with a z-component penetrating the Pt electrode. This magnetic field, together with the current along the x-axis, can yield an OHE signal along the y axis, the same one along which the ISHE is measured. The ordinary Hall resistance, which can contaminate the spin Hall signal, is $R_{xy}^{\text{OHE}} = R_{\text{H}}B_z/t_{\text{Pt}}$, with R_{H}, B_z, and t_{Pt} being the material-dependent Hall coefficient, the z-component of the magnetic field in the Pt wire, and the thickness of the Pt electrode, respectively. We combine electronic Hall measurements (to obtain R_{H}) with micromagnetic simulation (to extract the mean stray field component $\langle B_{\text{stray},z}\rangle$ created by the CoFe electrode) to show that the signal induced by the OHE is negligible in comparison with the ISHE.

To quantify R_{H} in our Pt wire, an angular-dependent Hall measurement with a fixed magnetic field (**H**) of 50 kOe is performed in a Hall cross of Pt that is deposited at the same time as the CoFe/Pt local spin Hall device, as shown in figures 6.6a and 6.1. Figure 6.6b presents the resulting Hall resistance as a function of the out-of-plane rotation in the xz plane (described by angle β). We assume that the OHE in our Pt is linear in the out-of-plane magnetic field, as confirmed by the excel-

lent fit (red line) of the measurement to $R_{xy}^{\text{OHE}}(\beta) = R_{xy}^{\text{OHE}} \cos(\beta + \beta_0) + b$ with $R_{xy}^{\text{OHE}} = (15.85 \pm 0.05)$ mΩ, $\beta_0 = -(0.5 \pm 0.2)^\circ$, and $b = -(0.43 \pm 0.03)$ mΩ. The Hall coefficient is $R_{\text{H}} = R_{xy}^{\text{OHE}} t_{\text{Pt}}/B_z = (2.5 \pm 0.8) \times 10^{-11} \text{m}^3/\text{C}$, as $t_{\text{Pt}} = 8$ nm and $B_z = 5$ T defined by a fixed value of the external magnetic field of $\mu_0 H$ (μ_0 is the vacuum permeability).

6

The magnitude of the stray fields originating from the CoFe electrode into the Pt electrode are determined using MUMAX3, which is an open-source software for micromagnetic simulations on graphics processing units (GPU) [183]. Figure 6.7b shows the CoFe/Pt structure used for these simulations, considering $t_{\text{Pt}} = 9$ nm, $t_{\text{CoFe}} = 15$ nm, $w_{\text{Pt}} = 215$ nm, and $w_{\text{CoFe}} = 185$ nm, which are comparable to the dimensions in the CoFe/Pt local spin Hall device studied in section 6.2. The wires are divided into a regular mesh of cuboid cells with dimensions of $(3.125 \times 3.125 \times 3\ \text{nm}^3)$. For this reason, the thickness of the Pt electrode in the simulation is chosen to be 1 nm thicker than the real electrode thickness. This, however, will not influence the result significantly, since the strongest stray field will be induced in the area closest to the FM electrode. A saturation magnetization of $M_{\text{sat}} = 1$ MA/m (the value for non-annealed CoFe) [184] and an exchange constant of $A_{\text{ex}} = 18$ pJ/m (the value for very thin Co) [185] are used for the simulations. We consider that there is no anisotropy, since our CoFe is polycrystalline.

First, we simulate the three components (x, y, and z) of magnetization in the CoFe electrode and its response to an external magnetic field sweep along the x-axis to imitate the ISHE measurement. Figure 6.7a shows the average magnetization in the area where the CoFe wire overlaps with the Pt electrode versus the magnitude of the external magnetic field, showing a coercive field of $H_{\text{c}} \sim 950$ Oe. The average magnetization in the x-direction is strongest, as expected. However, around H_{c}, a component in the z-direction appears, while the y-component stays rather constant over the full range of external magnetic fields. Figure 6.7b presents a top view of the simulated structure, including snapshots of magnetization at two different magnetic fields around H_{c}, which are displayed as blue dots in figure 6.7a.

Next, we simulate the stray field in the Pt electrode induced as a consequence of magnetization in the CoFe wire. Figure 6.7c shows that the CoFe magnetization induces an average stray field in the Pt electrode with strong components in the x-direction and z-direction. The z-component is the one we are interested in, as it will induce a transverse resistance due to the OHE in Pt, which adds to the spin Hall signal. We find that the average stray field in the z-direction reaches a maximum of $\langle B_{\text{stray},z} \rangle \sim 70$ mT close to the coercive field $H_{\text{c}} \sim 950$ Oe. For higher applied fields, $\langle B_{\text{stray},z} \rangle$ saturates to a value of about 25 mT. Figure 6.7d presents a top view

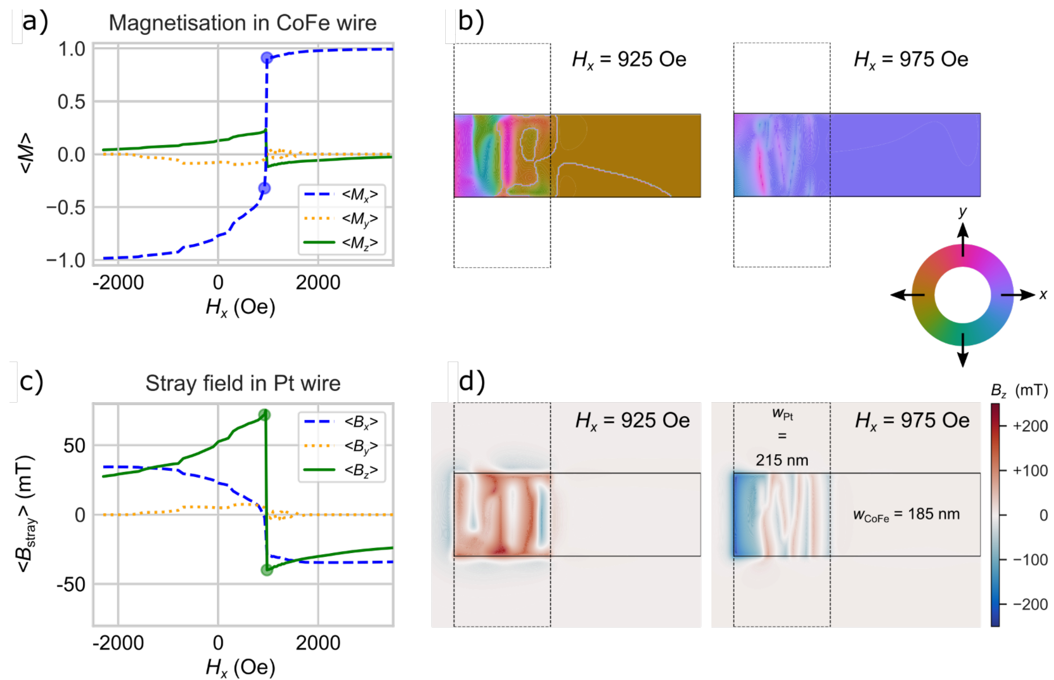

Figure 6.7: Micromagnetic simulations of the stray fields originating from a CoFe nanowire. a) The simulated mean magnetization components of CoFe in the area where the CoFe wire overlaps with the Pt wire as a function of a field H_x applied along the CoFe wire long axis. **b)** Snapshots of the in-plane magnetization (see color-wheel) at a height of $z = 9$ nm, which corresponds to the vertical middle of the CoFe electrode ($t_{\mathrm{CoFe}} = 15$nm, with the 3 nm cell height), at specific fields during the switching of the magnetization. The location of the snapshots in magnetic field are indicated by the blue dots in panel **a**. **c)** Mean stray-field components generated in the Pt wire overlapping with the CoFe wire as a function of H_x. The maximum value of $\langle B_{\mathrm{stray},z} \rangle$ reaches ~ 75 mT and saturates to about 25 mT at high saturation fields. **d)** Snapshots of the z-component of the stray field in the Pt wire at $z = 21$ nm (i.e., 6 nm above the CoFe wire) evaluated at the same fields as the CoFe magnetization in panel **b**. The green dots in panel **c** indicate the magnetic field position of the snapshot.

of the CoFe/Pt local spin Hall device with the z-component of the stray field at the intersection area of both wires.

The Hall resistance, which will appear in the ISHE measurement, i.e., that will contaminate the spin Hall signal, can be estimated by combining the Hall coefficient ($R_{\mathrm{H}} = 2.5 \times 10^{-11}\mathrm{m}^3$/C), the Pt wire thickness t_{Pt}, and the z-component of the magnetic stray field within the Pt wire. The maximum contribution of the OHE will be around the switching field, where $\langle B_{\mathrm{stray},z} \rangle \sim 70$ mT results in an OHE resistance of $0.2\ \mathrm{m}\Omega$, which is insignificant. Contamination of the transverse re-

sistance should be considered at the field of saturation, where the stray field is $\langle B_{\mathrm{stray},z}\rangle \sim 25$ mT, which yields an OHE resistance of $0.08\ \mathrm{m}\Omega$. This is about 0.3% of the total transverse resistance [$(24\pm2)\ \mathrm{m}\Omega$], meaning that contamination of the ISHE with the OHE is negligible.

6.6.3 The transverse resistance loop in the presence of the PHE

The PHE appears in the transverse resistance only if there is misalignment between the applied current I_{bias} and magnetization **m**. In the ISHE measurement setup, **m** is aligned along the easy axis of the FM electrode at low magnetic fields, and along the external magnetic field **H** at high fields. Therefore, at low fields, **m** will be parallel to I_{bias}, whereas, at high fields, a misalignment between **m** and I_{bias} can be introduced due to positioning of the device on the sample during fabrication and/or the placement of the sample inside the measurement station. Figure 6.8 shows a sketch of I_{bias}, **m**, and **H** for negative and positive misalignment angles (α_0) in our ISHE measurement configuration.

The angle between I_{bias} and **m** is given by $\varphi = \alpha + \alpha_0$, where α is the angle between the sample holder and **H** defined by the equipment. For $R_{\mathrm{T}}^{\mathrm{ISHE}}$ versus **H** measurements, α is set to $180°$. As shown in equation 6.2, the ISHE resistance and the PHE resistance are given by $R_{\mathrm{ISHE}} = a_{\mathrm{ISHE}} \cos(\varphi)$ and $R_{\mathrm{PHE}} = a_{\mathrm{PHE}} \sin(2\varphi)$, respectively. At low magnetic field (yellow area), I_{bias} and **m** are aligned because **H** is not strong enough to overcome the shape anisotropy, which aligns **m** along the easy axis of the FM electrode. In this situation, φ = 0°, i.e., R_{PHE} is zero and, therefore, we have only a contribution of the ISHE resistance. However, when we increase **H**, such that **m** aligns with **H** (green area), the misalignment angle is also induced between I_{bias} and **m** ($\varphi = \alpha_0$) and R_{PHE} becomes nonzero. The PHE resistance is negative or positive, depending on whether α_0 is negative (figure 6.8a) or positive (figure 6.8b), respectively.

Figures 6.8c and 6.8d display a sketch of the transverse resistance $R_{\mathrm{T}}^{\mathrm{ISHE}}(H)$ as a function of the magnetic field. In the ideal case, without misalignment and a vanishing PHE contribution, switching of the resistance states would be sharp and flat (square loop). However, in the presence of a misalignment angle, the shape of the $R_{\mathrm{T}}^{\mathrm{ISHE}}$ loop is altered because of the dependence on the strength of **H**, as discussed previously. Ideally, when sweeping **H** from negative to positive and considering a negative misalignment angle (see figure 6.8c), the transverse resistance starts at a value equal to $-R_{\mathrm{ISHE}} + R_{\mathrm{PHE}}$, which slowly decreases to $-R_{\mathrm{ISHE}}$ because **m** rotates towards the easy axis of the FM electrode, that is, parallel to I_{bias}, as **H** moves

to positive values. This creates the sharp dip in the R_T^{ISHE} loop. By further increasing **H**, **m** switches $180°$, but will be still parallel to I_{bias}, resulting in a transverse resistance of R_{ISHE}. Finally, at high magnetic field values, **m** aligns again along **H** and the transverse resistance obtains an additional contribution, $+R_{PHE}$. When sweeping from positive to negative magnetic field values, the $R_T^{ISHE}(H)$ curve has same shape, but is shifted by the magnetic hysteresis. Figure 6.8d shows similar behavior, although inverted because the positive misalignment angle induces a negative PHE resistance ($-R_{PHE}$). This specific shape is not precisely observed in our experimental measurement, which is most probably related to the fact that magnetization in the tip of the FM is not perfectly aligned along the easy axis of the FM at low magnetic field, as also observed in the micromagnetic simulations in figures 6.7a and 6.7b. Nevertheless, for both negative and positive misalignment angles, the PHE resistance has the same magnitude and sign at high positive and negative magnetic fields. Correspondingly, the spin Hall signal (ΔR_{ISHE}^{exp}) can be accurately extracted from the difference between the transverse resistance at field values above saturation of the PHE.

Notably, the sketch in figure 6.8 is made considering a material with a positive spin Hall angle, such as Pt used here. Materials with a negative spin Hall angle, such as Ta and W, will have positive and negative R_T^{ISHE} values at negative and positive magnetic field values, respectively, opposite to Pt. However, in the presence of a misalignment angle, the PHE characteristics in the R_T^{ISHE} loop (the dips and upturns around the switching fields, as presented here for Pt) will be equally valid in negative spin Hall materials.

6

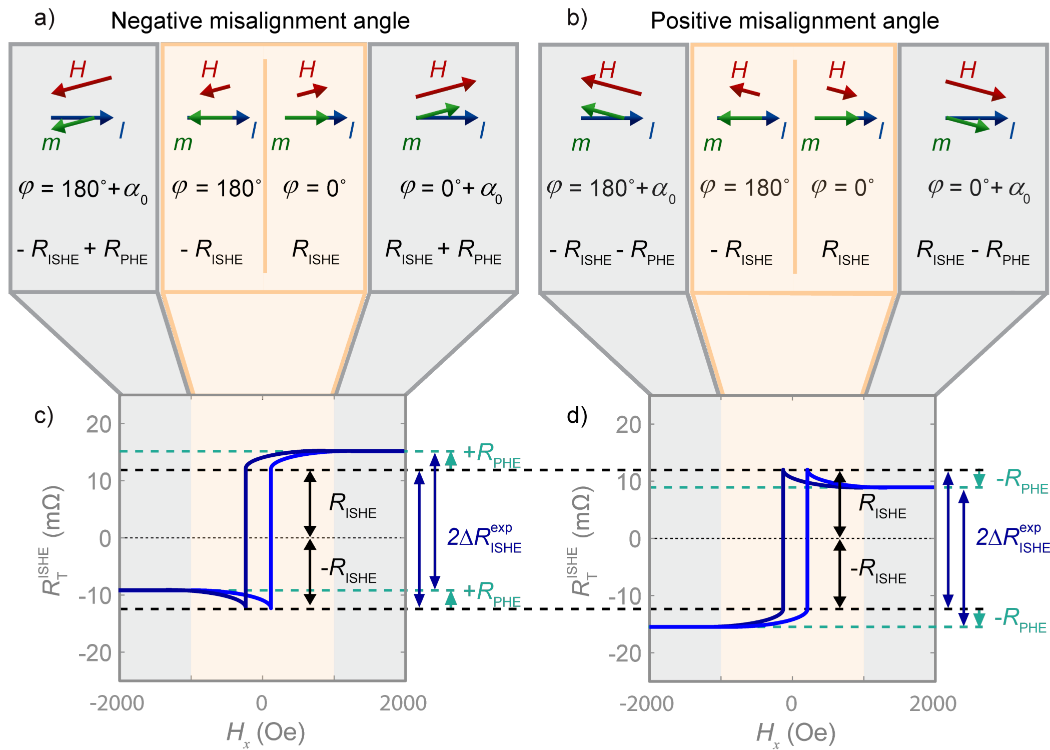

Figure 6.8: Expected shape of the transverse resistance $R_{\mathrm{T}}^{\mathrm{ISHE}}\,(H)$ loop induced by the PHE contribution. a) and **b)** Sketch of the alignment of the current I_{bias}, the magnetization **m** and the external magnetic field **H** at high (grey areas) and low magnetic field (yellow areas) for a negative and positive misalignment angle α_0 between I_{bias} and **m**. When I_{bias} and **m** are parallel, the transverse resistance is equal to the ISHE resistance, i.e., R_{ISHE}, if no other Hall effects are involved. If there is a misalignment between I_{bias} and **H**, the misalignment is transferred to **m** above a certain threshold value of **H**, therefore the PHE contribution R_{PHE} appears at magnetic fields above this threshold value only. **c)** and **d)** $R_{\mathrm{T}}^{\mathrm{ISHE}}\,(H)$ loop as a function of the applied magnetic field in the ISHE configuration, for negative and positive misalignment angles, respectively. The effect of the PHE on $R_{\mathrm{T}}^{\mathrm{ISHE}}$ is twofold. First, the PHE shifts the baseline signal up (negative misalignment angle) or down (positive misalignment angle). Secondly, the PHE induces specific shapes (dips and upturns) close to the switching field of the magnetization in the magnetic field dependence.

Chapter 7

Interfacial spin-charge interconversion in metallic Py/Cu/W lateral spin valve

Our first efforts towards the realization of a spin-based logic device, that is, the MESO device (section 1.3), have been presented in chapter 5 and chapter 6. Even more, we provide a guideline for achieving higher output voltage and current in the local spin Hall device in which the importance of the materials benchmarking is emphasized in the conclusions of chapter 5 (see also section 3.1). We suggest to replace the SOM in the local spin Hall device with another material that has a larger SCI efficiency ($\theta_{\text{SH}}\lambda$) than Pt in order to fulfill the requirements of the full MESO logic device.

Two obvious SOM candidates are W and Ta. Both materials have been studied extensively, theoretically and experimentally, and show a larger intrinsic SCI efficiency than the one of Pt [68, 69]. W and Ta have a negative spin Hall angle meaning that the SHE deflects electrons in opposite direction as compared to the SHE in Pt. However, this does not matter for the readout with our local spin Hall device because we probe the difference between the two saturated magnetic states. The enhancement of the spin Hall efficiency should lead to an increase in $\lambda_{\mathbf{eff}}$ (equation 5.2).

Additionally, the resistivities of W and Ta are in general larger than the resistivity of Pt. This would be advantageous for the geometrical factor G (equation 5.3). Albeit, the increase in resistivity would also generate more spin backflow, reducing the amount of injected spin current. To avoid a reduction of spin backflow for highly resistive SOM ($\rho_{\text{SOM}} > \rho_{\text{FM}}$), implementation of a resistive interface would be beneficial. Actually, we have already presented in section 5.7 the significant improvement of the spin Hall signal in a CoFe/Ta local spin Hall device with an AlO_x resistive interface.

In this chapter, we want to explore the material and spin properties of sputtered W to be able to select the growth conditions that result in high SCI. This will allow us to predict the spin Hall signal that is expected from a CoFe/W local spin Hall device. The higher resistivities and SCI efficiencies in W appear in the β-phase. Growth conditions for highly resistive W with an onset of superconductivity at low temperature are achieved. Additionally, GIXRD indicates that the β-phase W dominates in the W thin film. A non-local lateral spin valve is employed to acquire the spin diffusion length and the SCI efficiency of this W as the local spin Hall device do not permit for individual extraction of the spin properties θ_{SH} and λ (only $\theta_{\text{SH}}\lambda$). A large SCI is measured, however, an unexpected oxide interface layer with a significant interface resistance is observed between Cu and W electrodes, preventing the access to the spin properties of W. The interfacial spin absorption and SCI efficiency are quantified using the universal theoretical framework explained and derived in

chapter 3 (see also section 2.3.3 and 2.3.4). The interfacial spin-loss conductance and the interfacial spin-charge conductivity are larger compared to Cu/BiO_x and Cu/Au systems and the corresponding spin properties of Pt. However, the aim of this research was not to obtain a highly resistive interface layer with large SCI, but to study the bulk spin properties of W. The take-home message of this chapter is that the interface properties have to be carefully considered when studying spin transport in metallic devices.

7.1 Characterization of W

7

As mentioned in the introduction, W is a good candidate for spin-orbitronic devices, but more specifically, this is true for the β-phase of W because of the large spin Hall angles and resistivities, in contrast to the α-phase of W with smaller spin Hall angles and resistivities [186, 187]. The α-W is a thermodynamically stable phase with a body-centered-cubic structure and grain size of about 100 nm resulting in resistivities of $\sim$ 5–40 $\mu\Omega$ cm. Instead, β-W contains a meta-stable A15 structure with a grain size of $\sim$ 2–5 nm and resistivities of $\sim$ 100–300 $\mu\Omega$ cm [186–191]. Even more, the two phases can also be distinguished by their superconducting phase, while α-W condenses into the superconducting phase at only 15 mK, the superconducting temperature of β-W is 1-4 K [192].

The phase of W and, therefore, the electrical and spin properties depend strongly on the deposition conditions. Costa et al. [191] suggest that mono-crystalline β-W is preferred for the purpose of spintronic applications, but up to now most of the research in this field have focused on sputtered β-W that produces poly-crystalline structures. Generally, sputtering of β-W requires slow deposition rate, that is, low pressure and low power for the creation of the ionized Ar gas performed at room temperature in order to stabilize the β-W. Various reports indicate that using additional gases such as O_2 [190, 193–196] and N_2 [197, 198] during sputtering process stabilize β-W. Furthermore, annealing would be undesirable as this enables the movement of W atoms and, subsequently, increases the probability of growth of more stable α-phase with larger grain size [189]. On Si/SiO_x substrates, a commonly used substrate, β-W is reported to be stable for thin layers of $\sim$ 5–10 nm, however, by changing the substrate, thicker films of β-W can be achieved due to changes of stress in the W layer induced by the different substrates. [199].

A spin Hall angle of 0.4 with λ_W =3.5 nm is observed in β-W using a spin-orbit torque experiment [187]. However, according to Ref [199], the SCI analysis requires

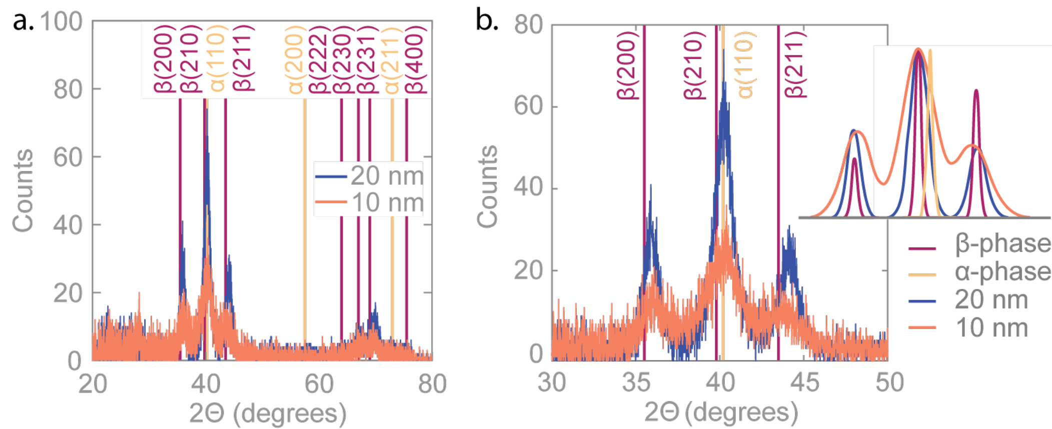

7

Figure 7.1: GIXRD on a thin film of sputtered W. a) GIXRD diffraction pattern, giving the number of counts versus the 2Θ angle, of two different thin films with a thickness of 10 nm (orange) and 20 nm (blue). The crystallographic diffraction peaks of the α-phase and β-phase of W are shown in yellow and purple, respectively. **b)** A zoom of GIXRD diffraction pattern for 2Θ between 30 ° and 50 °. The inset shows decomposition of the measured diffraction patterns into three Gaussian functions (orange and blue lines). A model of the crystallographic diffraction peak of the α-phase (yellow) and β-phase (purple) of W is also presented.

$t_W \gg \lambda_W$, while the experiment is done on thin films with a thickness of 3-9 nm. Also, it seems that interface resistance is not considered, which brings doubt about the accuracy of the spin properties. Another study using ST-FMR finds the spin Hall angle of β-W to be 0.3 but the spin diffusion length is not mentioned [186]. It is noteworthy that the SCI in W can be tuned by doping it with O [195] or with Ta [200, 201]. Since our research group had not performed an extensive study on W, we focused firstly on the growth of β-W. We studied the thin films of W deposited with different sputtering conditions always at room temperature using an Ar gas with a flow of 20 sccm and a rotation of 20 rpm. The thin films with varying power and Ar-pressure are inspected with XRD and GIXRD (see section 4.2.3 for details on these techniques) as well as electrically. Section 7.8.1 discusses some of the results based on resistivity measurements. For the remainder of the chapter, the W samples are sputtered at 3 mTorr of pressure and 10 W of power and we will now briefly present the GIXRD measurements and the resistivities of two W thin films.

Figure 7.1 gives the GIXRD analyses on two W thin films with a thickness of 10 nm and 20 nm. Figure 7.1a shows the diffraction pattern and indicates the crystallographic peaks associated to the α and β-phase of the W. A slight shift of the diffraction pattern compared to the crystallographic peaks is observed that can be

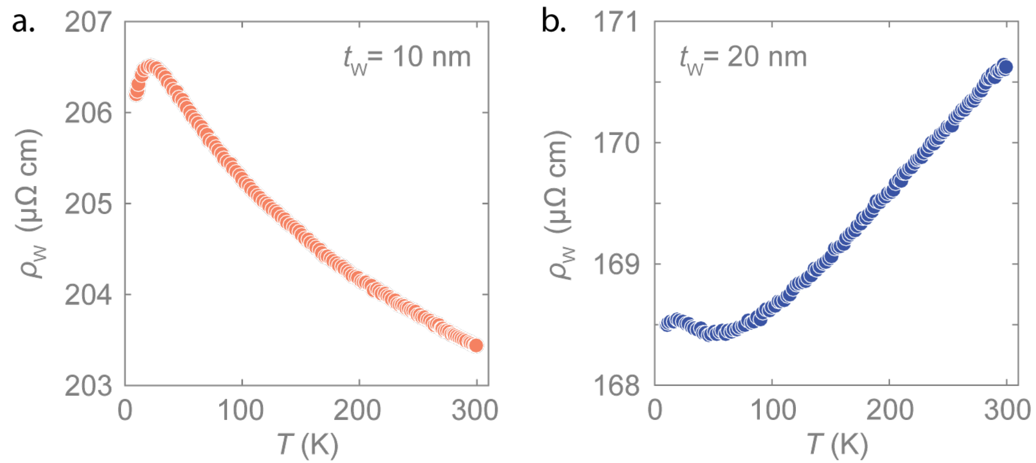

Figure 7.2: Thin film resistivities of W. The temperature dependence of the resistivity in thin films with thickness **a)** 10 nm and **b)** 20 nm measured by van der Pauw configuration. The average of the two orientations (horizontal and vertical) of the configuration is displayed.

better appreciated in figure 7.1b. Peak shifts may be due to the size of the grains. Also redistribution of the intensity of the $\beta(200)$ and $\beta(211)$ peaks can be due to structural reasons (specific types of defects) or due to the texture. Either way, both thin films have five peaks that are characteristic for β-W ($\beta(200)$, $\beta(210)$, $\beta(211)$, $\beta(230)$, $\beta(231)$). The grain size obtained from peak widths is $\sim$ 4 nm for the 10-nm-thick film and $\sim$ 7.5 nm for the 20-nm-thick film, which is also distinctive for β-W. The inset of figure 7.1b illustrates a decomposition of GIXRD data into three Gaussian functions and a presentation of peaks arising from the α and β-phase W. It is clear from this plot that the data mimics the model behaviour of the β-phase. If the α-phase were to be mixed with β-phase, the middle peak [close to the angles for $\beta(210)$ and $\alpha(110)$] would be substantially broader, than the two satellite peaks of the β-phase [$\beta(200)$ and $\beta(211)$], which is not the case. Another evidence for the W to be β-phase is that this middle peak would be substantially higher relative to the satellite peaks of the β-phase if the α-phase were to be present. Also, the experimental $\beta(200)$ and $\beta(211)$ peaks have about the same relative intensity as the β-phase model.

We have also investigated the electrical resistivity of the thin films. Figure 7.2a shows the resistivity of the 10-nm-thick film and figure 7.2b displays the resistivity of the 20-nm-thick film. Both thin films have a resistivity magnitude that would compare to β-W even though the temperature dependence of the resistivities does not show the same behaviour. The difference might come from distinct grain sizes or maybe

some α-phase was able to form in the 20-nm-thick film inducing a more metallic behaviour. Yet, the onset for superconductivity appeared either way which points again to the dominant presence of β-W. We continued with the deposition conditions used for these thin films to investigate the SCI in this W.

7.2 Py/Cu/W lateral spin valve

In this chapter, LSV devices are used to investigate the interface resistance (section 4.3.1) as well as the spin properties, that is, spin absorption and SCI (section **??**). Figure 7.4a displays a top-view SEM image of the Py/Cu/W nanostructure consisting of two Py electrodes, a W electrode placed in between the Py electrodes and a transverse Cu electrode connecting these three electrodes. The fabrication process as introduced in section 4.1 is repeated three times, once for each material. Step one involves the Py nanostructures, where the Py is deposited via e-beam evaporation (0.56 A s^{-1} and $p_{\text{dep}} \sim 3.1 \times 10^{-8}$ mbar). The second step includes the W nanostructure that is deposited by magnetron sputtering (0.11 A/s, $p_{\text{Ar}} = 3$ mTorr, $P = 10$ W, $p_{\text{Base}} \sim 2 \times 10^{-8}$ mTorr at room temperature). After this second step, Ar-ion milling is performed at grazing incidence to remove side walls of both the Py and W electrode. Lastly, the Cu nanostructures are done. After developing and before the deposition of Cu, Ar-ion milling is performed at normal incidence to clean the Py and W surfaces. Subsequently, 3 nm of Cu is deposited *in situ* by magnetron sputtering (1.88 A/s, $p_{\text{Ar}} = 3$ mTorr, $P = 250$ W, $p_{\text{Base}} \sim 3 \times 10^{-6}$ mTorr at room temperature) in an attempt to prevent the W from oxidizing and create a highly transparent interface between the Cu and the Py and W electrodes. Finally, the Cu is deposited by thermal evaporation (1.5 A s^{-1} and $p_{\text{dep}} \sim 1.7 \times 10^{-8}$ mbar).

The width and thickness of the electrodes for the device used in this study are $w_{\text{Py}} = 124$ nm, $t_{\text{Py}} = 30$ nm, $w_{\text{W}} = 188$ nm, $t_{\text{W}} = 4.5$ nm, $w_{\text{Cu}} = 123$ nm and $t_{\text{Cu}} = 90$ nm. The electrical transport measurements are carried out in a PPMS using a dc-reversal technique (section 4.2.1). For the measurements in this study, we used an in-plane magnetic field, a rotator, and a temperature range of $10 - 300$ K. The temperature dependence of the resistivities of the electrodes in this LSV are plotted in figure 7.3.

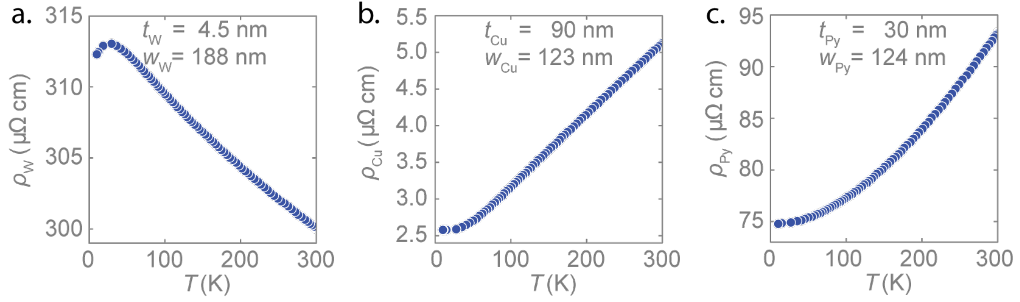

Figure 7.3: The resistivities of electrodes in Py/Cu/W LSV. The temperature dependence of the resistivity of the **a)** W electrode, **b)** Cu electrode, and **c)** Py electrode.

7.3 Characterization of the Cu/W interface

Proper investigation of interfaces is of utmost importance for the quantification of materials properties from electrical, spintronic and spin-orbitronic measurements. The role of interface resistance in spin Hall devices is emphasized in section 3.1. Furthermore, section 2.3 makes us aware that SCI can even appear at an interface itself. Therefore, we have derived the spin absorption (section 3.3.3) and SCI (section 3.3.4) in lateral spin valves considering the presence of an interface with resistance that can absorb spins and, on top of that, can manifest SCI. We study the Cu/W interface in the Py/Cu/W LSV combining electrical measurements, TEM and 3D FEM simulations (see chapter 4 for details on the experimental techniques) in order to find the right quantification of the spin diffusion length and the SCI parameter.

Figure 7.4a displays a SEM image of the Py/Cu/W LSV with the measurement configuration for probing the experimental interface resistance $R_\mathrm{i}^\mathrm{exp}$. Figure 7.4b shows the resulting interface resistance at various temperatures. $R_\mathrm{i}^\mathrm{exp}$ is observed to be negative, which is possible for low-impedance interface as discussed in section 4.3.1. A negative interface resistance is an artifact that comes from a inhomogeneous current density flow (see figure 4.4c) and voltage drop. 3D FEM simulations can be utilized to correct the interface resistance.

In the 3D FEM, a 3D geometrical model resembling the Cu and W electrodes is build and the electrical configuration is simulated as in the experimental measurement presented in figure 7.4a (see also figure 4.4). The variation of the contact impedance $R_\mathrm{i}A_\mathrm{i}$ at the Cu/W interface boundary is used to find the actual interface resistance R_i. The contact impedance for which the resistance in the FEM simu-

lation R_{FEM} is equal to $R_{\mathrm{i}}^{\mathrm{exp}}$ gives R_{i} (see figure 7.4c). The resulting R_{i} at different temperatures is plotted in figure 7.4d.

We find that R_{i} is a few Ω, which is higher than expected from an all-metallic interface. TEM has been performed to inquire about the reason behind this "high" interface resistance. Figure 7.5a shows a cross-sectional TEM image of the Cu/W interface. The element composition is inspected by EDAX in the region indicated by the orange square. The observed elements in this region are oxygen (O), W and Cu. Surprisingly, O appears in between the Cu and W electrodes as depicted in the

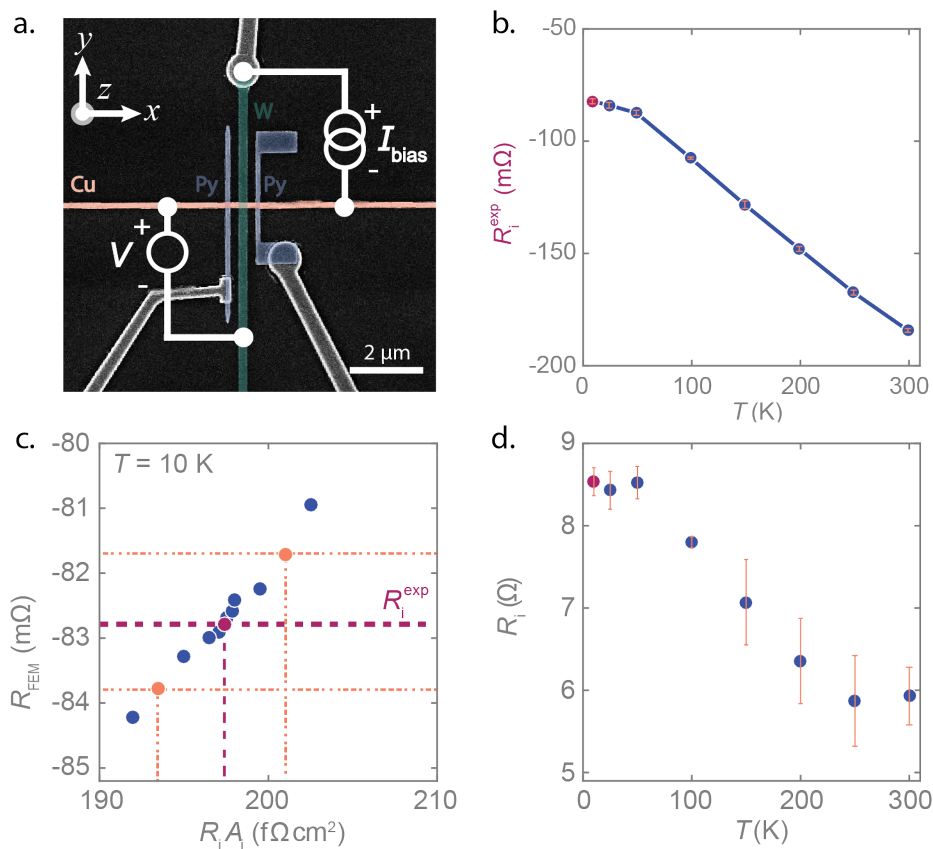

Figure 7.4: Interface resistance measurement and simulation. a) A false-color SEM image of a Py/Cu/W LSV with the Py, Cu and W electrodes indicated by blue, orange, and turquoise, respectively. The electrical configuration is the 4-probe interface resistance measurement of the Cu/W interface. **b)** Temperature dependence of the experimental interface resistance $R_{\mathrm{i}}^{\mathrm{exp}}$ of the Cu/W interface. **c)** 3D FEM simulated resistance R_{FEM} as a function of the contact impedance. By comparing the $R_{\mathrm{i}}^{\mathrm{exp}}$ with R_{FEM}, the actual interface resistance R_{i} can be obtained. **d)** R_{i} extracted from the 3D FEM simulation for various temperatures.

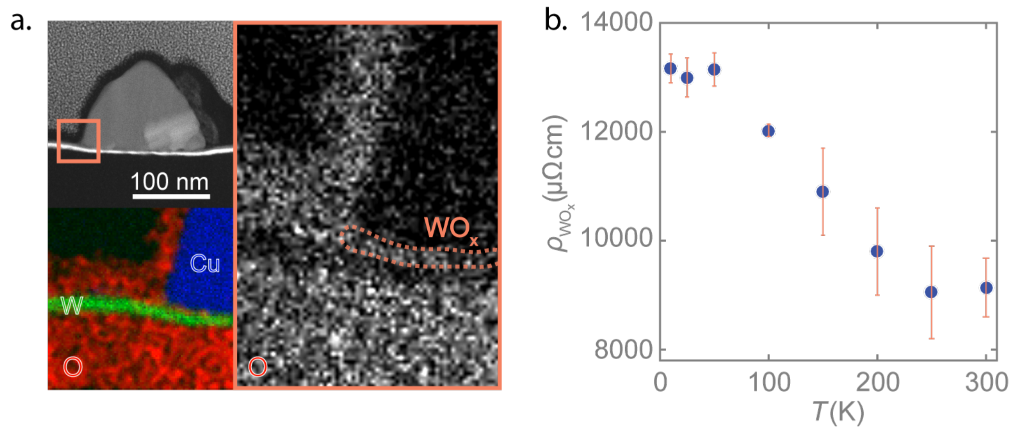

Figure 7.5: An oxide interface layer with a high resistivity. a) A TEM image of the Cu/W interface. Top left panel: cross-section of the Cu/W interface area. Bottom left panel: A zoom-in of the TEM image (orange square in the top panel) where an EDAX analysis has been performed. The false colors indicate the presence of O (red), Cu (orange), and W (green). Right panel: The result of the EDAX analysis for O point out that, in between the Cu and W electrodes, O is present. The area tagged by us as WO_x is also indicated. **b)** The resistivity of the WO_x layer with the temperature, extracted from the 3D FEM simulation.

main image. A deeper discussion on the elemental composition can be found in section 7.8.2. We find the W electrode thickness below the Cu electrode to be 2.8 nm thick. The oxide layer, which has a thickness of $\sim$ 1.5 nm, is most probably a mixture of W and O, even though the presence of Cu is not excluded, and is the source of the "high" interface resistance. As the composition of the interfacial layer is not precisely known, in the remainder of this chapter we will refer to this layer as the oxide layer and use the tag "WO_x".

The finite thickness of the oxide layer makes us revise the FEM simulation that has been performed to obtain R_i as the interface is no longer a boundary condition but an oxide layer which has to be included in the FEM. The geometry has been adapted accordingly, considering the structural details described in section 7.8.2. Although the thickness of the W underneath the Cu and away from the Cu is different, we consider the resistivity of the W electrode the be the same everywhere. The simulation has been preformed in the same way as explained before (figure 7.4a and figure 7.4d) with the only difference being that we vary the resistivity of the oxide layer ρ_{WO_x} instead of the contact impedance to match R_{FEM} with R_i^{exp} (section 4.3.1). Figure 7.5b graphs the resulting temperature dependence of ρ_{WO_x} which is relatively high compared to resistivities in the metal electrodes (figure 7.3).

Note that $\rho_{\mathrm{WO_x}} \sim R_{\mathrm{i}} t_{\mathrm{WO_x}}$, most probably because the $t_{\mathrm{WO_x}}$ is fairly thin. We conclude that we have a highly resistive oxide interface in the metallic Py/Cu/W LSV that has to be taken into account for the study on the spin absorption and SCI.

7.4 Spin absorption as the storyteller

Generally, the spin absorption technique in metallic LSV is used to estimate the spin diffusion length of the SOM (section 3.3.3). In those devices, the interface between the NM transport channel and the SOM is transparent or, in other words, the spin resistance of the interface is lower than the spin resistances of the NM and the SOM electrodes. In that situation, equation 3.39 can be put to use. One could also exploit the spin absorption to find the contribution of the interface via equation 3.30 if the spin properties of the SOM are known. However, in LSVs with highly resistive interfaces, that is, LSVs in which the spin resistance of the interface is dominant over the one of metallic SOM, there is no access to the spin properties of the SOM and only the interfacial properties can be explored by applying equation 3.42.

Figure 7.6a displays again the SEM image of our LSV (same as shown in figure 7.4) with the measurement configuration for the spin absorption technique. The non-local resistance is measured using the conventional LSV technique in a reference LSV without the W electrode ($R_{\mathrm{NL}}^{\mathrm{ref}}$, section 3.3.1) and the LSV with the W electrode ($R_{\mathrm{NL}}^{\mathrm{abs}}$, section 3.3.3). Figure 7.6b plots the magnetic field dependence of $R_{\mathrm{NL}}^{\mathrm{ref}}$ and $R_{\mathrm{NL}}^{\mathrm{abs}}$ at 10 K. The differences between the low and highly resistive state are the spin signals $\Delta R_{\mathrm{NL}}^{\mathrm{ref}}$ and $\Delta R_{\mathrm{NL}}^{\mathrm{abs}}$. $\Delta R_{\mathrm{NL}}^{\mathrm{abs}}$ is smaller than $\Delta R_{\mathrm{NL}}^{\mathrm{ref}}$, meaning that the placement of the W electrode with the interfacial oxide layer at the W/Cu interface does absorb spins.

Both experiments have been performed at different temperatures and figure 7.6c presents temperature dependence of the spin signals. Note that the spin absorption depends also on L, the distance between the FM injector and detector, and the width of the SOM electrode. Either way, the observed $\Delta R_{\mathrm{NL}}^{\mathrm{abs}}$ has the same order of magnitude as other all-metallic LSV where W is replaced by a Nb, Pt or Ta electrode [70, 76, 77], a CuIr, CuBi or AuW alloy electrode [90, 91, 95] or even by electrodes constructed out of metallic/oxide heterostructures [111, 116].

Interestingly, spins are being absorbed in our Py/Cu/W LSV even though the Cu/W contains a highly resistive interfacial oxide layer. Section 7.8.3 discusses the spin

properties of the Py and Cu electrodes which are necessary for determining the spin properties of the W electrode or the interfacial oxide layer. Then, the ratio of the spin signals $\Delta R_{NL}^{abs}/\Delta R_{NL}^{ref}$ (inset of figure 7.6d) is used to pinpoint where the spins are absorbed and to know which spin properties are probed (section 7.8.4).

An important notion is that if a negative interface resistance is considered to be a transparent interface and we neglect the interface resistance in our Py/Cu/W LSV, the fitting of equation 3.39 to $\Delta R_{NL}^{abs}/\Delta R_{NL}^{ref}$ gives $\lambda_W \approx 1.5$ nm (figure 7.14a). This is on the same order of magnitude as λ_W reported for W determined by SOT [187, 202] and as observed in Pt and Ta using LSVs [76, 77]. However, implementing the interface resistance (figure 7.4d), the fitting does not give a valid solution for the spin diffusion length (figure 7.14b).

Continuing the discussion on the spin sink, the spin diffusion equation for spin absorption indicates that the spin absorption must be dominated by the oxide interfacial layer, somewhat expected from the high resistivity of the oxide. The remaining question is now, whether the absorption occurs in the "bulk" oxide layer or at the Cu/WO_x interface. In both cases, we assume that the measured interface resistance comes from the oxide resistivity and the W/WO_x and Cu/WO_x interface are transparent, as we cannot distinguish between the three possible candidates. The absorption in the "bulk" oxide means that the spin sink effect occurs up to a certain thickness $\leq t_{WO_x}$ in the oxide layer. We have used again equation 3.39 supposing that the oxide layer with resistivity ρ_{WO_x} (figure 7.5b) is the SOM and the W just functions as a metallic electrode. λ_{WO_x} is found to be ~ 0.04 nm (figure 7.14c) that is smaller than the interatomic distance of typical transition metal oxides.

Consequently, the spin absorption have to take place at the Cu/WO_x interface and equation 3.42 is thus used. Equation 3.42 for interfacial spin absorption is similar to equation 3.39 besides the fact that the interfacial spin absorption is not described by a spin conductance G_{SOM} ($1/R_s^{SOM}$) depending on λ_{SOM} but by $G_s^{\parallel}$ given by the spin-loss conductance $G_{\parallel}$. Figure 7.6d presents $G_{\parallel}$ in our Py/Cu/W LSV obtained from $\Delta R_{NL}^{abs}/\Delta R_{NL}^{ref}$ at different temperatures (inset figure 7.6d). Table 7.1 compares the resulting $G_{\parallel}$ at the Cu/WO_x interface to Cu/BiO_x [116] and Cu/Au [111], which are analysed by the same method. $G_{\parallel}$ at the Cu/WO_x interface ($\sim 20 \times 10^{13}\ \Omega^{-1}\text{m}^{-2}$) is remarkably larger than the ones observed in the Cu/BiO_x and Cu/Au.

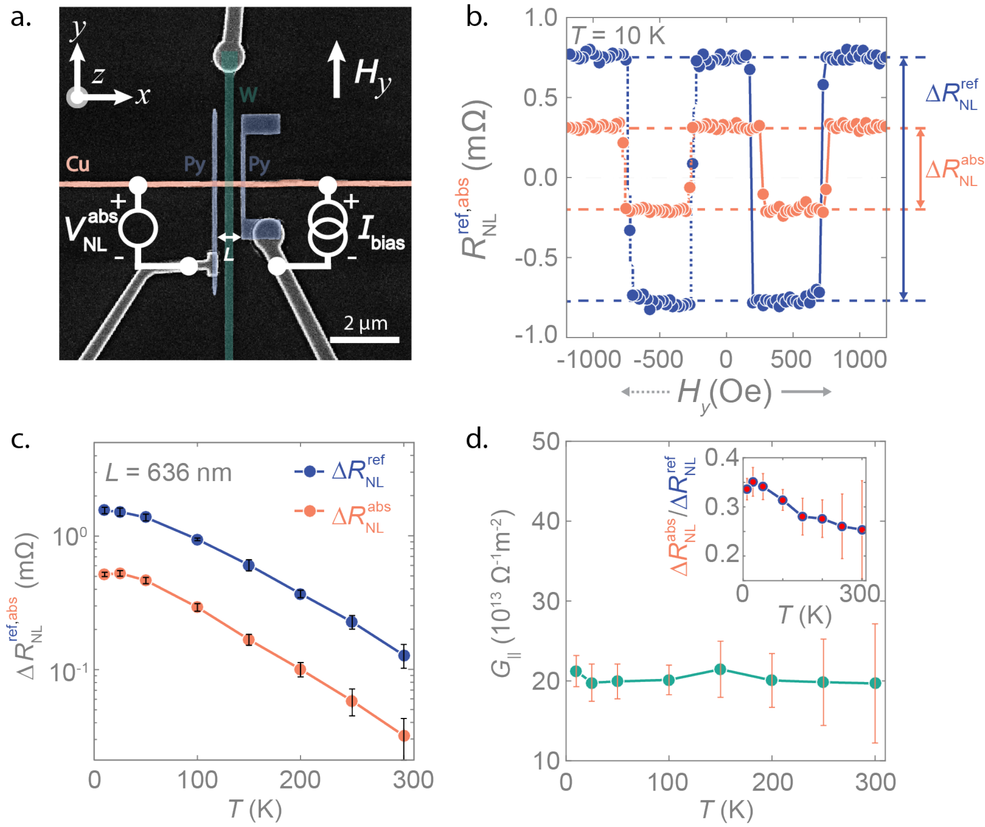

Figure 7.6: Spin absorption in the Py/Cu/W LSV. a) A false-color SEM image presenting a top view of the Py/Cu/W LSV including the spin absorption technique measurement configuration. The magnetic field is applied along the easy axis of the Py electrodes . **b)** The non-local resistance for the reference LSV (blue) and the LSV with the middle W electrode (orange) at 10 K. The difference between the low and high resistance state gives the spin signals $\Delta R_{\mathrm{NL}}^{\mathrm{ref}}$ and $\Delta R_{\mathrm{NL}}^{\mathrm{abs}}$ for the associated LSVs. **c)** The spin signals $\Delta R_{\mathrm{NL}}^{\mathrm{ref}}$ and $\Delta R_{\mathrm{NL}}^{\mathrm{abs}}$ at different temperatures. **d)** The temperature dependence of the interfacial spin-loss conductance $G_{\|}$ $(= G_{\mathrm{s}}^{\|}/A_{\mathrm{int}})$ obtained from applying equation 3.42 to the $\Delta R_{\mathrm{NL}}^{\mathrm{abs}}/\Delta R_{\mathrm{NL}}^{\mathrm{ref}}$ data displayed in the inset.

7.5 Electrical shunting in the Cu/WO$_{\mathrm{x}}$/W structure

Electrical shunting is essential for the evaluation of SCI in the non-local spin Hall device. In section 4.3.2, the electrical shunting in non-local spin Hall

Table 7.1: | **Summary of the interfacial spin absorption and spin-charge interconversion in different interfacial systems at 10 K.** The interfacial systems listed are Cu/Au [111], Cu/BiO$_x$ [116] and the Cu/WO$_x$ presented in this chapter. The spin absorption is given by the interfacial spin-loss conductance $G_{\|}$ and the SCI by the interfacial spin-charge conductivity σ_{SC}. The inverse Edelstein length λ_{IEE} follows from $\sigma_{SC}/G_{\|}$.

Materials system	$G_{\|}$ 10^{13} [Ω^{-1}m^{-2}]	σ_{SC} [Ω^{-1}cm^{-1}]	λ_{IEE} [nm]
Cu/Au	7.6 ± 0.6	-127 ± 8	-0.17
Cu/BiO$_x$	2.8 ± 0.2	44 ± 9	0.16 ± 0.03
Cu/WO$_x$	21 ± 2	-3500 ± 100	-1.6 ± 0.2

7

device constructed out of metallic NM and SOM electrodes is elaborated on. However, the highly resistive oxide layer at the Cu/W interface observed in the Py/Cu/W LSV will obviously influence the electrical shunting. That is why, before going into details of SCI in the Py/Cu/W LSV with interfacial oxide layer, the electrical shunting in the device will be assessed and the importance of the position of the injected charge current density imitating I_{ISHE} in the 3D FEM simulation will be emphasized.

A 3D FEM simulation will be used to find the electrical shunting, that is the fraction of the I_{ISHE} flowing through each layer in the Cu/WO$_x$/W structure (equation 4.3). The additional oxide layer changes the geometry in the 3D FEM to a tri-layer of Cu, W and WO$_x$. Figure 7.7a shows the heterostructure at the intersection of the Cu and W electrodes with the oxide layer. The electrical shunting is attained by simulating the average current density and, from this, the current flow in each component is calculated (see section 4.3.2 for more details). The spin absorption occurs at the Cu/WO$_x$ interface (section 7.4), subsequently the SCI and thus the generation of I_{ISHE} takes place at this interface as well. The voltage drop over the three components (Cu, WO$_x$ and W) is the same according to Kirchhoff's law. Equation 3.42 considers the current flow in the WO$_x$, indicated by the appearance of t_{WO_x} and σ_{WO_x}, such that even though V_{ISHE} will be probed at the W electrode, the electrical shunting factor that has to be considered is the one of the oxide, x_{WO_x}.

The generation of I_{ISHE} at the Cu/WO$_x$ interface bring about another discussion that is where to apply the charge current density in the 3D FEM simulation. Following the reasoning of section 4.3.2 based on the 1D model for electrical circuits, the charge current density j_c should be applied at the oxide layer as displayed in

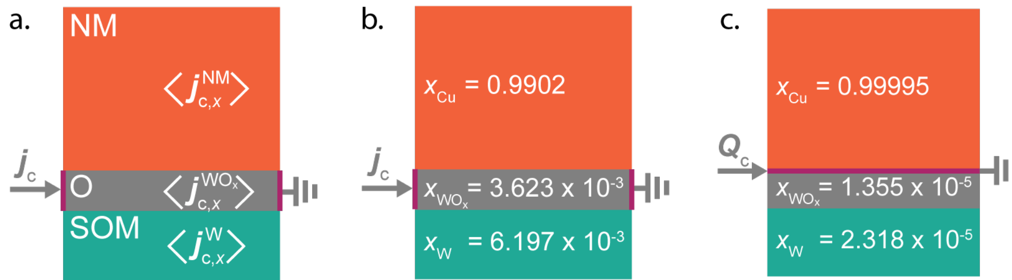

Figure 7.7: Electrical shunting in a metal/oxide/metal structure. a) The model constructed out of a NM (orange), oxide (grey) and SOM (turquoise) layer in the 3D FEM. The spin absorption occurs in the resistive oxide layer, indicating that spin-to-charge conversion also happens there. The charge current density j_c resembling the I_{ISHE} is in that case applied to the oxide layer. The x-component of the average j_c ($\langle j_{c,x} \rangle$) in each layer, that is simulated in the 3D FEM model, allows extracting the shunting factors. **b)** The shunting factor in each layer when j_c is applied to the oxide layer as in panel **a)**. **c)** The shunting factor in each layer when a line current source Q_c is applied to the Cu/WO_x interface.

figure 7.7a. Figure 7.7b shows the resulting shunting factors in each layer. However, as we have found that the origin of I_{ISHE} is at the Cu/WO_x interface, we have to adapt the model and apply j_c at the interface itself. Figure 7.7c displays x for each of the layers at 10 K. The change in x_{WO_x} is roughly two orders of magnitude. This big change appears in the Cu/WO_x/W structure because of the high resistivity of the oxide layer playing a dominant role in the structure. Note that I_{ISHE} in metallic NM/SOM structures is created in a region close to the interface with a thickness defined by λ_{SOM} and, therefore, the j_c imitating I_{ISHE} should be applied to this region. However, generally, NM and SOM have a "low" resistivity and a significant change in x for the two configuration in figure 7.7 is thus not observed. The details on the 3D FEM simulation used in this study is found in section 7.8.5. Figure 7.8 plots x for a temperature range of 10-300 K. The corresponding x_{WO_x} (figure 7.8b) is used in section 7.6 to quantify the SCI in the Cu/WO_x interface.

7.6 Interfacial spin-charge interconversion at the Cu/WO_x interface

We have observed quite strong spin absorption in our Py/Cu/W LSV even though a highly resistive oxide layer is located in between the Cu and W electrode (Section 7.4). The next question is whether this interface presents SCI. Figure 7.9a shows

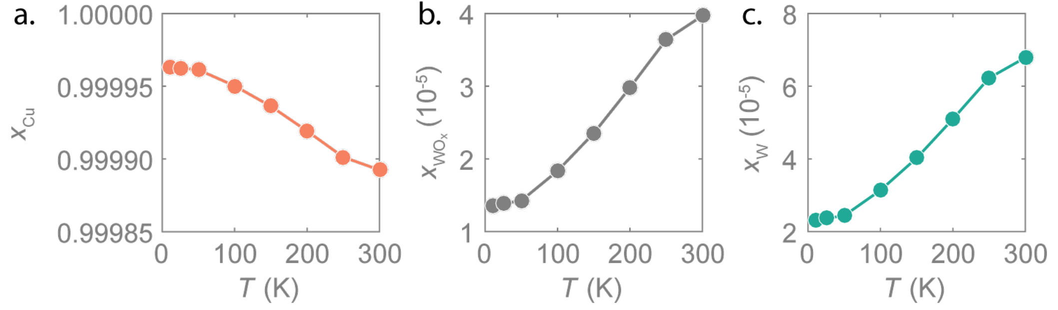

Figure 7.8: Electrical shunting factors in the Cu/WO$_x$/W structure. The shunting factor calculated with the 3D FEM simulation and equation 4.3 for **a)** the Cu electrode (x_{Cu}), **b)** the interfacial oxide layer ($x_{\mathrm{WO_x}}$), and **c)** the W electrode (x_{W}).

again the SEM image of the Py/Cu/W LSV, this time depicted together with the SHE measurement configuration. The details of the measurement can be found in section 3.3.4. Figure 7.9b presents the variation of spin-charge resistance R_{SC} with an external magnetic field H_x for different temperatures (10-300 K). By sweeping H_x, a change in R_{SC} is observed for the full temperature range, indicating that charge-to-spin conversion occurs at all the temperatures considered. This is an unexpected revelation considering the highly resistive oxide layer (section 7.3). The difference between the low and high resistance, $2\Delta R_{\mathrm{SC}}$, is called the spin-charge signal. Figure 7.9c plots the temperature dependence of $2\Delta R_{\mathrm{SC}}$. The interfacial SCI is described by equation 3.43:

$$\Delta R_{\mathrm{SC}} = x_{\mathrm{WO_x}} \frac{w_{\mathrm{Cu}} R_{\mathrm{s}}^{\mathrm{Py}}}{t_{\mathrm{WO_x}} \sigma_{\mathrm{WO_x}}} \frac{4 P_{\mathrm{Py}}^2 Q_{\parallel} \sigma_{\mathrm{SC}} e^{\frac{L}{2\lambda_{\mathrm{Cu}}}}}{r_1 r_{\mathrm{RI}} e^{\frac{L}{\lambda_{\mathrm{Cu}}}} + r_{\mathrm{RI}} - 2}$$

with $r_1 = 1 + 2Q_{\mathrm{Py}}$ and $r_{\mathrm{RI}} = 1 + 2Q_{\parallel}$. From this equation and using the gathered values of ΔR_{SC}, $Q_{\parallel}$ and x_{SOM}, we obtain the interfacial spin-charge conductivity σ_{SC}. Figure 7.9d shows that σ_{SC} at the Cu/WO$_x$ interface is fairly constant and has a magnitude of about $-3500\ \Omega^{-1}\mathrm{cm}^{-1}$. The negative sign of the σ_{SC} is also observed for the spin Hall conductivity σ_{SH} in bulk β-W. This seems reasonable because, even tough we could not extract the composition of the interfacial oxide layer, chances are high that W is involved, even more so now that the sign is the same. Table 7.1 indicates that σ_{SC} of this interface is notably higher compared to the Cu/BiO$_x$ and Cu/Au systems. Remarkably, the observed σ_{SC} is even higher than the σ_{SH} in Pt ($\sim 1600\ \Omega^{-1}\mathrm{cm}^{-1}$) [76].

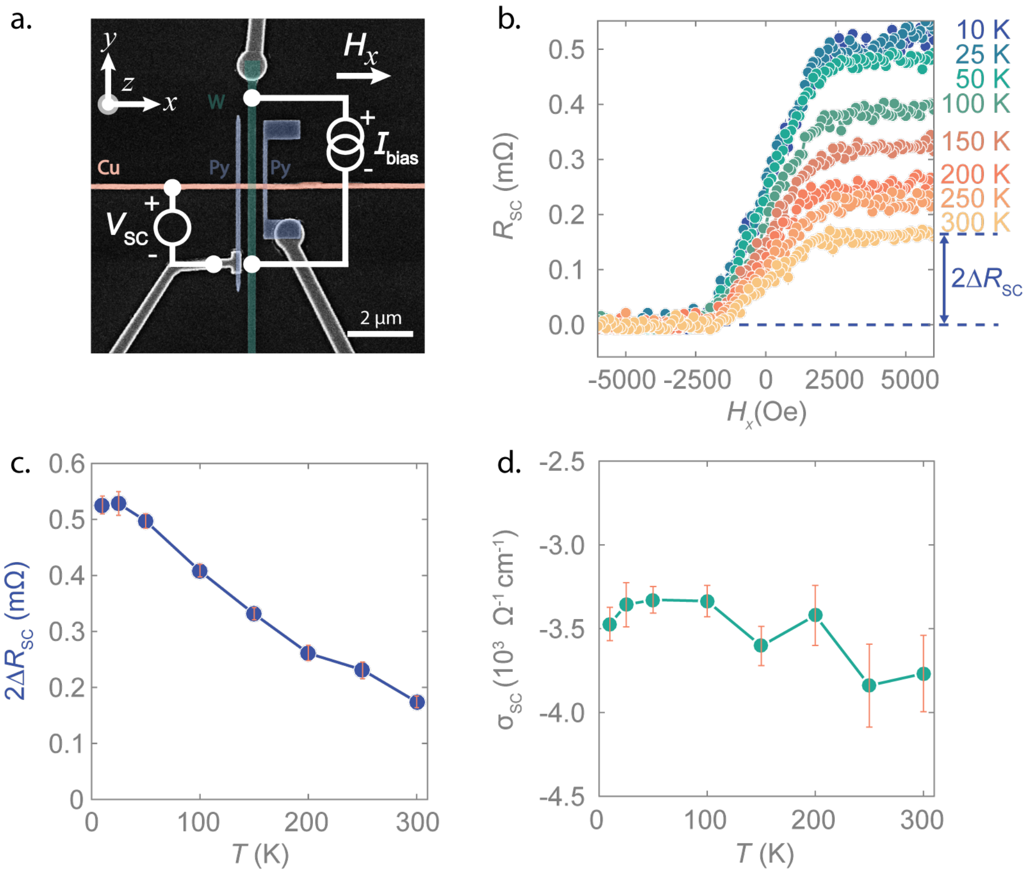

Figure 7.9: Charge-to-spin conversion at the Cu/WO$_x$ interface. a) A false color SEM image of the Py/Cu/W LSV with the measurement configuration for detection charge-to-spin conversion. The external magnetic field is oriented in the x-direction. **b)** The magnetic field dependence of the spin-charge resistance R_{SC} for various temperatures. R_{SC} is the average of the trace and retrace of the magnetic field. The difference between the low resistance state and the high resistance state is the spin-charge signal $2\Delta R_{SC}$. An off-set is added to R_{SC} such that the low resistance state is zero and the variation of $2\Delta R_{SC}$ can be clearly observed. **c)** The spin-charge signal as a function of temperature. **d)** The temperature dependence of the spin-charge conductivity for the Cu/WO$_x$ calculated with equation 3.43 combined with the obtained values for ΔR_{SC}, $Q_{\|}$, and x_{WO_x}.

Finally, we can combine the results of the interfacial spin-loss conductance ($G_{\|}$) and the interfacial spin-charge conductivity σ_{SC} to calculate the commonly used inverse Edelstein length λ_{IEE} (section 2.3.2) for the Cu/WO$_x$ interface. Remark that it is more convenient to display the spin and SCI properties as $G_{\|}$ and σ_{SC} because these are universal parameters that compare to bulk SCI via the spin conductance of the SOM (G_{SOM}) and spin Hall conductivity (σ_{SH}). Nevertheless, in the local spin

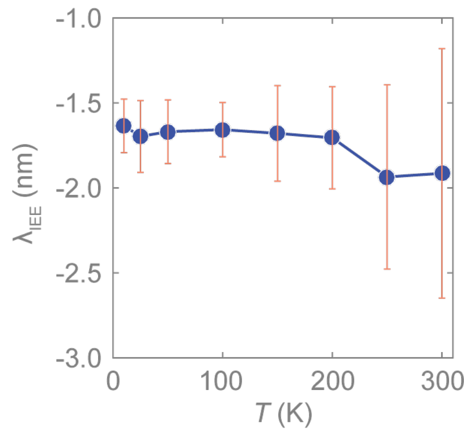

Figure 7.10: The inverse Edelstein length in the universal model for interfacial spin-charge interconversion. The temperature dependence of inverse Edelstein length λ_{IEE} resulting from the ratio between the interfacial spin-charge conductivity σ_{SC} (figure 7.9d) and the interfacial spin-loss conductance $G_{\|}$ (figure 7.6d).

Hall device, λ_{IEE} is equivalent to $\theta_{\mathrm{SH}}\lambda$, that is, the SCI efficiency that appears directly in λ_{eff} (section 5.4). Figure 7.10 graphs $\lambda_{\mathrm{IEE}} = \sigma_{\mathrm{SC}}/G_{\|}$ as a function of temperature. The resulting λ_{IEE} is an order of magnitude larger as the one observed in Cu/BiO_x and Cu/Au (table 7.1). and $(\theta_{\mathrm{SH}}\lambda)_{\mathrm{Pt}}$ in Pt [76]. Thus, this system is potentially interesting for efficient SCI in the local spin Hall device and, subsequently, for the magnetic-state readout in the MESO device.

A final remark on the SCI is that this device was not prepared with the idea of measuring interfacial SCI in a Cu/WO_x interface. Further more, we do not know the precise composition of the oxide layer and the composition might be quite inhomogeneous. This study might as well have been presented, wrongly, as results on the SCI of bulk W if we had not carefully considered the interface. Therefore, we want to use this work to emphasize how important it is to study every aspect of the device in order to obtain meaningful spin diffusion lengths and SCI parameters.

7.7 Conclusions

In this chapter, we firstly discuss the possibility of measuring SCI in β-phase W and we characterize our sputtered W. This W is implemented in a Py/Cu/W LSV in order to investigate its spin properties. However, we find an oxide layer at the Cu/W interface with a high resistivity that prevents absorption into the W electrode. We reason that the spin absorption actually happens at the Cu/WO_x interface with

$G_{\parallel} \approx 20 \times 10^{13}$ $\Omega^{-1}\mathrm{m}^{-2}$. Interfacial SCI is observed as well with $\sigma_{\mathrm{SC}} \approx -3500$ $\Omega^{-1}\mathrm{cm}^{-1}$. Ultimately, this interfacial system has an efficiency of $\lambda_{\mathrm{IEE}} \approx -1.6$ nm, which is one order of magnitude larger than other metallic interfaces or even Pt. In this study, no assumptions have been made on the origin of the SCI. The strong spin absorption and large σ_{SC} is quite surprising, since it was not our intention to study the interfacial SCI of a Cu/WO_x interface and the fabrication was not designed for this purpose. For the same reason, the composition of the oxide is not known and might be inhomogenous. However, SOT studies on W/CoFe [202] and CoFe/WO_x structures [195] shows large SCI efficiencies that are discussed to be of interfacial origin. Additionally, enhanced SCI efficiencies are observed in CuW alloys [203] and highly efficient SCI is measured in Cu/AlO_x interfaces [139] using spin-torque FMR. The lack of heavy elements in this Cu/AlO_x structure reveals SCI mediated through orbital transport. This type of orbital Hall effect and orbital Edelstein effect could also occur in our Cu/WO_x structure. In any case, the large SCI efficiency in the Cu/WO_x interface could be applicable to the MESO device. Finally, the Py/Cu/W LSV could have been mistaken for a transparent system, and analyzing the spin diffusion length of W in that way gives similar values as reported in bulk β-W ($\lambda_{\mathrm{W}} = 1.5$ nm). However, we deduce that the SCI occurs at the interface of the Cu and an oxide layer. This all shows that one has to very carefully characterize the interfaces when studying the spin properties of SOM in metallic nanodevices.

7.8 Appendices

7.8.1 The sputter conditions defining the W resistivity

The temperature dependence of the resistivity can give valuable information about the phase of W and/or the quality of the thin film. Figure 7.11 shows the temperature dependence for different sputtering conditions of W. In figures 7.11a to 7.11d, the pressure is changing from 1mTorr to 10 mTorr, while keeping the power constant at 10 W. Figure 7.11a presents a magnitude of the resistivity that compares to the one of the β-phase. Additionally, the signature of the β-phase that is the negative thermal coefficient and the onset of superconductivity at the lowest temperatures is observed. We observe that a pressure increase results in higher resistivities, however, the onset to the superconductive state disappears (figures 7.11c and 7.11d) meaning that the structure most likely gets amorphized or oxidized and β-phase is not stabilized. Therefore, we conclude that a lower pressure is preferable for obtaining β-phase W.

Figure 7.11e plots the resistivity for the sputtering conditions: 3 mTorr, 60 W and the thickness is 10 nm. This resistivity can be compared to figure 7.11b to explore the influence of sputtering with a higher power. In both cases, a similar behaviour is shown, but for 60 W (figure 7.11e) the resistivity is reduced with respect to 10 W (figure 7.11b). The local spin Hall device thrives with high resistivity SOM such that 10 W of power is more desirable at first hand. Note that one should investigate the spin properties to make a solid claim in this regard.

Lastly, figure 7.11f depicts the resistivity for a thin film with a thickness of 20 nm. The sputtering conditions are equal to the thin film in figure 7.11e. The resistivity is lower for the thicker thin film but, more importantly, the thermal coefficient is opposite. The resistivity is decreasing with decreasing temperature and no indication of superconductivity is present. All these are signatures of α-W. This observation is in agreement with the fact that the β-W is more stable in low thickness films about $\leq$ 10 nm on Si/SiO_x substrates [199]. Note that the thickness at which the α-phase starts to dominate over the β-phase is not only related to the deposition technique and condition but is also dependent on the type of substrate [199]. In this study, samples are fabricated on Si/SiO_2 (150 nm) substrates and the sputtering conditios for W are: 3 mTorr and 10 W.

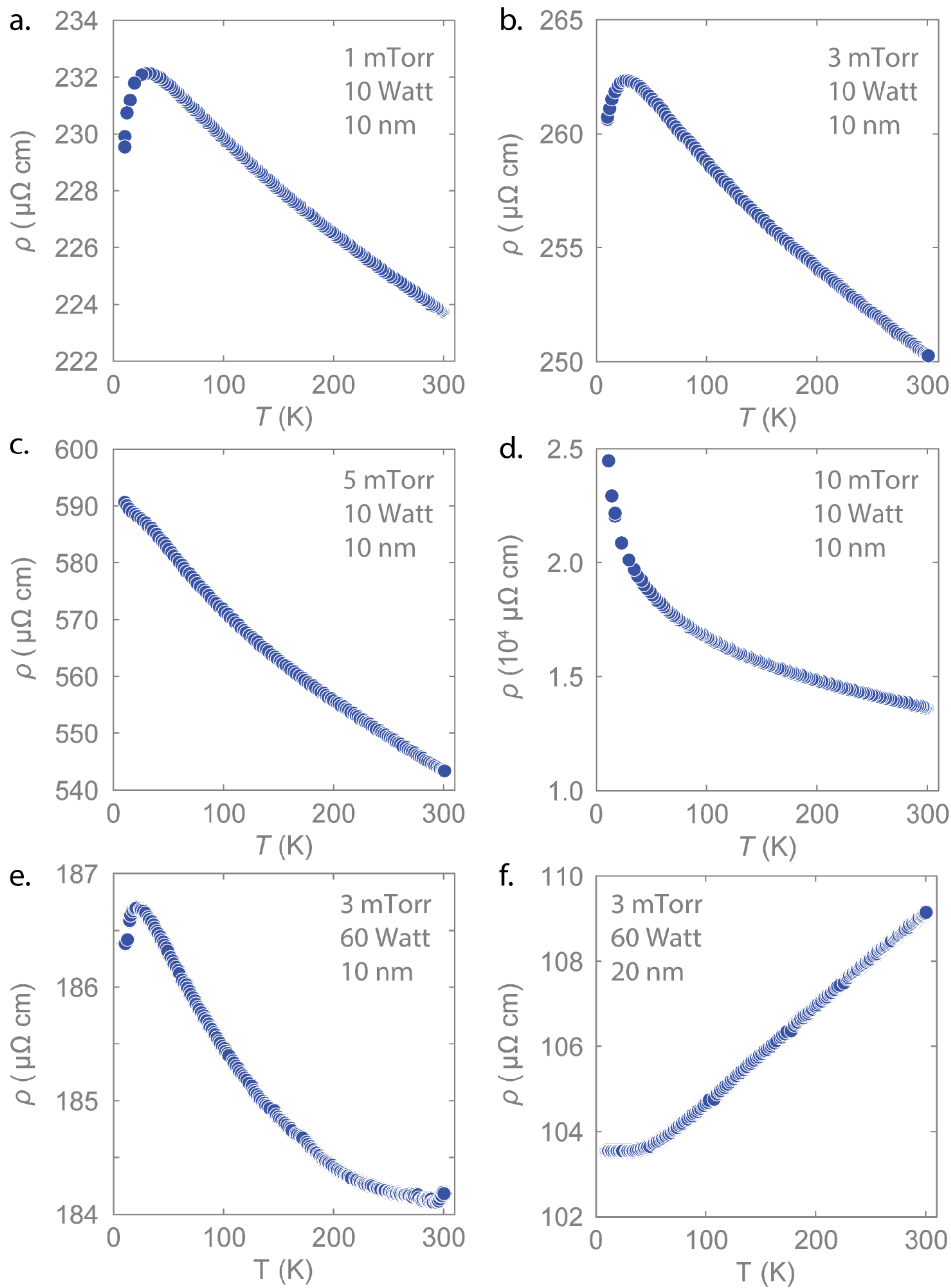

Figure 7.11: The resistivity for different sputtering conditions for W. The resistivity for W thin films with a thickness of 10 nm deposited with a power of 10 W and varying pressure: **a)** 1 mTorr, **b)** 3 mTorr, **c)** 5 mTorr, **d)** 10 mTorr. The resistivity for two W thin films deposited with a pressure of 3 mTorr and a power of 60 W for thin film thicknesses of **e)** 10 nm and **f)** 20 nm.

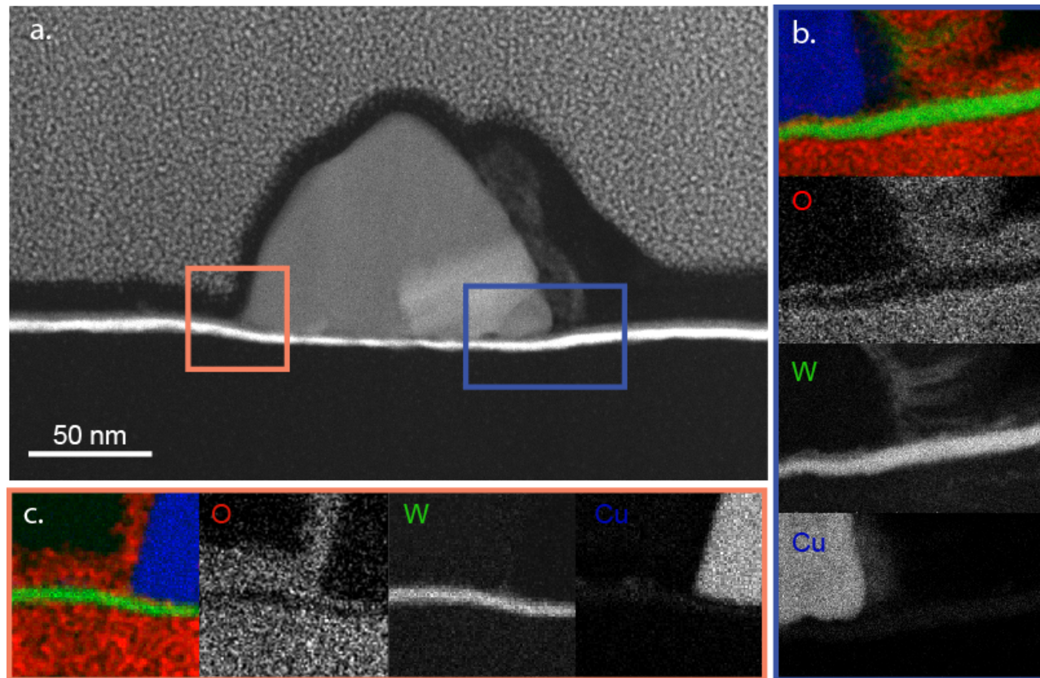

Figure 7.12: TEM image of the Cu/W interface. a) The large overview image shows the LSV cross-section of the transverse cut Cu electrode (gray) and longitudinal cut W electrode (white). **b)** The orange square and **c)** blue square areas where EDAX analyses have been performed. The element analysis identifies O, W, and Cu. Note that the images reveal the presence of O at the Cu/W interface.

7.8.2 TEM characterization of the Cu/W interface

Figure 7.12a present the cross-sectional TEM image of the Cu/W interface. EDAX is used to investigate the regions indicated by the orange and blue squares. The orange square is the same area as mentioned in section 7.3. Figures 7.12b and 7.12c display the observed elements (O, W and Cu) in these orange and blue regions, respectively. Detailed information about the W electrode can be acquired from the TEM images, such as the thickness of the W below the Cu electrode ($t_{\mathrm{W}} \sim 2.8$ nm). This is different from the electrode thickness of the W ($t'_{\mathrm{W}} \sim 4.5$ nm) because of the Ar-ion milling. The natural WO_x on top of the W electrode is about 3 nm.

The EDAX also shows the presence of O at the interface between the Cu and W electrodes. The oxide layer has a thickness of $\sim$ 1.5 nm. During the fabrication of the LSV, Ar-ion milling for WO_x removal combined with *in-situ* sputtering of a thin layer of Cu, should have prevented the interface from oxidizing. All the natural WO_x below the Cu has been removed during the Ar-ion milling as $t_{\mathrm{W}} < t'_{\mathrm{W}}$. Therefore,

the oxidation has taken place during the fast transfer from the ion-miller to the evaporator ~ 3 min. This can be related to several reasons, for example, the *in-situ* sputtered Cu layer is not thick enough or does not grow homogeneously on the W electrode and, therefore, does not fully protect the W from oxidation. Also, thin Cu itself can oxidize. The resolution of the TEM images are not good enough to identify the composition of the oxide layer, but we believe the oxide to be a mixture of W, Cu and O.

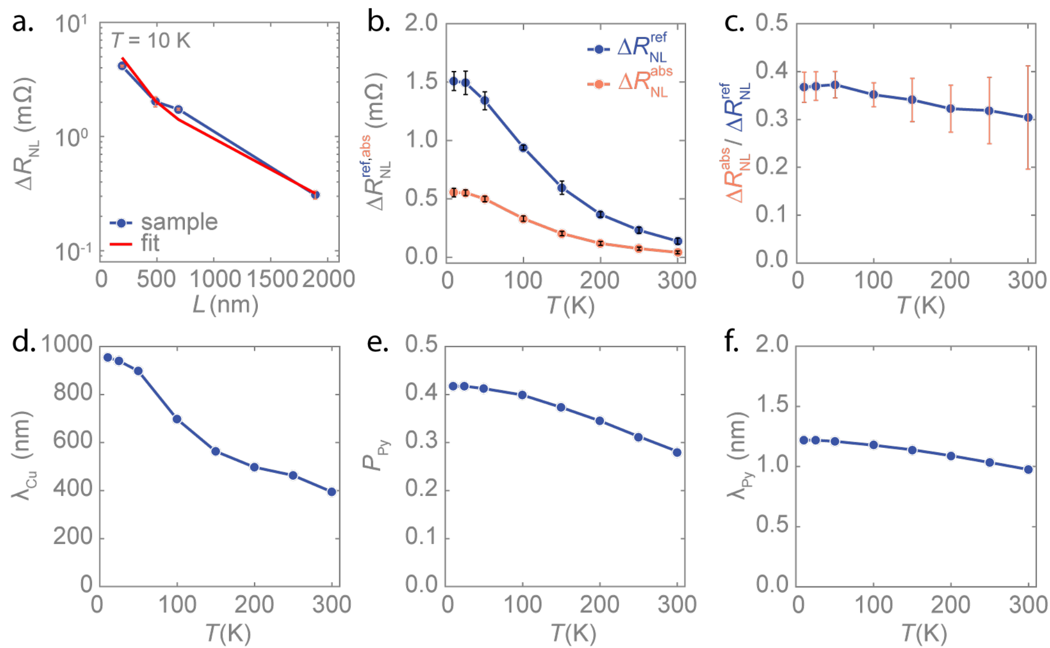

Figure 7.13: The exploration of the spin properties of Cu and Py. a) The non-local spin signal in a Py/Cu LSV for various lengths of the spin transport channel (i.e., the distance between the two Py electrodes). The red line is a fit with equation 3.17. **b)** The temperature dependence of the spin signal of a reference LSV $\Delta R_{\mathrm{NL}}^{\mathrm{ref}}$ (section 3.3.2) and the spin signal of a LSV with a middle Py electrode $\Delta R_{\mathrm{NL}}^{\mathrm{abs}}$ (section 3.3.3). **c)** The ratio of $\Delta R_{\mathrm{NL}}^{\mathrm{ref}}$ and $\Delta R_{\mathrm{NL}}^{\mathrm{abs}}$ which can be fitted to equation 3.30. Iterations of the fit with equation 3.17 and equation 3.30 result in the following spin properties: **d)** the spin diffusion length of the Cu, **e)** the spin polarization of the Py, and **f)** the spin diffusion length of the Py.

7.8.3 The spin properties of Py and Cu

The spin properties of the Py and Cu electrodes need to be known in order to establish the spin properties of a W electrode or, in our case, an oxide interface layer in a Py/Cu/W LSV. The protocol in ref. [204] has been followed to acquire the spin properties of the Py and Cu electrodes. The analysis involves two type of LSVs. The

first one are several conventional Py/Cu LSV (section 3.3.1) with different Py inter-electrode distances L. Figure 7.13a plots the resulting spin signal as a function of L. A fit to equation 3.17 can provide λ_{Cu} and P_{Py} by assuming a reasonable value for λ_{Py}. Secondly, the spin signal from a LSV (section 3.3.3) with a middle electrode of Py is measured and shown in figure 7.13b. The ratio of the two spin signal is presented in figure 7.13c, which is used via equation 3.39 to estimate λ_{Py} for the λ_{Cu} and P_{Py} values extracted from the first experiment. The final parameters, presented in figures 7.13d, 7.13e and 7.13f, come from iterating equation 3.17 and 3.39 several times, until a convergence is achieved. A Py/Cu interface resistance was measured but the spin resistance of the Py/Cu interface was not dominating, therefore we cannot separate the spin absorption of the bulk and the interface. P_{Py} and λ_{Py} are therefore effective values of the system and not necessarily representative of the Py electrode on its own. However, the spin parameters in figure 7.13 suffice for the purpose it has been used in this work, that is, extracting the spin properties of a middle electrode.

7.8.4 Spin diffusion length for bulk spin absorption

An analysis on the spin diffusion length considering different spin absorption scenarios, i.e., different spin sinks, has been performed to identify where the spins are absorbed. Figure 7.14a displays λ_{W} assuming a transparent Cu/W interface in our

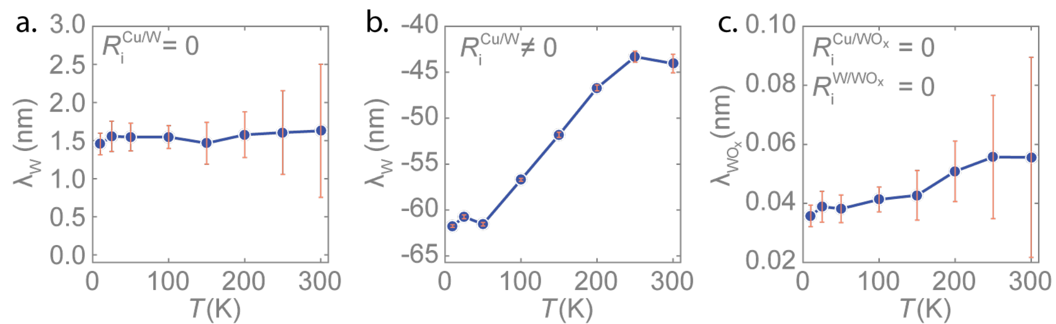

Figure 7.14: The spin diffusion length for three scenarios of bulk spin absorption in the Py/Cu/W LSV. The spin diffusion lengths coming from fitting equation 3.39 to the spin absorption data $\Delta R_{\mathrm{NL}}^{\mathrm{abs}}/\Delta R_{\mathrm{NL}}^{\mathrm{ref}}$ presented in figure 7.6. The spin diffusion length is determined for **a)** Spin absorption by the W electrode with a transparent Cu/W interface ($R_{\mathrm{i}}^{\mathrm{Cu/W}} = 0$); **b)** Spin absorption by the W electrode with a resistive Cu/W interface where $R_{\mathrm{i}}^{\mathrm{Cu/W}}$ is as presented in figure 7.4d; **c)** Spin absorption by the oxide interface layer with a transparent Cu/WO$_{\mathrm{x}}$ and W/WO$_{\mathrm{x}}$ interface ($R_{\mathrm{i}}^{\mathrm{Cu/WO_x}} = R_{\mathrm{i}}^{\mathrm{W/WO_x}} = 0$) and a resistivity $\rho_{\mathrm{WO_x}}$ (figure 7.5).

device. The signal is comparable to reported values for Pt and Ta [76, 77]. However, we have combined interface measurements and 3D FEM simulations to show that we have an interface resistance of several Ω at the Cu/W interface (section 7.3). In this scenario, equation 3.39 gives a negative λ_{W} as presented in figure 7.14b. A negative λ_{W} is not a physical quantity for a spin diffusion length. We have taken a close look at TEM images of the interface (figure 7.12) and find a oxide layer between the Cu and W electrode. This interface layer is incorporated to the 3D FEM simulations resulting in a resistivity (figure 7.5) that can be inserted in equation 3.39 in order to investigate spin absorption by the "bulk" oxide layer. The resulting $\lambda_{\mathrm{WO_x}} \sim 0.04$ nm, which is shorter than the interatomic distance in transition metal oxides, concluding that the spin absorption occurs at the Cu/$\mathrm{WO_x}$ interface.

7.8.5 3D FEM for shunting in the Cu/$\mathrm{WO_x}$/W structure

The 3D FEM model for shunting in two metallic electrodes is discussed in section 4.3.2. However, the presence of an oxide layer at the interface of the two metallic electrodes, as is the case for our Cu and W electrodes, indicated that the model has to be adapted while this can significantly alter the electrical shunting. Figure 7.15a shows the geometrical model with a tri-layer of Cu, $\mathrm{WO_x}$ and W and the mesh that is used for the 3D FEM simulations. The widths and thicknesses of the electrodes are obtained from SEM (figure 7.4a) and TEM (figure 7.12) images, respectively. Figure 7.15b presents the electrical potential as simulated by means of the 3D FEM that is created in the structure when a in-plane line current is applied to the Cu/$\mathrm{WO_x}$ interface. The line current source is blue and the ground line is located at the opposite side (cannot be seen from this angle) . Figure 7.15c shows the x-component of the charge current density flow though the Cu, $\mathrm{WO_x}$ and W layers. It can be seen that most of the current density passes though the Cu, which is also reflected in the shunting factor x_{Cu} (figure 7.8a).

A final comment on these simulations. We consider that Q_{c} flows through the oxide interface, that is, a current density source on one side of the oxide interface and a ground on the other side (figure 7.7), while, in reality, the SCI generates current at every point of the Cu/$\mathrm{WO_x}$ interface. Also, in the case of the bulk SCI, the current generation would be within a volume defined by the interface area and the effective thickness over which the SCI takes place. However, the implementation of this mechanism would make the simulation significantly more complicated. We have tested that the method we have adopted agrees fairly well with a more complicated and time consuming full 3D FEM simulation of the ISHE including the spin diffusion model as explained in Ref. [157].

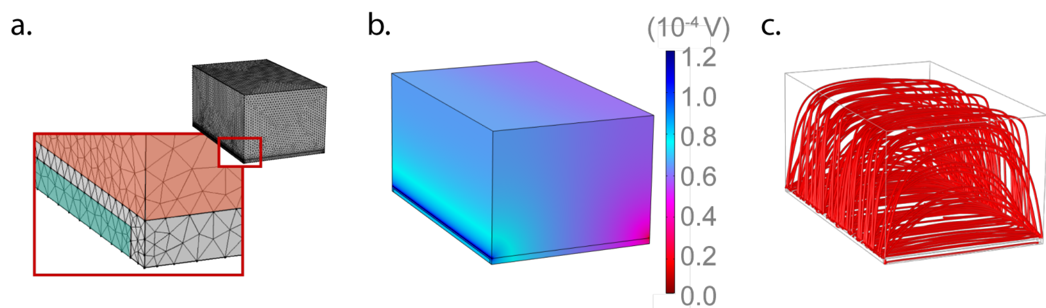

Figure 7.15: Details on the 3D FEM for shunting in the Cu/WO_x/W structure. a) 3D FEM geometry and mesh where the Cu, WO_x, and W layers are shown in orange, grey, and turquoise, respectively. **b)** Electrical potential in the structure when applying a line current source Q_c appearing in blue at the Cu/WO_x interface. The ground (line) is placed on the other side of the Cu electrode appearing in pink. **c)** The x-component distribution of the charge current density in the structure that is used to obtain the shunting.

Chapter 8

The future of the MESO-logic device

This thesis presents the first steps for the optimization of the magnetic-state readout component for the envisioned MESO-logic device. We established that reducing the device dimension of FM/SOM nanostructured devices leads to enhancement of the output current and voltage and that the materials system efficiency can be optimized by proper materials benchmarking (**chapter 5**). Even more, we showed that spurious effects in the device due to the local configuration can be avoided by properly designing the FM and SOM electrodes and, even more, the AHE can be used to increase the readout signals (**chapter 6**). Lastly, we demonstrate that the interface properties and interfacial SCI have to be carefully considered when studying spin transport in metallic devices. Additionally, such interface can display large SCI and might be applicable to the MESO-logic devices (**chapter 7**). The required output signals for the cascaded gates allowing logic operations with the MESO devices are not achieved yet. We did obtain a deeper understanding of the local spin Hall device and how to improve the output signals. Here, we discuss briefly some of these improvements and ideas that will define the goals for future research.

Regarding the materials benchmarking, materials system with large SCI efficiency and high resistivities seems to be promising for enhancement of the output signals. In this thesis, we have mentioned other metallic materials such as β-phase Ta or W. In the local CoFe/Ta devices, we observed indeed a significant enhancement of the output signals compared to the local CoFe/Pt device. We had to include a resistive layer (AlO_x) to overcome the conductivity mismatch between the CoFe and Ta in this device. Both, the change of SOM materials with higher SCI efficiency and the introduction of an interfacial layer contribute to the gain of generated output current and voltage. Further studies on the optimization of the resistive interfacial layers, will tell us if the required output voltage can be reached by the SO node via this approach.

However, 2D systems with interfacial SCI might be even more attractive. Using a LSV and the non-local spin Hall technique, we achieved, in a non-engineered highly resistive oxide/Cu interface, a spin-charge conductivity that is higher than the one in a comparable Cu/BiO_x system as well as the spin Hall conductivity of Pt. A systematic study on interfacial SCI in engineered NM/oxide systems can lead to even higher spin-charge conductivities such as $SrTiO_3$/Al which has been proven to own large and gate-tunable SCI in its 2DEG [120]. Other interesting systems with interfacial SCI are oxide/oxide interface [118, 205]. KTO_3/AlO_x is recently reported to attain a SCI efficiency that is among the highest reported in literature [121]. Also, the surface of topological insulators such as α-Sn or Bi_2Se_3 can be good candidates

[128, 170]. The local spin-orbit readout devices could benefit from implementation of such systems with interfacial SCI.

Proceeding with materials systems, large SCI efficiencies are also observed in graphene-based van der Waals heterostructures [135, 172, 173]. Even more, the reduction in the crystal symmetries of these 2D heterostructure allows detecting SCI of different spin polarizations. This opens the door for spin-orbit magnetic-state readout in ferromagnets with out-of-plane magnetization which is also mentioned in a recently published patent by Intel [206].

To continue with the role of the ferromagnet in the local spin Hall device, we have seen that the PHE does not influence the magnetic-state readout but that the AHE in the FM can negatively or positively influence the output signals depending of the design of the dimensional proportions of the electrodes in the local spin Hall device. One could think to design the device in such a way that the AHE contributes positively to output signals. Or a device that only depends on SCI via the AHE could be envisioned making the SOM redundant, even tough the AHE does not present scalability with the electrode width or length. A MESO logic device including two paramagnets for the magnetic-state readout is proposed [207]. Also, a fully magnetic state element for logic operations, a variable resistive magnetic device, has been patented [208].

An other step that needed to be taken was the implementation of the local spin Hall device in a MESO device, meaning to connect our readout device to the writing device, hence ME node [209]. We experimentally demonstrate for the first time a functional MESO device at room temperature, integrating both the SO and ME nodes in the same device [210]. The CoFe electrode is in direct contact with a $BiFeO_3$ ME layer. A voltage pulse switching the $BiFeO_3$ ferroelectric polarization and (anti) ferromagnetic state, reverses the CoFe magnetization through interfacial exchange coupling. The magnetic state is read by the local spin Hall device and the two logic states are unambiguously detected for several switching cycles.

We have made great progress towards the realization of the MESO logic device during this thesis, even though we did not reach the output current and voltage that can drive cascaded gates with the MESO devices. We provide a guideline for further improvement of the output signals including downscaling of the device dimensions, implementation of other materials system with large SCI efficiency and high resistivities, and adjusting the design by introducing a highly resistive interface. Further experiments are required to demonstrate the use of our device as a

current source for driving spin-logic circuits, but we anticipate that a MESO-logic device is a feasible solution for more energy efficient computing.

Bibliography

1. Ferain, I., Colinge, C. & Colinge, J.-P. Multigate transistors as the future of classical metal–oxide–semiconductor field-effect transistors. *Nature* **479,** 310–316 (2011).
2. Auth, C. *et al.* A 10nm high performance and low-power CMOS technology featuring 3rd generation FinFET transistors, Self-Aligned Quad Patterning, contact over active gate and cobalt local interconnects. *2017 IEEE International Electron Devices Meeting (IEDM),* 29.1.1–29.1.4 (2017).
3. Moore, G. Cramming more components onto integrated circuits. *Electronics* **38,** 114–117 (1965).
4. Dennard, R. *et al.* Design of ion-implanted MOSFET's with very small physical dimensions. *IEEE Journal of Solid-State Circuits* **9,** 256–268 (1974).
5. Holt, W. M. *1.1 Moore's law: A path going forward* in *2016 IEEE International Solid-State Circuits Conference (ISSCC)* (2016), 8–13.
6. Nikonov, D. E. & Young, I. A. Benchmarking of Beyond-CMOS Exploratory Devices for Logic Integrated Circuits. *IEEE Journal on Exploratory Solid-State Computational Devices and Circuits* **1,** 3–11 (2015).
7. Manipatruni, S., Nikonov, D. E. & Young, I. A. Beyond CMOS computing with spin and polarization. *Nature Physics* **14,** 338 (2018).
8. Alexander, M., Thomas, W., Viktor, S. & Siegfried, S. CMOS-compatible spintronic devices: a review. *Semiconductor Science and Technology* **31,** 113006 (2016).
9. Dieny, B. *et al.* Opportunities and challenges for spintronics in the microelectronics industry. *Nature Electronics* **3,** 446–459 (2020).
10. Baibich, M. N. *et al.* Giant Magnetoresistance of (001)Fe/(001)Cr Magnetic Superlattices. *Physical Review Letters* **61,** 2472–2475 (1988).

11. Binasch, G., Grünberg, P., Saurenbach, F. & Zinn, W. Enhanced magnetoresistance in layered magnetic structures with antiferromagnetic interlayer exchange. *Physical Review B* **39,** 4828–4830 (1989).
12. Julliere, M. Tunneling between ferromagnetic films. *Physics Letters A* **54,** 225–226 (1975).
13. Moodera, J. S., Kinder, L. R., Wong, T. M. & Meservey, R. Large Magnetoresistance at Room Temperature in Ferromagnetic Thin Film Tunnel Junctions. *Physical Review Letters* **74,** 3273–3276 (1995).
14. Parkin, S. S. *et al.* Giant tunnelling magnetoresistance at room temperature with MgO (100) tunnel barriers. *Nature Materials* **3,** 862–867 (2004).
15. Yuasa, S., Nagahama, T., Fukushima, A., Suzuki, Y. & Ando, K. Giant room-temperature magnetoresistance in single-crystal Fe/MgO/Fe magnetic tunnel junctions. *Nature Materials* **3,** 868–871 (2004).
16. Yuasa, S. Giant tunneling magnetoresistance in MgO-based magnetic tunnel junctions. *Journal of the Physical Society of Japan* **77,** 031001 (2008).
17. Parkin, S. S. P. *Spin Dependent Transport in Magnetic nanostructures* (eds Maekawa, S. & Shinjo, T.) (Taylor and Francis, 2002).
18. Chappert, C., Fert, A. & Dau, F. N. V. The emergence of spin electronics in data storage. *Nature Materials* **6,** 813–823 (2007).
19. Engel, B. *et al.* A 4-Mb toggle MRAM based on a novel bit and switching method. *IEEE Transactions on Magnetics* **41,** 132–136 (2005).
20. Slonczewski, J. Current-driven excitation of magnetic multilayers. *Journal of Magnetism and Magnetic Materials* **159,** L1–L7 (1996).
21. Berger, L. Emission of spin waves by a magnetic multilayer traversed by a current. *Physical Review B* **54,** 9353–9358 (1996).
22. *STT-MRAM: Introduction and market status* https://www.mram-info.com/stt-mram. (accessed: 08.12.2021).
23. Bhatti, S. *et al.* Spintronics based random access memory: a review. *Materials Today* **20,** 530–548 (2017).
24. Barla, P., Kumar Joshi, V. & Bhat, S. Spintronic devices: a promising alternative to CMOS devices. *Journal of Computational Electronics* **20,** 805–837 (2021).
25. Manchon, A. *et al.* Current-induced spin-orbit torques in ferromagnetic and antiferromagnetic systems. *Review Modern Physics* **91,** 035004 (2019).

26. Miron, I. M. *et al.* Perpendicular switching of a single ferromagnetic layer induced by in-plane current injection. *Nature* **476,** 189–193 (2011).
27. Manipatruni, S. *et al.* Scalable energy-efficient magnetoelectric spin–orbit logic. *Nature* **565** (2019).
28. Manipatruni, S. *et al.* Voltage control of unidirectional anisotropy in ferromagnet-multiferroic system. *Science Advances* **4,** eaat4229 (2018).
29. Lu, X. *et al.* Mechanical-force-induced non-local collective ferroelastic switching in epitaxial lead-titanate thin films. *Nature Communications* **10,** 3951 (2019).
30. Chu, Y.-H. *et al.* Electric-field control of local ferromagnetism using a magnetoelectric multiferroic. *Nature Materials* **7,** 478–482 (2008).
31. Uhlenbeck, G. & Goudsmit, S. Benchmarking of Beyond-CMOS Exploratory Devices for Logic Integrated Circuits. *Die Naturwissenschaften* **13,** 953–954 (1925).
32. Gerlach, W. & Stern, O. Der experimentelle Nachweis der Richtungsquantelung im Magnetfeld. *Physik* **9,** 349–352 (1922).
33. Feynman, R. P., Leighton, R. B. & Sands, M. *The Feynman lectures on physics, Vol. III: The new millennium edition: Quantum Mechanics* (Hachette UK, 2015).
34. Griffiths, D. J. *Introduction to Quantum Mechanics* 2nd, 154–156 (Pearson Prentice Hall, 2004).
35. Mott, N. The electrical conductivity of transition metals. *Proceedings of the Royal Society A: Mathematical, Physical and Engineering Sciences* **153,** 699–717 (1936).
36. Fert, A. & Campbell, I. Two-current conduction in nickel. *Physical Review Letters* **21,** 1190 (1968).
37. Valet, T. & Fert, A. Theory of the perpendicular magnetoresistance in magnetic multilayers. *Physical Review B* **48,** 7099–7113 (1993).
38. Elliott, R. Spin-Orbit Coupling in Band Theory—Character Tables for Some" Double" Space Groups. *Physical Review* **96,** 280 (1954).
39. Yafet, Y. in *Solid State Physics* 1–98 (Elsevier, 1963).
40. Sasaki, T. *et al.* Temperature dependence of spin diffusion length in silicon by Hanle-type spin precession. *Applied Physics Letters* **96,** 122101 (2010).
41. Zhou, Y. *et al.* Electrical spin injection and transport in germanium. *Physical Review B* **84,** 125323 (2011).

42. Villamor, E., Isasa, M., Hueso, L. E. & Casanova, F. Contribution of defects to the spin relaxation in copper nanowires. *Physical Review B* **87,** 094417 (2013).
43. Jedema, F., Nijboer, M., Filip, A. & Van Wees, B. Spin injection and spin accumulation in all-metal mesoscopic spin valves. *Physical Review B* **67,** 085319 (2003).
44. Mihajlović, G., Pearson, J., Bader, S. & Hoffmann, A. Surface spin flip probability of mesoscopic Ag wires. *Physical Review Letters* **104,** 237202 (2010).
45. Isasa, M. *et al.* Spin transport enhancement by controlling the Ag growth in lateral spin valves. *Journal of Physics D: Applied Physics* **48,** 215003 (2015).
46. Idzuchi, H., Fukuma, Y., Wang, L. & Otani, Y. Spin relaxation mechanism in silver nanowires covered with MgO protection layer. *Applied Physics Letters* **101,** 022415 (2012).
47. Ryu, J., Kohda, M. & Nitta, J. Observation of the D'yakonov-Perel'spin relaxation in single-crystalline Pt thin films. *Physical Review Letters* **116,** 256802 (2016).
48. Gamou, H., Ryu, J., Kohda, M. & Nitta, J. Different spin relaxation mechanisms between epitaxial and polycrystalline Ta thin films. *Applied Physics Express* **10,** 023003 (2017).
49. Dyakonov, M. & Perel, V. Spin orientation of electrons associated with the interband absorption of light in semiconductors. *Soviet Journal of Experimental and Theoretical physics* **33,** 1053 (1971).
50. Dyakonov, M. & Kachorovskii, V. Spin relaxation of two-dimensional electrons in noncentrosymmetric semiconductors. *Soviet Physics Semiconductors* **20,** 110–116 (1986).
51. Kikkawa, J. & Awschalom, D. Resonant spin amplification in n-type GaAs. *Physical Review Letters* **80,** 4313 (1998).
52. Koo, H. C. *et al.* Electrical spin injection and detection in an InAs quantum well. *Applied Physics Letters* **90,** 022101 (2007).
53. Hall, E. On a New Action of the Magnet on Electric Currents. *American Journal of Mathematics* **2,** 278–292 (1879).
54. Hall, E. XVIII. On the "Rotational Coefficient" in nickel and cobalt. *The London, Edinburgh, and Dublin Philosophical Magazine and Journal of Science* **12,** 157–172 (1881).
55. Karplus, R. & Luttinger, J. M. Hall Effect in Ferromagnetics. *Physical Review* **95,** 1154–1160 (1954).

56. Sinova, J., Valenzuela, S. O., Wunderlich, J., Back, C. H. & Jungwirth, T. Spin Hall effects. *Review Modern Physics* **87,** 1213–1260 (2015).
57. Dyakonov, M. & Perel, V. Current-induced spin orientation of electrons in semiconductors. *Physics Letters A* **35,** 459–460 (1971).
58. Mott, N. F. & Bohr, N. H. D. The scattering of fast electrons by atomic nuclei. *Proceedings of the Royal Society of London. Series A, Containing Papers of a Mathematical and Physical Character* **124,** 425–442 (1929).
59. Hirsch, J. E. Spin Hall Effect. *Physical Review Letters* **83,** 1834–1837 (1999).
60. Zhang, S. Spin Hall Effect in the Presence of Spin Diffusion. *Physical Review Letters* **85,** 393–396 (2000).
61. Murakami, S., Nagaosa, N. & Zhang, S.-C. Dissipationless Quantum Spin Current at Room Temperature. *Science* **301,** 1348–1351 (2003).
62. Sinova, J. *et al.* Universal Intrinsic Spin Hall Effect. *Physical Review Letters* **92,** 126603 (2004).
63. Kato, Y. K., Myers, R. C., Gossard, A. C. & Awschalom, D. D. Observation of the Spin Hall Effect in Semiconductors. *Science* **306,** 1910–1913 (2004).
64. Wunderlich, J., Kaestner, B., Sinova, J. & Jungwirth, T. Experimental Observation of the Spin-Hall Effect in a Two-Dimensional Spin-Orbit Coupled Semiconductor System. *Physical Review Letters* **94,** 047204 (2005).
65. Saitoh, E., Ueda, M., Miyajima, H. & Tatara, G. Conversion of spin current into charge current at room temperature: Inverse spin-Hall effect. *Applied Physics Letters* **88,** 182509 (2006).
66. Valenzuela, S. O. & Tinkham, M. Direct electronic measurement of the spin Hall effect. *Nature* **442,** 176–179 (2006).
67. Kimura, T., Otani, Y., Sato, T., Takahashi, S. & Maekawa, S. Room-Temperature Reversible Spin Hall Effect. *Physical Review Letters* **98,** 156601 (2007).
68. Hoffmann, A. Spin Hall Effects in Metals. *IEEE Transactions on Magnetics* **49,** 5172–5193 (2013).
69. Sagasta, E. *Spin-to-charge conversion in systems with spin-orbit coupling* PhD thesis (University of the Basque Country, 2019), p. 20.
70. Morota, M. *et al.* Indication of intrinsic spin Hall effect in $4d$ and $5d$ transition metals. *Physical Review B* **83,** 174405 (2011).
71. Stamm, C. *et al.* Magneto-Optical Detection of the Spin Hall Effect in Pt and W Thin Films. *Physical Review Letters* **119,** 087203 (2017).

72. Zhang, W., Han, W., Jiang, X., Yang, S.-H. & Parkin, S. Role of transparency of platinum-ferromagnet interface in determining intrinsic magnitude of spin Hall effect. *Nature Physics* **11,** 496–502 (2015).
73. Pham, V. T. *et al.* Evidence of interfacial asymmetric spin scattering at ferromagnet-Pt interfaces. *Physical Review B* **103,** L201403 (2021).
74. Rojas-Sánchez, J.-C. *et al.* Spin Pumping and Inverse Spin Hall Effect in Platinum: The Essential Role of Spin-Memory Loss at Metallic Interfaces. *Physical Review Letters* **112,** 106602 (2014).
75. Pai, C.-F., Ou, Y., Vilela-Leão, L. H., Ralph, D. & Buhrman, R. Dependence of the efficiency of spin Hall torque on the transparency of Pt/ferromagnetic layer interfaces. *Physical Review B* **92,** 064426 (2015).
76. Sagasta, E. *et al.* Tuning the spin Hall effect of Pt from the moderately dirty to the superclean regime. *Physical Review B* **94,** 060412 (2016).
77. Sagasta, E. *et al.* Unveiling the mechanisms of the spin Hall effect in Ta. *Physical Review B* **98,** 060410 (2018).
78. Tian, Y., Ye, L. & Jin, X. Proper Scaling of the Anomalous Hall Effect. *Physical Review Letters* **103,** 087206 (2009).
79. Zimmermann, B. *et al.* Skew scattering in dilute ferromagnetic alloys. *Physical Review B* **90,** 220403 (2014).
80. Jungwirth, T., Niu, Q. & MacDonald, A. H. Anomalous Hall Effect in Ferromagnetic Semiconductors. *Physical Review Letters* **88,** 207208 (2002).
81. Haldane, F. D. M. Berry Curvature on the Fermi Surface: Anomalous Hall Effect as a Topological Fermi-Liquid Property. *Physical Review Letters* **93,** 206602 (2004).
82. Guo, G. Y., Murakami, S., Chen, T.-W. & Nagaosa, N. Intrinsic Spin Hall Effect in Platinum: First-Principles Calculations. *Physical Review Letters* **100,** 096401 (2008).
83. Tanaka, T. *et al.* Intrinsic spin Hall effect and orbital Hall effect in $4d$ and $5d$ transition metals. *Physical Review B* **77,** 165117 (2008).
84. Nagaosa, N., Sinova, J., Onoda, S., MacDonald, A. H. & Ong, N. P. Anomalous Hall effect. *Review Modern Physics* **82,** 1539–1592 (2010).
85. Mott, N. F. The polarisation of electrons by double scattering. *Proceedings of the Royal Society of London. A: Mathematical, Physical and Engineering Sciences* **135,** 429–458 (1932).

86. Smit, J. The spontaneous Hall effect in ferromagnetics I. *Physica* **21,** 877–887 (1955).
87. Smit, J. The spontaneous Hall effect in ferromagnetics II. *Physica* **24,** 39–51 (1958).
88. Berger, L. Side-Jump Mechanism for the Hall Effect of Ferromagnets. *Physical Review B* **2,** 4559–4566 (1970).
89. Gradhand, M. *et al.* Perfect alloys for spin Hall current-induced magnetization switching. *Spin* **2,** 1250010 (2012).
90. Niimi, Y. *et al.* Extrinsic Spin Hall Effect Induced by Iridium Impurities in Copper. *Physical Review Letters* **106,** 126601 (2011).
91. Niimi, Y. *et al.* Giant Spin Hall Effect Induced by Skew Scattering from Bismuth Impurities inside Thin Film CuBi Alloys. *Physical Review Letters* **109,** 156602 (2012).
92. Niimi, Y. *et al.* Extrinsic spin Hall effects measured with lateral spin valve structures. *Physical Review B* **89,** 054401 (2014).
93. Obstbaum, M. *et al.* Tuning Spin Hall Angles by Alloying. *Physical Review Letters* **117,** 167204 (2016).
94. Ramaswamy, R. *et al.* Extrinsic Spin Hall Effect in $\mathrm{Cu}_{1-x}\mathrm{Pt}_x$. *Physical Review Applied* **8,** 024034 (2017).
95. Laczkowski, P. *et al.* Large enhancement of the spin Hall effect in Au by side-jump scattering on Ta impurities. *Physical Review B* **96,** 140405 (2017).
96. Alves-Santos, O. *et al.* Giant spin-charge conversion driven by nanoscopic particles of Ag in Pt. *Physical Review B* **96,** 060408 (2017).
97. Sangiao, S. *et al.* Anomalous Hall effect in Fe (001) epitaxial thin films over a wide range in conductivity. *Physical Review B* **79,** 014431 (2009).
98. Dresselhaus, G. Spin-Orbit Coupling Effects in Zinc Blende Structures. *Physical Review* **100,** 580–586 (1955).
99. Vas'ko, F. Spin splitting in the spectrum of two-dimensional electrons due to the surface potential. *Soviet Journal of Experimental and Theoretical physics* **30,** 541 (1979).
100. Bychkov, Y. A. & Rashba, E. I. Properties of a 2d electron gas with lifted spectral degeneracy. *Journal of Experimental and Theoretical Physics letters* **39,** 78–81 (1984).

101. Bychkov, Y. A. & Rashba, E. I. Oscillatory effects and the magnetic susceptibility of carriers in inversion layers. *Journal of Physics C: Solid State Physics* **17,** 6039–6045 (19804).

102. LaShell, S., McDougall, B. A. & Jensen, E. Spin Splitting of an Au(111) Surface State Band Observed with Angle Resolved Photoelectron Spectroscopy. *Physical Review Letters* **77,** 3419–3422 (1996).

103. Edelstein, V. Spin polarization of conduction electrons induced by electric current in two-dimensional asymmetric electron systems. *Solid State Communications* **73,** 233–235 (1990).

104. Rojas-Sánchez, J.-C. *et al.* Spin-to-charge conversion using Rashba coupling at the interface between non-magnetic materials. *Nature Communications* **4,** 2944 (2013).

105. Zhang, H. J. *et al.* Charge-to-Spin Conversion and Spin Diffusion in Bi/Ag Bilayers Observed by Spin-Polarized Positron Beam. *Physical Review Letters* **114,** 166602 (2015).

106. Matsushima, M. *et al.* Quantitative investigation of the inverse Rashba-Edelstein effect in Bi/Ag and Ag/Bi on YIG. *Applied Physics Letters* **110,** 072404 (2017).

107. Sangiao, S. *et al.* Control of the spin to charge conversion using the inverse Rashba-Edelstein effect. *Applied Physics Letters* **106,** 172403 (2015).

108. Jungfleisch, M. B. *et al.* Interface-driven spin-torque ferromagnetic resonance by Rashba coupling at the interface between nonmagnetic materials. *Physical Review B* **93,** 224419 (2016).

109. Nomura, A., Tashiro, T., Nakayama, H. & Ando, K. Temperature dependence of inverse Rashba-Edelstein effect at metallic interface. *Applied Physics Letters* **106,** 212403 (2015).

110. Isasa, M. *et al.* Origin of inverse Rashba-Edelstein effect detected at the Cu/Bi interface using lateral spin valves. *Physical Review B* **93,** 014420 (2016).

111. Pham, V. T. *et al.* Large spin-charge interconversion induced by interfacial spin-orbit coupling in a highly conducting all-metallic system. *Physical Review B* **104,** 184410 (2021).

112. Isshiki, H., Muduli, P., Kim, J., Kondou, K. & Otani, Y. Phenomenological model for the direct and inverse Edelstein effects. *Physical Review B* **102,** 184411 (2020).

113. Kondou, K., Tsai, H., Isshiki, H. & Otani, Y. Efficient spin current generation and suppression of magnetic damping due to fast spin ejection from nonmagnetic metal/indium-tin-oxide interfaces. *APL Materials* **6,** 101105 (2018).

114. Karube, S., Kondou, K. & Otani, Y. Experimental observation of spin-to-charge current conversion at non-magnetic metal/Bi_2O_3 interfaces. *Applied Physics Express* **9,** 033001 (2016).

115. Tsai, H., Karube, S. & Kondou, K. Clear variation of spin splitting by changing electron distribution at non-magnetic metal/Bi_2O_3 interfaces. *Scientific reports* **8,** 5564 (2018).

116. Sanz-Fernández, C. *et al.* Quantification of interfacial spin-charge conversion in hybrid devices with a metal/insulator interface. *Applied Physics Letters* **117,** 142405 (2020).

117. Johansson, A., Göbel, B., Henk, J., Bibes, M. & Mertig, I. Spin and orbital Edelstein effects in a two-dimensional electron gas: Theory and application to $\mathrm{SrTiO_3}$ interfaces. *Physical Review Research* **3,** 013275 (2021).

118. Lesne, E. *et al.* Highly efficient and tunable spin-to-charge conversion through Rashba coupling at oxide interfaces. *Nature Materials* **15,** 1261–1266 (2016).

119. Song, Q. *et al.* Observation of inverse Edelstein effect in Rashba-split 2DEG between $SrTiO_3$ and $LaAlO_3$ at room temperature. *Science Advances* **3,** e1602312 (2017).

120. Vaz, D. C. *et al.* Mapping spin–charge conversion to the band structure in a topological oxide two-dimensional electron gas. *Nature Materials* **18,** 1187–1193 (2019).

121. Vicente-Arche, L. M. *et al.* Spin–Charge Interconversion in $KTaO_3$ 2D Electron Gases. *Advanced Materials* **33,** 2102102 (2021).

122. Kondou, K. *et al.* Fermi-level-dependent charge-to-spin current conversion by Dirac surface states of topological insulators. *Nature Physics* **12,** 1027–1031 (2016).

123. Soumyanarayanan, A., Reyren, N., Fert, A. & Panagopoulos, C. Emergent phenomena induced by spin-orbit coupling at surfaces and interfaces. *Nature* **539,** 509–517 (2016).

124. Hou, D. *et al.* Interface induced inverse spin Hall effect in bismuth/permalloy bilayer. *Applied Physics Letters* **101,** 042403 (2012).

125. Zhou, X., Tang, M., Fan, X. L., Qiu, X. P. & Zhou, S. M. Disentanglement of bulk and interfacial spin Hall effect in ferromagnet/normal metal interface. *Physical Review B* **94,** 144427 (2016).

126. Li, S., Shen, K. & Xia, K. Interfacial spin Hall effect and spin swapping in Fe|Au bilayers from first principles. *Physical Review B* **99,** 134427 (2019).

127. Freimuth, F., Blügel, S. & Mokrousov, Y. Direct and inverse spin-orbit torques. *Physical Review B* **92,** 064415 (2015).

128. Rojas-Sánchez, J.-C. *et al.* Spin to Charge Conversion at Room Temperature by Spin Pumping into a New Type of Topological Insulator: α-Sn Films. *Physical Review Letters* **116,** 096602 (2016).

129. Amin, V. P., Zemen, J. & Stiles, M. D. Interface-Generated Spin Currents. *Physical Review Letters* **121,** 136805 (2018).

130. Tokatly, I. V., Krasovskii, E. E. & Vignale, G. Current-induced spin polarization at the surface of metallic films: A theorem and an ab initio calculation. *Physical Review B* **91,** 035403 (2015).

131. Amin, V. P. & Stiles, M. D. Spin transport at interfaces with spin-orbit coupling: Phenomenology. *Physical Review B* **94,** 104420 (2016).

132. Amin, V. P. & Stiles, M. D. Spin transport at interfaces with spin-orbit coupling: Formalism. *Physical Review B* **94,** 104419 (2016).

133. Linder, J. & Yokoyama, T. Spin Current in Generic Hybrid Structures due to Interfacial Spin-Orbit Scattering. *Physical Review Letters* **106,** 237201 (2011).

134. Borge, J. & Tokatly, I. V. Boundary conditions for spin and charge diffusion in the presence of interfacial spin-orbit coupling. *Physical Review B* **99,** 241401 (2019).

135. Safeer, C. *et al.* Room-temperature spin Hall effect in graphene/$MoSO_2$ van der Waals heterostructures. *Nano Letters* **19,** 1074–1082 (2019).

136. Galceran, R. *et al.* Control of spin–charge conversion in van der Waals heterostructures. *APL Materials* **9,** 100901 (2021).

137. Žutić, I., Matos-Abiague, A., Scharf, B., Dery, H. & Belashchenko, K. Proximitized materials. *Materials Today* **22,** 85–107 (2019).

138. Rojas-Sánchez, J.-C. & Fert, A. Compared Efficiencies of Conversions between Charge and Spin Current by Spin-Orbit Interactions in Two- and Three-Dimensional Systems. *Physical Review Applied* **11,** 054049 (2019).

139. Kim, J. *et al.* Nontrivial torque generation by orbital angular momentum injection in ferromagnetic-metal/$\mathrm{Cu/Al_2O_3}$ trilayers. *Physical Review B* **103,** L020407 (2021).

140. Bass, J. & Pratt, W. P. Spin-diffusion lengths in metals and alloys, and spin-flipping at metal/metal interfaces: an experimentalist's critical review. *Journal of Physics: Condensed Matter* **19,** 183201 (2007).

141. Han, W., Kawakami, R. K., Gmitra, M. & Fabian, J. Graphene spintronics. *Nature Nanotechnology* **9,** 794–807 (2014).

142. Han, W., Otani, Y. & Maekawa, S. Quantum materials for spin and charge conversion. *npj Quantum Materials* **3,** 27 (2018).

143. Takahashi, S. & Maekawa, S. Spin injection and detection in magnetic nanostructures. *Physical Review B* **67,** 052409 (2003).

144. Riego, P. *et al.* Absence of detectable current-induced magneto-optical Kerr effects in Pt, Ta, and W. *Applied Physics Letters* **109,** 172402 (2016).

145. Liu, L., Moriyama, T., Ralph, D. C. & Buhrman, R. A. Spin-Torque Ferromagnetic Resonance Induced by the Spin Hall Effect. *Physical Review Letters* **106,** 036601 (2011).

146. Jungwirth, T., Wunderlich, J. & Olejník, K. Spin Hall effect devices. *Nature Materials* **11,** 382–390 (2012).

147. Valenzuela, S. Non local electronic spin detection, spin accumulation and the spin Hall effect. *International Journal of Modern Physics B* **23,** 2413–2438 (2009).

148. Niimi, Y. & Otani, Y. Reciprocal spin Hall effects in conductors with strong spin–orbit coupling: a review. *Reports on Progress in Physics* **78,** 124501 (2015).

149. Liu, L., Chen, C.-T. & Sun, J. Z. Spin Hall effect tunnelling spectroscopy. *Nature Physics* **10,** 561–566 (2014).

150. Cao, Y. *et al.* Prospect of Spin-Orbitronic Devices and Their Applications. *iScience* **23,** 101614 (2020).

151. Liu, Y., Yuan, Z., Wesselink, R. J. H., Starikov, A. A. & Kelly, P. J. Interface Enhancement of Gilbert Damping from First Principles. *Physical Review Letters* **113,** 207202 (2014).

152. Dey, R., Prasad, N., Register, L. F. & Banerjee, S. K. Conversion of spin current into charge current in a topological insulator: Role of the interface. *Physical Review B* **97,** 174406 (2018).

153. Zhu, L., Ralph, D. C. & Buhrman, R. A. Spin-Orbit Torques in Heavy-Metal–Ferromagnet Bilayers with Varying Strengths of Interfacial Spin-Orbit Coupling. *Physical Review Letters* **122,** 077201 (2019).

154. Gupta, K., Wesselink, R. J. H., Yuan, Z. & Kelly, P. J. Spin transport at finite temperatures: A first-principles study for ferromagnetic|nonmagnetic interfaces. *Physical Review B* **104,** 205426 (2021).

155. Buttiker, M. Symmetry of electrical conduction. *IBM Journal of Research and Development* **32,** 317–334 (1988).

156. Torres, W. S. *et al.* Calculation method of spin accumulations and spin signals in nanostructures using spin resistors. *The European Physical Journal B* **91** (2018).

157. Pham, V. T. *et al.* Ferromagnetic/Nonmagnetic Nanostructures for the Electrical Measurement of the Spin Hall Effect. *Nano Letters* **16,** 6755–6760 (2016).

158. Omori, Y. *et al.* Inverse spin Hall effect in a closed loop circuit. *Applied Physics Letters* **104,** 242415 (2014).

159. Daire, A., Goeke, W. & Tupta, M. A. New instruments can lock out lock-ins. *Keithley Instruments, Inc. http://www.tek.com/sites/tek.com/files/media/ document /resources/Lock-In% 20WP. pdf* (2006).

160. Pedersen, R. & Vernon Jr, F. Effect of film resistance on low-impedance tunneling measurements. *Applied Physics Letters* **10,** 29–31 (1967).

161. Pomeroy, J. M. & Grube, H. "Negative resistance" errors in four-point measurements of tunnel junctions and other crossed-wire devices. *Journal of Applied Physics* **105,** 094503 (2009).

162. Yan, W. *et al.* Large room temperature spin-to-charge conversion signals in a few-layer graphene/Pt lateral heterostructure. *Nature Communications* **8,** 661 (2017).

163. Nguyen, M.-H., Ralph, D. C. & Buhrman, R. A. Spin Torque Study of the Spin Hall Conductivity and Spin Diffusion Length in Platinum Thin Films with Varying Resistivity. *Physical Review Letters* **116,** 126601 (12 2016).

164. Zahnd, G. *et al.* Spin diffusion length and polarization of ferromagnetic metals measured by the spin-absorption technique in lateral spin valves. *Physical Review B* **98,** 174414 (2018).

165. Wang, L. *et al.* Giant Room Temperature Interface Spin Hall and Inverse Spin Hall Effects. *Physical Review Letters* **116,** 196602 (2016).

166. Bauer, G. E., Saitoh, E. & Van Wees, B. J. Spin caloritronics. *Nature Materials* **11,** 391–399 (2012).

167. Sayed, S., Hong, S. & Datta, S. Transmission-Line Model for Materials with Spin-Momentum Locking. *Physical Review Applied* **10,** 054044 (2018).

168. Garello, K. *et al.* Symmetry and magnitude of spin–orbit torques in ferromagnetic heterostructures. *Nature Nanotechnology* **8,** 587–593 (2013).

169. Liu, L. *et al.* Spin-torque switching with the giant spin Hall effect of tantalum. *Science* **336,** 555–558 (2012).

170. Mellnik, A. *et al.* Spin-transfer torque generated by a topological insulator. *Nature* **511,** 449–451 (2014).

171. Ghiasi, T. S., Ingla-Aynés, J., Kaverzin, A. A. & van Wees, B. J. Large proximity-induced spin lifetime anisotropy in transition-metal dichalcogenide/graphene heterostructures. *Nano Letters* **17,** 7528–7532 (2017).

172. Benitez, L. A. *et al.* Tunable room-temperature spin galvanic and spin Hall effects in van der Waals heterostructures. *Nature materials* **19,** 170–175 (2020).

173. Herling, F. *et al.* Gate tunability of highly efficient spin-to-charge conversion by spin Hall effect in graphene proximitized with $WSeO_2$. *APL Materials* **8,** 071103 (2020).

174. Geuzaine, C. GetDP: a general finite-element solver for the de Rham complex. *Proceedings in Applied Mathematics and Mechanics* **7,** 1010603–1010604 (2007).

175. Geuzaine, C. & Remacle, J.-F. Gmsh: A 3-D finite element mesh generator with built-in pre- and post-processing facilities. *International Journal for Numerical Methods in Engineering* **79,** 1309–1331 (2009).

176. Jan, J.-P. *Solid State Physics* (eds Seitz, F. & Turnbull, D.) 1–96 (Academic Press, New York, 1957).

177. McGuire, T. & Potter, R. Anisotropic magnetoresistance in ferromagnetic 3d alloys. *IEEE Transactions on Magnetics* **11,** 1018–1038 (1975).

178. Kokado, S., Tsunoda, M., Harigaya, K. & Sakuma, A. Anisotropic Magnetoresistance Effects in Fe, Co, Ni, Fe4N, and Half-Metallic Ferromagnet: A Systematic Analysis. *Journal of the Physical Society of Japan* **81,** 024705 (2012).

179. Pippard, A. B. *Magnetoresistance in metals* (Cambridge university press, 1989).

180. Li, Z. *et al.* Planar Hall effect in $PtSeO_2$. *Journal of Applied Physics* **127,** 054306 (2020).

181. Mizuno, H., Isshiki, H., Kondou, K., Zhu, Y. & Otani, Y. Influence of planar Hall effect on the output signal in a T-shaped spin conversion device. *Applied Physics Letters* **119,** 092401 (2021).

182. Campbell, I., Fert, A. & Pomeroy, R. Evidence for two current conduction iron. *Philosophical Magazine* **15,** 977–983 (1967).

183. Vansteenkiste, A. *et al.* The design and verification of MuMax3. *AIP advances* **4,** 107133 (2014).

184. Vernon, S. P., Lindsay, S. M. & Stearns, M. B. Brillouin scattering from thermal magnons in a thin Co film. *Physical Review B* **29,** 4439–4442 (1984).

185. Shirane, G., Minkiewicz, V. J. & Nathans, R. Spin Waves in 3d Metals. *Journal of Applied Physics* **39,** 383–390 (1968).

186. Pai, C.-F. *et al.* Spin transfer torque devices utilizing the giant spin Hall effect of tungsten. *Applied Physics Letters* **101,** 122404 (2012).

187. Hao, Q. & Xiao, G. Giant Spin Hall Effect and Switching Induced by Spin-Transfer Torque in a $\mathrm{W/Co_{40}Fe_{40}B_{20}/MgO}$ Structure with Perpendicular Magnetic Anisotropy. *Physical Review Applied* **3,** 034009 (2015).

188. Petroff, P., Sheng, T. T., Sinha, A. K., Rozgonyi, G. A. & Alexander, F. B. Microstructure, growth, resistivity, and stresses in thin tungsten films deposited by rf sputtering. *Journal of Applied Physics* **44,** 2545–2554 (1973).

189. Hao, Q., Chen, W. & Xiao, G. Beta (β) tungsten thin films: Structure, electron transport, and giant spin Hall effect. *Applied Physics Letters* **106,** 182403 (2015).

190. Choi, D. Phase transformation in thin tungsten films during sputter deposition. *Microelectronic Engineering* **183-184,** 19–22 (2017).

191. Costa, M., Costa, A., Hu, J., Wu, R. & Muniz, R. β-tungsten: a promising metal for spintronics. *Journal of Physics: Condensed Matter* **30,** 305802 (2018).

192. Lita, A. E. *et al.* Tuning of tungsten thin film superconducting transition temperature for fabrication of photon number resolving detectors. *IEEE Transactions on Applied Superconductivity* **15,** 3528–3531 (2005).

193. Rossnagel, S. M., Noyan, I. C. & Cabral Jr, C. Phase transformation of thin sputter-deposited tungsten films at room temperature. *Journal of Vacuum Science & Technology B: Microelectronics and Nanometer Structures Processing, Measurement, and Phenomena* **20,** 2047–2051 (2002).

194. Radić, N. *et al.* Sputter-deposited amorphous-like tungsten. *Surface and Coatings Technology* **180-181,** 66–70 (2004).

195. Demasius, K.-U. *et al.* Enhanced spin-orbit torques by oxygen incorporation in tungsten films. *Nature Communications* **7,** 10644 (2016).

196. Noyan, I., Shaw, T. & Goldsmith, C. Inhomogeneous strain states in sputter deposited tungsten thin films. *Journal of Applied Physics* **82,** 4300–4302 (1997).

197. Kilbane, F. M. & Habig, P. S. Superconducting transition temperatures of reactively sputtered films of tantalum nitride and tungsten nitride. *Journal of Vacuum Science and Technology* **12,** 107–109 (1975).

198. Wen, M. *et al.* Growth, stress and hardness of reactively sputtered tungsten nitride thin films. *Surface and Coatings Technology* **205,** 1953–1961 (2010).

199. Lee, J.-S., Cho, J. & You, C.-Y. Growth and characterization of α and β-phase tungsten films on various substrates. *Journal of Vacuum Science & Technology A* **34,** 021502 (2016).

200. Sui, X. *et al.* Giant enhancement of the intrinsic spin Hall conductivity in β-tungsten via substitutional doping. *Physical Review B* **96,** 241105 (2017).

201. Derunova, E. *et al.* Giant intrinsic spin Hall effect in W_3Ta and other A15 superconductors. *Science advances* **5,** eaav8575 (2019).

202. Takeuchi, Y. *et al.* Spin-orbit torques in high-resistivity-W/CoFeB/MgO. *Applied Physics Letters* **112,** 192408 (2018).

203. Coester, B. *et al.* Enhanced spin Hall conductivity in tungsten-copper alloys. *Journal of Magnetism and Magnetic Materials* **523,** 167545 (2021).

204. Sagasta, E. *et al.* Spin diffusion length of Permalloy using spin absorption in lateral spin valves. *Applied Physics Letters* **111,** 082407 (2017).

205. Trier, F. *et al.* Oxide spin-orbitronics: spin-charge interconversion and topological spin textures. *Nature Reviews Materials* (2021).

206. Manipatruni, S., Nikonov, D. E. & Young, I. A. *Perpendicular magnetoelectric spin orbit logic.* US Patent 11,038,099. (2021).

207. Manipatruni, S., Nikonov, D. E. & Young, I. A. *Magnetoelectric spin orbit logic with paramagnets.* US Patent 11,114,144. (2021).

208. Manipatruni, S., Nikonov, D. E. & Young, I. A. *Magnetic state element for circuits.* US Patent 11,139,389. (2021).

209. Lin, C.-C. *et al.* Experimental demonstration of integrated magneto-electric and spin-orbit building blocks implementing energy-efficient logic. *2019 IEEE International Electron Devices Meeting (IEDM),* 37.3.1–37.3.4 (2019).

210. Vaz, D. C. *et al.* Demonstration of a magneto-electric spin-orbit device. *2021 IEEE International Electron Devices Meeting (IEDM),* accepted (2021).

Glossary

1D	one-dimensional
2D	two-dimensional
2DEG	two-dimensional electron gas
3D	three-dimensional
AC	alternating current
AHE	anomalous Hall effect
ALU	arithmetic logic unit
BC	boundary condition
CMOS	complementary metal-oxide-semiconductors
CPU	central processing unit
DC	direct current
e-beam	electron-beam
EBL	electron-beam lithography
FEM	finite element method
FM	ferromagnetic metal
FMR	ferromagnetic resonance
GIXRD	grazing incidence x-ray diffraction
GMR	giant magnetoresistance
IREE	inverse Rashba-Edelstein effect
ISHE	inverse spin Hall effect
LSV	lateral spin valve
ME	magneto-electric
MESO	magneto-electric spin-orbit
MR	magnetoresistance
MRAM	magnetoresistive random access memory
MTJ	magnetic tunnel junction
NM	non-magnetic metal
O	oxide

OHE	ordinary Hall effect
PHE	planar Hall effect
PPMS	physical property measurement system
PVD	physical vapour deposition
REE	Rashba-Edelstein effect
SCI	spin-charge interconversion
SEM	Scanning electron microscopy
SHE	spin Hall effect
SO	spin-orbit
SOC	spin-orbit coupling
SOM	spin-orbit coupling material
SOT	spin-orbit torque
STT	spin-transfer torque
TEM	Transmission electron microscopy
TMR	tunneling magnetoresistance

List of Publications

This thesis is based on the following publications

Spin-orbit magnetic state readout in scaled ferromagnetic/heavy metal nanostructures.
Van Tuong Pham*, **Inge Groen***, Sasikanth Manipatruni, Won Young Choi, Dmitri E. Nikonov, Edurne Sagasta, Chia-Ching Lin, Tanay A. Gosavi, Alain Marty, Luis E. Hueso, Ian A. Young & Fèlix Casanova.
Nature Electronics **3**, 309–315 (2020).

Disentangling Spin, Anomalous, and Planar Hall Effects in Ferromagnet—Heavy-Metal Nanostructures.
Inge Groen, Van Tuong Pham, Naëmi Leo, Alain Marty, Luis E. Hueso & Fèlix Casanova.
Physical review applied **15**, 044010 (2021).

Interfacial spin-charge interconversion in metallic Py/Cu/W lateral spin valves.
Inge Groen, Van Tuong Pham, Stefan Ilic, Won Young Choi, Edurne Sagasta, Nerea Ontoso, Diogo C. Vaz, Isabal Arango, Andrey Chuvilin, F. Sebastian Bergeret, Luis E. Hueso, Ilya V. Tokatly, & Fèlix Casanova.
In preparation.

Other publications:

Omnidirectional spin-to-charge conversion in graphene/$NbSe_2$ van der Waals heterostructures.
Josep Ingla-Aynés, **Inge Groen**, Franz Herling, Nerea Ontoso, C.K. Safeer, Fernando de Juan, Luis Hueso, Marco Gobbi, Fèlix Casanova.
submitted (2021).

Demonstration of a magneto-electric spin-orbit device.
Diogo C. Vaz*, Chia-Ching Lin*, John Plombon, Won Young Choi, **Inge Groen**, Isabel Arango, Van Tuong Pham, Dmitri E. Nikonov, Hai Li, Punyashloka Debashis, Scott Clendenning, Tanay A. Gosavi, Vincent Garcia, Stephane Fusil, Manuel Bibes, Yen-Lin Huang, Bhagwati Prasad, Ramamoorthy Ramesh, Felix Casanova & Ian A. Young.
2021 IEEE International Electron Devices Meeting (IEDM), accepted (2021).

Large spin-charge interconversion induced by interfacial spin-orbit coupling in a highly conducting all-metallic system.
Van Tuong Pham, Haozhe Yang, Won Young Choi, Alain Marty, **Inge Groen**, Andrey Chuvilin, F. Sebastian Bergeret, Luis E. Hueso, Ilya V. Tokatly & Fèlix Casanova.
Physical Review B 104, 184410 (2021).

Experimental demonstration of integrated magneto-electric and spin-orbit building blocks implementing energy-efficient logic.
Chia-Ching Lin, Tanay A. Gosavi, Dmitri E. Nikonov, Yen-Lin Huang, Bhagwati Prasad, Won Young Choi, **Inge Groen**, Jun-Yang Chen, D.C. Mahendra, Huichu Liu, Kaan Oguz, Emily S. Walker, John Plombon, Benjamin Buford, Carl H. Naylor, Jian-Ping Wang, Fèlix Casanova, Ramesh Ramamoorthy & Ian A. Young.
2019 IEEE International Electron Devices Meeting (IEDM), 37–3 (2019).

Two-dimensional superconductivity at the (111) $LaAlO_3$/$SrTiO_3$ interface.
A. M. R. V. L. Monteiro, D. J. Groenendijk, **I. Groen**, J. de Bruijckere, R. Gaudenzi, H. S. J. van der Zant, & A. D. Caviglia.
Physical Review B **96**, 020504(R) (2017).

* equal contribution